

16-1

A NUMERICAL STUDY OF DISPLACEMENT BODY AND CURVATURE EFFECTS
ON INCOMPRESSIBLE AND COMPRESSIBLE LAMINAR BOUNDARY LAYERS

by

Stephen Fay Wornom

Thesis submitted to the Graduate Faculty of the
Virginia Polytechnic Institute and State University
in partial fulfillment of the requirements for the degree of

DOCTOR OF PHILOSOPHY

in

Engineering Mechanics

May 1971

(NASA-TM-X-67593) A NUMERICAL STUDY OF
DISPLACEMENT BODY AND CURVATURE EFFECTS ON
INCOMPRESSIBLE AND COMPRESSIBLE LAMINAR
BOUNDARY LAYERS Ph.D. Thesis - Va. S.F.
Wornom (NASA) May 1971 218 p

N72-15280

Unclas

CSCL 20D G3/12 13818

LA (NASA CR OR TMX OR AD NUMBER)

(CATEGORY)

Reproduced by
NATIONAL TECHNICAL
INFORMATION SERVICE
U S Department of Commerce
Springfield VA 22151

A NUMERICAL STUDY OF DISPLACEMENT BODY AND CURVATURE EFFECTS
ON INCOMPRESSIBLE AND COMPRESSIBLE LAMINAR BOUNDARY LAYERS

by

Stephen Fay Wornom

Thesis submitted to the Graduate Faculty of the
Virginia Polytechnic Institute and State University
in partial fulfillment of the requirements for the degree of

DOCTOR OF PHILOSOPHY

in

Engineering Mechanics

APPROVED:

M. J. Werle
Chairman, Dr. M. J. Werle

R. Thomas Davis
Dr. R. T. Davis

F. J. Maher
Prof. F. J. Maher

R. P. McNitt
Dr. R. P. McNitt

D. T. Mook
Dr. D. T. Mook

Leon Rutland
Dr. L. W. Rutland

Daniel Frederick
Dr. D. Frederick

May 1971
Blacksburg, Virginia

A NUMERICAL STUDY OF DISPLACEMENT BODY
AND CURVATURE EFFECTS ON INCOMPRESSIBLE
AND COMPRESSIBLE LAMINAR BOUNDARY LAYERS

By Stephen Fay Wornom

ABSTRACT

A numerical study has been made to develop a technique for studying displacement body and curvature effects on incompressible and compressible laminar boundary layers.

This technique has been applied to study such effects on incompressible flow around cylinders at moderate to low Reynolds numbers and for compression ramps at hypersonic Mach numbers by employing a finite-difference method to obtain numerical solutions.

The results indicate the technique can be applied successfully in both regimes and does predict the correct trend in regions of large curvature and displacement body effects.

This study concludes that curvature corrections should only be attempted in cases where all displacement effects can be fully accounted for.

TABLE OF CONTENTS

	PAGE
TABLE OF CONTENTS	ii
LIST OF FIGURES	vi
LIST OF TABLES	xi
NOMENCLATURE	xii
CHAPTER	
I. FORMULATION OF THE PROBLEM	
1.1 Introduction	1
1.2 Formulation of the Governing Equations	5
1.3 Summary of Governing Equations in Boundary- Layer Variables	20
1.4 The Governing Equations in Similarity Variables .	23
1.5 Boundary-Layer Properties	28
1.6 Reduction to the Incompressible Case	30
II. LONGITUDINAL CURVATURE AND DISPLACEMENT-SPEED EFFECTS ON INCOMPRESSIBLE BOUNDARY LAYERS	
2.1 Introduction	35
2.2 Governing Equations	35
2.3 The Pressure Gradient Parameter, β_e	38
a. General Discussion	38
b. Solutions Aft of a Stagnation Point	42
c. Solutions in a Stagnation point Region	44

CHAPTER	PAGE
2.4 Outline of the Numerical Solution Technique . . .	48
2.5 Discussion of Results	49
a. Wall Pressure Data	49
b. Curvefit Representation of the Pressure Distributions	51
c. Effects of Curvature and Displacement Speed on Wall Pressure Distributions	54
d. Displacement-Body Effects	55
e. The Viscous Pressure Gradient Parameter, β_v	56
f. Shear Stress Distributions	58
g. Comparisons With Experimental and Numerical Shear Stress Data	60
h. Curvefitting Difficulties	65
2.6 Conclusions	67
III. A STUDY OF LONGITUDINAL CURVATURE EFFECTS ON COMPRESSIBLE BOUNDARY LAYER FLOW WITH DISPLACEMENT THICKNESS INTERACTION	
3.1 Introduction	69
3.2 Governing Equations	71
a. Viscous Region	71
b. Inviscid Region	71

CHAPTER	PAGE
3.3 Solution at a General Station	80
a. Initial Estimates of Inviscid Properties . . .	81
b. Interaction Technique	81
3.4 Initial Profiles	86
a. Hypersonic Limit Method	86
b. Modified Hypersonic Limit Method	92
3.5 Discussion of Results	94
a. Flat-Plate Studies	94
1. Initialization Procedures and Effects . . .	95
2. Downstream Instabilities	96
3. Comparison of Experimental and Theoretical	
Flat-Plate Results	98
b. Compression Ramp Studies	101
1. Geometry and Flow Conditions	101
2. Displacement Effects	102
3. Curvature Effects	103
4. The Complete Second-Order Solution	106
3.6 Conclusions	109
IV. GENERAL CONCLUSIONS	111
V. BIBLIOGRAPHY	112
VI. APPENDIX A: Numerical Analysis Section	117
VII. APPENDIX B: The Blasius Shear Stress for a Given Wall	
Pressure Distribution	122

CHAPTER	PAGE
VIII. ACKNOWLEDGEMENTS	197
IX. VITA	198

LIST OF FIGURES

FIGURE	PAGE
2.1. Coordinate system	130
2.2. Surface pressure distributions at $Re_d = 174, 175,$ and 177	131
2.3. Curvefits of the surface pressure distributions	
(a) $Re_d = 40$	132
(b) $Re_d = 174$	133
(c) $Re_d = 175$	134
(d) $Re_d = 177$	135
(e) $Re_d = 200$	136
2.4. Theoretical wall pressure distributions	
(a) $Re_d = 40$	137
(b) $Re_d = 174$	138
(c) $Re_d = 175$	139
(d) $Re_d = 177$	140
(e) $Re_d = 200$	141
2.5 Theoretical displacement bodies	
(a) $Re_d = 40$	142
(b) $Re_d = 174$	143
(c) $Re_d = 175$	144
(d) $Re_d = 177$	145
(e) $Re_d = 200$	146

FIGURE	PAGE
2.6. First-order displacement thickness for a potential velocity distribution	147
2.7. Viscous pressure gradient parameter distribution at $Re_d = 175$	148
2.8. Surface shear stress distributions	
(a) $Re_d = 40$	149
(b) $Re_d = 174$	150
(c) $Re_d = 175$	151
(d) $Re_d = 177$	152
(e) $Re_d = 200$	153
2.9. Test tunnel wall effects on experimental pressure data $Re_d = 175$	154
2.10. Test tunnel wall effects on computed shear stress results $Re_d = 175$	155
2.11. Comparison of experimental and numerical shear stress distributions $Re_d = 175$	156
2.12. Comparison of experimental and analytical shear stress distributions $Re_d = 174$	157
2.13. Comparison of higher-order boundary-layer solutions with Navier-Stokes solutions at $Re_d = 40$	158
2.14. Comparison of higher-order boundary-layer solutions with Navier-Stokes solutions at $Re_d = 200$	159
2.15. Inviscid pressure gradient parameter distribution using curvefit A at $Re_d = 200$	160

FIGURE	PAGE
2.16. Shear stress distribution for curvefit A at $Re_d = 200$	161
2.17. Inviscid surface pressure gradient distribution for curvefit A at $Re_d = 200$	162
2.18. Inviscid pressure gradient parameter distribution using curvefit B at $Re_d = 200$	163
2.19. Inviscid surface pressure gradient distribution for curvefit B at $Re_d = 200$	164
2.20. Shear stress distribution for curvefit B at $Re_d = 200$	165
2.21. Comparison of wall pressure curvefits to experimental data at $Re_d = 174$	166
2.22. Effect of wall pressure curvefits on surface shear stress at $Re_d = 174$	167
3.1. Variation of assumed and calculated values of δ'' . . .	168
3.2. Influence of initial profiles on δ''	169
3.3. Influence of initial profiles on wall pressure	170
3.4. Effect of step size on flat-plate leading-edge solution	171
3.5. Effect of step size on wall pressure	172
3.6. The effect of derivative laws on oscillatory behavior	173
3.7. Effect of averaging V profiles on wall pressure . . .	174

FIGURE	PAGE
3.8. Influence of averaging the normal velocity for the $M_\infty = 9.6$ flat-plate case	175
3.9. Induced pressure on nearly insulated flat plate at $M_\infty = 9.6$	176
3.10. Displacement-body effects on flat-plate displacement thickness	177
3.11. Displacement-body effect on flat-plate skin friction . .	178
3.12. Induced pressure on flat plate at $M_\infty = 12.0$	179
3.13. Comparison of theory with experiment - - hypersonic flat- plate heat transfer distribution	180
3.14. Displacement-body effects on flat-plate displacement thickness	181
3.15. Displacement-body influence on flat-plate skin friction	182
3.16. Displacement-body effects on wall pressure - - no curvature correction	183
3.17. Boundary-layer growth over a cubic body	184
3.18. Displacement-body effects on wall heat transfer	185
3.19. The effect of inviscid curvature corrections on wall pressure	186
3.20. Influence of inviscid curvature correction	187
3.21. Effect of curvature on noninteracting solution	188

FIGURE	PAGE
3.22. The influence of displacement-body and curvature effects on wall pressure	189
3.23. The influence of displacement and curvature effects on wall heat transfer	190
3.24. The influence of displacement-body and curvature effects on skin friction	191
3.25. Effect of free-stream Mach number on wall pressure . .	192
3.26. Free-stream Mach number influence on wall heat transfer	193
3.27. Effect of free-stream unit Reynolds number on wall pressures	194
3.28. Effect of free-stream unit Reynolds number on heat transfer to wall	195
3.29. Skin friction distribution near separation	196

LIST OF TABLES

TABLE	PAGE
I. Numerical Values of dU_e/ds at the Stagnation Point . . .	126
II. Coefficients for Equation (2.5-3)	127
III. Data Points Used in the Wall Pressure Curvefits	128
IV. Coefficients for Equation (2.5-5)	129

NOMENCLATURE

a^*	cylinder radius
a_{2n}	wall pressure series expansion coefficients for equation (2.5-5)
A_2	wall pressure series expansion constant from equation (2.3-23)
b_2, b_4, \dots	surface velocity series expansion coefficients for equation (2-B)
B	constant defined in equation (3.2-24c)
\underline{c}^*	distance from cylinder centerline to leading edge of wake splitter plate
\bar{C}	strong interaction pressure law constant appearing in equation (3.4-6)
C'	viscosity law parameter defined in equation (1.2-7b)
C^*	viscosity law constant = 198.6°R for air
$C(s)$	linear viscosity law proportionally constant in equation (1.2-8a)
C_∞	the value of $C(s)$ for constant wall temperature
C_2, C_4, \dots	wall pressure series expansion coefficients for equation (2.5-3)
C_f	skin friction coefficient: $C_f = \tau_{wall}^* / \frac{1}{2} \rho_\infty^* U_\infty^{*2}$
\bar{C}_f	C_f / ϵ
$C_{p_{wall}}$	wall pressure coefficient: $C_{p_{wall}} = (p_{wall}^* - p_\infty^*) / \frac{1}{2} \rho_\infty^* U_\infty^{*2}$

C_p^*	specific heat at constant pressure
d^*	cylinder diameter
D_2, D_2, \dots	wall pressure series expansion coefficients for equation (2.5-3)
e	the constant of equation (7-B): $e = \pi/360$
E_2, E_4, \dots	Gortler series expansion coefficients - see equation (3-B)
f_0'', f_2'', \dots	expansion coefficients defined in equation (4-B)
F	normalized s-component of velocity in the boundary layer: $F = u/u_m$
G	normalized total enthalpy: $G = H/H_e$
h	longitudinal coordinate scale factor: $h = 1 + \kappa n$
\tilde{h}^*	width of the test facility test section
H	nondimensional total enthalpy: $H = T + u^2/2$
H_e	inviscid total enthalpy constant
I	curvature integral defined by equation (2.3-2)
\tilde{I}	curvature integral defined by equation (1.6-3e); $\tilde{I} = h^2 I$
I_o	I evaluated at $s = 0$
IP, IQ	indices for the surface pressure expansions given by equation (2.5-3)
k^*	heat conductivity coefficient
L^*	dimensional length for flat-plate study
λ	viscosity parameter: $\lambda = (\rho\mu)/(\rho_e\mu_e)$
M_e	inviscid Mach number at $n = 0$

n	nondimensional distance normal to the surface - see Figure 2.1: $n = n^*/a^*$
N	stretched normal coordinate $N = n/\epsilon$
p	nondimensional pressure in the boundary-layer region: $p = p^*/\rho_\infty^* U_\infty^{*2}$
P	nondimensional pressure in the inviscid region $P = P^*/\rho_\infty^* U_\infty^{*2}$
$q_{F.P.}$	heat transfer to flat plate, $dP_e/ds = 0$
q_{wall}	nondimensional heat transfer coefficient, $q_{wall} = q_{wall}^*/\rho_\infty^* U_\infty^{*3}$
q_{wall}^*	dimensional heat transfer to wall $q_{wall}^* = (k^* \partial T^*/\partial n^*)_{wall}$
Q	integral defined by equation (3.4-10) or (3.4-19)
r	nondimensional cylindrical coordinate of a point s, n - see Figure 2.1: $r = r^*/a^*$
r_o	cylindrical radius of an axisymmetric body - see Figure 2.1: $r_o = r_o^*/a^*$
R	r/r_o
Re	for incompressible study: $Re = \text{Reynolds number}$ based upon the cylinder radius $Re = \frac{\rho_\infty^* U_\infty^* a^*}{\mu_\infty^*}$ for compressible study: $Re = \frac{\rho_\infty^* U_\infty^* s^*}{\mu_r^*(T_r^*)}$
Re_d	for incompressible study: $Re_d = \text{Reynolds number}$ based upon cylinder diameter

Re_{s_∞}	compressible study: Reynolds number based upon free-stream conditions $Re_{s_\infty} = \frac{\rho_\infty^* U_\infty^* s^*}{\mu_\infty^*}$
s	nondimensional surface distance - see Figure 2.1: $s = s^*/a^*$
\tilde{s}	$s/2$
St_∞	Staunton number, $St_\infty = \frac{q_{wall}^*}{\rho_\infty^* U_\infty^* (H_\infty^* - H_{wall}^*)}$
\overline{St}_∞	$\overline{St}_\infty = St_\infty/\epsilon$
T_1, T_2	Chebyshev polynomials - see equation (2.5-4)
T	temperature
T_r^*	reference temperature: $T_r^* = U_\infty^{*2}/C_p^*$
u	nondimensional longitudinal velocity in the boundary layer: $u = u^*/U_\infty^*$
u_1, u_2	order velocity terms: $u = u_1 + u_2 + \dots$
U	nondimensional longitudinal velocity in the inviscid region: $U = U^*/U_\infty^*$
U_{e1}, U_{e2}	order surface velocity terms: $U_e = U_{e1} + U_{e2} + \dots$
U'_0	stagnation point velocity gradient: $U'_0 = (dU_e/ds)_s = 0$
v	nondimensional normal velocity component in the boundary layer: $v = v^*/U_\infty^*$
\overline{v}	nondimensional normal velocity component in Navier-Stokes equations
V	transformed normal velocity in the boundary layer - see equation (1.4-6a)

\tilde{V}	nondimensional velocity component in the inviscid region: $\tilde{V} = \tilde{V}^*/U_\infty^*$
V_{e1}, V_{e2}	ordered normal velocity terms, $V_e = V_{e1} + V_{e2} + \dots$
\bar{W}	irrotational constant defined by equation (1.2-40)
x	arguments of the Chebyshev polynomials - see equation (2.5-4)
$\bar{\chi}$	hypersonic similarity parameter; $\bar{\chi} = M_\infty^3 \sqrt{\frac{C_\infty}{Re_{s_\infty}}}$
α	empirical constant in equation (2.3-22a)
$\bar{\alpha}$	proportionality constant appearing in equation (3.4-15)
β	inviscid pressure gradient parameter - see equation (1.4-15)
$\bar{\beta}$	defined in equation (3.4-5b)
β_v	viscous pressure gradient parameter - see equation (2.2-5)
δ	boundary-layer displacement thickness - see equation (1.5-6)
$\bar{\delta}$	boundary-layer displacement thickness measured in the η coordinate
δ_1	first-order displacement thickness: $\delta_1 = \int_0^\infty \left(1 - u_1/U_{e1} \right) dN$
θ_1	first-order momentum thickness $\theta_1 = \int_0^\infty \frac{u_1}{U_{e1}} \left(1 - \frac{u_1}{U_{e1}} \right) dN$

ΔG	an increment of the representative function G
ϵ	$1/\sqrt{\text{Re}}$
ξ	transformed surface coordinate: see equation (1.4-1)
γ	ratio of specific heats
σ	Prandtl number: $\sigma = \frac{\mu^* C_p^*}{k^*}$
θ_{wall}	surface inclination angle
κ	nondimensional surface curvature - see Figure 2.1: $\kappa = \kappa^* a^*$
ϕ	angular position relative to the cylinder stagnation point
η	transformed normal coordinate: see equation (1.4-2)
ρ	mass density
$\bar{\rho}$	mass density in inviscid region
μ	viscosity
ω	vorticity function
Ω_{wall}	vorticity function reported by Kawaguti (1953) and Thoman and Szewczyk (1969)
τ_{wall}^*	wall shear stress: $\tau_{\text{wall}}^* = (\mu^* \partial u^* / \partial n^*)_{\text{wall}}$

Superscripts

$*$	dimensional quantities
j	0 for 2-D flow and 1 for axisymmetric flow

Subscripts

e	inviscid quantities evaluated at $n = 0$
w	viscous quantities evaluated at $N = 0$

∞	inviscid quantities in the free stream
s,N,	derivative with respect to the respective subscript
wall	viscous quantities evaluated at $N = 0$
F. P.	flat-plate solution ($dP_e/ds = 0$) at $N = 0$
o	denotes stagnation values
m	denotes viscous matching quantity
NS	denotes new station value
OS	denotes old station value
r	reference quantity

I. FORMULATION OF THE PROBLEM

1.1 Introduction

Since the 1950's, much attention has been given to higher-order boundary-layer theory due to the academic challenge it presents and also in hope that this inclusion of higher-ordered terms would enable one to extend the boundary-layer concept to flow problems which normally would be considered to exceed the limits of classical or first-order theory.

Even though higher-ordered terms were beginning to be calculated in the 1950's, it was only recently, in the 1960's, that all second-order contributions were correctly identified. This was accomplished by Van Dyke (1962a, 1962b) for incompressible theory and independently by Van Dyke (1962c), Maslen (1963), and Lenard (1962) for compressible theory, all of whom employed the method of matched asymptotic expansions which results in two separate sets of governing equations - one for the classical or first-order contribution and another for the second-order contributions.

Effects to be studied here which were found to be of higher order in an asymptotic sense can generally be classified as arising either due to the surface curvature of the body under consideration or due to its boundary layer interacting with the external flow field. Of the two second-order effects which will appear in this study, perhaps the easiest to understand and usually the most difficult to calculate

is what is termed the displacement-body or displacement-speed effect which arises due to the boundary layer interacting with the external mainstream. This effect appears as a result of the viscosity influence near a solid surface which tends to slow down the fluid in the region near the wall and force it outward so that the effective body presented to the mainstream is the original body plus the displacement thickness of the boundary layer. Since the boundary-layer thickness is not known beforehand, the difficulty in computing this effect is immediately recognized. The other higher-order effect considered here is that of surface curvature and presents no unusual difficulties.

In addition to clearly indicating what the second-order contributions are, another advantage of filtering out what are normally higher-order effects as done by Van Dyke, Maslen, and Lenard is that all higher-order equations are linear and therefore can be divided into several additive effects each of which has a simpler physical meaning. However, the purpose of this study is to examine problems where there are large displacement and curvature effects. Thus, the distinction between a first-order and a normally second-order effect may be small and as such some advantage may be gained if we do not try to separate them as normally done but rather seek only to filter out those strictly third-order and higher contributions which appear in the analysis. The final equations will therefore contain both the first-order and second-order contributions given by Van Dyke, Maslen, and Lenard plus some additional third-order terms.

Most studies of higher-order effects have been made adopting the equations which have the higher-order contributions filtered out. In reviewing the literature, we examine subsonic and supersonic external flows separately since there appear basic differences in the nature of their governing equations which affect the ease with which displacement effects can be computed. Attention here is paid to cases where displacement effects have been computed since once these are known the effects of surface curvature can be easily handled. For subsonic theory, the effect of displacement speed cannot usually be calculated directly owing to the fact that the external governing equations are elliptic thereby making its effect dependent upon the entire course of the boundary layer. Thus, there have been very few cases where displacement effects have been computed in subsonic theory. Kuo (1953) calculated the displacement effect for flow over a finite flat plate. Few shapes other than the finite flat plate have been investigated, of these Van Dyke (1964) treated the parabolic cylinder where he was able to calculate the displacement effect only near the leading edge. Devan (1964) treated the Rankine half-body numerically.

In supersonic or hypersonic flow, the inviscid or outer flow equations are hyperbolic thereby making the displacement effect local in influence and therefore simpler in theory to calculate. Maslen (1952) treated the semi-infinite plate with its mixed subsonic and supersonic external flow regimes employing linearized subsonic and supersonic inviscid theory for the flow due to displacement effects. Most investigations of compressible second-order effects have been

applied to blunt bodies in hypersonic flow. Individual second-order effects at a stagnation point have been calculated by Lenard (1962), Davis and Flügge-Lotz (1964a), and Fannelöp and Flügge-Lotz (1965), whereas extended solutions around blunt bodies were first reported by Davis and Flügge-Lotz (1964b) for a sphere, paraboloid, and hyperboloid, and by Fannelöp and Flügge-Lotz (1964) for a circular cylinder.

Of particular interest in this study are bodies with sharp leading edges which are placed in a hypersonic mainstream. For problems of this nature, there arise very large displacement effects - particularly near the leading edge. Hayes and Probst (1959) reviewed the early literature relating to this subject which, due to the strong viscous interaction present, is usually treated separately from supersonic flows. There are many approximate solutions for flat plates in hypersonic flow appearing in the literature. Dewey (1963) adopted the local similarity concept for his analysis. Later, Chan (1966) employed the momentum-integral method in his study. More recently, Sullivan (1969) employed Lees (1956) cold-wall similarity analysis to extract an approximate solution. Only one exact solution⁺ has been reported for a flat plate in hypersonic flow and that was by Flügge-Lotz and Blottner (1962). Only in one case, has this theory been extended to cover bodies with surface curvature and this was reported by Stollery (1970) who did not include surface curvature effects in his approximate analysis. Thus to the author's knowledge, no studies have been

⁺Exact in the sense that no approximations were made to the governing boundary-layer equations.

made in this area which include both displacement and curvature effects.

The first problem to be investigated in this study is that of flow around a circular cylinder at moderate to low Reynolds numbers. This flow will be investigated employing the composite second-order incompressible boundary-layer equations and it is felt that displacement and curvature effects should be sizable for the Reynolds number cases studied. The second flow problem to be studied is that of flow up a compression ramp in hypersonic flow. It has been noted by Van Dyke (1969) that even for high Reynolds numbers, the effects of displacement and surface curvature become significant for large Mach number flows. For this study, the compressible second-order boundary-layer equations will be employed.

From this study, large displacement and curvature effects were found to exist. However, when both displacement and curvature effects were accounted for, the differences observed in the wall properties from that predicted by classical boundary-layer theory were only noticeable in regions where the displacement effect could no longer be classified as a higher-order effect and this occurred near the leading edge of the compression ramp in hypersonic flow.

1.2 Formulation of the Governing Equations

For flow of a viscous fluid past a stationary body, Prandtl (1904) observed that as the Reynolds number becomes large, a thin layer develops near the body surface where the effects of viscosity and heat transfer are significant and outside of which they are negligible.

Prandtl formalized this concept from an order of magnitude analysis of the full Navier-stokes equations and thereby produced the now famous boundary-layer equations. Following this lead, Van Dyke (1962a) used the method of matched asymptotic expansions to obtain a formal statement of the boundary-layer concept valid to second order in the inverse square root of Reynolds number. Analyses of the individual first and second-order effects for several incompressible flows were made by Van Dyke (1962a) and (1962b). Similiar analyses for compressible flow were made independently by Maslen (1963), Lenard (1962), and Van Dyke (1962c). Applications of these are discussed in Van Dyke (1969). Here we choose not to filter out all higher-ordered terms or to separate the second-order contribution from the first order Prandtl boundary-layer equations. The purpose of this approach is to determine a composite set of equations which formally will contain both the Prandtl boundary-layer equations and the second-order contributions given by Maslen (1963), Lenard (1962), and Van Dyke (1962c).

The analysis⁺ begins by defining the perturbation parameter

$$\epsilon = 1/\sqrt{Re}, \quad (1.2-1a)$$

and thereafter stretching the normal coordinate and velocities according to the relation

⁺The following analysis was first presented by Davis, Werle, and Wornom (1970) and is presented here as a review and in order to show more of the details.

$$n = \epsilon N, \quad (1.2-1b)$$

and

$$\bar{v} = \epsilon v, \quad (1.2-1c)$$

with all other variable assumed to be order one.

These are now introduced into the Navier-Stokes equations given by Van Dyke (1962c) with all terms of $O(1)$ and $O(\epsilon)$ kept so that the governing equations valid to second order (i.e., $O(\epsilon)$) become:

CONTINUITY EQUATION

$$(r^j \rho u)_s + (hr^j \rho v)_N = 0 \quad (\text{exact}) \quad (1.2-2)$$

where $j = 0$ for plane flow and $j = 1$ for axisymmetric flow;

S-MOMENTUM EQUATION

$$\rho \left[u u_s + v(hu)_N \right] + \frac{\partial p}{\partial s} = \frac{1}{hr^j} \frac{\partial}{\partial N} (r^j h^2 \tau), \quad (1.2-3a)$$

where the shear stress is given by

$$\tau = \mu(u_N - h_N u/h) \quad (1.2-3b)$$

N-MOMENTUM EQUATION

$$p_N = \frac{h_N}{h} \rho u^2 \quad (1.2-4)$$

ENERGY EQUATION

$$\rho(uH_s + hvH_N) = \frac{1}{r^j} \frac{\partial}{\partial N} \left[hr^j (q + u\tau) \right], \quad (1.2-5a)$$

where

$$q = \frac{\mu}{\sigma} \frac{\partial T}{\partial N}, \quad (\text{heat transfer}) \quad (1.2-5b)$$

$$H = T + \frac{1}{2} u^2, \quad (\text{total enthalpy}) \quad (1.2-5c)$$

and

$$\sigma = \frac{\mu^* C_p^*}{k^*}. \quad (\text{Prandtl number}) \quad (1.2-5d)$$

In the above equations the coordinate scale factors r and h are defined as

$$r = r_0 + \epsilon N \cos \theta_{\text{wall}}, \quad (1.2-6a)$$

and

$$h = 1 + \epsilon \kappa N. \quad (1.2-6b)$$

The viscosity law employed here will be either

a. Sutherland's law

$$\mu = \frac{1 + C'}{T + C'} T^{3/2}, \quad (1.2-7a)$$

where

$$C' = \frac{C^*}{(\gamma - 1) M_{\infty}^2 T_{\infty}^*}, \quad (1.2-7b)$$

and $C^* = 198.6^\circ\text{R}$ for air, or the

b. Linear viscosity law

$$\frac{\mu}{\mu_\infty} = C(s) \frac{T}{T_\infty}, \quad (1.2-8a)$$

where μ_∞ is calculated using the Sutherland viscosity law and $C(s)$ is determined by requiring the linear law to match Sutherland's law at the wall, that is,

$$C(s) = \frac{1 + C^*/T_\infty^*}{T_w/T_\infty + C^*/T_\infty^*} \sqrt{\frac{T_w}{T_\infty}}. \quad (1.2-8b)$$

Only cases of constant wall temperature will be studied here so that here

$$C(s) = C_\infty = \text{constant}. \quad (1.2-8c)$$

The boundary conditions represent the no-slip condition on velocity

$$u(s, 0) = 0, \quad (1.2-9a)$$

the injection velocity at the boundary

$$v(s, 0) = v_w(s), \quad (1.2-9b)$$

and the total enthalpy at the wall

$$H(s, 0) = H_w(s), \quad (1.2-9c)$$

or the adiabatic wall condition

$$\left(\frac{\partial H}{\partial N} \right)_{\text{wall}} = 0. \quad (1.2-9d)$$

The outer boundary conditions are more subtle than the wall conditions because the edge of the boundary layer is not well defined. For this reason we must look for matching conditions to mate the viscous flow to the outer inviscid flow state.

In the present investigation, only cases where the outer flow was irrotational were studied. Thus the first matching condition will require that as N goes to infinity (i.e., the region where the boundary layer merges with the inviscid flow), the boundary-layer vorticity should asymptotically approach the inviscid value.⁺ Mathematically stated

$$\omega \sim 0, \quad \text{as } N \rightarrow \infty, \quad (1.2-10)$$

where to second order the vorticity in the boundary layer is given by

$$\omega = \frac{1}{\epsilon} h^{-1} (hu)_N. \quad (1.2-11)$$

⁺The fact that the outer boundary condition must be applied at infinity can be seen by letting n_0 be a point in the region where the boundary layer merges with the inviscid flow. Then the matching conditions are applied as

$$N \rightarrow N_0 = n_0 / \epsilon. \quad (1.2-10a)$$

Since boundary-layer theory becomes exact in the limit as $\epsilon \rightarrow 0$, then $N \rightarrow \infty$ at the outer reaches of the viscous region.

From equations (1.2-10) and (1.2-11), we find that

$$(hu)_N \rightarrow 0 \quad \text{as } N \rightarrow \infty, \quad (1.2-12)$$

which results in

$$hu \sim f(s) \quad \text{as } N \rightarrow \infty. \quad (1.2-13)$$

To determine the function $f(s)$, we apply the matching condition that the viscous u -velocity profile as N becomes large matches the inviscid profile near the body surface. This is the same matching condition as used by Murphy (1953), Van Dyke (1969), and Davis, Whitehead, and Wornom (1970). This implies that

$$f(s)/h \sim U(s,n) \quad \text{for small } n, \quad (1.2-14)$$

where $U(s,n)$ is the inviscid U -component of velocity. Noting that $h = 1 + \kappa n$, we can expand both sides of equation (1.2-14) in a Maclaurin series for small n to obtain

$$f(s)(1 - \kappa n + \dots) \sim U(s,0) + \left(\frac{\partial U}{\partial n} \right)_{s,0} n + \dots \quad (1.2-15)$$

From the condition that the outer inviscid flow be irrotational comes the relation that

$$\frac{\partial(hU)}{\partial n} - \frac{\partial \tilde{v}}{\partial s} = 0. \quad (1.2-16)$$

Now if we solve equation (1.2-16) for $\frac{\partial U}{\partial n}$ and substitute it into equation (1.2-15), we find that

$$f(s)(1 - \kappa n + \dots) \sim U(s,0)(1 - \kappa n) + \left(\frac{\partial \tilde{V}}{\partial s}\right)n + \dots \text{ for small } n. \quad (1.2-17)$$

In the outer flow the V-component of velocity can be expanded as

$$\tilde{V} = \tilde{V}_1 + \epsilon \tilde{V}_2 + \dots \quad (1.2-18)$$

Thus equation (1.2-17) can be expressed as

$$f(s)(1 - \kappa n + \dots) \sim U(s,0)(1 - \kappa n) + \left[\left(\frac{\partial \tilde{V}_1}{\partial s}\right)_{s,0} + \epsilon \left(\frac{\partial \tilde{V}_2}{\partial s}\right)_{s,0} \right] n + \dots \quad (1.2-19)$$

Noting that $U(s,0) = U_e(s)$, $(\partial \tilde{V}_1 / \partial s)_{s,0} = 0$ for any body, and $n = O(\epsilon)$ for proper matching, we find from equation (1.2-19) that to second order

$$f(s) = U_e(s). \quad (1.2-20)$$

Here U_e is the inviscid surface speed on the body under consideration and must be valid to second order, that is, it must contain the displacement-speed effects delineated by Van Dyke (1962c). Therefore, the resulting matching condition on the u-component of velocity becomes

⁺See Van Dyke (1962c).

$$u \sim u_m = U_e/h \quad \text{as } N \rightarrow \infty. \quad (1.2-21)$$

The outer boundary condition on enthalpy can be found as follows.

As $N \rightarrow \infty$ in equations (1.2-3) and (1.2-5), it will be required that the viscous terms vanish (i.e., the governing equations yield the inviscid flow equations). This gives the condition that

$$\rho(u_m H_s + h v H_N) \sim 0 \quad \text{as } N \rightarrow \infty. \quad (1.2-22)$$

Letting H be denoted as H_m as $N \rightarrow \infty$, it is seen that

$$H_m = \text{constant} \quad (1.2-23)$$

is a solution to equation (1.2-22). The obvious choice for the constant is

$$H_m = H_e, \quad (1.2-24)$$

where H_e is the inviscid total enthalpy on the body surface here taken to be constant.

Therefore, the matching condition on total enthalpy becomes

$$H \sim H_m = H_e \quad \text{as } N \rightarrow \infty. \quad (1.2-25)$$

In addition to the boundary and matching conditions given by equations (1.2-9), (1.2-21), and (1.2-25), we must also identify how the following quantities match with the inviscid flow. As $N \rightarrow \infty$ the viscous terms must approach the following inviscid matching profiles, denoted by the m subscript,

$$\mu \sim \mu_m, \quad (1.2-26a)$$

$$T \sim T_m, \quad (1.2-26b)$$

$$p \sim p_m, \quad (1.2-26c)$$

and

$$\rho \sim \rho_m. \quad (1.2-26d)$$

Letting N become large in equation (1.2-5c), we find after substitution from equations (1.2-21) and (1.2-25) that

$$T_m \sim H_e - u_m^2/2. \quad (1.2-27)$$

Similarly, equations (1.2-7) and (1.2-8) give that

$$\mu_m = \frac{1 + C'}{T_m + C'} T_m^{3/2}, \quad (1.2-28a)$$

or

$$\frac{\mu_m}{\mu_\infty} = C_\infty \frac{T_m}{T_\infty}. \quad (1.2-28b)$$

Letting N approach infinity in the s -momentum equation and noting that the viscous terms will be required to vanish as $N \rightarrow \infty$, we obtain

$$\rho_m u_m \frac{\partial u_m}{\partial s} + \frac{\partial p_m}{\partial s} \sim 0 \quad \text{as } N \rightarrow \infty. \quad (1.2-29)$$

If we now substitute $\frac{\partial u_m}{\partial s}$ from equation (1.2-27) into equation (1.2-29), we find that

$$\frac{\partial p_m}{\partial s} = \rho_m \frac{\partial T_m}{\partial s}. \quad (1.2-30)$$

Making the substitution for ρ_m in equation (1.2-30) from the equation of state, we find upon integration that

$$p_m(s, N) = \left[T_m(s, N) \right]^{\frac{\gamma}{\gamma - 1}} W(N) \quad \text{as } N \rightarrow \infty. \quad (1.2-31)$$

To determine the function $W(N)$, we apply the matching condition that the viscous pressure distribution for large N should match the inviscid pressure for small n , that is,

$$p_m(s, N) \sim P(s, n) \quad \text{for small } n, \quad (1.2-32)$$

where $P(s, n)$ is the external inviscid pressure.

For small n we can express $P(s, n)$ in a Maclaurin series about $n = 0$. Thus

$$P(s, n) = P(s, 0) + \left(\frac{\partial P}{\partial n} \right)_{s, 0} n + \dots \quad (1.2-33)$$

From Van Dyke (1962c), the n -momentum equation evaluated at $n = 0$ becomes

$$\left(\frac{\partial P}{\partial n} \right)_{s, 0} = -\rho_e \left[U_e \left(\frac{\partial \tilde{V}}{\partial s} \right)_{s, 0} + \tilde{V}_e \left(\frac{\partial \tilde{V}}{\partial n} \right)_{s, 0} - \kappa U_e^2 \right], \quad (1.2-34)$$

where $U_e = U(s, 0)$, $\tilde{V}_e = \tilde{V}(s, 0)$, and $\rho_e = \bar{\rho}(s, 0)$. This can now be substituted into equation (1.2-33) to obtain

$$P(s, n) = P_e - \rho_e \left[U_e \left(\frac{\partial \tilde{V}}{\partial s} \right)_{s, 0} + \tilde{V}_e \left(\frac{\partial \tilde{V}}{\partial n} \right)_{s, 0} - \kappa U_e^2 \right] n + \dots \quad (1.2-35a)$$

where

$$P_e(s) = P(s, 0). \quad (1.2-35b)$$

To second order within the boundary-layer region, equation (1.2-35) may be written as (using the equation of state)

$$P(s, n) = P_e \left(1 + \frac{\gamma}{\gamma - 1} \frac{U_e^2}{T_e} \epsilon \kappa N \right) + O(\epsilon^2). \quad (1.2-36)$$

Noting that

$$T_m = (T_e + U_e^2/2) - u_m^2/2, \quad (1.2-37)$$

equation (1.2-31) can be written as

$$p_m = W(N) \left[T_e + \frac{1}{2} U_e^2 \left(1 - \frac{1}{h^2} \right) \right]^{\frac{\gamma}{\gamma-1}}, \quad (1.2-38)$$

which when expanded for small n gives

$$p_m = W(N) T_e^{\frac{\gamma}{\gamma-1}} \left[1 + \frac{\gamma}{\gamma-1} \frac{U_e^2}{T_e} \kappa n + \dots \right]. \quad (1.2-39)$$

If we now apply the matching condition that $p_m(s, N) \sim P(s, n)$ for small n , we find that equation (1.2-36) and (1.2-39) give that

$$W(N) = \bar{W} = P_e / T_e^{\frac{\gamma}{\gamma-1}} = \text{constant} \quad (1.2-40)$$

for irrotational flow. Thus, equation (1.2-31) may be written as

$$p_m(s, N) = P_e \left(\frac{T_m}{T_e} \right)^{\frac{\gamma}{\gamma-1}}, \quad (1.2-41)$$

where P_e and T_e are the inviscid pressure and temperature on the body under consideration. Likewise, from the equation of state,

$\rho_m(s, N)$ can be written as

$$\rho_m(s, N) = \rho_e \left(\frac{T_m}{T_e} \right)^{\frac{1}{\gamma-1}}, \quad (1.2-42)$$

where ρ_e is the inviscid density on the body under consideration.

It was noted previously that the viscous terms would be required to vanish from the energy and s-momentum equations as $N \rightarrow \infty$. As the equations now stand this is not true. To see this, let N approach infinity in the s-momentum equation, where the right-hand side (RHS) becomes

$$\text{RHS} \sim \frac{1}{hrj} \frac{\partial}{\partial N} \left[h^2 r^j \mu_m \left(-2 \frac{h_N}{h} \frac{U_e}{h} \right) \right] \quad \text{as } N \rightarrow \infty, \quad (1.2-43)$$

which when expanded gives

$$\begin{aligned} \text{RHS} \sim \frac{1}{hrj} & \left[\left(2h h_N r^j \mu_m + j h^2 r_N^j \mu_m + h^2 r^j u_m^2 \frac{h_N}{h} \frac{\partial \mu_m}{\partial T_m} \right) \left(-2 \frac{h_N}{h} u_m \right) \right. \\ & \left. + \left(h^2 r^j \mu_m \right) \left\{ + 4 \left(\frac{h_N}{h} \right)^2 u_m \right\} \right]. \end{aligned} \quad (1.2-44)$$

Noting that $h = 1 + \epsilon N$, $r = r_0 + \epsilon N \cos \theta_{\text{wall}}$, thus $h_N = r_N = O(\epsilon)$, we see that although the viscous terms do not vanish, they can be seen from equation (1.2-44) to go to third order. Since the governing equations are valid formally only to second order, these third-order terms which are bothersome to the numerical analysis can be corrected for by subtracting the limiting form of these same terms from the RHS. Applying this correction the s-momentum equation becomes

$$\rho \left[u u_s + v(hu)_N \right] + \frac{\partial p}{\partial s} = \frac{1}{hrj} \frac{\partial}{\partial N} \left[h^2 r^j \mu \left(u_n - \frac{h_N}{h} u \left\{ 1 - \frac{2u_m}{u} \frac{\mu_m}{\mu} \right\} \right) \right]. \quad (1.2-45)$$

Similarly, letting N approach infinity in the energy equation we find that the RHS becomes

$$\text{RHS} \sim \frac{1}{r^j} \frac{\partial}{\partial N} \left[\frac{hr^j \mu_m}{\sigma} (1 - 2\sigma) \frac{h_N}{h} u_m^2 \right] \text{ as } N \rightarrow \infty, \quad (1.2-46a)$$

which after expansion becomes

$$\text{RHS} \sim \frac{1}{r^j} \left[\frac{(1 - 2\sigma)}{\sigma} \left\{ j h_N r_N^j \mu_m^2 u_m^2 + r^j \frac{\partial \mu_m}{\partial T_m} \frac{h_N^2}{h} u_m^4 - 2 r^j \mu_m^2 u_m^2 \frac{h_N^2}{h} \right\} \right]. \quad (1.2-46b)$$

Again, the RHS does not vanish as required but it can be seen from equation (1.2-46b) to be third order and as such will be corrected for the same manner as the s-momentum equation. Applying this correction, the energy equation becomes

$$\rho(uH_s + hvH_N) = \frac{1}{r^j} \frac{\partial}{\partial N} \left[\frac{hr^j \mu}{\sigma} \left\{ \frac{\partial H}{\partial N} - (1 - \sigma) u \frac{\partial u}{\partial N} - \sigma u^2 \frac{h_N}{h} - (1 - 2\sigma) \frac{\mu_m}{\mu} \frac{h_N}{h} u_m^2 \right\} \right]. \quad (1.2-47)$$

One final modification which leads to a simpler computational scheme involves writing the pressure gradients in equations (1.2-4) and (1.2-45) in terms of the velocity profile by first integrating equation (1.2-4) from any point N_0 to an arbitrary point N to give

$$p(s, N) = p(s, N_0) + \int_{N_0}^N \frac{h_N}{h} \rho u^2 dN. \quad (1.2-48)$$

Realizing that

$$p_m(s, N) = p_m(s, N_0) + \int_{N_0}^N \frac{h_N}{h} \rho_m u_m^2 dN, \quad (1.2-49)$$

equation (1.2-48) can be written as

$$p(s, N) = p_m(s, N) + \left[p(s, N_0) - p_m(s, N_0) \right] + \int_N^{N_0} \frac{h_N}{h} \left(\rho_m u_m^2 - \rho u^2 \right) dN. \quad (1.2-50)$$

In the limit as $\epsilon \rightarrow 0$ for n_0 fixed, $N_0 = \frac{n_0}{\epsilon} \rightarrow \infty$ and

$p(s, N_0) \rightarrow p_m(s, N_0)$, so that equation (1.2-50) becomes

$$p(s, N) = p_m(s, N) + \int_N^\infty \frac{h_N}{h} \left(\rho_m u_m^2 - \rho u^2 \right) dN, \quad (1.2-51)$$

where $p_m(s, N)$ is given by equation (1.2-41).

1.3 Summary of Governing Equations in Boundary-Layer Variables

The compressible boundary-layer equations valid formally to second order are

the CONTINUITY EQUATION

$$\left(r^j \rho u \right)_s + \left(h r^j \rho v \right)_N = 0, \quad (1.3-1)$$

the S-MOMENTUM EQUATION

$$\begin{aligned} \rho \left[u u_s + v(hu)_N \right] - \rho_m u_m \frac{\partial u_m}{\partial s} + \frac{\partial}{\partial s} \left[\int_N^\infty \frac{h_N}{h} \left(\rho_m u_m^2 - \rho u^2 \right) dN \right] \\ = \frac{1}{hr^j} \frac{\partial}{\partial N} \left[h^2 r^j \mu \left(u_N - \frac{h_N}{h} u \left\{ 1 - \frac{2u_m}{u} \frac{\mu_m}{\mu} \right\} \right) \right] \end{aligned} \quad (1.3-2)$$

and the ENERGY EQUATION

$$\begin{aligned} \rho(uH_s + hvH_N) = \frac{1}{r^j} \frac{\partial}{\partial N} \left[\frac{hr^j \mu}{\sigma} \left\{ \frac{\partial H}{\partial N} - (1 - \sigma)u \frac{\partial u}{\partial N} - \sigma u^2 \frac{h_N}{h} \right. \right. \\ \left. \left. - (1 - 2\sigma) \frac{\mu_m}{\mu} \frac{h_N}{h} u_m^2 \right\} \right] \end{aligned} \quad (1.3-3)$$

The pressure in the boundary layer is given by

$$p(s, N) = p_m(s, N) + \int_N^\infty \frac{h_N}{h} \left(\rho_m u_m^2 - \rho u^2 \right) dN \quad (1.3-4)$$

EQUATION OF STATE

$$p(s, N) = \frac{\gamma - 1}{\gamma} \rho (H - u^2/2) \quad (1.3-5)$$

VISCOSITY LAWS

Two viscosity laws will be employed. They are:

a. The Sutherland viscosity law

$$\mu = \frac{1 + C'}{T + C'} T^{3/2}, \quad (1.3-6a)$$

where

$$C' = \frac{C^*}{(\gamma - 1) M_\infty^2 T_\infty^*}, \quad (1.3-6b)$$

and

b. The linear viscosity law

$$\mu = C_\infty \frac{\mu_\infty}{T_\infty} T, \quad (1.3-7a)$$

where

$$C_\infty = \frac{1 + C^*/T_\infty^*}{T_w/T_\infty + C^*/T_\infty^*} \sqrt{\frac{T_w}{T_\infty}}. \quad (1.3-7b)$$

In equations (1.3-6b) and (1.3-7b), C^* is taken to be 198.6°R for air.

BOUNDARY CONDITIONS

The boundary conditions are the no-slip condition

$$u(s, 0) = 0, \quad (1.3-8a)$$

the surface injection condition

$$V(s, 0) = V_w(s), \quad (1.3-8b)$$

a specified wall temperature

$$H(s, 0) = H_w(s), \quad (1.3-8c)$$

or the adiabatic wall condition

$$(\partial H / \partial N)_{\text{wall}} = 0. \quad (1.3-8d)$$

The matching profiles which constitute the outer boundary conditions are

$$u(s, N) \sim u_m = U_e/h \quad \text{as } N \rightarrow \infty, \quad (1.3-8e)$$

$$H(s, N) \sim H_m = H_e \quad \text{as } N \rightarrow \infty, \quad (1.3-8f)$$

$$p(s, N) \sim p_m = p_e (T_m/T_e)^{\frac{\gamma}{\gamma-1}} \quad \text{as } N \rightarrow \infty, \quad (1.3-8g)$$

$$\rho(s, N) \sim \rho_m = \rho_e (T_m/T_e)^{\frac{1}{\gamma-1}} \quad \text{as } N \rightarrow \infty, \quad (1.3-8h)$$

and

$$T(s, N) \sim T_m = H_e - u_m/2 \quad \text{as } N \rightarrow \infty. \quad (1.3-8i)$$

In the above equations u_m , H_m , p_m , ρ_m , and T_m are the inviscid profiles that the viscous profiles must match as the boundary layer merges with the inviscid flow region.

1.4 The Governing Equations in Similarity Variables

It will prove convenient later if the governing equations are put into similarity form so that when a self-similar solution exists the equations will reduce to the proper form. The similarity form is also better suited for numerical solution since the boundary layer does not grow as fast in these coordinates.

Following the example of Hayes and Probstein (1959), Blottner (1970), and Davis, Whitehead, and Wornom (1970), we choose the transformed independent coordinates ξ and η to be

$$\xi = \int_0^s \rho_e \mu_e U_e r_o^{2j} ds, \quad (1.4-1)$$

and

$$\eta = \frac{U_e}{\sqrt{2\xi}} \int_0^N \frac{\rho r^j}{h} dN. \quad (1.4-2)$$

Equations (1.4-1-2) are generalized forms of the Görtler and Howarth-Dorodnitsyn transformations. Note that for the incompressible case $\rho = \rho_e = \mu_e = 1$ and equations (1.4-1-2) reduce to the expressions employed by Davis, Whitehead, and Wornom (1970) and for classical or first-order theory $h = 1$ and $r = r_o$ so that equations (1.4-1) and (1.4-2) reduce to those coordinates originally due to Levy (1954) and Lees (1956) and adopted by Blottner (1970), and others.

The transformed tangential component of velocity is defined as

$$F = u/u_m, \quad (1.4-3)$$

and the transformed total enthalpy is defined by

$$G = H/H_m. \quad (1.4-4)$$

Applying the above transformations to the continuity equation we obtain upon integration that

$$hr^j \rho v = -\partial \xi / \partial s \frac{\partial}{\partial \xi} \left(\sqrt{2\xi} \int_0^\eta F d\eta \right) - \frac{\partial \eta}{\partial s} \sqrt{2\xi} F + \rho_w r_o^j v_w. \quad (1.4-5)$$

The transformed v-component of velocity will be chosen to be

$$V = - \sqrt{2\xi} \frac{\partial}{\partial \xi} \left(\sqrt{2\xi} \int_0^\eta F \, d\eta \right) + \rho_w r_0^j v_w \sqrt{2\xi} / (\partial \xi / \partial s) . \quad (1.4-6a)$$

Thus, in terms of the similarity V-component of velocity the physical v-component becomes

$$v = \frac{1}{\rho r_0^j h} \left(\frac{\partial \xi}{\partial s} \frac{V}{\sqrt{2\xi}} - \frac{\partial \eta}{\partial s} \sqrt{2\xi} F \right) . \quad (1.4-6b)$$

Differentiating equation (1.4-6a) the transformed continuity equation can be written as

$$\frac{\partial V}{\partial \eta} + 2\xi \frac{\partial F}{\partial \xi} + F = 0 . \quad (1.4-6c)$$

In the new coordinate system the convective operator becomes

$$\rho \left(u \frac{\partial}{\partial s} + h v \frac{\partial}{\partial N} \right) = \frac{\rho u_m}{2\xi} \frac{\partial \xi}{\partial s} \left[2\xi F \frac{\partial}{\partial \xi} + V \frac{\partial}{\partial \eta} \right] . \quad (1.4-7)$$

Applying the above transformations to equations (1.3-2-3) the transformed second-order compressible boundary-layer equations are obtained as

CONTINUITY EQUATION

$$\frac{\partial V}{\partial \eta} + 2\xi \frac{\partial F}{\partial \xi} + F = 0 , \quad (1.4-8)$$

S-MOMENTUM EQUATION

$$\begin{aligned} \frac{\partial}{\partial \eta} \left\{ \frac{R^{2j} l}{h^2} \left[\frac{\partial F}{\partial \eta} - \frac{2h\eta}{h} \left(F - \frac{\rho l_m}{\rho_m l} \right) \right] h^2 \right\} &= \beta \left(F^2 - \frac{\rho_m}{\rho} \right) + 2\xi F \frac{\partial F}{\partial \xi} + \\ &+ V \frac{\partial F}{\partial \eta} + \left(2\beta \tilde{I} + 2\xi \frac{\partial \tilde{I}}{\partial \xi} \right) / \rho, \end{aligned} \quad (1.4-9)$$

ENERGY EQUATION

$$\begin{aligned} \frac{\partial}{\partial \eta} \left[R^{2j} l \left\{ \frac{\partial G}{\partial \eta} + \frac{u_m^2}{H_e} \left[(\sigma - 1) F \frac{\partial F}{\partial \eta} + (1 - 2\sigma) \frac{h\eta}{h} \left(F^2 - \frac{\rho l_m}{\rho_m l} \right) \right] \right\} \right] \\ = \sigma \left(2\xi F \frac{\partial G}{\partial \xi} + V \frac{\partial G}{\partial \eta} \right). \end{aligned} \quad (1.4-10)$$

The pressure at any point in the boundary layer is given by

$$p(s, N) = p_m + u_m^2 \tilde{I}, \quad (1.4-11)$$

where u_m and p_m are given by equations (1.3-8e) and (1.3-8g).

EQUATION OF STATE

$$p = \frac{\gamma - 1}{\gamma} \rho (H_e G - u^2/2). \quad (1.4-12)$$

Quantities not defined in equations (1.4-8-12) are defined as

$$R = r/r_0, \quad (1.4-13)$$

$$l = (\rho \mu) / (\rho_e \mu_e), \quad (1.4-14)$$

$$\beta = \frac{2\xi}{u_m} \frac{\partial u_m}{\partial \xi} = \frac{2\xi}{u_e} \frac{dU_e}{d\xi} - \frac{2\xi}{h} \frac{\partial h}{\partial \xi} , \quad (1.4-15)$$

$$\tilde{I} = h^2 \int_{\eta}^{\infty} \frac{h_{\eta}}{h^3} \rho_m \left(1 - \frac{\rho F^2}{\rho_m} \right) d\eta , \quad (1.4-16)$$

and

$$l_m = (\rho_m \mu_m) / (\rho_e \mu_e) . \quad (1.4-17)$$

Equations (1.3-6-8) supply the remaining relations needed for computing a solution.

BOUNDARY CONDITIONS

The boundary conditions are the no slip condition

$$F(\xi, 0) = 0 , \quad (1.4-18a)$$

a specified wall temperature

$$G(\xi, 0) = H_{\text{wall}} / H_e , \quad (1.4-18b)$$

or zero heat transfer

$$(\partial G / \partial \eta)_{\text{wall}} = 0 , \quad (1.4-18c)$$

the surface blowing velocity

$$V(\xi, 0) = V_w(\xi) , \quad (1.4-18d)$$

the outer matching condition on velocity

$$F \sim 1 \quad \text{as} \quad N \rightarrow \infty, \quad (1.4-18e)$$

and the outer matching condition on total enthalpy

$$G \sim 1 \quad \text{as} \quad N \rightarrow \infty. \quad (1.4-18f)$$

1.5 Boundary-Layer Properties

The dimensionless coefficient of skin friction is defined as

$$C_f = \frac{\tau_{\text{wall}}^*}{\frac{1}{2} \rho_{\infty}^* U_{\infty}^{*2}} = \frac{2\epsilon \rho_w \mu_w r_o j U_e^2}{\sqrt{2\xi}} \left(\frac{\partial F}{\partial \eta} \right)_{\text{wall}}, \quad (1.5-1a)$$

where

$$\tau_{\text{wall}}^* = \left(\mu^* \frac{\partial u^*}{\partial n^*} \right)_{\text{wall}}. \quad (1.5-1b)$$

This leads to the usual definition of skin friction

$$\bar{C}_f = C_f / \epsilon = \frac{2\rho_w \mu_w r_o j U_e^2}{\sqrt{2\xi}} \left(\frac{\partial F}{\partial \eta} \right)_{\text{wall}}. \quad (1.5-2)$$

The dimensionless coefficient of heat transfer is given by the Stanton number defined as

$$St_{\infty} = \frac{q_{\text{wall}}^*}{\rho_{\infty}^* U_{\infty}^* (H_{\infty}^* - H_w^*)} = \frac{\epsilon H_e \rho_w \mu_w r_o j U_e}{\sigma \sqrt{2\xi} (T_o - T_w)} \left(\frac{\partial G}{\partial \eta} \right)_{\text{wall}}, \quad (1.5-3)$$

where

$$q_{\text{wall}}^* = \left(\frac{\mu^* C_p^*}{\sigma} \frac{\partial T^*}{\partial n^*} \right)_{\text{wall}} . \quad (1.5-4)$$

We can remove the Reynolds number dependence from the Stanton number by defining

$$\bar{St}_\infty = St_\infty / \epsilon = \frac{H_e \rho_w \mu_w r_o j_{U_e}}{\sigma \sqrt{2\xi} (T_o - T_w)} \left(\frac{\partial G}{\partial \eta} \right)_{\text{wall}} . \quad (1.5-5)$$

The definition of the displacement thickness requires the mass rate of flow of inviscid fluid past a body thickened by an amount δ (measured in the N coordinate) to be equal to the viscous mass flow past the real body. This definition yields the following relation for the displacement thickness

$$\int_{\delta}^{\infty} r^j \rho_m u_m dN = \int_0^{\infty} r^j \rho u dN, \quad (1.5-6)$$

where the displacement body is located at $n = \epsilon \delta$. When written in similarity variables, equation (1.5-6) becomes

$$\int_0^{\bar{\delta}} \frac{\rho_m}{\rho} d\eta = \int_0^{\infty} \left(\frac{\rho_m}{\rho} - F \right) d\eta, \quad (1.5-7)$$

where $\bar{\delta}$ is the displacement thickness measured in the η coordinate. The relation between the transformed and physical displacement thickness is given implicitly from equation (1.4-2) where it is seen that δ can

be written as

$$\delta = \frac{\sqrt{2\xi}}{U_e r_{0j}} \int_0^{\bar{\delta}} \frac{h}{\rho R j} d\eta . \quad (1.5-8)$$

1.6 Reduction to the Incompressible Case

For the incompressible case the density is assumed constant and the variations in temperature are assumed small so that the energy equation is uncoupled from the momentum law. Thus, for the incompressible case $\rho = \rho_e = \mu_e = 1$ in accordance with the nondimensional scheme and the governing equations become the CONTINUITY EQUATION

$$\frac{\partial V}{\partial \eta} + 2\xi \frac{\partial F}{\partial \xi} + F = 0 , \quad (1.6-1)$$

and the S-MOMENTUM EQUATION

$$\frac{\partial}{\partial \eta} \left\{ \frac{R^{2j}}{h^2} \left[\frac{\partial F}{\partial \eta} - \frac{2h_\eta}{h} (F - 1) \right] h^2 \right\} = \beta (F^2 - 1) + 2\xi F \frac{\partial F}{\partial \xi} + V \frac{\partial F}{\partial \eta} + 2\beta \tilde{I} + 2\xi \frac{\partial \tilde{I}}{\partial \xi} , \quad (1.6-2)$$

where

$$R = r/r_0 , \quad (1.6-3a)$$

$$h = 1 + \epsilon \frac{\sqrt{2\xi} \kappa}{U_e r_{0j}} \int_0^\eta \frac{h}{R j} d\eta , \quad (1.6-3b)$$

$$\beta = \beta_e + 2\xi h \frac{\partial}{\partial \xi} \left[\frac{1}{h} \right] , \quad (1.6-3c)$$

$$\beta_e = \frac{2\xi}{U_e} \frac{dU_e}{d\xi} = \frac{2\xi}{U_e^2 r_o^{2j}} \frac{dU_e}{ds}, \quad (1.6-3d)$$

and

$$\tilde{I} = h^2 \int_{\eta}^{\infty} \frac{h_{\eta}}{h^3} (1 - F^2) d\eta. \quad (1.6-3e)$$

The transformed similarity coordinates ξ and η are given by

$$\xi = \int_0^s U_e r_o^{2j} ds, \quad (1.6-4a)$$

and

$$\eta = \frac{U_e r_o^j}{\sqrt{2\xi}} \int_0^N \frac{R^j}{h} dN. \quad (1.6-4b)$$

Expanding the LHS of equation (1.6-2) we obtain

$$\text{LHS} = h^2 \frac{\partial}{\partial \eta} \left(\frac{R^{2j}}{h^2} \frac{\partial F}{\partial \eta} \right) + \frac{2h_{\eta} R^{2j}}{h} \left(\frac{h_{\eta\eta}}{h_{\eta}} - \frac{h_{\eta}}{h} + 2j \frac{R_{\eta}}{R} \right) (1 - F), \quad (1.6-5)$$

which can further be simplified by noting that

$$\frac{\partial h}{\partial \eta} = \frac{\partial h}{\partial N} \frac{\partial N}{\partial \eta} = \frac{\epsilon \kappa \sqrt{2\xi}}{U_e r_o^j} \frac{h}{R^j}. \quad (1.6-6a)$$

Thus, $h_{\eta\eta}/h_{\eta}$ can be written as

$$h_{\eta\eta}/h_{\eta} = h_{\eta}/h - jR_{\eta}/R. \quad (1.6-6b)$$

With this simplification the s-momentum equation becomes⁺

$$h^2 \frac{\partial}{\partial \eta} \left[\frac{R^2 j}{h^2} \left(\frac{\partial F}{\partial \eta} \right) \right] = \beta(F^2 - 1) + 2\xi F \frac{\partial F}{\partial \xi} + V \frac{\partial F}{\partial \eta} + 2\beta \tilde{I} + 2\xi \frac{\partial \tilde{I}}{\partial \xi}. \quad (1.6-7)$$

To determine the pressure in the boundary layer we must first take the limit of equation (1.3-8g) as the flow Mach number goes to zero.

To do this, we write equation (1.3-8g) in terms of the inviscid Mach number M_e to obtain

$$p_m = P_e \left[1 + \frac{\gamma - 1}{2} M_e^2 \left(1 - \frac{1}{h^2} \right) \right]^{\frac{\gamma}{\gamma - 1}}, \quad (1.6-8)$$

which when expanded for small M_e before letting $M_e \rightarrow 0$ yields

$$p_m = P_e + \frac{1}{2} U_e^2 \left(1 - \frac{1}{h^2} \right) \text{ as } M_e \rightarrow 0. \quad (1.6-9)$$

Thus, the pressure at any point in the incompressible boundary layer is given by

$$p(\xi, \eta) = P_e + \frac{1}{2} U_e^2 \left(1 - \frac{1}{h^2} \right) + u_m^2 \tilde{I}, \quad (1.6-10)$$

Where u_m is given by equation (1.3-8e). The boundary conditions are given by equations (1.4-18a) and (1.4-18d-e).

⁺The remaining third-order term in equation (1.6-5) has been neglected.

The incompressible forms of the boundary-layer properties are given as the modified skin friction coefficient

$$\bar{C}_f = \frac{\tau_{wall}^*}{\frac{1}{2} \rho_\infty^* U_\infty^{*2}} / \epsilon = \frac{2r_o^j U_e^2}{\sqrt{2\xi}} \left(\frac{\partial F}{\partial \eta} \right)_{wall}, \quad (1.6-11a)$$

where

$$\tau_{wall}^* = \mu_\infty^* \left(\frac{\partial u^*}{\partial n^*} \right)_{wall}, \quad (1.6-11b)$$

and

$$C_f = \epsilon \bar{C}_f. \quad (1.6-11c)$$

The displacement thickness from equation (1.5-7) becomes in the transformed coordinate

$$\bar{\delta} = \int_0^\infty (1 - F) d\eta, \quad (1.6-12a)$$

and the physical coordinate value is given as

$$\int_{\bar{\delta}}^\infty R^j u_m dN = \int_0^\infty R^j u dN. \quad (1.6-12b)$$

Thus, we have shown that the second-order incompressible boundary-layer equations presented by Davis, Whitehead, and Wornom (1970) are the limit form of the equations presented in Section 1.4 as $M_\infty \rightarrow 0$.

In Chapter II, the incompressible second-order boundary-layer equations will be employed to study the effects of longitudinal curvature on wall properties for flow around a circular cylinder at moderate Reynolds numbers where the displacement-body effects are approximately known.

II. LONGITUDINAL CURVATURE AND DISPLACEMENT- SPEED EFFECTS ON INCOMPRESSIBLE BOUNDARY LAYERS

2.1 Introduction

The major difficulty in applying the equations formulated in Chapter I to a particular flow problem arises because at the present time, the inviscid flow parameters necessary to match the boundary-layer flow to the inviscid flow outside of the boundary-layer cannot be easily calculated to second-order for an arbitrarily shaped body.

The purpose of this chapter is to develop a procedure for numerically solving the incompressible equations valid to second-order and to apply the procedure to cases where displacement-speed effects can be approximately determined. This application will give a test of curvature effects and will indirectly determine whether or not displacement-speed effects are important.

The particular flow problem to which the theory will be applied is that of flow around a circular cylinder. This problem was chosen because the effects of curvature should become important at moderate to low Reynolds numbers and because experimental and numerical data in the form of wall pressure and shear stress distributions are generally available in the open literature.

2.2 Governing Equations

The governing equations have been formulated by Davis, Whitehead, and Wornom (1970) and as was shown in Chapter I, their resulting

equations are the incompressible counterpart of the second-order compressible boundary-layer equations formulated there.

The inviscid pressure gradient parameter β given in equation (1.4-15) monitors the pressure gradient the inviscid flow produces in the ξ direction. It will prove beneficial later in the incompressible study to also examine the flow in terms of what pressure gradient the viscous flow sees. To do this we need to look at the viscous pressure gradient in the ξ direction. Differentiating equation (1.6-10) with respect to ξ we find that

$$\frac{\partial P}{\partial \xi} = \frac{dP_e}{d\xi} + U_e \frac{dU_e}{d\xi} - \frac{U_e}{h} \frac{\partial}{\partial \xi} \left[\frac{U_e}{h} \right] (1 - 2\tilde{I}) + \frac{U_e^2}{h^2} \frac{\partial \tilde{I}}{\partial \xi}, \quad (2.2-1a)$$

where

$$\tilde{I} = h^2 \int_{\eta}^{\infty} \frac{h_{\eta}}{h^3} (1 - F^2) d\eta. \quad (2.2-1b)$$

Note that⁺

$$\frac{dP_e}{d\xi} + U_e \frac{dU_e}{d\xi} = 0. \quad (2.2-2)$$

Rewriting equation (2.2-1a) in terms of the inviscid pressure gradient parameter β , we find

$$\frac{\partial P}{\partial \xi} = -\frac{U_e^2}{2\xi h^2} \left[\beta(1 - 2\tilde{I}) - 2\xi \frac{\partial \tilde{I}}{\partial \xi} \right]. \quad (2.2-3)$$

⁺This will be shown in Section 2.3a to be valid to second-order.

If we define the viscous pressure gradient parameter as

$$\beta_v = -\frac{2\xi h^2}{U_e^2} \frac{\partial P}{\partial \xi}, \quad (2.2-4)$$

it can be seen that the viscous pressure gradient parameter β_v will always be opposite in sign of the actual ξ pressure gradient.

Substituting equation (2.2-3) into equation (2.2-4) we obtain the following relation for β_v

$$\beta_v(\xi, \eta) = \beta(\xi, \eta)(1 - 2\tilde{I}) - 2\xi \frac{\partial \tilde{I}}{\partial \xi}, \quad (2.2-5)$$

which gives a direct measure of the longitudinal pressure gradient at any point in the viscous flow region.

Now examining the governing equations given in Section 1.6, it can be seen that to numerically solve a general flow problem, it is necessary in general to know $\beta_e(\xi)$, $U_e(\xi)$, $\kappa(\xi)$, $r_o(\xi)$, $\cos \theta_{\text{wall}}(\xi)$, and an ϵ . However, for the case of flow around a circular cylinder $j = 0$ and, therefore, the only necessary parameters are $\beta_e(\xi)$, $U_e(\xi)$, $\kappa(\xi)$, and ϵ .

In the present study, putting $\epsilon = 0$, reduces the governing equations to the classical or first-order boundary-layer equations. For this case U_e , the inviscid surface speed, can be taken from potential theory or it can be calculated from experimentally measured wall pressures using Bernoulli's equation under the assumption that the pressure is constant across the boundary layer.

However, if the governing equations are to be valid to second-order, then U_e must include displacement-body effects. At the present time this cannot be done directly. The next section seeks to show how this difficulty can be overcome if the wall pressure distribution is known.

2.3 The Pressure Gradient Parameter, β_e

a. General Discussion. - From equation (1.6-10) we find that the wall pressure is given by

$$P_{\text{wall}} = p(\xi, 0) = P_e + U_e^2 I, \quad (2.3-1)$$

where

$$I = \int_0^\infty \frac{h\eta}{h^3} (1 - F^2) d\eta. \quad (2.3-2)$$

The inviscid pressure, P_e , and velocity, U_e , can be related to each other by first noting that to second order in the inviscid flow region the s component of the Navier-Stokes equation is (see Van Dyke (1962a))

$$U \frac{\partial U}{\partial s} + \tilde{V} \frac{\partial(hU)}{\partial n} + \frac{\partial P}{\partial s} = 0. \quad (2.3-3)$$

On the body surface $U = U_e(s)$, $h = 1$, $P = P_e(s)$, and $\tilde{V} = \tilde{V}_e(s)$.

Therefore, on the surface, equation (2.3-3) becomes

$$U_e \frac{dU_e}{ds} + \left[\tilde{V} \frac{\partial(hU)}{\partial n} \right]_{\tilde{n}=0} + \frac{dP_e}{ds} = 0. \quad (2.3-4)$$

In the inviscid flow region the flow is assumed irrotational.

This leads to the result that

$$\frac{\partial \tilde{V}}{\partial s} = \frac{\partial(hU)}{\partial n}. \quad (2.3-5)$$

Substituting this result into equation (2.3-4) we find that

$$U_e \frac{dU_e}{ds} + \tilde{V}_e \frac{d\tilde{V}_e}{ds} + \frac{dP_e}{ds} = 0. \quad (2.3-6)$$

But from Van Dyke (1962a) the inviscid normal velocity component can be expanded as

$$\tilde{V}_e = \tilde{V}_{e1} + \epsilon \tilde{V}_{e2}. \quad (2.3-7)$$

On any surface without injection

$$\tilde{V}_e = 0 + \epsilon \tilde{V}_{e2}(s, 0), \quad (2.3-8)$$

which leads to the result that

$$\tilde{V}_e \frac{d\tilde{V}_e}{ds}$$

is third order.

Therefore to second-order

$$\frac{dP_e}{ds} + U_e \frac{dU_e}{ds} = 0, \quad (2.3-9)$$

or

$$P_e + \frac{1}{2} U_e^2 = \text{constant}. \quad (2.3-10)$$

Evaluating the constant at the free-stream conditions gives

$$P_e + \frac{1}{2} U_e^2 = P_\infty + \frac{1}{2} U_\infty^2. \quad (2.3-11)$$

Upon substituting U_e from equation (2.3-11) into equation (2.3-1) we obtain

$$P_e = \frac{p_{\text{wall}} - (1 + 2P_\infty)I}{1 - 2I}, \quad (2.3-12)$$

where I is given by equation (2.3-2). For classical or first-order boundary-layer theory $\epsilon = 0$ and therefore $I = 0$. Thus from equation (2.3-12), one recovers the well known result that to first order, the inviscid surface pressure is equal to the wall pressure. To obtain the inviscid surface pressure valid to second order, equations (2.3-12), (2.3-2), and (1.2-6b) show that the actual wall pressure must be corrected for longitudinal curvature effects.

Since the inviscid parameters necessary for a numerical solution are β_e and U_e , it is convenient to look at equation (2.3-12) in terms of U_e . Using equation (2.3-11), equation (2.3-12) can be written as

$$U_e = \left[\frac{1 - C_{p_{wall}}}{1 - 2I} \right]^{1/2}, \quad (2.3-13)$$

where

$$C_{p_{wall}} = 2(p_{wall} - P_{\infty}). \quad (2.3-14)$$

Equation (2.3-13) gives the inviscid surface speed to second order that would be necessary to produce the observed wall pressure distribution. Thus, equation (2.3-13) should include the displacement speed.

$C_{p_{wall}}$ can be computed using experimentally measured wall pressure distributions, thus leaving only the integral I , (defined in equation (2.3-2)) to be determined from the boundary-layer solutions. Assuming that the governing equations have been programmed for numerical solutions, the integral I can be determined in the following manner. As was noted earlier, once the program has a $\beta_e(\xi)$, $U_e(\xi)$, $\kappa(\xi)$, and an ϵ , it can numerically calculate a boundary-layer solution at a particular station. To determine I and the value of U_e to second order, an iterative approach will be used. We will guess a value of U_e at a station, from this determine a β_e and then

compute a boundary-layer profile. Taking the value of I from this boundary-layer profile, a new value of U_e will be calculated from equation (2.3-13). Using this value of U_e , and new β_e will be determined and another iteration will be made on the boundary-layer solution. This process of updating the value of U_e after each iteration on the boundary-layer solution will be continued until I (and therefore U_e) converges.

b. Solutions Aft of a Stagnation Point. - The initial guess of U_e at any station downstream of the stagnation point is obtained from the following relation⁺,

$$U_{e(\text{New Station})} = U_{e(\text{Old Station})} + \left(\frac{dU_e}{ds} \right)_{(\text{New Station})} \Delta s \quad (2.3-15)$$

In this relation Δs is the step size in the s -coordinate and $\left(\frac{dU_e}{ds} \right)_{\text{New Station}}$ was obtained by a linear extrapolation of the previous two values back along the body. With the initial first guess of U_e and $\frac{dU_e}{ds}$ at the new station, β_e is calculated using equation (1.6-4a) and the definition,

⁺Since equation (2.3-15) is a two-term Taylor series expansion for $U_{e \text{ New}}$, the value of dU_e/ds used should have been the value at the previous station. However, for purposes of programming simplicity and the fact that equation (2.3-15) only supplied an initial guess, $(dU_e/ds)_{\text{New Station}}$ was used instead.

$$\beta_e(\xi) = \frac{2\xi}{U_e^2} \frac{dU_e}{ds}. \quad (2.3-16)$$

With these values of β_e , U_e , and ξ a boundary-layer profile is computed. After each iteration the inviscid surface speed is updated using equation (2.3-13). $\frac{dU_e}{ds}$ is updated after each iteration from the following relation.

$$\frac{dU_e}{ds} = \frac{[U_e(\text{present iteration}) - U_e(\text{previous station})]}{\Delta s}. \quad (2.3-17)$$

Once U_e , ξ , and $\frac{dU_e}{ds}$ have been updated, β_e is updated and another iteration is made on the solution. This process of updating the values of U_e and $\frac{dU_e}{ds}$ is continued until some criteria of convergence has been reached. If $\Delta\beta_e \leq 10^{-5}$ and $\Delta F_{\eta_w} \leq 10^{-5}$ where

$$\Delta\beta_e = |\beta_e(\text{last iteration}) - \beta_e(\text{present iteration})|, \quad (2.3-18)$$

and

$$\Delta F_{\eta_w} = \left| \left(\frac{\partial F}{\partial \eta} \right)_{\text{wall}} (\text{last iteration}) - \left(\frac{\partial F}{\partial \eta} \right)_{\text{wall}} (\text{present iteration}) \right|, \quad (2.3-19)$$

the solution was considered to have converged for this study. Note here that for numerical solutions of the first-order and second-order problems ΔF_{η_w} was held at 10^{-5} .

c. Solutions in a Stagnation Point Region.- At the stagnation point ξ and U_e are zero. Thus it can be seen from equation (1.6-1) and (1.6-7) that the ξ derivatives drop out of the governing equations which then reduce to ordinary differential equations dependent only upon the parameter β and the scale factor h . β is computed using equations (1.6-3c) and (2.3-16) while h is computed from equation (1.6-3b) using an initial guess of h to evaluate the integral for the first iteration and the calculated value for the next iteration and so forth until the boundary-layer solution converges. Because U_e and ξ are zero at the stagnation point, equation (2.3-16) which is used in computing β and equation (1.6-3b) which is used to compute h become indeterminate at the stagnation point. To obtain the values of β_e and $\sqrt{2\xi}/U_e$ (the indeterminate term in equation (1.6-3b) at the stagnation point, we must expand U_e in a Taylor series about the stagnation point for small s . Thus $U_e(0 + s)$ becomes

$$U_e = U'_0 s + \dots, \quad (2.3-20)$$

where U'_0 is the value of dU_e/ds at the stagnation point.

Using equations (2.3-20), (1.6-4a), and (2.3-16) we find that at the stagnation point,

$$\beta_e = 1, \quad (2.3-21)$$

and

$$\frac{\sqrt{2\xi}}{U_e} = \frac{1}{\sqrt{U'_0}}. \quad (2.3-22)$$

Thus the major difficulty at the stagnation point will be determining the proper value of U'_0 . To do this, note that from equation (2.3-13) we see that for U_e to be equal to zero at the stagnation point, C_p must be 1 there. Both Homann (1936) and Grove, Shair, Petersen, and Acrivos (1964) have shown this to be true to second order.⁺

Expanding $C_{p_{wall}}$ about the stagnation point, we obtain

$$C_{p_{wall}} = 1 + A_2 s^2 + \dots \quad (2.3-23)$$

Substituting the expansions of U_e and $C_{p_{wall}}$ about the stagnation point into equation (2.3-13) and taking the limit as s goes to zero, we find that

⁺Homann (1936) and Grove, Shair, Petersen, and Acrivos (1964) have shown analytically from a boundary-layer analysis that at the stagnation point

$$C_{p_{wall}} = 1 + \frac{\alpha}{Re_d} + \dots, \quad (2.3-22a)$$

where α is a constant. Using a boundary-layer concept, they found α to be equal to 8. More recently, Takami and Keller (1969) assumed equation (2.3-22a) to be correct and estimated α to be 5.985 through comparison with their numerical solutions of the Navier-Stokes equations at Reynolds numbers of 50 and 60. Dennis and Chang's (1969) numerical solutions for Reynolds numbers from 50 to 100 also give $\alpha \approx 6$.

$$U'_0 = \sqrt{-A_2} (1 - 2I_0)^{-1/2}, \quad (2.3-24)$$

where I_0 is the value of the integral I at the stagnation point.

Noting that for a circular cylinder $\kappa(\xi) = 1$, equation (2.3-2) in boundary-layer coordinates becomes

$$I_0 = \epsilon \int_0^\infty \frac{1}{h^3} \left(1 - \frac{h^2 u^2}{U_e^2} \right) dN. \quad (2.3-25)$$

As an initial guess of U'_0 at the stagnation point, a second-order estimate of equation (2.3-24) will be made. To do this, we only need a first-order estimate of the integral in equation (2.3-25) and this can be found by substituting the following expansions for u and U_e ,

$$u = u_1 + \epsilon u_2 + \dots \quad (2.3-26)$$

$$U_e = U_{e1} + \epsilon U_{e2} + \dots \quad (2.3-27)$$

into equation (2.3-25) and keeping only terms of first order in that integral. Therefore equation (2.3-25) becomes

$$I_0 = \epsilon \int_0^\infty \left(1 - \frac{u_1^2}{U_{e1}^2} \right) dN, \quad (2.3-28)$$

which can be expanded into

$$I_o = \epsilon \left[\int_0^\infty \left(1 - \frac{u_1}{U_{e1}} \right) dN + \int_0^\infty \frac{u_1}{U_{e1}} \left(1 - \frac{u_1}{U_{e1}} \right) dN \right] . \quad (2.3-29)$$

We can now identify the two integrals in equation (2.3-29) as being the first-order displacement thickness δ_1 , and the first-order momentum thickness θ_1 so that we may write that

$$I_o = \epsilon(\delta_1 + \theta_1) . \quad (2.3-30)$$

From Schlichting (1968), the first-order values of δ_1 and θ_1 at a stagnation point for a cylinder are

$$\delta_1 = 0.458 , \quad (2.3-31)$$

and

$$\theta_1 = 0.206 , \quad (2.3-32)$$

where the value of dU_e/ds at the stagnation point used to obtain these values was taken from potential theory.

Thus the initial guess of U'_o at the stagnation point will be taken from the following relation

$$U'_o = \sqrt{-A_2} (1 - 1.328\epsilon)^{-1/2} , \quad (2.3-33)$$

where $I_0 = 0.664\epsilon$ has been substituted into equation (2.3-24). The constant A_2 is to be determined from the wall pressure distribution in accord with equation (2.3-23).

After each iteration on the boundary-layer solution, U'_0 is updated using equation (2.3-24) until U'_0 satisfies the following convergence criteria $\Delta U'_0 \leq 10^{-5}$ where

$$\Delta U'_0 = |U'_0(\text{present iteration}) - U'_0(\text{last iteration})|, \quad (2.3-34)$$

and $\Delta F_{\eta_w} \leq 10^{-5} \cdot \Delta F_{\eta_w}$ was defined in equation (2.3-19).

Table I gives the initial values of U'_0 obtained from equation (2.3-33) using a series of various wall pressure distributions that will be discussed in detail in Section 2.5b. Also included in this table are the final values of U'_0 obtained from the iterated boundary-layer solutions.

2.4 Outline of the Numerical Solution Technique

The second-order boundary-layer equations have been programmed for numerical solution using an implicit finite-difference method similar to that developed by Flüge-Lotz and Blottner (1962) and as applied to higher-order boundary-layer theory by Davis, Whitehead, and Wornom (1970).⁺ We want to outline here the procedure used to numerically solve the governing equations when correcting the wall pressure for curvature effects to obtain the second-order inviscid

⁺Details of the method of solution are given in Appendix A.

surface pressure. For a general station away from the stagnation point the following procedure is employed:

1. The initial estimate of U_e is taken from equation (2.3-15). The initial estimate of dU_e/ds is made by extrapolating the previous two station values to the new station.
2. ξ and β_e are computed using equations (1.6-4a) and (2.3-16) and one iteration on the boundary-layer solution is performed.
3. Using equations (2.3-18-19) a check is made to see whether the solution has converged. If not, the value of I from this solution is used to update the values of U_e and dU_e/ds through equations (2.3-13) and (2.3-17).
4. Steps 2 and 3 are repeated until the solution converges.

At the stagnation point the initial guess of dU_e/ds is taken from equation (2.3-33). For each iteration thereafter, dU_e/ds was updated using equation (2.3-24).

2.5 Discussion of Results

a. Wall Pressure Data. - Four sets of experimental wall pressure data were used in this study. They were the experimental data of Thom (1933) at $Re_d = 174$, and three sets of experimental data by Grove, Shair, Petersen, and Acrivos (1964) -- two at $Re_d = 175$ and the other at $Re_d = 177$. The Reynolds number Re_d is defined as

$$Re_d = \frac{\rho_{\infty}^* U_{\infty}^* d^*}{\mu_{\infty}^*}, \quad (2.5-1)$$

where d^* = diameter of the test cylinder.

The d^*/\tilde{h}^* ratios employed in these experiments were 0.025, 0.1, 0.05, and 0.05 respectively, where

$$\frac{d^*}{\tilde{h}^*} = \frac{\text{diameter of test cylinder.}}{\text{width of test section}}. \quad (2.5-2)$$

All four sets of experimental data were assumed to represent steady flow conditions although only the data at Reynolds numbers 175 and 177 were taken using a splitter plate behind the cylinder to insure wake stability. Figure 2.2 shows the variation of the experimentally measured wall pressure distributions for Reynolds numbers 174, 175 ($d^*/\tilde{h}^* = 0.05$ distribution only), and 177. The exact reasons for the wide variations is not known but it seems to closely associated with the splitter plate influence.

Two numerically obtained wall pressure distributions were also used in this study. The first was obtained by Kawaguti (1953) from a numerical solution of the steady-state incompressible Navier-Stokes

⁺The second-order boundary-layer equations were nondimensionalized with respect to the nose radius of curvature shown in Figure 2.1. Therefore, the Reynolds numbers appearing in the governing equations through ϵ is based on the radius of the cylinder. However, when referring to the different Reynolds number cases, the Reynolds number stated will be based on the cylinder diameter which is the Reynolds number used in reporting the experimental and numerical data.

equations at Reynolds number 40. The second one was obtained by Thoman and Szewczyk (1969) from a numerical solution of the time-dependent incompressible Navier-stokes equations at Reynolds number 200.

b. Curvefit Representation of the Pressure Distributions.- In order to be able to compute the surface pressure at arbitrary stations along the surface, least-square curvefits were applied to all the wall pressure distributions used here.

Since steady-flow conditions are assumed, the wall pressure should be symmetrical with respect to the body coordinate measured from the stagnation point. For this reason, the four sets of experimental data and the numerical wall pressure distributions were fitted to a curve over the interval -180° to $+180^\circ$ by a least-squares technique using the ratio of two Chebyshev polynomials of the form

$$C_{P_{wall}} = \frac{P_{wall}^* - P_{\infty}^*}{\frac{1}{2} \rho_{\infty}^* U_{\infty}^{*2}} = \frac{\sum_{n=0}^{IP} C_n T_n(x)}{\sum_{n=0}^{IQ} D_n T_n(x)}, \quad (2.5-3)$$

where IP is the number of terms in the numerator expansion and IQ is the number of terms in the denominator. $T_n(x)$ is given by the recursion relation

$$T_n(x) = 2xT_{n-1}(x) - T_{n-2}(x), \quad (2.5-4)$$

where $T_0 = 1$, $T_1 = x$, $T_2 = 2x^2 - 1, \dots$ and x is contained on the interval $-1 \leq x \leq 1$. Further details concerning Chebyshev polynomials are given by Carnahan, Luther, and Wilkes (1969). Table II lists the coefficients C_0, C_2, C_4, \dots and D_0, D_2, D_4, \dots for the different curvefits used. Because the wall pressure was taken to be an even function of the body coordinate s , the odd coefficients were determined to be zero when the data was fitted over the interval -180° to $+180^\circ$.

The criteria upon which the selection of the curvefits used in this study was based will be presented in Section 2.5h where some of the curvefit difficulties encountered will also be discussed.

The wall pressure data was not tabulated in the literature for the Reynolds numbers 40, 175, 177, and 200 cases. Table III gives the data points for these cases as they were read from graphs given in the cited references. These points were the basis for the wall pressure distributions employed in this study. Figure 2.3a-f show comparisons between the pressure distribution curvefits selected for this study and the data points used in obtaining such.

It was pointed out in Section 2.3c that at the stagnation point $C_{p_{wall}}$ should be equal to 1 to second order. Note that this is not true of the wall pressure data shown in Figures 2.3a-d. This difference at the stagnation point is an indication of third and higher-order effects present in the data.

Figure 2.3e and 2.3f show $C_{p_{wall}}$ to be approximately 1 at the stagnation point for the Reynolds number 200 wall pressure data. This

appears to be an inconsistency as equation (2.3-22a) implies that the stagnation value should be approximately 1.03 or 1.04. It is not known how serious this inconsistency is, but some difficulties were encountered in trying to find accurate curvefit representations of this particular wall pressure data in the stagnation region (see Sect. 2.5h). This inconsistency may have been the cause, but this is not known for sure.

At other points along the body away from the stagnation point, the third-order corrections influence on the wall pressure distribution is not known. For want of a better method, the stagnation point values of these higher-order effects (i.e., α/Re_d) were assumed representative for all s and subsequently subtracted out of all the pressure data. This amounts to translating the wall pressure curvefit distribution after the data has been curvefitted⁺ so that C_{pwall} equals 1 at the stagnation point⁺⁺.

⁺When the wall pressure data was translated before curvefitting, the resulting curvefit still required shifting because it usually was not identically equal to 1 at the stagnation point. Such an unequal shifting of the data and the curvefit resulted in a poorer representation of the wall pressure data than the above method.

⁺⁺Other authors, namely, Dimopoulos and Hanratty (1968) fitted the Reynolds number 174 wall pressure data to a polynomial of the form

$$\frac{p_{wall}^* - P_{\infty}^*}{\frac{1}{2} \rho_{\infty}^* U_{\infty}^{*2}} = \sum_{n=0}^6 a_{2n} \phi^{2n}. \quad (2.5-5)$$

Using this pressure distribution, they obtained a Blasius series solution of the classical boundary-layer equations for the shear-stress distribution. It should be noted that in doing their Blasius solution, Dimopoulos and Hanratty (1968) did not need to shift their pressure distribution since the stagnation value of C_{pwall} does not appear in the final Blasius shear-stress equation.

c. Effects of Curvature and Displacement Speed on Wall Pressure

Distributions. - Figures 2.4a-e show the following wall pressure distributions for all of the Reynolds number cases studied. Curve (1) gives the inviscid surface pressure distribution obtained from potential theory and it is the same in all the figures.⁺ Curve (2) shows the wall pressure distribution taken from either experimental or numerical data. Curve (3) shows the inviscid surface pressure valid to second order obtained from equation (2.3-12) and the second-order boundary-layer solution.⁺⁺ Looking at the results in a different light, curve (3) shows the inviscid surface pressure to second order that would be required to produce the observed wall pressure distribution shown by curve (2). As such, the difference between curve (3) and curve (2) can be attributed to curvature through equation (2.3-12). Without the curvature correction, equation (2.3-12) implies the wall pressure is equal to the inviscid surface pressure.

Figures 2.4a-e also give some indication of the effect the boundary-layer displacement thickness has on the inviscid surface pressure. If one assumes the inviscid surface pressure distribution

⁺Due to the presence of a wake behind a cylinder even at high Reynolds numbers, the inviscid potential pressure distribution is meaningless for $\phi \geq 100^\circ$.

⁺⁺Curve (4), shown in Figure 2.4c only, shows the wall pressure that results from a solution of the second-order equations using the potential theory inviscid surface pressure distribution to compute β_e . Thus, curve (4) gives the wall pressure that would exist if the inviscid pressure were given by curve (1).

at infinite Reynolds number to be given by potential theory,⁺ then the difference between curves (1) and (3) of Figures 2.4a-e can be viewed as a measure of the second-order contribution to the inviscid flow (i.e., that due to flow over the displacement body).

d. Displacement-Body Effects.-For the governing equations to be valid to second order, the inviscid surface speed U_e must be the inviscid surface speed on the cylinder surface due to flow over the displacement body. In Section 1.4 we defined a displacement thickness δ such that the mass rate of flow of inviscid fluid past a body thickened by an amount δ is equal to the amount of viscous flow past the real body. This definition yielded the following relation for the displacement thickness δ

$$\int_{\delta}^{\infty} \frac{U_e}{h} dN = \int_0^{\infty} u dN. \quad (2.5-6)$$

In terms of the displacement thickness δ , the displacement body for a cylinder is then given by $1 + \epsilon\delta$.

Figures 2.5a-e show the displacement bodies obtained in this study for solutions of the complete⁺⁺ second-order equations. It should be noted also that for the complete second-order solution, the inviscid surface pressure shown in Figures 2.4a-e is the inviscid surface

⁺Due to the presence of a wake behind a cylinder even at very high Reynolds numbers, this point is uncertain.

⁺⁺Complete here refers to solutions of the second-order equations where the inviscid flow parameters are also valid to second-order.

pressure which boundary-layer theory says is induced on the cylinder surface due to flow over these displacement bodies. The thickness of the boundary layer for the Reynolds number 40 case gives an indication that these solutions are an extreme test of the limitations of the boundary-layer concept.

Figure 2.6 shows the displacement body obtained from a classical boundary-layer solution at Reynolds number 177 using the inviscid surface pressure taken from potential theory to compute β_e . Whereas in Figures 2.5a-e the inviscid flow sees the approximate displacement body, this is not true for the solution shown in Figure 2.6 where the inviscid solution is also for a cylinder. Note that Figure 2.6 gives evidence of a singularity in the displacement thickness derivative at separation.⁺ However, Figure 2.5d shows that when the viscous flow was made consistent with the inviscid flow (i.e., the complete second-order solution), there appeared to be no evidence of such an impending singularity at separation.

e. The Viscous Pressure Gradient Parameter β_v .- Figure 2.7 shows the values of the inviscid and viscous pressure gradient parameters on the cylinder surface for the Reynolds number 177 case.⁺⁺ Also shown are the values at the outer reaches of the viscous flow region (i.e., where $F = 1.0000$). The large variation in the viscous

⁺Brown and Stewartson (1969) have shown that if there is a singularity in the shear stress at separation, there will also be a singularity in the derivative of the displacement thickness.

⁺⁺The other Reynolds numbers cases were similar.

pressure gradient parameter is an indication of large pressure gradients existing across the boundary layer. From Figure 2.7 and also equations (1.4-18e), (2.2-1b), and (2.2-5) it can be seen that

$$\beta_V \rightarrow \beta \quad \text{as} \quad N \rightarrow \infty. \quad (2.5-7)$$

It is often suggested that separation of the classical boundary-layer flow from a body results from the boundary layer being subjected to a positive pressure gradient. For classical boundary-layer theory one need only monitor the inviscid pressure gradient parameter β_e to determine when the boundary layer sees a positive pressure gradient. The reason for this is that for classical boundary-layer theory the pressure is assumed constant across the boundary layer and as a result, the viscous pressure gradient in the ξ direction is equal to the inviscid pressure gradient. However, for the second-order equations the viscous pressure gradient is not equal to the inviscid pressure gradient. For this case the viscous pressure gradient parameter β_V must be monitored.⁺ Monitoring β_V , Figure 2.7 shows the portion of the boundary layer nearest the wall undergoing a positive viscous pressure gradient at separation. This causes the flow to separate at the wall and in turn causes the rest of the boundary layer to separate with it.

⁺Note from Figure 2.7 that if one were to monitor the inviscid pressure gradient parameter β , he would lead to the conclusion that the boundary layer was undergoing a negative pressure gradient at separation.

f. Shear Stress Distributions. - Figures 2.8a-e show the shear stress distributions obtained in this study. In each of these, curve (1) shows the solution to the equations valid to second order using the inviscid surface conditions obtained from equation (2.3-13) by iteration and as such, represents the complete second-order solution. The remaining curves will now be discussed in terms of how they compare with curve (1). Comparison of the complete second-order solution, curve (1), with experimental results will be left for a later section.

Curve (2) shows the solution to the classical first-order boundary-layer equations using the inviscid surface pressure distribution obtained from potential theory. This solution is the same for all Reynolds numbers. The shear stress given by this solution can be seen to be very much higher than curve (1).

Curve (3) shows the solution to the classical boundary-layer equations taking the inviscid surface pressure to be approximately equal to the observed wall pressure distribution. It was quite surprising to find this solution virtually equal to the second-order solution except near separation. This result can be rationalized in the following way. Near the wall where N is small, h is approximately equal to 1, and u is approximately equal to zero.

Substituting these approximations into the governing equations ⁺ gives a zero normal pressure gradient and reduces the remaining two equations to the classical boundary-layer equations. Therefore, the flow near the wall is approximately governed by the classical boundary-layer equations even when curvature terms are included. Since both of the solutions, curve (1) and curve (3), see the same wall pressure gradient, this apparently results in their shear stress distributions being approximately equal. We note in passing that, based on this point, it is natural to conclude that an accurate means of obtaining the wall pressures is needed in order to calculate the wall shear.

Curve (4) (shown in Figure 2.8c only) gives the solution to the second-order equations using the inviscid surface pressure distributions from potential theory to compute β_e . This solution makes no attempt to correct the inviscid surface pressure (potential) for curvature effects. The wall pressure for this solution is not the observed wall pressure distribution but the wall pressure that comes out of equation (2.3-1). For the Reynolds number 175 case, this wall pressure is shown by curve (4) in Figure 2.4c -- the wide difference

⁺The second-order incompressible boundary-layer equations are given as:

continuity equation. $u_s + (hv)_N = 0$, (2.5-8)

s-momentum equation. $u u_s + v(hu)_N + p_s = h \left[\frac{1}{h} (hu)_N \right]_N$, (2.5-9)

N-momentum equation. $p_N = \frac{h_N}{h} u^2$. (2.5-10)

between this and the actual wall pressure apparently causing the difference in the shear stress distributions observed in Figure 2.8c. Note that for this case the boundary-layer solution failed to converge after 30 iterations⁺ (the maximum allowed for this particular case) to the degree of accuracy required for this study.⁺⁺ It is also worthy of note that this solution lies closer to the complete second-order solution than curve (2) shown in Figure 2.8c.

Curve (5) shows the solution to the second-order equations using the wall pressure distribution to compute β_e , that is, taking the inviscid surface pressure to be approximately equal to the wall pressure distribution. This assumption is often made since the measured wall pressure distribution should contain displacement effects. If the pressure is approximately constant across the boundary layer, then it would seem that taking the observed wall pressure distribution to be approximately equal to the inviscid surface pressure would be a valid assumption. However, as was noted earlier, this assumption is not a very good one for the Reynolds numbers studied here as can be seen from the results in Figures 2.4a-e and also from the shear stress results shown in Figures 2.8a-e.

g. Comparisons with Experimental and Numerical Shear Stress Data.-

In order to properly compare the numerical shear stress distributions with experimental data, wall pressure and shear stress distributions

⁺Thirty iterations at that particular station.

⁺⁺Computer output showed that the solution was in the process of converging when the 30 iteration limit was reached.

were needed which were taken at the same Reynolds number and under the same test conditions. However, none were to be found in the literature.

The experimentally measured wall pressure and shear stress distributions appear to be very sensitive to the test parameters d^*/\tilde{h}^* , defined in equation (2.5-2) and \underline{c}^*/d^* defined as the distance from the cylinder centerline to the front edge of the wake splitter plate ratioed to the diameter of the cylinder.

The influence of \underline{c}^*/d^* ratio on the measured wall pressure can be partly seen in Figure 2.2. For a Reynolds number difference of 2 between the 175 and 177 case, there is a slight change in the wall pressure data. For the 175 case, \underline{c}^*/d^* was approximately 2.5, d^*/\tilde{h}^* was 0.05. For the Reynolds number 177 case, \underline{c}^*/d^* was 3.4 and d^*/\tilde{h}^* was 0.05.

The effect of the d^*/\tilde{h}^* ratio on the measured wall pressure distribution was shown experimentally by Grove, Shair, Petersen, and Acrivos (1964). To illustrate here how much the d^*/\tilde{h}^* ratios influence the numerical shear stress results, the measured wall pressure distribution at Reynolds number 175 with $\underline{c}^*/d^* = 2.5$ and $d^*/\tilde{h}^* = 0.1$ was employed in addition to the Reynolds number 175 case previously mentioned with a $d^*/\tilde{h}^* = 0.05$ and a $\underline{c}^*/d^* = 2.5$. Figure 2.9 shows a significant difference in the two Reynolds number 175 wall pressure distributions. Figure 2.10, which was obtained from a solution of the classical boundary-layer equations taking the inviscid surface pressure to be approximately equal to the observed wall

distribution[†] shows a comparison between the two resulting shear stress distributions. Note from Figure 2.10, that the d^*/\tilde{h}^* ratio does not appear to have much influence on the shear stress distribution in the stagnation region. However, at points further back along the body, the influence becomes noticeable. Figure 2.10 strongly suggests that when comparing numerical shear stress distributions obtained by this method with experimental shear stress data that, in addition to matching the Reynolds number, one should also match as closely as possible the d^*/\tilde{h}^* ratio at which the wall pressure and shear stress data were taken.

Of all the experimental shear stress data found in the literature, the closest (in terms of the Reynolds number and test conditions) to the Reynolds number 175 case where a splitter plate was used, was the data at Reynolds number 167 with a c^*/d^* ratio of 2.5 and a d^*/\tilde{h}^* ratio of 0.0833. Figure 2.11 shows a comparison between the classical boundary-layer shear stress solution using the measured wall pressure to compute β_e and the experimental shear stress data at Reynolds number 167. Since Figures 2.9 and 2.10 show the wall pressure and the resulting shear stress distribution to be very sensitive to the d^*/\tilde{h}^* ratio, this fact should be kept in mind when studying Figure 2.11.

[†]In Section 2.5f, this solution was shown to be virtually the same as the complete second-order solution. Therefore, because this solution requires less computer time to run, it will be employed for comparison purposes.

For the Reynolds number 174 wall pressure distribution which was taken without the aid of a splitter plate, the nearest experimental shear stress data was at Reynolds number 151. However, the d^*/\tilde{h}^* ratio for the Reynolds number 174 case was 0.025, whereas for the Reynolds number 151 case, d^*/\tilde{h}^* was 0.0833. Because of the wide difference between the d^*/\tilde{h}^* ratios used in obtaining the experimental wall pressure and shear stress distributions for this case, it was felt that any conclusions arrived at by comparison with this data would seem open to question. Therefore this comparison was not made.

Similarly, for the Reynolds number 177 case, the large differences in d^*/\tilde{h}^* ratios used to obtain the wall pressure and shear stress data prevented a comparison of such.

Note, however, that Dimopoulos and Hanratty (1968) did compare the Reynolds number 151 shear stress data with a Blasius series solution using a curvefit of the Reynolds number 174 wall pressure by Thom (1933) to compute β_e .⁺ The good agreement between experiment and theory which they report, apparently results from an inconsistency in their Blasius solution. Using the Blasius series taken from Rosenhead (1963),⁺⁺ and the wall pressure representations and constants

⁺Equation (2.5-5) gives the form of their curvefit representation.

⁺⁺There seems to be some question as to which Blasius series solution Dimopoulos and Hanratty (1968) used. Dimopoulos and Hanratty (1968) report they used the Blasius solution given by Rosenhead (1963). However, Dimopoulos (1968) reported that he used the Blasius solution given by Schlichting (1960).

of Dimopoulos and Hanratty (1968) (see eq. (2.5-5) and Table IV) we could not reproduce their reported shear stress distributions. Figure 2.12 shows the Blasius shear stress distribution obtained in this study for the Reynolds number 174 case using the curvefit coefficients of Dimopoulos and Hanratty (1968). Also shown in Figure 2.12 is the Blasius solution reported by Dimopoulos and Hanratty (1968) along with the Reynolds number 151 shear stress data with which they compared.

Two checks were made on our Blasius solution. Taking the inviscid surface speed on a cylinder ($U_e = 2 \sin \phi$), substitution was made into Bernoulli's equation and expanded to obtain a pressure relation of the form of equation (2.5-5). Picking off the coefficients in equation (2.5-5) substitution was then made into our Blasius equation which was written in terms of these coefficients. Our Blasius solution, using the constants taken from potential theory, compared exactly with that reported by Schlichting (1968). The second check was a finite-difference solution to the same equation using the wall pressure curvefit to compute β_e . Figure 2.12 shows that our Blasius solution agrees with the finite-difference solution except near separation.

Figure 2.12 shows that their good agreement was apparently due to an inconsistency in their Blasius solution. Appendix B gives the Blasius solution obtained in this study in terms of the constants in the curvefit equation given by Dimopoulos and Hanratty (1968).

Because the Reynolds numbers 40 and 200 wall pressure distributions were taken from numerical solutions of the full Navier-Stokes equations, the shear stress distributions were available from the same

"test" conditions. Using the following relation, the shear stress distributions were obtained from the vorticity distributions on the cylinder surface reported by Kawaguti (1953) and Thoman and Szewczyk (1969)

$$\bar{C}_f = \frac{-2\Omega_{\text{wall}}}{\sqrt{\text{Re}}} . \quad (2.5-11)$$

Figures 2.13 and 2.14 show comparisons between the boundary-layer shear stress distributions and the shear stress distributions obtained by Kawaguti (1953) and Thoman and Szewczyk (1969). Figures 2.13 and 2.14 shows good agreement between the boundary-layer solution and the full Navier-Stokes solution. Why there seems to be better agreement between the boundary-layer solution and the Navier-Stokes solution at Reynolds number 40 rather than Reynolds number 200 is not known.

h. Curvefitting Difficulties.- The selection of the particular wall pressure curvefits used in this study was based on two criteria. The first criteria was that when a particular wall pressure curvefit was used to compute β_e , the β_e distribution computed had to be a well-behaved function. The second criteria consisted of selecting (from among all the curvefits that satisfied the first criteria), the curvefit which to the eye, appeared to best represent the wall pressure data.

Since most of the curvefit difficulties encountered were with the Reynolds number 200 wall pressure data, this case will be used for illustration. Two curvefits of the Reynolds number 200 wall pressure

data will be discussed -- curvefit A and curvefit B. Curvefit A, shown in Figure 2.3e, appeared to give the best representation of the Reynolds number 200 pressure data of all the different curvefits tried. However, it did not satisfy the first criteria. Figure 2.15 shows the β_e distribution that results when computed using this wall pressure distribution. The unexpected flat portion from approximately 20° to 40° is what is termed here as a not well-behaved function. How this flat part of the β_e distribution affects the boundary-layer shear stress results can be seen in Figure 2.16. Up to the flat part of the β_e distribution, the boundary-layer shear stress agrees fairly well with the more exact Navier-Stokes solutions of Thoman and Szewczyk (1969). Then the effect of the flat portion of the β_e distribution seems to be to shift the numerical results away from the Navier-Stokes solution. The reason for the horizontal portion in Figure 2.15 can be traced back to the derivative of the wall pressure shown in figure 2.17. Whenever the wall pressure derivative became flat in the approximate area shown, the β_e distribution computed from that curvefit distribution also changed in the same area. Figure 2.3e shows curvefit B which was selected as the best curvefit satisfying both of the criteria given above. Figures 2.18 and 2.19 show that both the pressure derivative and the computed β_e using curvefit B are well behaved. Figure 2.20 shows a comparison between the classical boundary-layer shear stress and the numerical shear stress.

It should be noted here that, although the wall pressure curvefits selected were the best we could obtain, it was felt that some,

particularly curvefit B of the Reynolds number 200 wall pressure data, did not represent the data accurately enough. Examining Figure 2.3e, it can be seen, for example, that curvefit B does not represent the stagnation region wall pressure data very well.⁺ Upon examining the shear stress results obtained by using curvefit B to compute β_e and the shear stress results obtained by using curvefit A to compute β_e , it is noted that curvefit A, which gave the best representation of the stagnation region wall pressure data also compared more favorably with the experimental results in that region. Further evidence that the numerical shear stress is sensitive to the wall pressure representation can be seen from Figures 2.21 and 2.22. Figure 2.21 shows a comparison between two different wall pressure representations of the Reynolds number 174 data. Both appear to be fairly good representations of the wall pressure data. However, Figure 2.22 shows that when both pressure distributions are used to compute β_e and a classical boundary-layer solution, one pressure distribution leads to separation whereas the other does not.

2.6 Conclusions

In summary, the accuracy of the method presented here for studying the effects of curvature on boundary layers at moderate Reynolds numbers seems to be limited by the accuracy of the measured wall pressure data and the accuracy of the wall pressure curvefit representation. Although

⁺In Section 2.5b it was noted that the stagnation value of $C_{p_{wall}}$ appeared to be low (implied by eq. 2.3-22a)). Whether this contributed to the poor curvefit representation in the stagnation region is not known.

there was a lack of experimental shear stress data taken under the same test conditions as the wall pressure data, what data there was strongly indicates that given a very accurate wall pressure representation, the agreement between the boundary-layer shear stress and the experimental shear stress data would be very good, even for Reynolds numbers as low as 40 for cylinders. In addition, we conclude the following:

1. For all the Reynolds number cases studied, the effects of longitudinal curvature on the boundary-layer wall pressure are significant as attested to by Figures 2.4a-e. This implies that if one knew the second-order inviscid surface conditions and wanted to determine the wall pressure (viscous), the omission of longitudinal curvature effects would result in large errors in the flow properties at the wall.

2. For the Reynolds number cases studied, large pressure gradients (implied above) were found to exist across the boundary layer. This would seem to exclude any hope of obtaining a good representation of the flow from classical boundary-layer theory. However, to the contrary, it was found that if one had a measured wall pressure distribution and was only interested in shear stress results, a classical boundary-layer solution using the measured wall pressure distribution to compute β_e would be sufficient.

3. For the complete second-order solution, there appeared to be no evidence of an oncoming singularity in the displacement thickness on a cylinder at separation such as is indicated by a classical boundary-layer solution.

III. A STUDY OF LONGITUDINAL CURVATURE EFFECTS ON COMPRESSIBLE BOUNDARY-LAYER FLOW WITH DISPLACEMENT THICKNESS INTERACTION

3.1 Introduction

In Chapter II, the effects of longitudinal curvature on incompressible boundary-layer flow were studied for the case of flow around a circular cylinder by taking the measured wall pressure distribution and determining what the inviscid properties were that produce that wall pressure. By this indirect method the effects of longitudinal curvature and displacement speed were ascertained to second order.

In this chapter, we want to study the effects of curvature on compressible boundary-layer flow for a case where the displacement-body effects can be computed directly using some approximate method to compute the inviscid flow properties. Attention then is drawn toward supersonic flows where a multitude of approximate schemes are available - for example, linear thin airfoil theory or other comparable models.

For this reason, it was decided to extend the finite-difference work of Flügge-Lotz and Blottner (1962) in which they computed directly the displacement-body effects on a flat plate in hypersonic flow. Here interest will be directed toward curved body surfaces at hypersonic speeds.

Although the analysis by Cheng, Hall, Golian, and Hertzberg (1961) was not restricted to flat plates, it was not until 1969 that the curved surface case was studied. At that time, Stollery (1969) extended the analysis of Cheng et al. (1961) and Sullivan (1969) to

cover curved body surfaces in regions of strong and weak interaction. These approximate theories did not, however, take into account variations in pressure across the displacement body or boundary layer due to the curvature of the body as will be done in the present study.

In addition to studying curvature effects, this chapter also seeks to shed light on the possible existence of a saddle-point type behavior that can emerge in these types of problems from numerical solutions. Such behavior for the strong interaction problem was observed by Garvine (1968) with his viscous shock-layer flat-plate solution. Baum (1968) observed similar findings with his supersonic boundary-layer solutions. However, the more recent papers of Sullivan (1969), Stollery (1970), and Cheng, Chen, Mobley, and Huber (1970) did not encounter a saddle-point behavior. If indeed a saddle-point behavior does exist for this type of interaction problem, it should show up in the present study and will have to be overcome. Once the interaction process is modeled correctly, the way will be clear for further studies on curved surfaces in supersonic flows.

The particular problem to be investigated here is that of two-dimensional laminar flow up a cubic compression ramp at Mach numbers 6, 8, and 12.25. This problem was chosen because the displacement-body effects should be sizable and the curvature effects can be easily handled since the surface curvature is everywhere analytic. In addition there exists some experimental data due to Stollery (1970) for the Mach number 12.25 case which will serve as a basis of comparison in this study.

3.2 Governing Equations

a. Viscous Region. - The governing equations for the viscous region are the second-order compressible boundary-layer equations presented in Section 1.4 of Chapter I. Details of the numerical method of solution used here are given in Appendix A.

b. Inviscid Region. - Examining the governing equations for the viscous region, it is seen that the inviscid properties necessary to compute the boundary-layer solution at a particular station are P_e , T_e , μ_e , ρ_e , U_e , $dU_e/d\xi$, and ξ . In this section, it will be shown how to relate these to the inviscid pressure P_e and pressure gradient dP_e/ds at the desired station. Once μ_e , ρ_e , and U_e are known, ξ is determined by numerical integration employing a trapezoidal rule.

For this study, the tangent-wedge formula is employed to compute the inviscid pressure on the displacement body under the assumption that the displacement body is a streamline for the inviscid flow model. With this approximation the pressure at any point on the displacement body is taken to be equal to the pressure on a wedge whose half-angle equals the local inclination angle of the displacement-body tangent. Physically this approximation gains its validity from the fact that at hypersonic speeds the shock layer is sufficiently thin on slender bodies to assume that the variations in pressure and streamline angles will be small across the shock layer. Thus, the surface values are approximately the same as those at the shock. In addition to the above limitations, the tangent-wedge approximation can be seen to

neglect centrifugal-force effects that result from curvature of the body. None the less, this pressure law has become generally acceptable as a model of hypersonic inviscid flows and will be employed here due to its extreme simplicity. It was also adopted by Flügge-Lotz and Blottner (1962), Sullivan (1969), Stollery (1970), and other authors and thus its use here allows a direct comparison with other viscous solutions. Another important feature as pointed out by Sullivan (1969) is that the tangent-wedge approximation gives a single relation valid for both the strong and weak interaction regimes.

From Hayes and Probstein (1959) the tangent-wedge pressure law can be written as

$$P_{DB}/P_{\infty} = 1 + \gamma M_{\infty}^2 \theta^2 \left[\sqrt{\left(\frac{\gamma+1}{4}\right)^2 + \frac{1}{M_{\infty}^2 \theta^2}} + \frac{\gamma+1}{4} \right], \quad (3.2-1a)$$

where

$$\theta = \theta_{wall} + \epsilon \frac{d\delta}{ds}, \quad (3.2-1b)$$

and it is understood that the local inclination angle, θ , of the displacement-body tangent is sufficiently small as to make the $\sin \theta \approx \theta$ a valid approximation.

In equation (3.2-1a), P_{DB} is the inviscid pressure induced on the displacement-body surface. To determine the inviscid pressure on the actual body in terms of the pressure on the displacement body, we first expand the pressure about the body surface in a Maclaurin series thus obtaining

$$P(s, o + \epsilon \delta) = P_{DB} = P(s, o) + \left(\frac{\partial P}{\partial n} \right)_{s, o} \epsilon \delta + \dots \quad (3.2-2)$$

Noting that $P(s, o) = P_e$, equation (3.2-2) can be solved for P_e to obtain

$$P_e = P_{DB} - \left(\frac{\partial P}{\partial n} \right)_{s, o} \epsilon \delta - \dots \quad (3.2-3)$$

From equation (3.2-3), it is seen that to obtain P_e formally valid to second order we need only to retain terms in the $\left(\frac{\partial P}{\partial n} \right)_{s, o}$ term to $O(1)$. To do this, we note that the inviscid n-momentum equation written in terms of the present coordinate system as given by Van Dyke (1962c) is

$$\frac{\partial P}{\partial n} = -\bar{\rho} \left(\frac{U}{h} \frac{\partial \tilde{V}}{\partial s} + \tilde{V} \tilde{V}_n - \frac{h_n U^2}{h} \right). \quad (3.2-4)$$

If we now apply the ordering scheme given by Van Dyke (1962c), that is,

$$U = U_1 + \epsilon U_2 + \dots \quad (3.2-5a)$$

$$\bar{\rho} = \bar{\rho}_1 + \epsilon \bar{\rho}_2 + \dots \quad (3.2-5b)$$

$$\tilde{V} = \tilde{V}_1 + \epsilon \tilde{V}_2 + \dots \quad (3.2-5c)$$

to equation (3.2-4), we obtain

$$\begin{aligned} \frac{\partial P}{\partial n} = & -(\bar{\rho}_1 + \epsilon \bar{\rho}_2 + \dots) \left[\frac{(U_1 + \epsilon U_2 + \dots)}{h} \left(\frac{\partial \tilde{V}_1}{\partial s} + \frac{\epsilon \partial \tilde{V}_2}{\partial s} + \dots \right) + \right. \\ & \left. + (\tilde{V}_1 + \epsilon \tilde{V}_2 + \dots) \left(\frac{\partial \tilde{V}_1}{\partial n} + \frac{\epsilon \partial \tilde{V}_2}{\partial n} + \dots \right) - \kappa \frac{(U_1 + \epsilon U_2 + \dots)^2}{h} \right]. \end{aligned} \quad (3.2-6)$$

On the body surface $h = 1$ and $\tilde{V}_1(s, 0) = 0$, thus to $O(1)$ equation (3.2-6) becomes

$$\left(\frac{\partial P}{\partial n} \right)_{s,0} = \kappa \bar{\rho}_1(s, 0) U_1^2(s, 0). \quad (3.2-7a)$$

Noting that $\bar{\rho}_1(s, 0)$ and $U_1(s, 0)$ are simply the inviscid surface values for the case where displacement-body effects are neglected, they can be easily calculated once they are related to the inviscid pressure by setting $\theta = \theta_{\text{wall}}$ in the tangent-wedge pressure law. However, it was found that the variation in pressure across the displacement body was very large for the compression ramp study, and it was reasoned that some advantage might be gained by including the higher-ordered terms in the last expression in equation (3.2-6). For this reason, it was decided to take

$$\left(\frac{\partial P}{\partial n} \right)_{s,0} = \kappa \rho_e U_e^2, \quad (3.2-7b)$$

where ρ_e and U_e are the inviscid surface values which include displacement-body effects.

Upon substitution from equation (3.2-7b), equation (3.2-3) may now be written as

$$P_e = P_{DB} - \kappa \rho_e U_e^2 \epsilon \delta. \quad (3.2-8)$$

Here ρ_e and U_e depend implicitly on P_e as will be shown later and an iterative solution will be employed to extract the value of P_e from equation (3.2-8).

Note that for the flat-plate study the curvature is zero and equation (3.2-8) gives the result that to second order $P_e = P_{DB}$.

In order to relate T_e , μ_e , ρ_e , and U_e to the inviscid surface pressure P_e , it will be assumed that the shock layer is isentropic as was done by Flügge-Lotz and Blottner (1962) as well as most other investigators of the problem.

Note that for the present model, the inviscid pressure on the displacement body is given by the tangent-wedge pressure law which although being approximate is nevertheless generally accepted as being valid. In addition to the inviscid pressure, it is necessary to have two other properties with which to define the isentropic flow. The second property is

$$H_e = H_\infty, \quad (3.2-9)$$

which in no way limits the flow model since it is exact.

The remaining property sought is the isentropic constant here taken to be the free-stream value given by

$$P_e/\rho_e^\gamma = P_\infty/\rho_\infty^\gamma. \quad (3.2-10)$$

This assumption is not without precedent since all previous authors have adopted it. The alternate approach of evaluating the isentropic constant directly behind the leading-edge shock is unacceptable since the effective shock angle is not known a priori. However, it should be pointed out that downstream along the body the outer reaches of the boundary layer merges with an inviscid flow that has crossed a much weaker portion of the leading-edge shock and as such the effective isentropic constant in this portion of the flow would be expected to be nearer to the free-stream value. Thus, the inviscid surface pressure is taken to be related to the temperature through the relation

$$P_e/P_\infty = (T_e/T_\infty)^{\frac{\gamma}{\gamma-1}}. \quad (3.2-11)$$

Assuming that P_e/P_∞ is computed from the tangent-wedge relation, equation (3.2-11) may be solved for T_e to obtain

$$T_e = T_\infty (P_e/P_\infty)^{\frac{\gamma-1}{\gamma}}, \quad (3.2-12)$$

which can be used to evaluate μ_e by either the Sutherland viscosity law (equation (1.3-6)) or the linear viscosity law equation (1.3-7).

Substituting for T_e/T_∞ in equation (3.2-12) from the equation of state, we find that

$$\rho_e = (P_e/P_\infty)^{\frac{1}{\gamma}}, \quad (3.2-13)$$

where it is noted that $\rho_\infty = 1$ in the present nondimensional scheme.

To obtain U_e as a function of P_e/P_∞ , we note that on the body surface

$$H_e = T_e + U_e^2/2 \quad (3.2-14)$$

from the total enthalpy relation. If we first write the total enthalpy constant H_e as

$$H_e = T_\infty + U_\infty^2/2 \quad (3.2-15)$$

and note that $U_\infty = 1$ and $T_\infty = \frac{1}{(\gamma-1)M_\infty^2}$, equation (3.2-14) can be solved for U_e to find that

$$U_e = \left[1 + \frac{1 - (P_e/P_\infty)^{\frac{\gamma-1}{\gamma}}}{\frac{\gamma-1}{2} M_\infty^2} \right]^{1/2}. \quad (3.2-16)$$

Thus, we have shown through equations (3.2-12-16) that assuming an isentropic flow behind the shock, T_e , μ_e , ρ_e , and U_e can be related to the inviscid surface pressure P_e .

Similarly $dU_e/d\xi$ can be related to the pressure gradient by first noting that

$$\frac{dU_e}{d\xi} \pm \frac{dU_e}{ds} \frac{ds}{d\xi} = \frac{1}{\rho_e \mu_e U_e} \frac{dU_e}{ds} \quad (3.2-17)$$

To relate the pressure gradient dP_e/ds to the velocity gradient dU_e/ds , we observe that the inviscid s-momentum equation when written in terms of the present coordinate system is from Van Dyke (1962c)

$$\frac{\partial P}{\partial s} = -\bar{\rho} \left[U \frac{\partial U}{\partial s} + \tilde{v} \frac{\partial (hU)}{\partial n} \right]. \quad (3.2-18)$$

Employing the irrotationality condition given in equation (1.2-16), equation (3.2-18) when evaluated at the wall becomes

$$\frac{dP_e}{ds} = -\rho_e \left[U_e \frac{dU_e}{ds} + \tilde{v}_e \left(\frac{\partial \tilde{v}}{\partial s} \right)_{s,0} \right]. \quad (3.2-19)$$

Ordering terms in the above equation according to equation (3.2-5), we obtain that to second order

$$\frac{dP_e}{ds} = -\rho_e U_e \frac{dU_e}{ds}, \quad (3.2-20)$$

which allows equation (3.2-17) to be written in the desired form

$$\frac{dU_e}{d\xi} = \frac{-dP_e/ds}{\rho_e^2 \mu_e U_e^2}. \quad (3.2-21)$$

[†]The analysis presented here is for the plane flow case. Thus $j = 0$.

Returning to equation (3.2-8), we may now write it in the following form once substitution has been made for ρ_e and U_e^2 from equations (3.2-13) and (3.2-16)

$$\frac{P_e}{P_\infty} = \frac{P_{DB}}{P_\infty} - \frac{\kappa \epsilon \delta}{P_\infty} \left[\left(1 + \frac{2}{(\gamma-1)M_\infty^2} \right) \left(\frac{P_e}{P_\infty} \right)^{1/\gamma} - \frac{2}{(\gamma-1)M_\infty^2} \frac{P_e}{P_\infty} \right]. \quad (3.2-22)$$

To determine the surface pressure gradient dP_e/ds in terms of the displacement-body pressure gradient, we differentiate equation (3.2-22) with respect to the s -coordinate and solve for dP_e/ds to obtain

$$\begin{aligned} \frac{dP_e}{ds} = & \left[\frac{dP_{DB}}{ds} - \epsilon \frac{d(\kappa \delta)}{ds} \left\{ \left[1 + \frac{2}{(\gamma-1)M_\infty^2} \right] \left(\frac{P_e}{P_\infty} \right)^{1/\gamma} - \frac{2}{(\gamma-1)M_\infty^2} \frac{P_e}{P_\infty} \right\} \right. \\ & \cdot \left. \left[1 + \frac{\epsilon \kappa \delta}{P_\infty} \left\{ \frac{1}{\gamma} \left[1 + \frac{2}{(\gamma-1)M_\infty^2} \right] \left(\frac{P_e}{P_\infty} \right)^{-\frac{\gamma-1}{\gamma}} - \frac{2}{(\gamma-1)M_\infty^2} \right\} \right]^{-1} \right] \end{aligned} \quad (3.2-23)$$

Note that equation (3.2-22) cannot be solved explicitly for the inviscid pressure P_e . Thus, when equations (3.2-22-23) are applied at a station, an initial guess of P_e/P_∞ will be used to evaluate equations (3.2-22-23) for the first iteration, thereafter the value of P_e/P_∞ from the previous iteration will be used until the overall solution and thus P_e/P_∞ converges.

To compute dP_{DB}/ds necessary for evaluating equation (3.2-23), the tangent-wedge pressure law is differentiated to give

$$\frac{dP_{DB}}{ds} = \frac{\gamma P_{\infty} M_{\infty} (\epsilon \delta'' + \theta'_{wall})}{(1 + B^2 M_{\infty}^2 \theta^2)^{1/2}} \left[1 + 2B^2 M_{\infty}^2 \theta^2 + 2B M_{\infty} \theta (1 + B^2 M_{\infty}^2 \theta^2)^{1/2} \right]^+, \quad (3.2-24a)$$

where

$$\theta = \theta_{wall} + \epsilon \frac{d\delta}{ds}, \quad (3.2-24b)$$

and

$$B = \frac{\gamma + 1}{4}. \quad (3.2-24c)$$

In summary, the inviscid properties necessary to compute a boundary-layer solution at a particular station are P_e , T_e , μ_e , ρ_e , U_e , $\frac{dU_e}{d\xi}$, and ξ . This section has shown how these are related to the inviscid surface pressure P_e and its gradient dP_e/ds and as such the problem is now reduced to one of determining P_e and dP_e/ds . Furthermore, through equations (3.2-1) and (3.2-24) the values of P_e and dP_e/ds can be seen to depend only upon the unknowns δ' and δ'' . Thus, once δ' and δ'' are known all inviscid properties can be computed.

3.3 Solution at a General Station

As was noted in Section 3.2, all inviscid properties can be calculated once δ' and δ'' are known. Therefore, the overall method of solution can be summarized as follows. (1) Make an initial

[†]Note that $()' \equiv \frac{d}{ds}$ and this notation will be used interchangeably.

estimate of δ' and δ'' . With these estimates calculate all the inviscid properties and make one iteration on the boundary-layer solution. (2) From that boundary-layer profile, integrate equation (1.5-7) and determine the displacement thickness δ^+ . Employing finite-difference formulas calculate δ' and δ'' . (3) Repeat steps (1) and (2) until the solution has converged within some acceptable error.

a. Initial Estimates of Inviscid Properties.- To apply the solution technique at some general station, we will estimate the inviscid properties necessary to compute a boundary-layer profile by adopting the following estimates on δ' and δ'' .

$$\delta'_{NS} = \delta'_{OS} + \delta''_{OS} \Delta s, \quad (3.3-1a)$$

and

$$\delta''_{NS} = \delta''_{OS} + \delta'''_{OS} \Delta s, \quad (3.3-1b)$$

where Δs is the step size in the s -coordinate and the subscripts NS and OS refer to the new station and old station respectively.

b. Interaction Technique.- Using the initial guess at the boundary-layer profile described immediately above, equation (1.5-7) is integrated to determine the new estimate of the displacement thickness δ . With the following two-point derivative laws

⁺See Appendix A for details of method employed to calculate δ once δ is determined from equation (1.5-7).

$$\delta_1' = (\delta_1 - \delta_2)/\Delta s_1, \quad (3.3-2a)$$

$$\delta_1'' = (\delta_1' - \delta_2')/\Delta s_1, \quad (3.3-2b)$$

$$\delta_1''' = (\delta_1'' - \delta_2'')/\Delta s_1, \quad (3.3-2c)$$

or the three-point derivative laws

$$\delta_1' = \frac{\Delta s_1(\Delta s_1 + \Delta s_2)}{\Delta s_2} \left[\delta_1 \left(\frac{1}{\Delta s_1^2} - \frac{1}{(\Delta s_1 + \Delta s_2)^2} \right) - \frac{\delta_2}{\Delta s_1^2} + \frac{\delta_3}{(\Delta s_1 + \Delta s_2)^2} \right], \quad (3.3-3a)$$

$$\begin{aligned} \delta_1'' = \frac{2\Delta s_1(\Delta s_1 + \Delta s_2)}{\Delta s_2} & \left[\frac{\delta_2}{\Delta s_1^3} - \frac{\delta_3}{(\Delta s_1 + \Delta s_2)^3} - \delta_1 \left(\frac{1}{\Delta s_1^3} - \frac{1}{(\Delta s_1 + \Delta s_2)^3} \right) \right. \\ & \left. + \delta_1' \left(\frac{1}{\Delta s_1^2} - \frac{1}{(\Delta s_1 + \Delta s_2)^2} \right) \right], \quad (3.3-3b) \end{aligned}$$

$$\delta_1''' = \frac{\Delta s_1(\Delta s_1 + \Delta s_2)}{\Delta s_2} \left[\delta_1'' \left(\frac{1}{\Delta s_1^2} - \frac{1}{(\Delta s_1 + \Delta s_2)^2} \right) - \frac{\delta_2''}{\Delta s_1^2} + \frac{\delta_3''}{(\Delta s_1 + \Delta s_2)^2} \right], \quad (3.3-3c)$$

the displacement thickness derivatives are updated. In the above difference formulas the error in the two-point law is $O(\Delta s)$. The advantage of the three-point laws is that the error in the δ'

formula is $O(\Delta s^2)$. Figure A shows the grid for both laws which have been written for a variable step size.

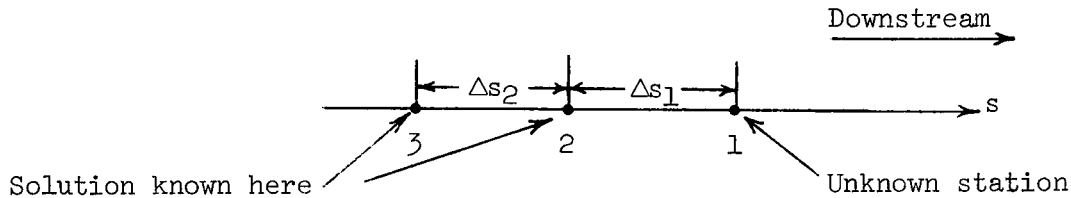


Figure A

Using the new estimates of δ' and δ'' the inviscid properties can be updated and another boundary-layer profile calculated and this cycle one would hope to repeat until the solution converges, that is, stops changing within some criteria. However, it was found that the above iteration process was divergent which is in agreement with the results of Flügge-Lotz and Blottner (1962). The technique they employed to obtain a convergent scheme is as follows. Assuming a value of P_e/P_∞ , the inviscid properties were computed and a boundary-layer profile was calculated from which a new estimate of P_e/P_∞ was made. Assuming a second value of P_e/P_∞ , the above process was repeated. Then with the assumed and corresponding calculated values of P_e/P_∞ between two consecutive iterations, a linear extrapolation was made to determine the value on an assumed versus calculated plot where $(P_e/P_\infty)_{\text{assumed}}$ equaled $(P_e/P_\infty)_{\text{calculated}}$. With this value as the new assumed value, the above cycle was continued until the

⁺Flügge-Lotz and Blottner (1962) computed the pressure gradient with a two-point difference formula between the pressure at the new station and the pressure at the previous station.

actual calculated value of P_e/P_∞ equaled the assumed value within some acceptable error.

The method employed here to obtain a stable interaction process is very similar to that employed by Flügge-Lotz and Blottner (1962). At a new station the initial estimate of δ'' is held fixed when calculating the inviscid pressure gradient on the displacement body (equation (3.2-24)) until the calculated value of δ'' stops changing to some arbitrary level which in this study required

$$\Delta\delta''/\delta''_{ave} \leq 10^{-5}, \quad (3.3-4a)$$

where

$$\Delta\delta'' = \left| \delta''(\text{present iteration}) - \delta''(\text{previous iteration}) \right|, \quad (3.3-4b)$$

and

$$\delta''_{ave} = \frac{1}{2} \left| \delta''(\text{present iteration}) + \delta''(\text{previous iteration}) \right|. \quad (3.3-4c)$$

Although the δ'' value used to compute dP_{DB}/ds is held fixed in the above process, δ' is allowed to adjust according to equation (3.3-2a) or (3.3-3a). Thus, the inviscid properties are updated after each iteration.

The value of δ'' which was held fixed when computing the pressure gradient we will call δ''_G , the subscript indicating a guessed value. The calculated value of δ' corresponding to δ''_G will be called δ''_C

meaning calculated. If we now make a plot of all δ_G'' versus δ_C'' points, then it can be seen that the desired solution has been found at a particular station when $\delta_C'' = \delta_G''$. This being true, we need only to check to see whether $\delta_C'' = \delta_G''$ within some prescribed criteria. If

$$\Delta\delta_{GC}''/\delta_{GC}'' \leq 10^{-3}, \quad (3.3-5a)$$

where

$$\Delta\delta_{GC}'' = \left| \delta''(\text{calculated value}) - \delta''(\text{guessed value}) \right|, \quad (3.3-5b)$$

and

$$\delta_{GC}'' = \frac{1}{2} \left| \delta''(\text{calculated value}) + \delta''(\text{guessed value}) \right|, \quad (3.3-5c)$$

is met, the solution was considered to have converged at a particular station. If equation (3.3-5) was not satisfied then the present δ_G'', δ_C'' point and the previous one were used to linearly extrapolate what the desired value of δ'' should be. With this extrapolated value of δ'' as the new δ_G'' value, a new δ_C'' value was computed and equation (3.3-5) was checked again. The process of extrapolating the two previous values of δ_G'' and δ_C'' to obtain a new δ_G'' value was continued until equation (3.3-5) was satisfied.⁺ When satisfied the program moves on to the next station. Figure 3.1 shows the variation of δ_G'' and δ_C'' for the $M_\infty = 9.6$ flat-plate case. In all

⁺This method was found to be stable for accuracies as small as 10^{-8} in equation (3.3-5a).

examples this variation was found to be approximately linear and the most guessed values necessary was 3 or 4.

The station at which the interaction is initiated is special in that the above technique cannot be applied there. The methods employed to obtain the initial profiles are given in the next section.

3.4 Initial Profiles

As was noted in Chapter I in order to begin the numerical integration of the boundary-layer equations, the solution must be known at the initial station. Thus the profiles at the initial station must be fed in or computed in some manner.

The present study will be limited to bodies with a sharp leading edge whose leading-edge surface is approximately flat and at zero angle of attack relative to the mainstream. Thus, near the leading edge where the interaction will be initiated, we will adopt for our analysis the boundary-layer equations without curvature effects. Two similarity methods will be put forth with which to compute the initial profiles. The first considered is the classical strong interaction solution here called the hypersonic limit method, and the second its modified form.

a. Hypersonic Limit Method. - The similarity method presented here for obtaining initial profiles and inviscid properties is basically the one given by Lees and Probstein (1953) who obtained a first-order estimate to the displacement thickness and surface pressure by expanding these quantities in asymptotic series and calculating the leading term in the expansions. The first-order estimate obtained by Lees and Probstein (1953) was subsequently adopted by Flügge-Lotz and Blottner (1962)

in their work with insulated walls. The reason for the present version is to allow for a wider variation in wall temperature.

With this method, we note following the analysis of Hayes and Probstein (1959) or Sullivan (1969) that certain simplifications become apparent if one considers the case where the inviscid Mach number M_e tends toward infinity. Writing equation (3.2-14) in terms of the inviscid Mach number we obtain that

$$\frac{T_e}{H_e} = \frac{1}{1 + \frac{\gamma - 1}{2} M_e^2} \rightarrow 0 \quad \text{as} \quad M_e \rightarrow \infty, \quad (3.4-1a)$$

$$\frac{2T_e}{U_e^2} = \frac{1}{\frac{\gamma - 1}{2} M_e^2} \rightarrow 0 \quad \text{as} \quad M_e \rightarrow \infty, \quad (3.4-1b)$$

and

$$\frac{2H_e}{U_e^2} = \frac{1}{\frac{\gamma - 1}{2} M_e^2} + 1 \rightarrow 1 \quad \text{as} \quad M_e \rightarrow \infty. \quad (3.4-1c)$$

If we assume also a linear temperature-viscosity law thus making $\lambda = 1$ and set the $\frac{\partial}{\partial \xi}$ terms equal to zero in equations (1.4-8-10), the limit form of the governing equations for the self-similar flow are obtained as

CONTINUITY EQUATION

$$\frac{dV}{d\eta} + F = 0, \quad (3.4-2)$$

S-MOMENTUM EQUATION

$$F'' - VF' - \bar{\beta}(G - F^2) = 0, \quad (3.4-3)$$

and the

ENERGY EQUATION

$$G'' - \sigma VG' + 2(\sigma - 1)(FF')' = 0, \quad (3.4-4)$$

where $\bar{\beta}$ which is given by

$$\bar{\beta} = \left(1 + \frac{2T_e}{U_e^2}\right) \frac{2\xi}{U_e} \frac{dU_e}{d\xi} \left(\frac{U_e^2}{2T_e}\right), \quad (3.4-5a)$$

in the hypersonic limit goes to

$$\bar{\beta} = -\frac{\gamma - 1}{\gamma} \int_0^s \frac{P_e}{P_\infty} dx \frac{\frac{d}{ds}(P_e/P_\infty)}{(P_e/P_\infty)^2}. \quad (3.4-5b)$$

This last result is obtained by first employing the definition of ξ along with the hypersonic limit value of $U_e \approx \text{constant}$ implied by equation (3.4-1c). Thus, it can be seen that in order to obtain the initial profiles from a numerical solution of equations (3.4-2-4), one must first determine the proper value of $\bar{\beta}$ in equation (3.4-3).

Following the lead of Shen (1952) and Hayes and Probstein (1959), we adopt the following pressure model

$$P_e/P_\infty = \bar{C} s^{-1/2}, \quad (3.4-6)$$

where \bar{C} is a constant which must be determined.

Substitution of equation (3.4-6) into equation (3.4-5b) leads to the familiar result (see for example Hayes and Probstein(1959)).

$$\bar{\beta} = \frac{\gamma - 1}{\gamma}. \quad (3.4-7)$$

Thus, with the value of $\bar{\beta}$ given by equation (3.4-7), it can be seen that solutions to equations (3.4-2-4) depend only upon the boundary condition $G_{\text{wall}} = H_w/H_e$ which when supplied allows one to compute the initial profiles.

In addition to the initial profiles, one must also know all the inviscid properties at the initial station, all of which can be computed from equation (3.4-6) once \bar{C} has been determined.

To compute \bar{C} , we first observe that when curvature effects are neglected, equation (1.5-6) may be written as

$$\delta = \frac{\sqrt{2\xi}}{\rho_e U_e} \int_0^\infty \left(\frac{T}{T_e} - \frac{U}{U_e} \right) d\eta, \quad (3.4-8)$$

which becomes in the hypersonic limit

$$\delta = \frac{\gamma - 1}{2} M_\infty^2 \sqrt{2\mu_\infty C_\infty} \frac{\left[\int_0^s \frac{P_e/P_\infty}{P_e/P_\infty} dx \right]^{1/2}}{P_e/P_\infty} Q = (\gamma - 1) M_\infty^2 \sqrt{\frac{\mu_\infty C_\infty}{\bar{C}}} Q s^{3/4}, \quad (3.4-9)$$

where

$$Q = \int_0^\infty (G - F^2) d\eta. \quad (3.4-10)$$

The derivative of the displacement thickness given in equation (3.4-9), is now substituted into the tangent-wedge pressure law and the resulting pressure set equal to that obtained by equation (3.4-6) to give in the limit of $M_\infty \rightarrow \infty$

$$\bar{C} s^{-1/2} = 2\gamma B M_\infty^2 \epsilon \left(\frac{d\delta}{ds} \right)^2, \quad (3.4-11)$$

where near the leading edge we have made use of the fact that

$$\theta = \theta_{\text{wall}} + \epsilon \frac{d\delta}{ds} \approx \epsilon \frac{d\delta}{ds}, \quad (3.4-12)$$

and B is given by equation (3.2-24c). After substitution for δ in equation (3.4-11) from equation (3.4-9), we find that

$$\bar{C} = \frac{3}{4} (\gamma - 1) M_\infty^3 \sqrt{\frac{C_\infty}{\text{Re}_{S_\infty}}} (2\gamma B)^{1/2} Q s^{1/2}, \quad (3.4-13)$$

where

$$\text{Re}_{S_\infty} = \frac{\rho_\infty^* U_\infty^* S^*}{\mu_\infty^*}, \quad (3.4-14)$$

which now allows us to write equation (3.4-6) in the standard form

$$P_e/P_\infty = \bar{\alpha} \bar{X}, \quad (3.4-15)$$

where here

$$\bar{\alpha} = \frac{3}{4} (\gamma - 1) \sqrt{2\gamma B} Q, \quad (3.4-16)$$

and

$$\bar{\chi} = M_{\infty}^3 \sqrt{\frac{C_{\infty}}{Re_{s_{\infty}}}} \quad (3.4-17)$$

The only inviscid property at the initial station not known but required for later solutions is ξ which can now be computed by substituting equation (3.4-6) into the definition of ξ , integrating to obtain

$$\xi = 2\mu_{\infty} \bar{C} C_{\infty} s^{1/2} \quad (3.4-18)$$

In equation (3.4-15), $\bar{\chi}$ is recognized as the hypersonic interaction parameter which indicates large displacement induced pressures in regions of large $\bar{\chi}$. Thus, regions of large $\bar{\chi}$ have come to be called strong interaction regions whereas regions of small $\bar{\chi}$ have come to be called weak interaction regions. Note that once the wall temperature is specified, equations (3.4-2-4) can be solved numerically and Q (equation (3.4-10)) can be evaluated thus determining $\bar{\alpha}$ for that particular wall temperature. Hayes and Probstein (1959) present tables of $\bar{\alpha}$ versus wall temperature for a representative range of flow variables as obtained from an analysis similar to the above but originally presented by Lees and Probstein (1953).

b. Modified Hypersonic Limit Method.- In the discussion of results, it will be shown that a bump appears in the computed surface pressure gradient when the above hypersonic limit method is employed to obtain the initial profiles and inviscid properties. Because the bump appeared immediately downstream of the initial station, it was reasoned that one source of it was due to the fact that at the initial station the inviscid properties were the hypersonic limit ones whereas at the succeeding stations this limit is not applied. That is to say, when computing the inviscid properties at the second station, there are terms included which were considered of higher order at the initial station where the hypersonic limit was applied. Therefore, in order to remove one possible source of the bump, the modified hypersonic limit method was formulated. This formulation consists of keeping higher-ordered terms when computing the inviscid properties at the initial station, thus making that station more consistent with the downstream stations. As before, we will take the inviscid surface pressure to be correctly given by equations (3.4-15) and (3.4-16-17) where Q in the modified method is given by

$$Q = \int_0^{\infty} \left(G - \frac{U_e^2}{2H_e} F^2 - \frac{T_e}{H_e} F \right) d\eta , \quad (3.4-19)$$

which in the hypersonic limit can be seen to reduce to equation (3.4-10). In addition, we will assume also that the governing equations for initial profiles are correctly given by the limit equations

(3.4-2-4) and (3.4-7). Thus, it is seen that the initial profiles for both hypersonic limit methods are identical and the only difference is in the method employed to obtain the inviscid properties.

To compute $\bar{\alpha}$ from equations (3.4-16) and (3.4-19), an iterative approach will be taken. Assuming the initial profiles have been numerically obtained, $\bar{\alpha}$ is estimated and the necessary values of T_e and U_e to numerically integrate equation (3.4-19) are determined. With this value of Q , a new estimate of $\bar{\alpha}$ is made and the cycle repeated until $\bar{\alpha}$ is calculated within some acceptable error.

Once $\bar{\alpha}$ is determined, all inviscid properties with the exception of ξ are known. To compute ξ in the modified method, we will set the relation of $\bar{\beta}$ given in equation (3.4-5a) equal to its hypersonic limit value and solve for ξ . Thus,

$$\xi = - \frac{\gamma - 1}{\gamma} \frac{\rho_e^2 \mu_e T_e U_e}{\left(1 + \frac{2T_e}{U_e^2} \frac{dPe}{ds} \right)}, \quad (3.4-20)$$

which can now be computed. The value of δ necessary to compute δ' at the next station is obtained from equation (3.4-8) whereas δ' is determined by equating equation (3.4-15) to the tangent-wedge pressure law and solving for δ' .

To compute the additional values of δ and δ' necessary to apply the three-point difference laws at the next station the following procedure was adopted. For the modified method δ' was computed as stated except s is given a value two Δs steps upstream of the

desired station. The additional value of δ for the modified method is obtained from a two-term upstream Taylor series expansion about the initial station. For the hypersonic limit method δ and its derivatives were computed from equation (3.4-9) by taking a value of s two Δs steps upstream from the desired station.

3.5 Discussion of Results

a. Flat-Plate Studies.- The first case investigated was that of flow over a flat plate with displacement thickness interaction. This case was originally investigated employing finite-difference methods by Flügge-Lotz and Blottner (1962). Thus, this case will serve as a test case with which to compare the present study.

The other justification for studying this case lies in a controversy over whether or not branching solutions result when problems of this nature---particularly the flat-plate case---are investigated numerically. Garvine (1968) observed a saddle-point (or branching) behavior with his viscous shock-layer solution for the flat plate. Similar behavior was noted by Baum (1968) with his supersonic boundary-layer solutions. However, Flügge-Lotz and Blottner (1962), Sullivan (1969), Stollery (1970), and Cheng, Chen, Mobley, and Huber (1970) did not observe any tendency toward branching solutions and thus a reworking of the hypersonic flat-plate case seems appropriate as a test of the generality of Flügge-Lotz and Blottner's technique.

1. Initialization Procedures and Effects.- In Section 3.4, two methods were given with which to compute the initial profiles necessary to begin the interaction. The method adopted in this study was the second of these - the modified hypersonic limit method. The reason for selecting this method can be seen from Figure 3.2 where the second derivative of displacement thickness - the most sensitive solution function, is shown for the case of a plate in a Mach 12 free-stream. Figure 3.2 shows an oscillatory type behavior developing when the hypersonic limit method is employed to obtain the initial profiles but shows a smooth transition when the above modified scheme is employed. Since the pressure is a function of δ' it becomes apparent that δ'' reflects the behavior of the pressure gradient in the s-direction. Thus, to assure a smooth pressure gradient in the s-direction for the first several stations the modified method was adopted. Figure 3.3 shows the wall pressures corresponding to the above case for both hypersonic limit methods. The differences in wall pressure between the two methods can be seen to fall outside of the plotting resolution implying the oscillations of Figure 3.2 are apparently of only secondary importance to the overall solution.

Figure 3.4 gives an indication of the effect of step size on the solution near the initial station in terms of how it influences δ'' . From equation (3.4-9), we obtain upon differentiation that for the strong interaction region (large \bar{x})

$$\delta'' \sim s^{-5/4} . \quad (3.5-1)$$

Thus, on Figure 3.4 equation (3.5-1) should appear as a straight line and with this in mind step sizes of 0.0025 and 0.005 were chosen since they yielded the approximate desired behavior.

Figure 3.5 shows the step size effect on the computed surface pressure to be very small and to diminish as the solution proceeds downstream again pointing to the basic consistency of the present method.

2. Downstream Instabilities.- As the solution marched downstream there appeared an oscillatory behavior in the computed surface pressure gradient for the flat-plate case (and the compression ramp case discussed later) resulting in an unwanted termination of the computation. A similar behavior was observed by Cheng, Chen, Mobley, and Huber (1970) with their fully viscous shock-layer solutions in which they found the instability to enter through the continuity equation. They reasoned that its cause was due to the diminishing wall slip influence allowed in their solution which resulted in a loss in accuracy in the technique used to integrate the continuity equation. The instability in this study also seemed to originate with the continuity equation although no concrete explanation can be offered as to its origin.

Initially, it was believed that the oscillatory behavior was associated with the method employed to obtain the initial profiles and/or related to the original step size employed. Therefore, the first modifications made were those reported in the previous section. When those modifications failed to eliminate the instability it was then felt that the oscillatory behavior might be related to errors

present in the finite-difference derivative laws used to compute δ' and δ'' . Thus, a study was made to determine if the more accurate three-point derivative laws would be more appropriate. Figure 3.6 shows the computed second derivative of displacement thickness employing both laws and it can be seen that the three-point difference laws allows the solution to proceed further downstream to an s of 0.11 before running into the stability problem again. From Figure 3.6, it became apparent that although the derivative difference scheme exerted some influence on controlling the instability and apparently eliminated it for a while, another method would have to be found to abolish it from the problem.

Taking a hint from the identification by Chen et al. (1970) of the continuity equation as the source of the instability, the method adopted here for filtering out this oscillatory behavior consisted of simply averaging the V -velocity profile - as it was being calculated - with its counterpart for the same value of η one station back along the body. Such a technique is formally valid to the same order as the difference equations, that is, to order Δs and therefore introduces no new errors to the solution. Figure 3.7 shows the computed surface pressure for the $M_\infty = 9.6$ flat-plate case for both the solution with and without the averaging technique. The pressure gradient behavior can be seen in Figure 3.8 where the second derivative of displacement thickness is shown to vary smoothly over the entire region considered for the filtered solution.

Since the $M_\infty = 12$ flat-plate case showed no oscillatory behavior this case was run with and without the averaging technique to ascertain what effect the averaging had on the computed solution. As might have been expected, the differences between the two solutions was virtually undetectable.

3. Comparison of Experimental and Theoretical Flat-Plate Results

Example 1

The first case studied was the $M_\infty = 9.6$ flat-plate case previously investigated by Flügge-Lotz and Blottner (1962). The flow conditions for this case are given as

$$M_\infty = 9.6 \quad (3.5-2a)$$

$$T_\infty^* = 82.34^\circ\text{R} \quad (3.5-2b)$$

$$\gamma = 1.4 \quad (4.5-2c)$$

$$\sigma = 1.0 \quad (3.5-2d)$$

$$\text{Re}_{S_\infty} / s^* = 0.846 \times 10^5 \quad (3.5-2e)$$

$$T_w / T_o = 1.0 \quad (3.5-2f)$$

and

$$L^* = 1 \text{ inch.} \quad (3.5-2g)$$

Figure 3.9 shows the pressure induced on the plate surface when a linear viscosity-temperature law is employed to compute the numerical

solution. Also shown are favorable comparisons with the results reported by Flügge-Lotz and Blottner (1962) and the experimental data of Bertram and Blackstock (1961). The present solution was initiated at $s = 0.01$ which corresponds to a $\bar{\chi}$ of approximately 25 and is therefore in the strong interaction regime. Figure 3.10 shows the above displacement thickness to be slightly lower than that predicted by classical boundary-layer theory. As s becomes large, the skin friction behavior can be seen from Figure 3.11 to approach that predicted by classical boundary-layer theory.

Example 2

The flow conditions for the second example are

$$M_{\infty} = 12 \quad (3.5-3a)$$

$$T_0^* = 3960^{\circ}\text{R} \quad (3.5-3b)$$

$$\gamma = 1.4 \quad (3.5-3c)$$

$$\sigma = 0.70 \quad (3.5-3d)$$

$$\text{Re}_{s_{\infty}}/s^* = 0.79 \times 10^5 \quad (3.5-3e)$$

$$T_w/T_0 = 0.15 \quad (3.5-3f)$$

and

$$L^* = 1 \text{ inch.} \quad (4.5-3g)$$

This case was previously investigated by Sullivan (1969) who obtained an approximate solution by employing Lees (1956) cold-wall similarity analysis. The interaction for the present example was initiated at $s = 0.01$ which corresponds to a \bar{X} of approximately 58.

Figure 3.12 shows the pressure induced on the plate surface when a linear temperature-viscosity law is employed for the numerical solution. Also shown are the approximate solution of Sullivan (1969), the second-order weak interaction theory reported in Hayes and Probstein (1959), and some experimental data by Hall and Golian (1960) along with two points from the present study employing Sutherland's viscosity law-equation (1.3-6). As can be seen from Figure 3.12, for $\bar{X} \leq 6.5$ the present solution employing a linear temperature-viscosity law virtually reproduces the second-order weak interaction result. The differences between the values of wall pressure obtained by employing the linear law and Sutherland's viscosity law indicate only a small influence due to the viscosity law employed.

Shown in Figure 3.13 is the heat transfer to the wall along with the experimental data of Hall and Golian (1960). The agreement appears acceptable.

The displacement thickness and skin friction for the above case are shown in Figures 3.14-15 and for large s are observed to approach the behavior predicted by classical boundary-layer theory thus indicating a diminishing displacement-body effect.

b. Compression Ramp Studies

1. Geometry and Flow Conditions.- The locus of points on the body surface are given by $y = x^3/150$ up to $x = 5.1$ inches where the cubic surface merges with a 28° wedge.

The flow conditions for this case are taken from Stollery (1970), who in addition to experimentally investigating the flow also calculated some approximate solutions with various approximate inviscid pressure laws. However, in his analysis, curvature effects were neglected and one of the purposes of this chapter is to determine whether curvature effects are important for problems of this type. The flow conditions studied here were

$$M_\infty = 6, 8, \text{ and } 12.25 \quad (3.5-4a)$$

$$T_0^* = 2340^\circ\text{R} \quad (3.5-4b)$$

$$\gamma = 1.4 \quad (3.4-4c)$$

$$\sigma = 0.72 \quad (3.5-4d)$$

$$\text{Re}_{s_\infty}/s^* = 0.858 \times 10^5, 0.458 \times 10^5, \text{ and } 0.258 \times 10^5 \quad (3.5-4e)$$

$$T_w/T_0 = 0.223 \quad (3.5-4f)$$

and

$$L^* = 1 \text{ inch.} \quad (3.5-4g)$$

Sutherland's viscosity law was employed for the ramp study.

2. Displacement Effects.- The first study was made at $M_\infty = 12.25$ and was aimed at determining the effects of the displacement body on the wall pressure for the case where curvature effects were neglected- hereafter referred to as the displacement problem. Figure 3.16 shows the wall pressure that results from flow over the displacement-body when curvature effects are neglected. Also shown in Figure 3.16 is the wall pressure when displacement-body effects are ignored, that is, $\theta = \theta_{\text{wall}}$. As can be seen from Figure 3.16, the wall pressure which includes displacement-body effects predicts the trend in the experimental data very well up to an x of approximately 2.5. From $x \simeq 3$ on, the displacement solution approaches the wall pressure where displacement effects are ignored thus indicating that the local body angle θ_{wall} is dominating the displacement-body effect. This behavior is verified by the displacement thickness distribution of Figure 3.17 - showing a marked thinning of the boundary layer aft of the $x = 3$ point. Figure 3.17 also shows a comparison between the displacement thickness obtained in the present study by considering displacement-body effects alone and the approximate theories of Cheng et al. (1961) and Sullivan (1969) as applied by Stollery (1970). Thus, it is encouraging to find the present solution closely following that given by Stollery using Sullivan's method and clearly delineating a marked thinning downstream on the body. Figure 3.18 gives the wall heat transfer ratio $q/q_{F.P.}$ where $q_{F.P.}$ is the heat transfer predicted by classical boundary-layer theory which was found for this case to be

$$q_{F.P.} = 0.2503 s^{-1/2}, \quad (3.5-5)$$

along with the experimental data of Stollery (1970). The solution which includes displacement-body effects appears to predict the trend reasonably well up to $x = 2$ but thereafter drops below the experimental results.

As was mentioned previously in Section 3.5a(2), the instability discussed there appeared for the above case when the averaging technique on the V-velocity profile was not employed. However, in this case the instability appeared at a much larger value of $s (x \approx 1.86)$ and the point at which it appeared was found to depend on the step size Δs . For example, when the step size was doubled aft of $x = 1.1$ over the previous step size, the instability did not appear until $x \approx 2.32$. Thus it appears that a second possible method of eliminating the instability would result from a careful selection of the step size increment (Δs).

3. Curvature Effects. - In the study of the effects of surface curvature on flow up the Mach 12.25 compression ramp, an attempt was made to analyze curvature as it affects the inviscid properties by allowing for a pressure variation across the displacement body, independent of curvature as it affects the viscous region by also allowing for a pressure variation across the boundary layer.

The first such investigation sought to determine the effect on the interaction problem of allowing for a pressure variation across

the displacement body with no variation in the boundary-layer pressure. Figure 3.19 shows the wall pressure that results from that case where only the inviscid curvature corrections associated with the displacement body were considered, that is, the pressure across the boundary layer was taken to be constant while the pressure across the displacement body was taken to vary according to equation (3.2-22). Also shown in Figure 3.19 is the wall pressure for the displacement problem alone. From Figure 3.19, it can be seen that the curvature correction is surprisingly large - Figure 3.20 showing the increase to be on the order of 20 to 50 percent in the region of interest. Figure 3.20 shows that the pressure correction closely follows the local variation of the ratio of displacement thickness to the radius of curvature (or $\kappa\delta$). It is quite clear then that even with the relatively small values of $\kappa\delta$ shown in Figure 3.20, the inviscid normal pressure gradient encountered implies sizable normal pressure gradients are to be expected in the viscous region therefore indicating our solutions are necessarily incomplete at this point.

When an attempt was made to analyze boundary-layer curvature effects without first adjusting the inviscid flow properties for displacement or curvature effects (i.e., we took $\theta = \theta_{\text{wall}}$), a branching type behavior was observed in the flow properties as the solution marched away from the leading edge. Figure 3.21 shows the above resulting wall pressure distribution dropping off towards zero (corresponding to an expanding flow) when the computation terminated. The cause for this behavior seems to be the low

estimates of inviscid surface pressure near the leading edge obtained by taking $\theta = \theta_{\text{wall}}$ coupled with the increasing variation in pressure across the boundary layer - approximately 13 percent at the point of termination. Noting that the surface curvature is negative, it can be seen from equations (1.2-4) and (1.2-6b) that the maximum pressure in the boundary layer must occur at the wall which from equations (1.3-8g), (1.3-8e), (1.3-8i), and (1.4-11) is obtained as

$$P_{\text{wall}} = P_e + U_e^2 \tilde{I}_{\text{wall}}. \quad (3.5-6)$$

From equation (3.5-6), it is observed that if the estimate of P_e is low⁺ then there will be a correspondingly low value of wall pressure in the boundary layer. When this is coupled with a large variation in pressure across the boundary layer, the resulting effect is to cause low, unrealistic densities to occur in the outer reaches of the viscous region. This in turn results in a subsequent increase in displacement thickness that would have been offset had interaction effects been included simultaneously. However, since displacement effects are not included there exists no mechanism by which the boundary layer can adjust to the real problem. We note that a method was found to filter out this expansion branch and consists of averaging the pressure integral in equation (1.4-16) in exactly the same manner as the V-velocity profile was averaged to eliminate the oscillatory

⁺In the region of concern, Figure 3.16 shows this estimate ($\theta = \theta_{\text{wall}}$) to be 50 to 90 percent lower than that predicted by the displacement problem solution.

instability. Figure 3.21 shows the wall pressure obtained when the averaging technique is employed along with the inviscid surface pressure obtained as stated by taking $\theta = \theta_{\text{wall}}$. Exactly why this correction works is unknown but it is worth repeating that the inclusion of displacement effects would itself relieve the problem and is therefore not of immediate concern to the overall effort.

When displacement-body effects were included for the above case in addition to the boundary-layer curvature effects already accounted for, the branching type behavior which occurred near the leading edge was overcome temporarily but reappeared again at approximately $x \approx 1.57$. The reason for its reappearance is due once again to low estimates of the inviscid surface pressure. However, for this case the cause of the low surface estimates of P_e is due to the large variation in pressure across the displacement body which exists but has not been accounted for here. Figure 3.20 indicates the inviscid surface value of pressure at $x = 1.5$ should be approximately 50 percent higher than the displacement-body value which was used for this case. With the inclusion of this final surface curvature effect, we come to what will be referred to as the complete second-order solution.

2. The Complete Second-Order Solution. - When all the second-order effects due to displacement body and surface curvature were accounted for, no branching type behavior was observed in the flow properties. Figure 3.22 gives the wall pressure for the complete second-order solution along with the wall pressure predicted by classical or first-order boundary-layer theory, that is, neglecting

displacement and curvature effects. Near the leading edge where the surface curvature is small, Figure 3.22 shows the displacement effect to be large and to diminish as the solution proceeds downstream. In addition, Figure 3.22 implies that although the effects of displacement speed and longitudinal curvature cause large pressure gradients to exist across both the displacement body and the boundary layer all along the body surface, their effect on the wall pressure is only noticeable in regions where the displacement speed is clearly the dominant effect. Figure 3.23 shows the trend in the wall heat transfer data to be predicted reasonably well by the complete solution up to $x \approx 2$. The skin friction for the complete solution is given in Figure 3.24 along with the values predicted by classical boundary-layer theory and the present interaction technique when curvature effects are neglected. Even though we realized that the displacement effect was dominant near the leading edge, it was nevertheless quite surprising to learn from Figure 3.23 that the curvature effect does not noticeably influence the skin friction distribution for values of x less than approximately 2.5.

One final test of the technique developed here for studying displacement and curvature effects consists of varying the flow Mach number and free-stream unit Reynolds number to determine their influence on the computed wall pressure and heat transfer. Figures 3.25 and 3.26 show the effect of free-stream Mach number on the computed wall pressure and heat transfer respectively and it is observed that a decrease in Mach number results in a decrease in the computed

wall pressure but an increase in the wall heat transfer rate. The effect of varying the free-stream Reynolds number while holding the flow Mach number fixed can be seen in Figures 3.27 and 3.28 where the corresponding distributions of wall pressure and heat transfer are shown. From Figures 3.27 and 3.28, it is observed that small decreases in the free-stream unit Reynolds number give rise to an increase in the computed wall pressure and a reduction in the heat transfer rate. Of special interest is the solution shown in Figures 3.27 and 3.28 which terminated due to separation of the viscous flow from the ramp surface. Figure 3.29, which gives the skin friction distribution in the region where it goes to zero, shows no unusual behavior as the point of zero shear stress is approached - in fact the computation proceeded downstream of the zero shear stress point ($\bar{C}_f = 0$) before the numerical method employed to solve the boundary-layer equations became completely unstable due to the reversed flow region near the wall occurring downstream of the separation point.⁺ In noninteracting boundary-layer theory, it is generally accepted that the skin friction derivative $d\bar{C}_f/ds$ has a singularity at the point of separation and several studies have been made on this phenomena (see for example Brown and Stewartson (1969)). There was some doubt as to whether the compressible nonadiabatic wall case was singular at separation. However, recent studies by Werle and Senechal (1971) have implied that this case is also singular. It has been suggested that if the boundary layer were

⁺We note here that since a reversed flow region occurs aft of the zero skin friction point, there arises some question as to whether the solution is valid beyond that point.

allowed to interact with the mainstream as done in this study, there would not occur a singularity in the skin friction derivative at the separation point as obtained in noninteracting theory. This behavior in the presence of interaction is confirmed in Figure 3.29 where it is seen that no singularity is observed at the point of separation. Thus this verification stands out as an important result obtained from this study.

3.7 Conclusions

From this study of displacement and curvature effects, the following conclusions were reached.

1. No branching behavior was observed for flat-plate interaction solutions.
2. Instabilities may occur in the numerical technique downstream of the leading edge unless the continuity equation solution is damped by a method similar to the averaging technique employed here.
3. Accounting for boundary-layer curvature effects requires a good estimate of the inviscid surface pressure in order to avoid low unrealistic pressures in hypersonic boundary layers. Large inviscid and viscid pressure variations were found to exist across the displacement body and boundary layer for hypersonic flow over curved surfaces.
4. When the boundary layer is allowed to interact with the mainstream, there appears no singularity in the skin friction derivative at the point where the boundary layer separates from the body surface.

5. The technique developed here to handle the complete second-order theory predicts the trend in the wall properties for regions of strong interaction with the mainstream and merges with the behavior predicted by classical boundary-layer theory for regions of weak interaction.

IV. GENERAL CONCLUSIONS

From this study of displacement and curvature effects, the following conclusions were reached:

1. Finite-difference methods can be applied to the composite second-order boundary-layer equations to obtain numerical solutions. No new difficulties were encountered from such an application that are not also present in similar numerical solutions of the first-order or classical equations.
2. For cases where the influence of displacement speed and curvature are both large, these effects must be accounted for simultaneously in order to avoid sizable errors in the wall properties as well as numerical difficulties.
3. If one is only interested in wall properties, good estimates of these quantities can be obtained from numerical solutions of the first-order equations taking the inviscid surface pressure to be approximately equal to the observed wall pressure.
4. Comparisons of the composite second-order solutions with experiment are respectable.

V. BIBLIOGRAPHY

1. Baum, Eric, (1968), "An Interaction Model of a Supersonic Laminar Boundary Layer on Sharp and Rounded Backward Facing Steps," AIAA Journal, Vol. 6, No. 3, pp. 440-447.
2. Bertram, M. H., and Blackstock, T. A., (1961), "Some Simple Solutions to the Problem of Predicting Boundary-Layer Self-Induced Pressures," NASA Tech. Note D-798.
3. Blottner, F. G., (1970), "Finite Difference Methods of Solution of the Boundary Layer Equations," AIAA Journal, Vol. 8, No. 2, pp. 193-205.
4. Brown, S. N., and Stewartson, K., (1969), "Laminar Separation," Annual Review of Fluid Mechanics, Vol. 1, pp. 45-72.
5. Carnahan, B., Luther, H. A., and Wilkes, J. O., (1969), Applied Numerical Methods, John Wiley and Sons, Inc., New York.
6. Chan, Y. Y., (1966), "Integral Methods in Compressible Boundary Layers and Their Application," Physics of Fluids, Vol. 9, No. 2, pp. 350-358.
7. Cheng, H. K., Hall, J. G., Golian, T. C., and Hertzberg, A., (1961), "Boundary Layer Displacement and Leading-Edge Bluntness Effects in High Temperature Hypersonic Flow," J. Aero. Sci., Vol. 28, No. 5, pp. 353-381.
8. Cheng, H. K., Chen, S. Y., Mobley, R., and Huber, C. R., "The Viscous Hypersonic Slender-Body Problem: A Numerical Approach Based on a System of Composite Equations," The Rand Corp., Memorandum RM-6193-PR, Santa Monica, California.
9. Davis, R. T., Werle, M. J., and Wornom, S. F., (1970), "A Consistent Formulation of Compressible Boundary-Layer Theory With Second-Order Curvature and Displacement Effects," AIAA Journal, Vol. 8, No. 9, pp. 1701-1703.
10. Davis, R. T., Whitehead, R. E., and Wornom, S. F., (1970), "The Development of an Incompressible Boundary-Layer Theory Valid to Second-Order," Report VPI-E-70-1, Department of Engineering Mechanics, Virginia Polytechnic Institute, Blacksburg, Virginia.
11. Davis, R. T., (1970), "Numerical Solution of the Hypersonic Viscous Shock-Layer Equations," AIAA Journal, Vol. 8, No. 5, pp. 843-851.

12. Davis, R. T., and Flügge-Lotz, I., (1964a), "The Laminar Compressible Boundary Layer in the Stagnation-Point Region of an Axisymmetric Blunt Body Including the Second-Order Effect of Vorticity Interaction." Int. J. Heat and Mass Trans., Vol. 7, pp. 341-370.
13. Davis, R. T., and Flügge-Lotz, I., (1964b), "Second-Order Boundary-Layer Effects in Hypersonic Flow Past Axisymmetric Blunt Bodies," J. Fluid Mech., Vol. 20, Part 4, pp. 593-623.
14. Dennis, S. C. R., and Chang, G., (1969), "Numerical Studies of a Viscous Liquid Past a Circular Cylinder," appearing in High-Speed Computing in Fluid Dynamics, edited by F. N. Frenkeil and K. Stewartson, published by American Institute of Physics.
15. Devan, L., (1964), "Second Order Incompressible Laminar Boundary Layer Development on a Two-Dimensional Semi-Infinite Body," Ph.D. Dissertation, Univ. Calif., Los Angeles.
16. Dewey, C. F., Jr., (1963), "The Use of Local Similarity Concepts in Hypersonic Viscous Interaction Problems," AIAA Journal, Vol. 1, No. 1, pp. 20-33.
17. Dimopoulos, H. G., and Hanratty, T. J., (1968), "Velocity Gradients at the Wall for Flow Around a Cylinder for Reynolds Numbers Between 60 and 360," J. Fluid Mech., Vol. 33, Part 2, pp. 303-319.
18. Dimopoulos, H. G., (1968), "Wall Shear Stress Distributions for Flow Around a Circular Cylinder, $60 \leq Re \leq 340$," Ph.D. Thesis, University of Illinois, Urbana, Illinois.
19. Fannelöp, T. K., and Flügge-Lotz, I., (1965), Z. Flugwiss Vol. 13, pp. 282-296.
20. Fannelöp, T. K., and Flügge-Lotz, I., (1964), "Two-Dimensional Viscous Hypersonic Flow Over Simple Blunt Bodies Including Second-Order Effects," TR-144, Div. of Engineering Mechanics, Stanford University.
21. Flügge-Lotz, I., and Blottner, F. G., (1962), "Computation of the Compressible Laminar Boundary Layer Flow Including Displacement Thickness Interaction Using Finite-Difference Methods," Div. of Engineering Mechanics, Stanford University, Tech. Rep. No. 131.
22. Garvine, R. W., (1968), "Upstream Influence in Viscous Interaction Problems," Physics of Fluids, Vol. 11, No. 7, pp. 1413-1423.

23. Grove, A. S., Shair, F. H., Petersen, E. E., and Acrivos, A., (1964), "An Experimental Investigation of the Steady Separated Flow Past a Circular Cylinder," J. Fluid Mech., Vol. 19, p. 60.
24. Hall, J. G., and Golian, T. C., (1960), "Shock Tunnel Studies of Hypersonic Flat Plate Air Flow," Cornell Aero. Lab. Report No. AD-1052-A-10; Buffalo, New York.
25. Hayes, W. D., and Probst, R. F., (1959), Hypersonic Flow Theory, Academic Press, New York.
26. Homann, F., (1936), "Der Einfluss grösser Zähigkeit bei der Stromung um den Zylinder and um die Kugel," Translation: NASA Tech. Memo., No. 1334, (1952).
27. Kawaguti, M., (1953), "Numerical Solution of the Navier-Stokes Equations for the Flow Around a Circular Cylinder at Reynolds Number 40." J. Phys. Soc. of Japan, Vol. 8, pp. 747-757.
28. Kuo, Y. H., (1953), J. Math. and Phys., Vol. 32, pp. 83-101.
29. Lees, L., (1956), "Laminar Heat Transfer Over Blunt-Nosed Bodies at Hypersonic Flight Speeds," Jet Propulsion, Vol. 26, pp. 259-269, 274.
30. Lees, L., and Probst, R. F., (1953), Hypersonic Flows of a Viscous Fluid, (Unpublished monograph with limited circulation). Copies available through the Brown University Library, Brown Univ., Providence, R. I.
31. Lenard, M., (1962), "Stagnation Point Flow of a Variable Property Fluid at Low Reynolds Numbers," Cornell University Thesis.
32. Levy, S., (1954), "Effect of Large Temperature Changes (Including Viscous Heating) Upon Laminar Boundary Layers With Variable Free-Stream Velocity," J. Aero. Sci., Vol. 21, pp. 459-474.
33. Maslen, S. H., (1952), "Second Approximation to Laminar Compressible Boundary Layer on a Flat Plate in Slip Flow," NACA Tech. Note No. 2818.
34. Maslen, S. H., (1963), "Second Order Effects in Laminar Boundary Layers," AIAA Journal, Vol. 1, pp. 33-40.
35. Murphy, J. S., (1953), "Some Effects of Surface Curvature on Laminar Boundary-Layer Flow," J. Aero. Sci., Vol. 20, pp. 338-344.

36. Prandtl, L., (1904), "Über Flüssigkeitsbewegung bei sehr kleiner Reibung, Verh. III, Int. Math. Kongr., Heidelberg, pp. 484-91. Teubner Leipzig. In English as "Motion of Fluids With Very Little Viscosity," NACA Tech. Memo., No. 452.
37. Richtmyer, R. D., (1957), "Difference Methods for Initial-Value Problems," Interscience Publishers, Inc., New York.
38. Rosenhead, L., (1963), ed., Laminar Boundary Layers, Oxford Univ. Press.
39. Schlichting, H., (1960), Boundary-Layer Theory, 4th edition, New York: McGraw-Hill.
40. Schlichting, H., (1968), Boundary-Layer Theory, 6th edition, New York: McGraw-Hill.
41. Shen, S.G., (1952), "An Estimate of Viscosity Effect on the Hypersonic Flow Over an Insulated Wedge," J. Math. Phys., Vol. 31, pp. 192-205.
42. Stollery, J. L., (1969), "Hypersonic Viscous Flow Over Concave and Convex Surfaces," Proceedings of the Symposium on Viscous Interaction Phenomena in Supersonic and Hypersonic Flow, Aeronautical Research Labs., Wright-Patterson Air Force Base, Ohio.
43. Stollery, J. L., (1970), "Hypersonic Viscous Interaction on Curved Surfaces," J. Fluid Mech., Vol. 43, Part 3, pp. 497-511.
44. Sullivan, P. A., (1969), "On the Interaction of a Laminar Hypersonic Boundary Layer and a Corner Expansion Wave." AIAA Paper No. 69-137.
45. Takami, H., and Keller, H. B., (1969), "Steady Two-Dimensional Viscous Flow of an Incompressible Fluid Past a Circular Cylinder," appearing in High-Speed Computing in Fluid Dynamics, edited by F. N. Frenkeil and K. Stewartson, published by American Institute of Physics.
46. Thom, A., (1933), "The Flow Past Circular Cylinders at Low Speeds," Proc. Roy. Soc. A., Vol. 141, pp. 651-668.
47. Thoman, D. C., and Szewczyk, A. A., (1969), "Time Dependent Viscous Flow Over a Circular Cylinder," appearing in High-Speed Computing in Fluid Dynamics, edited by F. N. Frenkeil and K. Stewartson, published by the American Institute of Physics.

48. Van Dyke, M., (1962a), "Higher Approximations in Boundary-Layer Theory, Part 1. General Analysis," J. Fluid Mech., Vol. 14, pp. 161-177.
49. Van Dyke, M., (1962b), "Higher Approximations in Boundary-Layer Theory, Part 2. Application of Leading Edges," J. Fluid Mech., Vol. 14, pp. 481-495.
50. Van Dyke, M., (1962c), "Second Order Compressible Boundary-Layer Theory With Application to Blunt Bodies in Hypersonic Flow," Hypersonic Flow Research (ed., F. R. Riddell), pp. 37-76, New York Academic Press.
51. Van Dyke, M., (1964), "Higher Approximations in Boundary-Layer Theory, Part 3. Parabola in Uniform Stream," J. Fluid Mech. 19, pp. 145-159.
52. Van Dyke, M., (1969), "Higher Order Boundary-Layer Theory," in Annual Review of Fluid Mechanics, Annual Reviews, Inc., Palo Alto, California, pp. 265-292.
53. Werle, M. J., and Senechal, J. D., (1971), "A Note on Numerical Solutions for Compressible Separating Flows," Submitted to the J. Fluid Mech.
54. Werle, M. J., and Davis, R. T., (1966), "Integral Equations for Incompressible Second-Order Boundary Layers," Int. J. Engr. Sci., Vol. 4, pp. 423-431, Pergamon Press.

VI. APPENDIX A
NUMERICAL ANALYSIS SECTION

The method presented here for obtaining numerical solutions to the boundary-layer equations is basically the one developed by Flügge-Lotz and Blottner (1962) for solving parabolic differential equations with some later modifications by Davis (1970). The presentation here follows closely that of Davis (1970).

The s-momentum and energy equations can be written in the general form of a parabolic differential equation which is

$$\frac{\partial^2 w}{\partial \eta^2} + \alpha_1 \frac{\partial w}{\partial \eta} + \alpha_2 w + \alpha_3 + \alpha_4 \frac{\partial w}{\partial \xi} = 0, \quad (1-A)$$

where ξ and η are the similarity coordinates.

We now replace the derivatives in equation (1-A) with finite-difference quotients by first expanding for the unknown quantity, w , in the η direction about the point m, n (see Figure 1-A) by means of a Taylor series expansion, and then determining the derivatives to give a truncation error on the order of the step size squared.

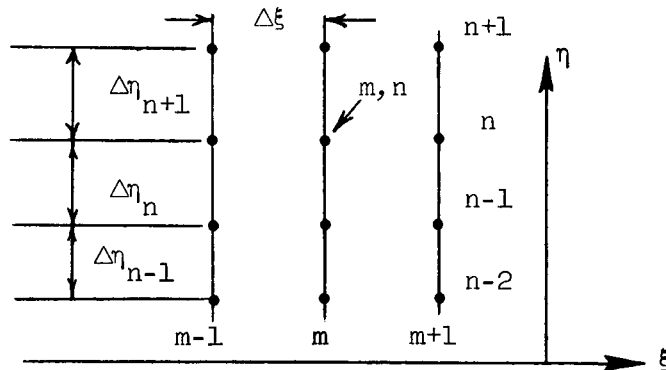


Figure 1-A

Adopting a variable grid step size in the η direction to allow for more grid points in the region near the body where the changes are the most rapid, the derivatives at the point m, n for a central difference scheme are obtained as

$$\begin{aligned}
 (\partial w / \partial \eta)_{m,n} = & \left[\Delta \eta_{n-1} / \Delta \eta_n (\Delta \eta_n + \Delta \eta_{n-1}) \right] w_{m,n+1} \\
 & + \left[(\Delta \eta_n - \Delta \eta_{n-1}) / \Delta \eta_n \Delta \eta_{n-1} \right] w_{m,n} \\
 & - \left[\Delta \eta_n / \Delta \eta_{n-1} (\Delta \eta_n + \Delta \eta_{n-1}) \right] w_{m,n-1} \\
 & - \frac{1}{6} (\partial^3 w / \partial \eta^3)_{m,n} \Delta \eta_n \Delta \eta_{n-1} , \quad (2-A)
 \end{aligned}$$

and

$$\begin{aligned}
 (\partial^2 w / \partial \eta^2)_{m,n} = & \left[2 / \Delta \eta_n (\Delta \eta_n + \Delta \eta_{n-1}) \right] w_{m,n+1} \\
 & - (2 / \Delta \eta_n \Delta \eta_{n-1}) w_{m,n} + \left[2 / \Delta \eta_{n-1} (\Delta \eta_n \right. \\
 & \left. + \Delta \eta_{n-1}) \right] w_{m,n-1} - \frac{1}{12} (\partial^4 w / \partial \eta^4)_{m,n} \Delta \eta_n \Delta \eta_{n-1} \\
 & - \frac{1}{3} (\partial^3 w / \partial \eta^3)_{m,n} (\Delta \eta_n - \Delta \eta_{n-1}) \\
 & - \frac{1}{12} (\partial^4 w / \partial \eta^4)_{m,n} (\Delta \eta_n - \Delta \eta_{n-1})^2 . \quad (3-A)
 \end{aligned}$$

The derivative in the ξ direction is given by a two-point difference scheme which has a truncation error of $O(\Delta \xi)$ if equation (1-A) is evaluated at station m (assuming stations $m-1$, $m-2$, ... to be known) and $O(\Delta \xi^2)$ if equation (1-A) is evaluated at the point $m-1/2$ (Crank-Nicholson scheme).

Substitution of these difference quotients into equation (1-A) yields a difference equation of the form

$$A_n w_{n-1} + B_n w_n + C_n w_{n+1} = D_n, \quad (4-A)$$

which can be readily solved (see Richtmyer (1957)) once the boundary conditions are specified.

SOLUTION PROCEDURE FOR INCOMPRESSIBLE STUDY

The overall method of solution as applied to the complete second-order incompressible equations is as follows. Beginning at the stagnation point the $\partial w / \partial \xi$ term is equal to zero thus reducing equation (1-A) to an ordinary differential equation. After making initial guesses of all flow profiles and carefully evaluating all inviscid properties to avoid indeterminacies, integrate the s-momentum equation using the numerical method. Next integrate the continuity and the pressure integral equations employing a trapezoidal rule. With these new estimates of the pressure integral and velocity profiles update the inviscid properties and remaining flow variables and resolve the s-momentum equation once again and continue this cycle until the solution stops changing within some acceptable error. After convergence has been reached step down the body one station and repeat the above process using the previous station solution as the initial guess at the new station flow profiles. At downstream stations, the $\partial w / \partial \xi$ is evaluated using the previous station flow profile.

SOLUTION PROCEDURE FOR COMPRESSIBLE STUDY

The overall method of solution for the interaction study differs only slightly from the incompressible case. For the complete second-order solution we begin at the selected initial station where the $\partial w / \partial \xi$ term is set equal to zero. After making initial guesses at the inviscid properties and flow profiles, we integrate the energy equation using the numerical method. With this new estimate of the total enthalpy profile; update all viscous properties related to temperature. Next, upon solving the s-momentum equation, integrate the continuity equation, the pressure integral, and the displacement thickness integrals employing trapezoidal rules. After obtaining new estimates of displacement thickness and its derivatives, update the inviscid properties and return to integrate the energy equation thus completing the cycle. When convergence has been reached, the program steps down the body one station and continues this process.

The method employed here to extract the displacement thickness from equation (1.5-7) is as follows. We first integrate both sides of equation (1.5-7). Now, we must determine at what point the left-hand integral is equal to the complete right-hand integral. This is done by a simple Fortran "IF" statement. If the desired value of the left-hand integral falls exactly on a grid point, then $\bar{\delta}$ is simply the value of η at that grid point. Should the desired left-hand integral value fall between two grid point, a linear extrapolation was employed to determine the correct value of displacement thickness. Knowing, $\bar{\delta}$, δ was then computed from equation (1.5-8).

Step size for the incompressible study

For both the incompressible and compressible study, a constant step size was taken in the η direction and was $\Delta\eta = 0.1$. For the incompressible investigation a step size of $\Delta s = \pi/720$ was chosen along the body surface.

Step size for the compressible study

a variable step size was chosen for the compression ramp interaction investigation. For $x < 0.5$, $\Delta s = 0.0025$, for $0.5 \leq x < 0.8$, $\Delta s = 0.005$, and for $x \geq 0.8$ Δs was 0.01. The run time for the complete second-order solution at $M = 12.25$, $Re_{s_\infty} = 0.858 \times 10^5$ with these step sizes was 59 minutes on a CDC 6000 series computer. For the $M = 6, 8$ cases, the run-time was approximately 23 minutes.

VII. APPENDIX B

THE BLASIUS SHEAR STRESS FOR A GIVEN WALL

PRESSURE DISTRIBUTION

The form of the wall pressure distribution is that given by Dimopoulos and Hanratty (1968)

$$\frac{p_{\text{wall}}^* - P_{\infty}^*}{\frac{1}{2} \rho_{\infty}^* U_{\infty}^{*2}} = \sum_{n=0}^6 a_{2n} \phi^{2n}, \quad (1-B)$$

where ϕ is measured in degrees.

From Rosenhead (1963), the inviscid velocity is assumed of the form

$$U_e^* = U_{\infty}^* U_0' \tilde{s} \left(1 + b_2 \tilde{s}^2 + b_4 \tilde{s}^4 + b_6 \tilde{s}^6 + \dots \right), \quad (2-B)$$

The odd terms in equation (2-B) for the assumed symmetrical flow are zero as noted by Rosenhead (1963). The constants U_0' , b_2 , b_4 ... are unknowns and must be determined in terms of the constants in equation (1-B).

The Blasius shear stress is given by

$$\frac{\tau_{\text{wall}}^*}{\rho_{\infty}^* U_{\infty}^{*2} U_0'^2} \left[\frac{\rho_{\infty}^* U_{\infty}^* U_0' d^*}{\mu_{\infty}^*} \right]^{1/2} = \tilde{s} \left(E_0 + \tilde{s}^2 E_2 + \tilde{s}^4 E_4 + \tilde{s}^6 E_6 + \tilde{s}^8 E_8 \right), \quad (3-B)$$

where

$$E_0 = f''_0(0), \quad (4a-B)$$

$$E_2 = b_2 f''_2(0), \quad (4b-B)$$

$$E_4 = b_4 f''_4(0) + b_2^2 f''_{22}(0), \quad (4c-B)$$

$$E_6 = b_6 f''_6(0) + b_4 b_2 f''_{42}(0) + b_2^3 f''_{222}(0), \quad \text{and} \quad (4d-B)$$

$$+ E_8 = b_8 f''_8(0) + b_6 b_2 f''_{62}(0) + b_4^2 f''_{44}(0) + b_4 b_2^2 f''_{422}(0) + b_2^4 f''_{4444}(0). \quad (4e-B)$$

The functions "f" are tabulated in Rosenhead (1963). We wish now to determine the constants b_2, b_4, \dots in terms of the wall pressure constants given in equation (1-B).

Noting that for a cylinder

$$s^* = \phi \frac{\pi}{360} d^*, \quad (5-B)$$

then defining

$$e = \frac{\pi}{360} \quad (6-B)$$

gives

$$U_e^* = U_\infty^* U_o' e \phi \left(1 + e^2 b_2 \phi^2 + e^4 b_4 \phi^4 + e^6 b_6 \phi^6 + \dots \right). \quad (7-B)$$

[†]This term was not given by Rosenhead (1963).

The inviscid flow is assumed to be governed by Bernoulli's equation⁺ which can be written as

$$\frac{dP_e^*}{d\phi} = -\rho_\infty^* U_e^* \frac{dU_e^*}{d\phi} . \quad (8-B)$$

Substituting the expressions for U_e^* and P_e^* ($P_e^* \approx p_{wall}^*$) into equation (8-B), we obtain the following relations for the constants b_2, b_4, \dots ,

$$b_2 = \frac{1}{2} \frac{a_4}{a_2 e^2} , \quad (9a-B)$$

$$b_4 = \left(\frac{1}{2} \frac{a_6}{a_2} - \frac{a_4^2}{8a_2^2} \right) / e^4 , \quad (9b-B)$$

$$b_6 = \left(\frac{1}{2} \frac{a_8}{a_2} - \frac{1}{4} \frac{a_4 a_6}{a_2^2} + \frac{1}{16} \frac{a_4^3}{a_2^3} \right) / e^6 , \quad (9c-B)$$

and

$$b_8 = \left[\frac{1}{2} \frac{a_{10}}{a_2} - \frac{1}{8} \left(\frac{2a_4 a_8}{a_2^2} + \frac{a_6^2}{a_2^2} \right) - \frac{5}{128} \frac{a_4^4}{a_2^4} + \frac{3}{16} \frac{a_4^2 a_6}{a_2^3} \right] / e^8 . \quad (9d-B)$$

The constant U_0' given in equation (7-B) is given by

⁺ Here we take $U_e^2 + \tilde{V}_e^2 \approx U_e^2$

$$U'_0 = \frac{\sqrt{-a_2}}{e} \quad (10-B)$$

We need now to express the shear stress given by equation (3-B) in terms of the skin friction used in this study which is

$$\bar{C}_f = \frac{\tau_{wall}^*}{\frac{1}{2} \rho_\infty^* U_\infty^{*2}} \sqrt{Re} . \quad (11-B)$$

This works out to be

$$\bar{C}_f = \sqrt{2} U'_0{}^{3/2} \tilde{s} \left(E_0 + \tilde{s}^2 E_2 + \tilde{s}^4 E_4 + \tilde{s}^6 E_6 + \tilde{s}^8 E_8 \right) . \quad (12-B)$$

TABLE I.- NUMERICAL VALUES OF dU_e/ds AT THE STAGNATION POINT

Re_d	$U'_0 = dU_e/ds$						
	40	174	175 ^a	175 ^b	177	200 ⁺	200 ⁺⁺
Potential theory value	2.000	2.000	2.000	2.000	2.000	2.000	2.000
Initial guess equation (2.3-33)	1.793	1.634	1.808	1.824	1.818	2.046	1.574
Final value iterative solution	1.799	1.645	1.813	---	1.823	2.042	1.587

^aHere $d^*/\tilde{h}^* = 0.05$

^bHere $d^*/\tilde{h}^* = 0.10$

⁺Obtained using curvefit A given in Figure 2.3e

⁺⁺Obtained using curvefit B given in Figure 2.3e

TABLE II.- COEFFICIENTS FOR EQUATION (2.5-3)

Re_d	40	174	175 ^a	175 ^b	177	200 ⁺	200 ⁺⁺
C_0	-0.558049	-0.742972	-0.433693	-0.535618	-0.408033	-0.689683	-0.671619
C_2	-0.766625	-1.096550	-0.508736	-0.818143	-0.480901	-1.013466	-0.783360
C_4	-0.226734	-0.441596	-0.051834	-0.355295	-0.051616	-0.388269	-0.048946
C_6	-0.149193	-0.153810	-0.055420	-0.101078	-0.038286	-0.074742	-0.079605
C_8	- - -	- - -	0.033631	- - -	0.028899	-0.004973	0.046323
D_0	1.0	1.0	1.0	1.0	1.0	1.0	1.0
D_2	1.312803	1.438642	1.110520	1.520587	1.173784	1.493048	1.051067
D_4	0.581078	0.650948	0.222962	0.704213	0.260563	0.608359	0.248946
D_6	0.195990	0.176749	- - -	0.178288	- - -	0.111925	- - -
D_8	0.042673	0.027034	- - -	0.018078	- - -	- - -	- - -

^aHere $d^*/\tilde{h}^* = 0.05$

^bHere $d^*/\tilde{h}^* = 0.10$

⁺For curvefit A in Figure 2.3e; Here $C_{10} = 0.000755$ and $C_{12} = -0.001139$.

⁺⁺For curvefit B in Figure 2.3e

TABLE III.- DATA POINTS USED IN THE WALL PRESSURE CURVE FITS

⁺

$\phi \backslash Re_d$	C_{pwall} 40
0°	1.120
18.8°	0.918
37.5°	0.281
56.3°	-0.394
75.0°	-0.824
93.7°	-0.927
112.5°	-0.824
131.1°	-0.694
150.0°	-0.607
168.8°	-0.563
180.0°	-0.544

⁺⁺

$\phi \backslash Re_d$	C_{pwall}		
	175 ^a	175 ^b	175 ^c
0°	1.032	1.202	1.050
20°	0.651	0.887	0.666
40°	0.0	0.095	-0.025
60°	-0.575	-0.666	-0.633
80°	-0.726	-0.950	-0.747
100°	-0.596	-0.760	-0.595
120°	-0.476	-0.601	-0.482
140°	-0.438	-0.557	-0.418
160°	-0.426	-0.538	-0.406
180°	-0.438	-0.532	-0.392

^aHere $d^*/\tilde{h}^* = 0.05$ ^bHere $d^*/\tilde{h}^* = 0.10$ ^cHere $d^* h^* = 0.05$
⁺⁺⁺

$\phi \backslash Re_d$	C_{pwall} 200
0°	1.000
13.950°	0.814
20.925°	0.642
27.900°	0.451
34.875°	0.232
41.850°	0.
48.825°	-0.256
55.800°	-0.479
62.725°	-0.721
69.750°	-0.894
76.725°	-0.991
83.700°	-1.032
90.675°	-1.022
97.650°	-0.977
104.625°	-0.922
111.600°	-0.874
125.550°	-0.791
139.500°	-0.731
153.450°	-0.698
167.400°	-0.684
180.000°	-0.675

⁺Data taken from Kawaguti (1953)⁺⁺Data taken from Grove, Shair, Petersen,
and Acrivos (1964)⁺⁺⁺Data taken from Thoman and Szweczyk (1969)

TABLE IV.- COEFFICIENTS FOR EQUATION (2.5-5)

⁺

a_0	1.072
$a_2 \times 10^4$	-8.003
$a_4 \times 10^8$	10.592
$a_6 \times 10^{12}$	-6.240
$a_8 \times 10^{16}$	1.752
$a_{10} \times 10^{20}$	-0.207
$a_{12} \times 10^{24}$	0.005

⁺Reported by Dimopoulos and Hanratty (1968) for $Re_d = 174$

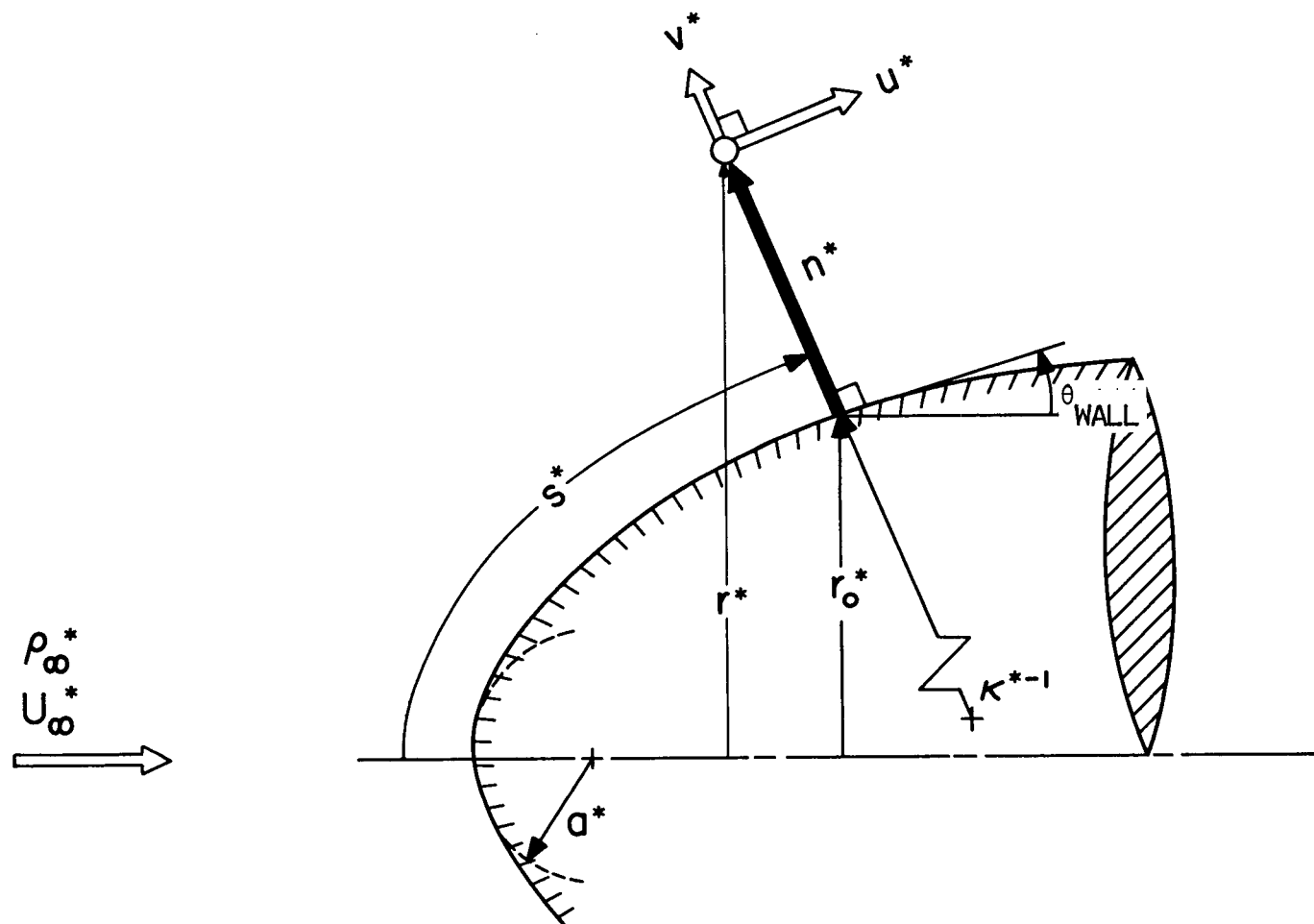


Figure 2.1 Coordinate System

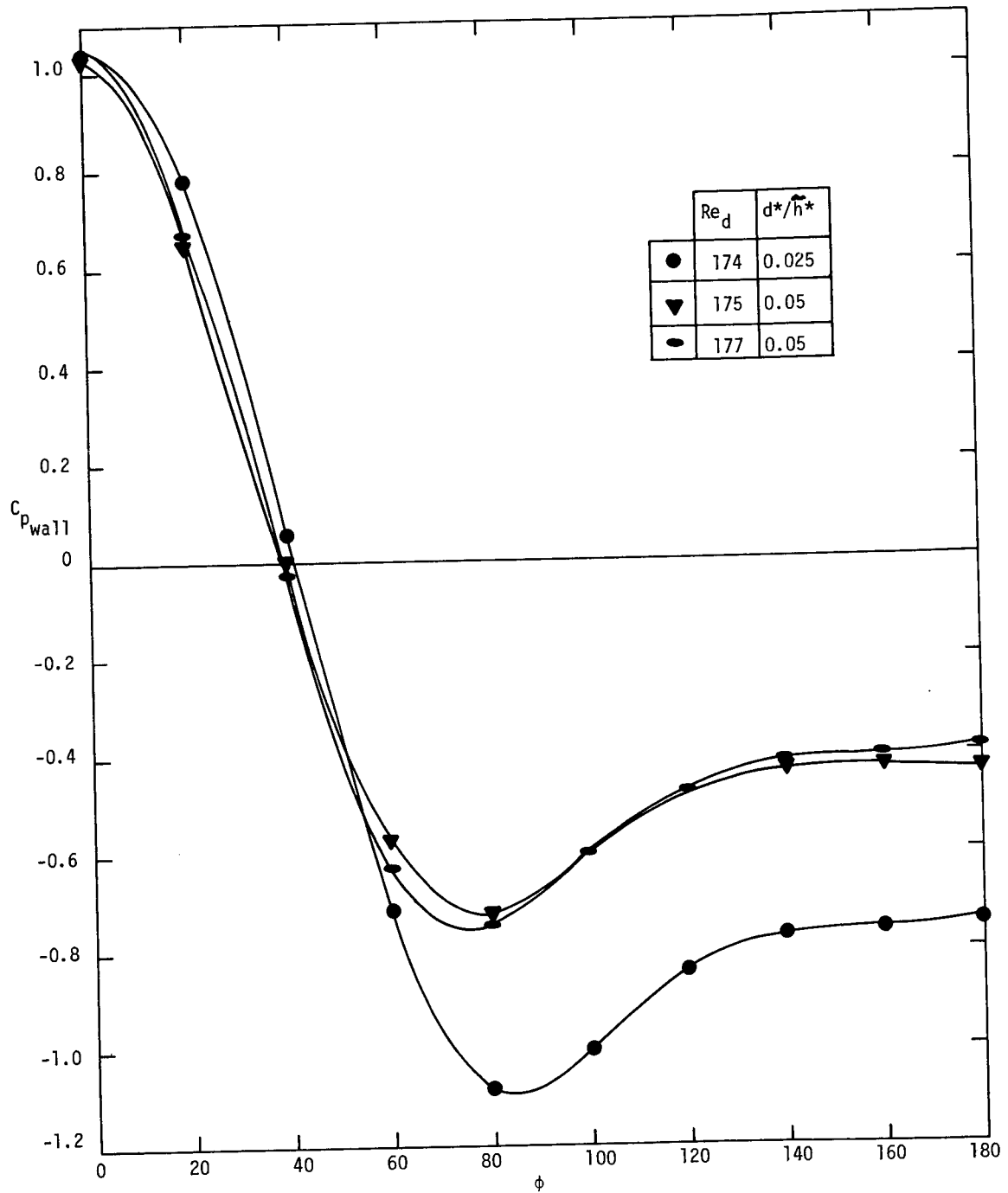


Figure 2.2 Surface Pressure Distributions at $Re_d = 174, 175, \text{ and } 177$.

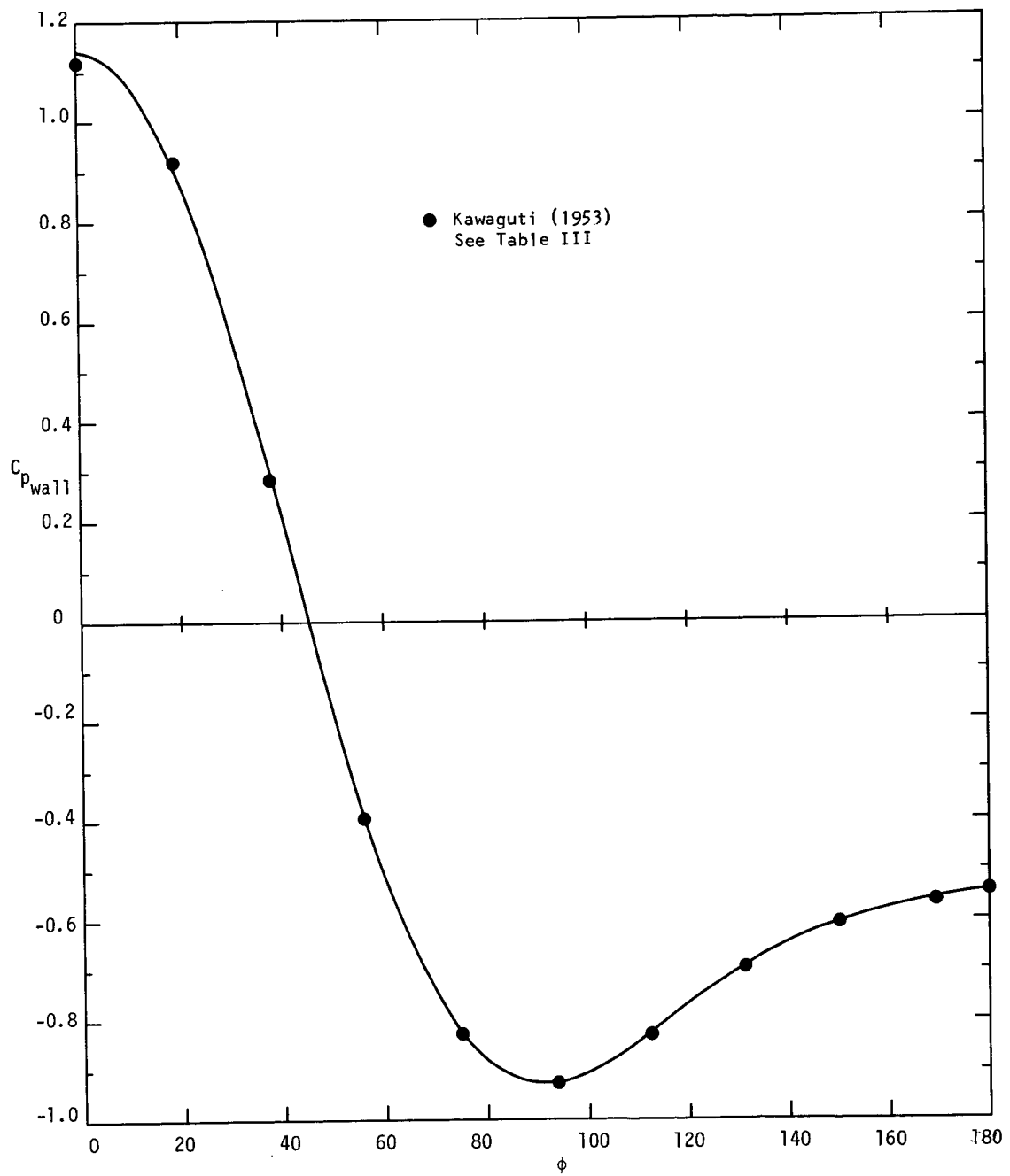


Figure 2.3 Curvefits of the Surface Pressure Distributions (a) $Re_d = 40$.

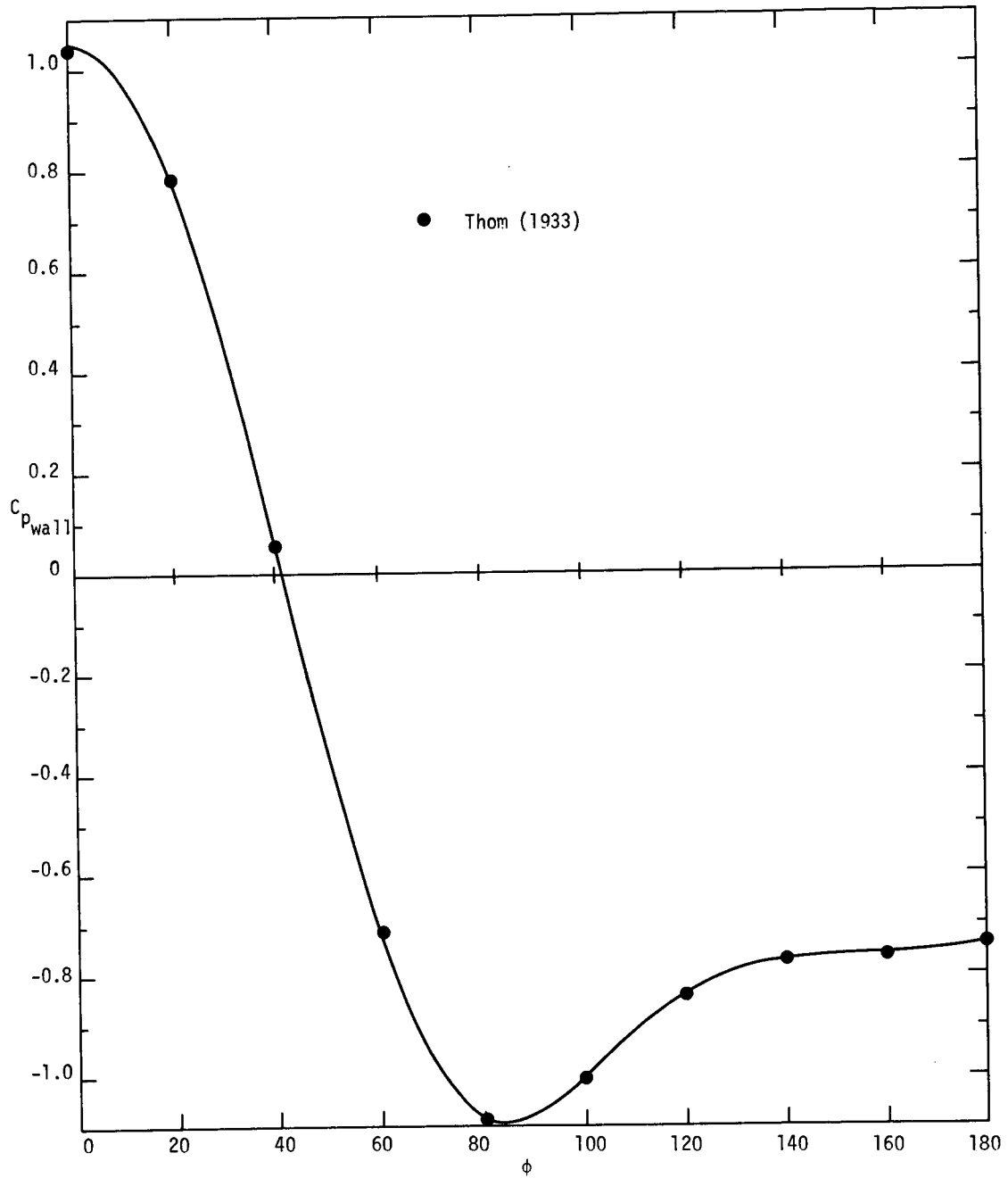


Figure 2.3 Continued (b) $Re_d = 174$

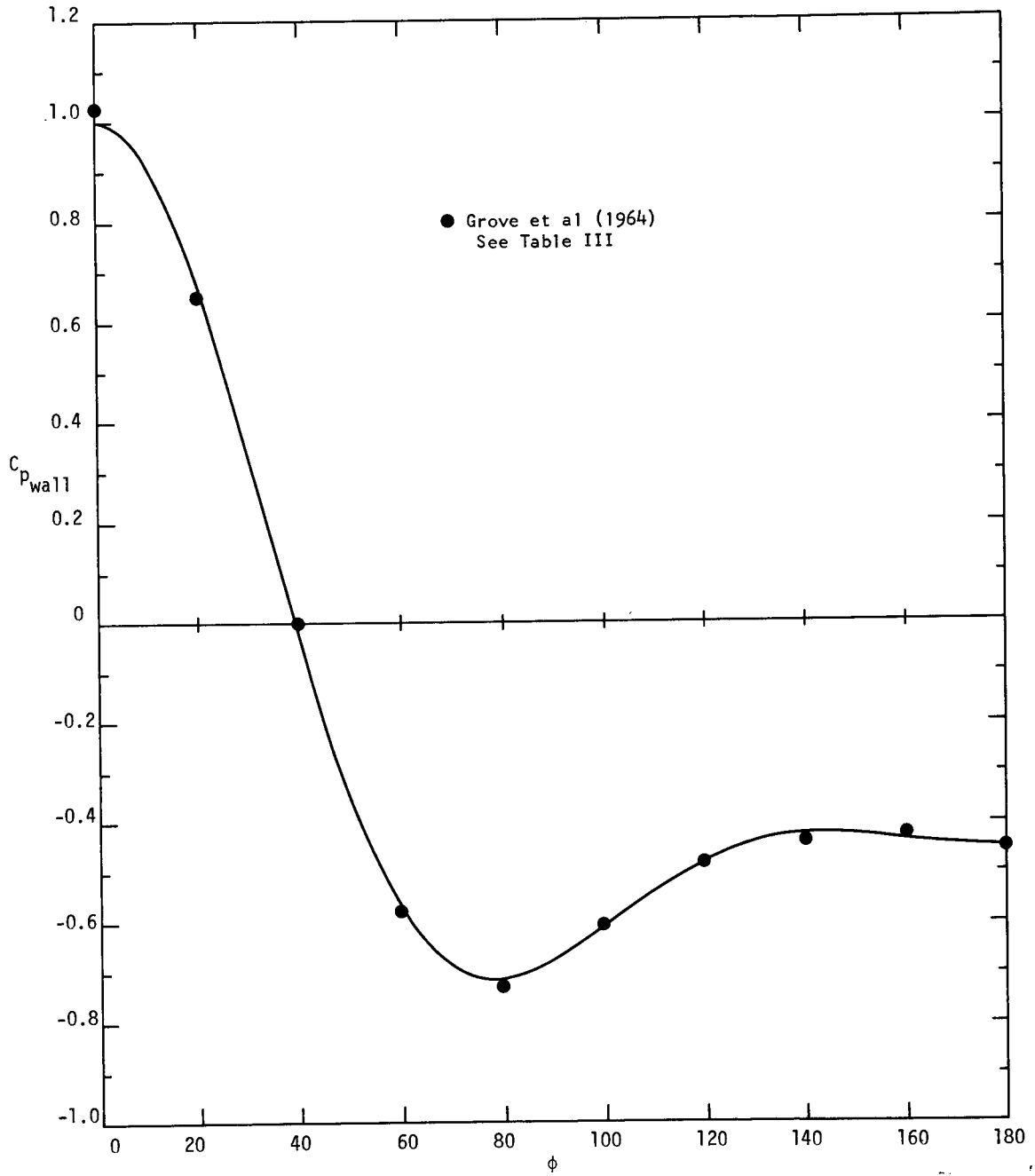


Figure 2.3 Continued (c) $Re_d = 175$

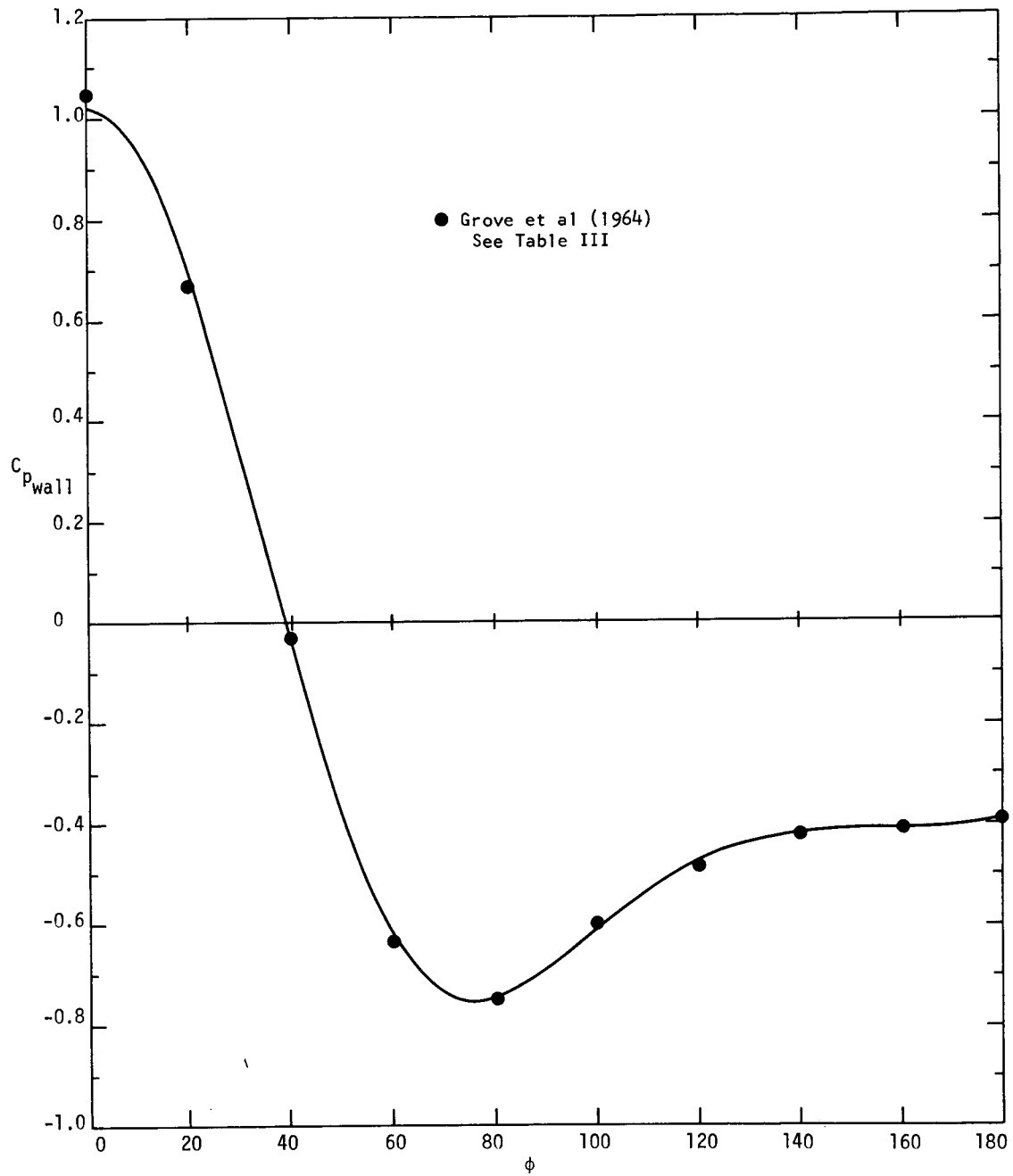


Figure 2.3 Continued (d) $Re_d = 177$

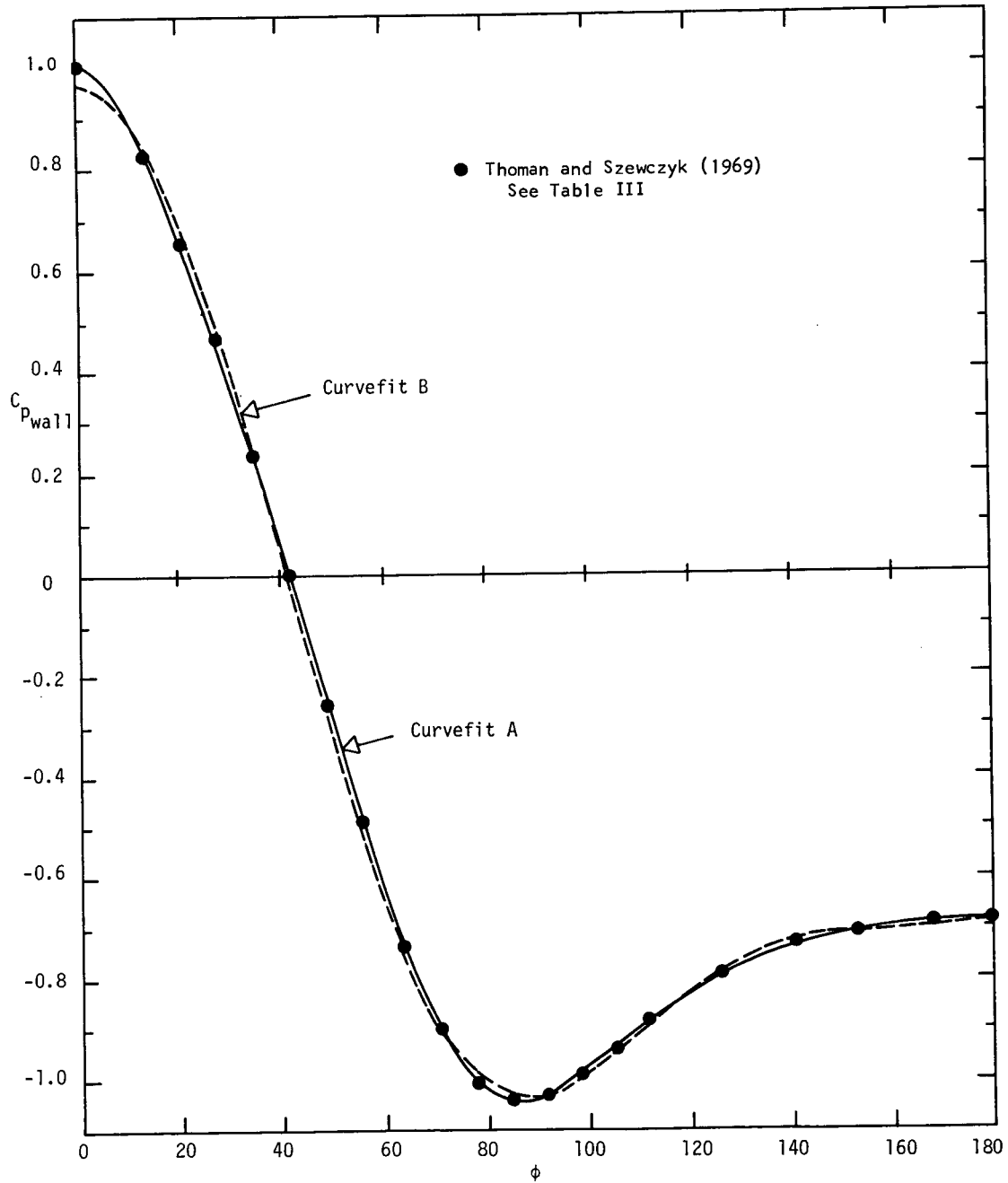


Figure 2.3 Concluded (e) $Re_d = 200$

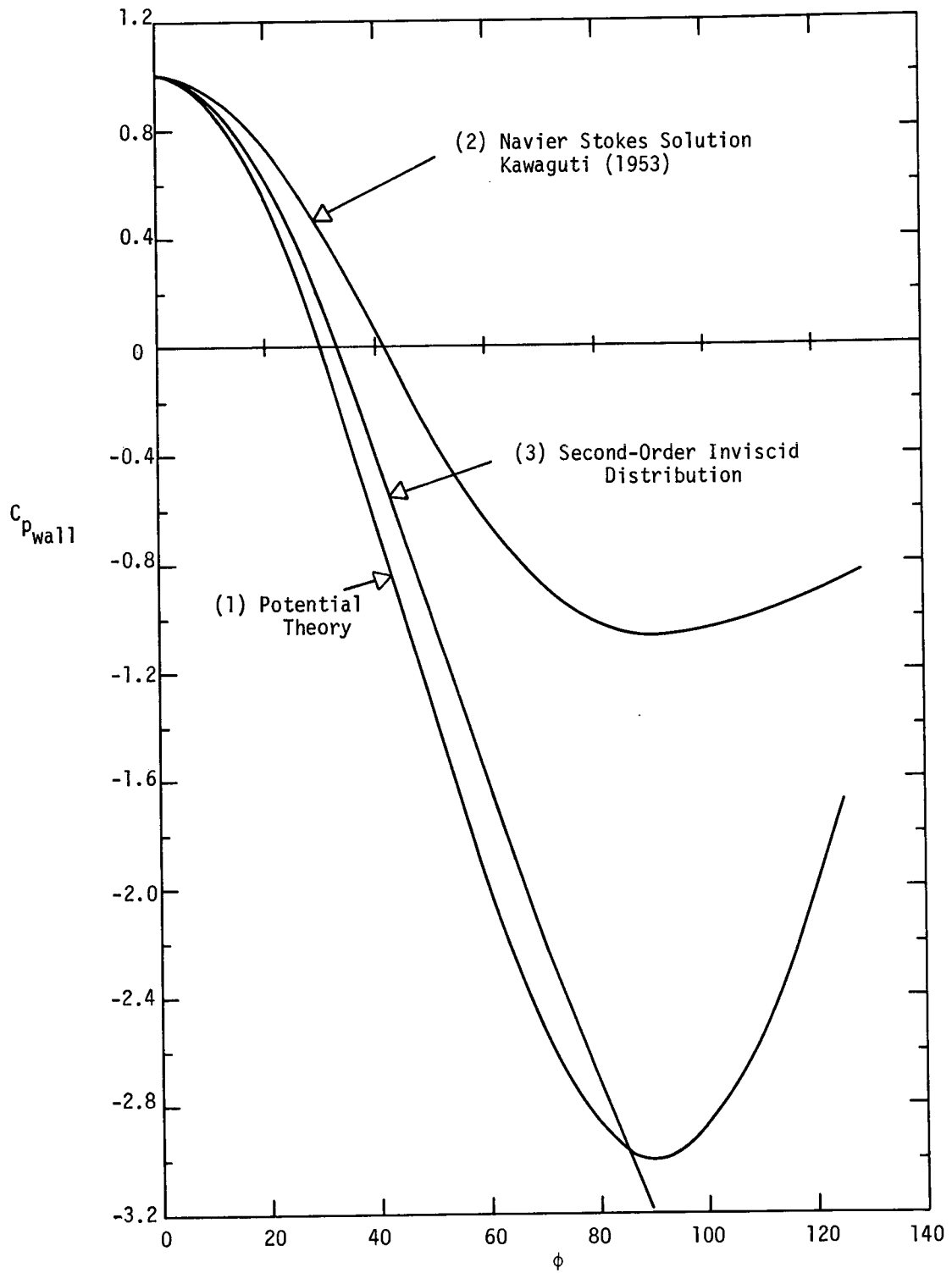


Figure 2.4 Theoretical Wall Pressure Distributions (a) $Re_d = 40$.

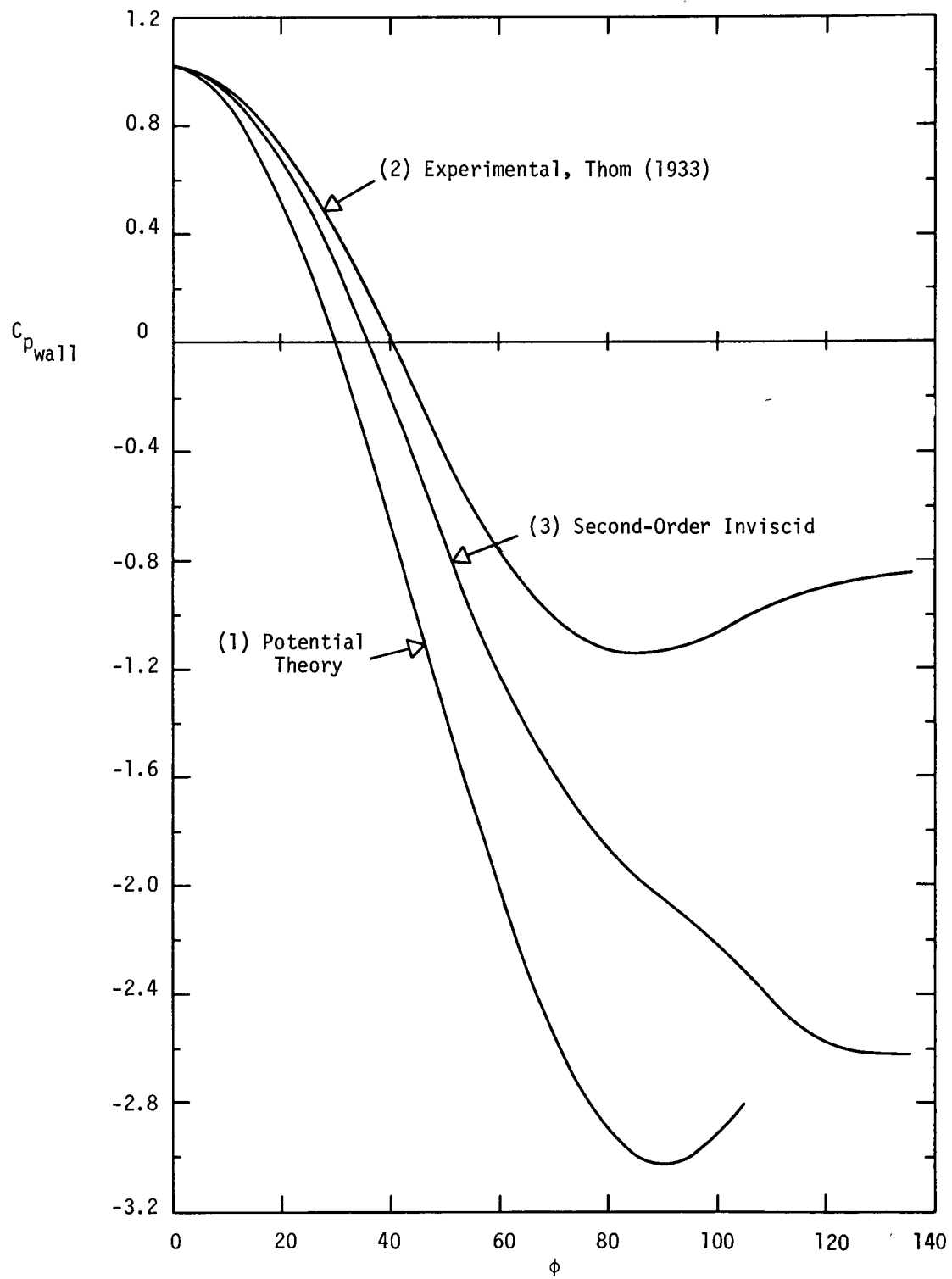


Figure 2.4 Continued (b) $Re_d = 174$.

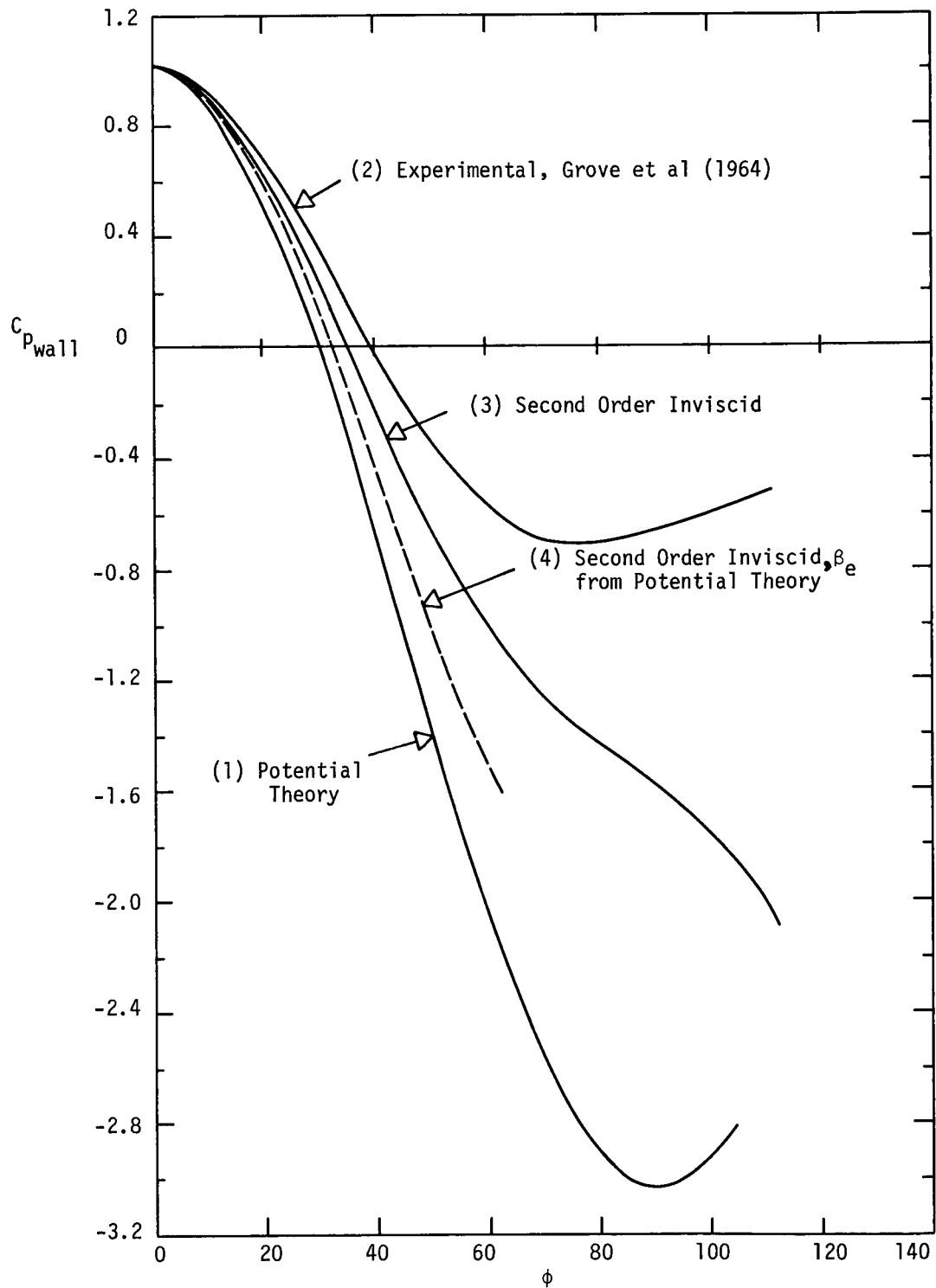


Figure 2.4 Continued (c) $Re_d = 175$

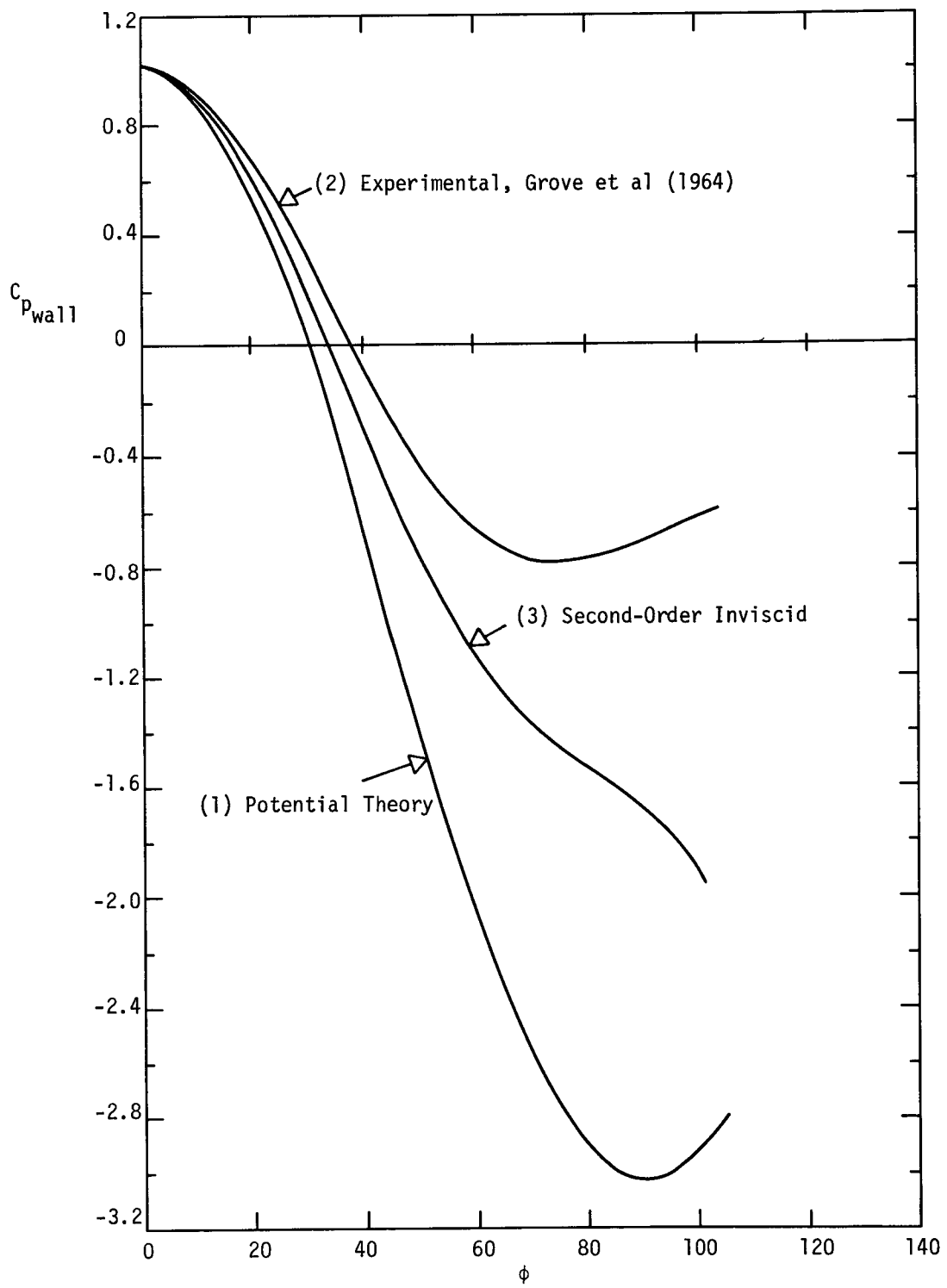


Figure 2.4 Continued (d) $Re_d = 177$

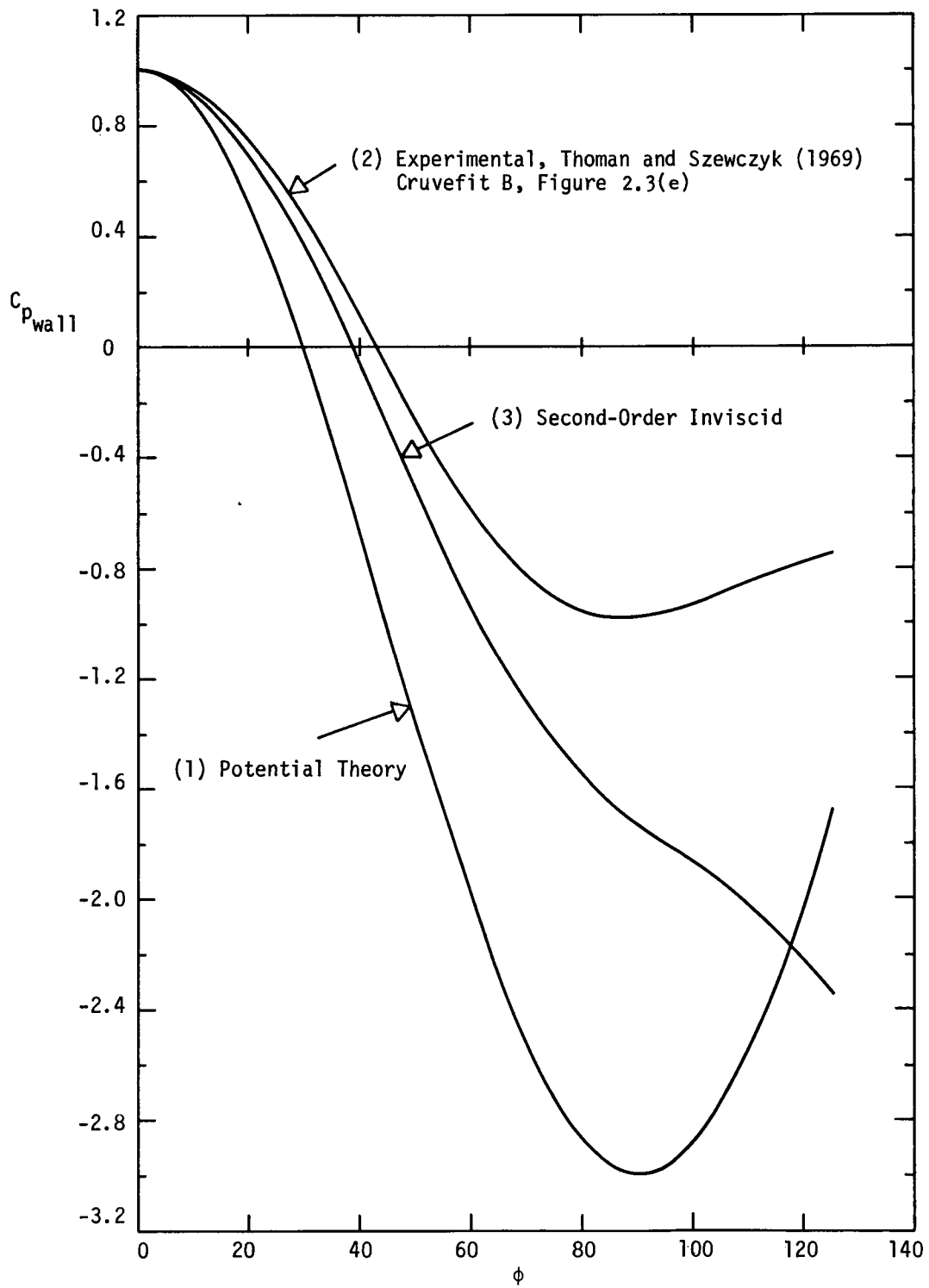


Figure 2.4 Concluded (e) $Re_d = 200$

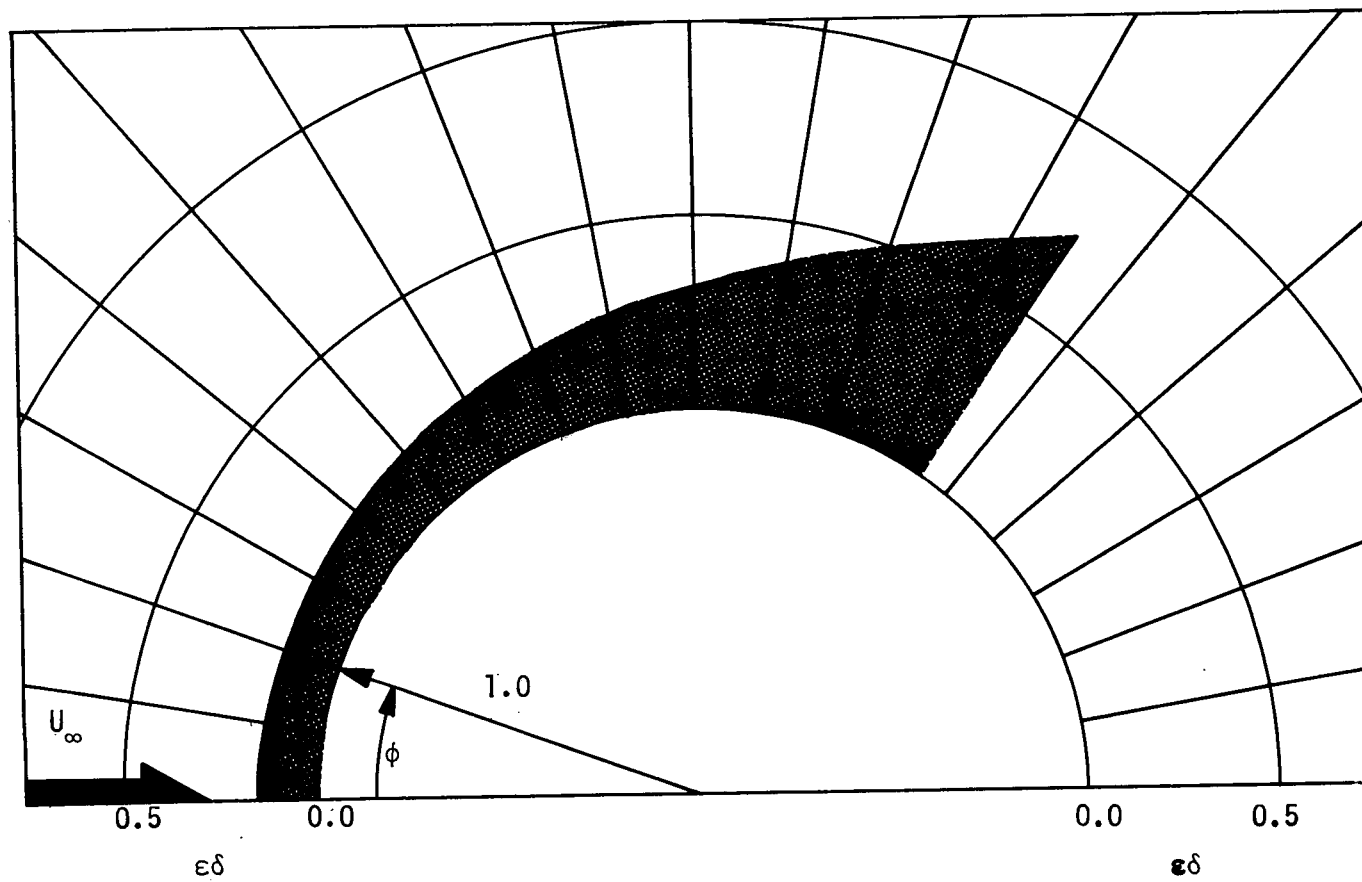


Figure 2.5 Theoretical Displacement
Bodies
(a) $Re_d = 40$

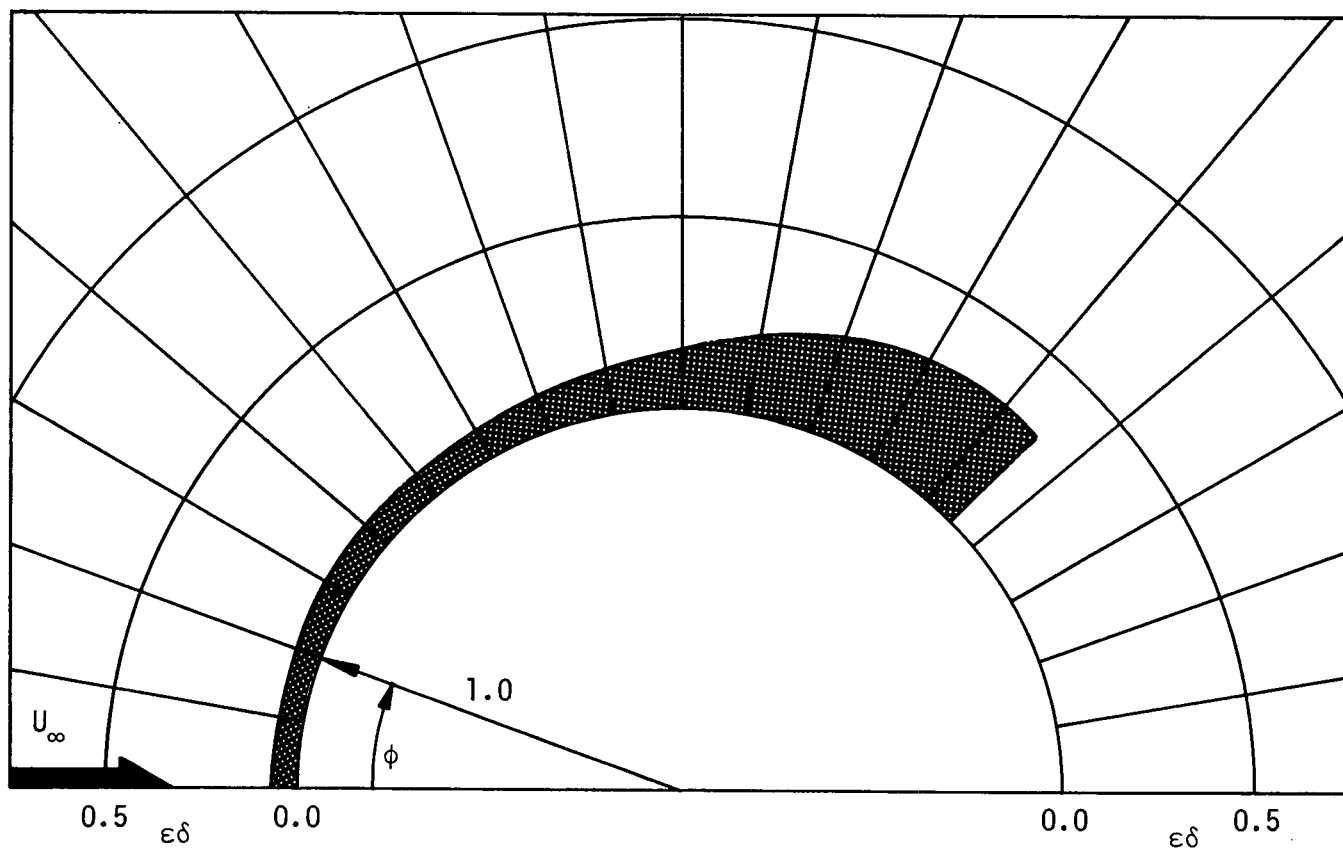


Figure 2.5 Continued

(b) $Re_d = 174$

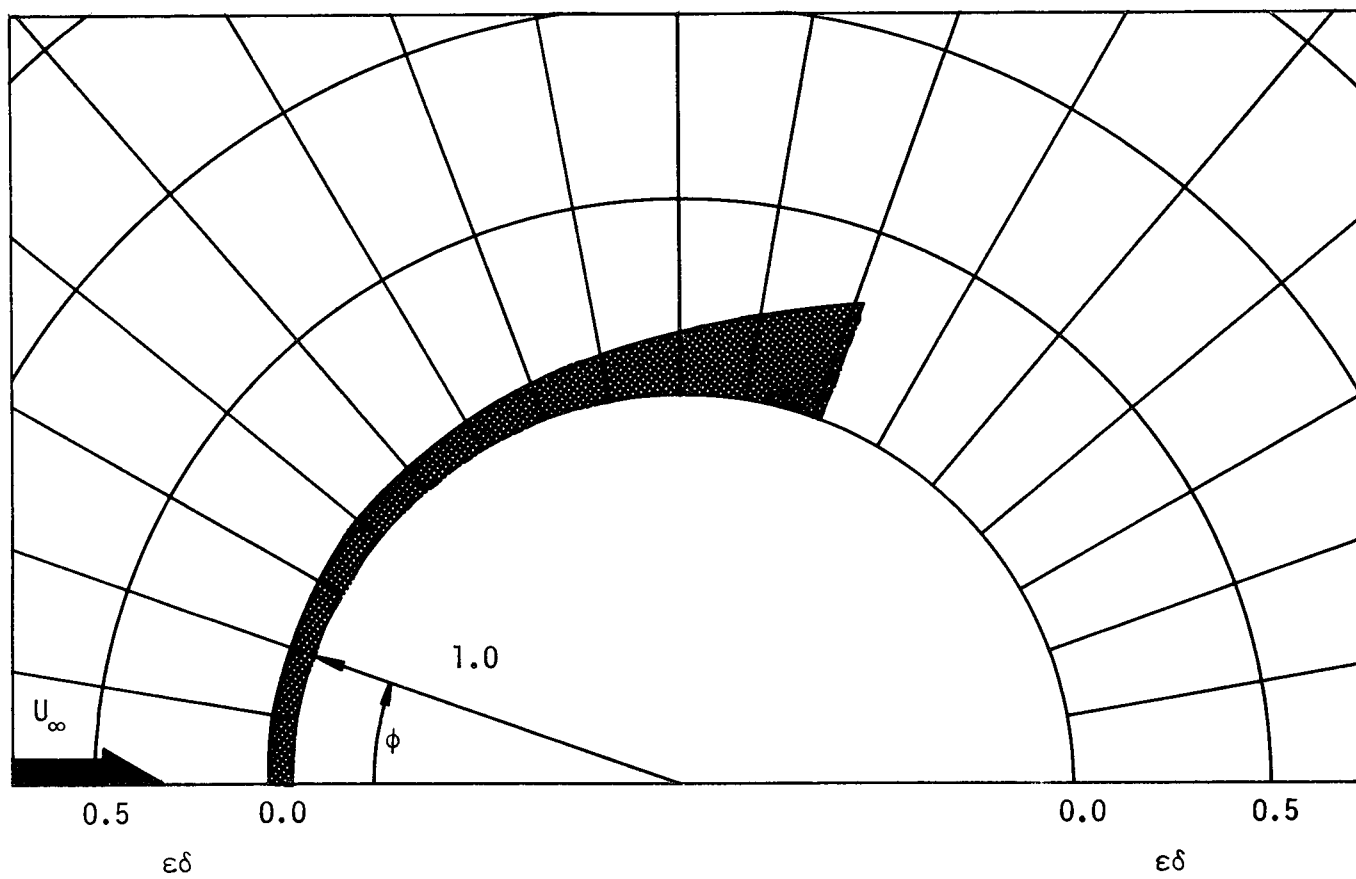


Figure 2.5 Continued
(c) $Re_d = 175$

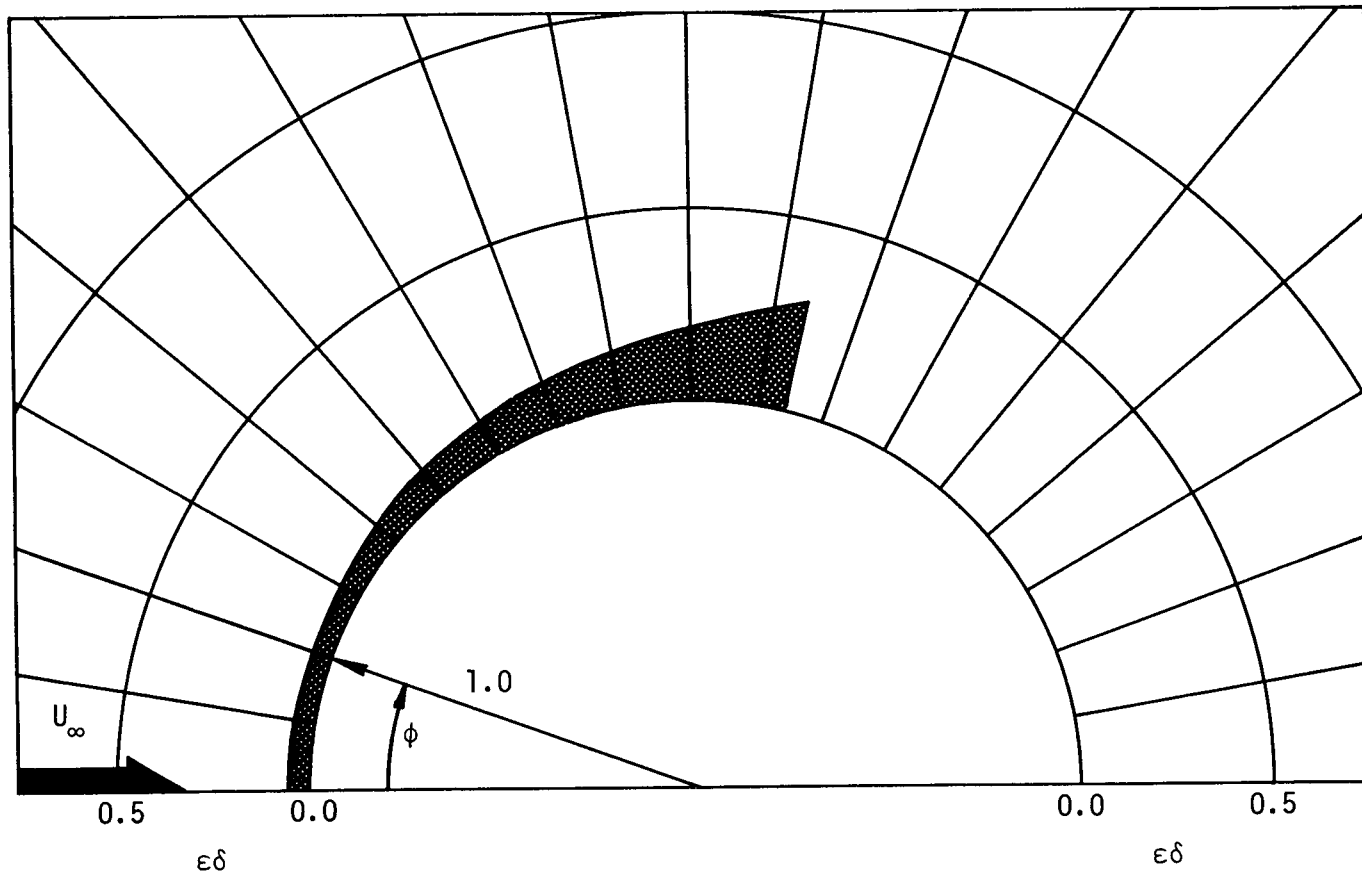


Figure 2.5 Continued
(d) $Re_d = 177$

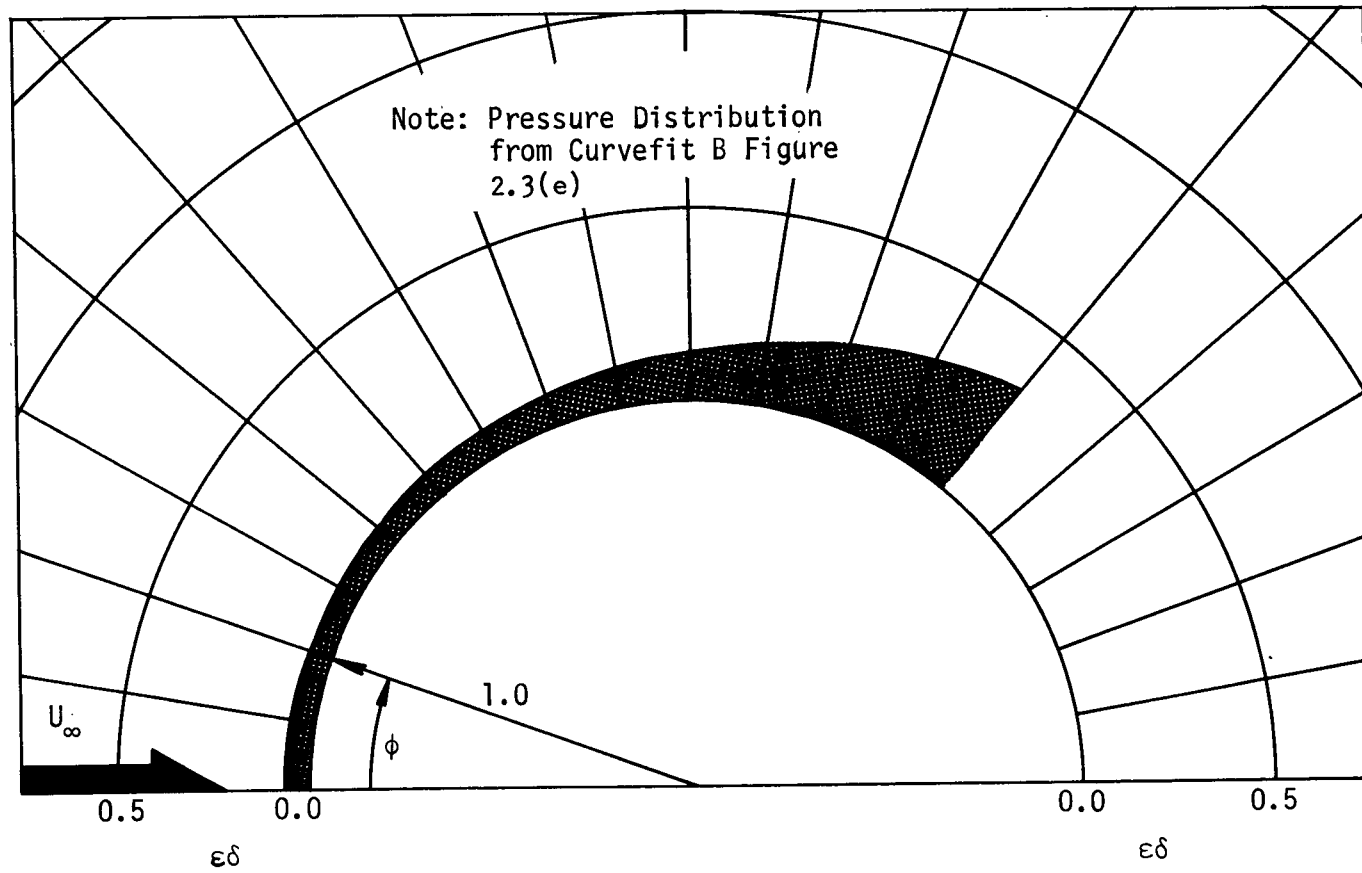


Figure 2.5 Concluded
(e) $Re_d = 200$

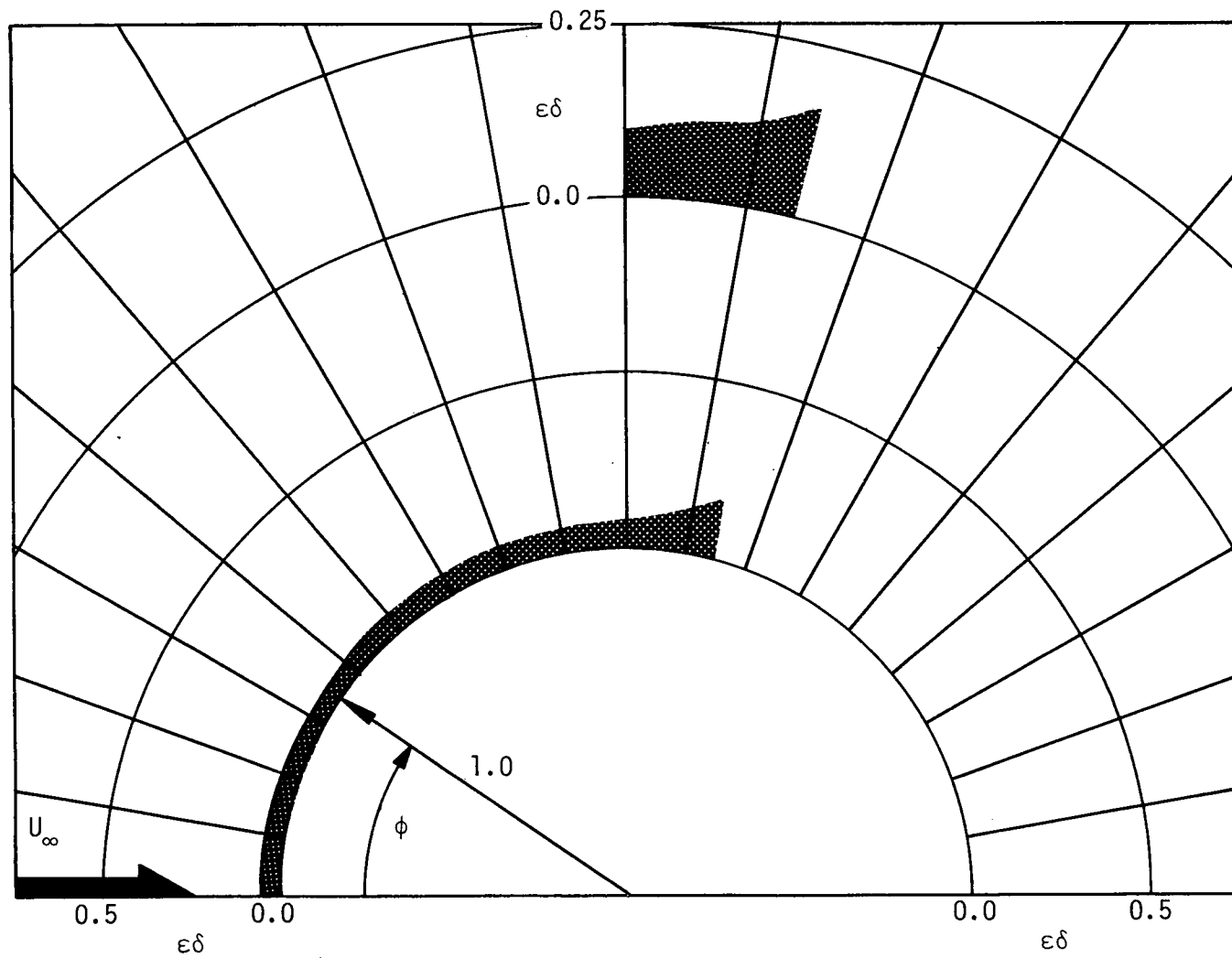


Figure 2.6 First-Order Displacement Thickness for a Potential Velocity Distribution.

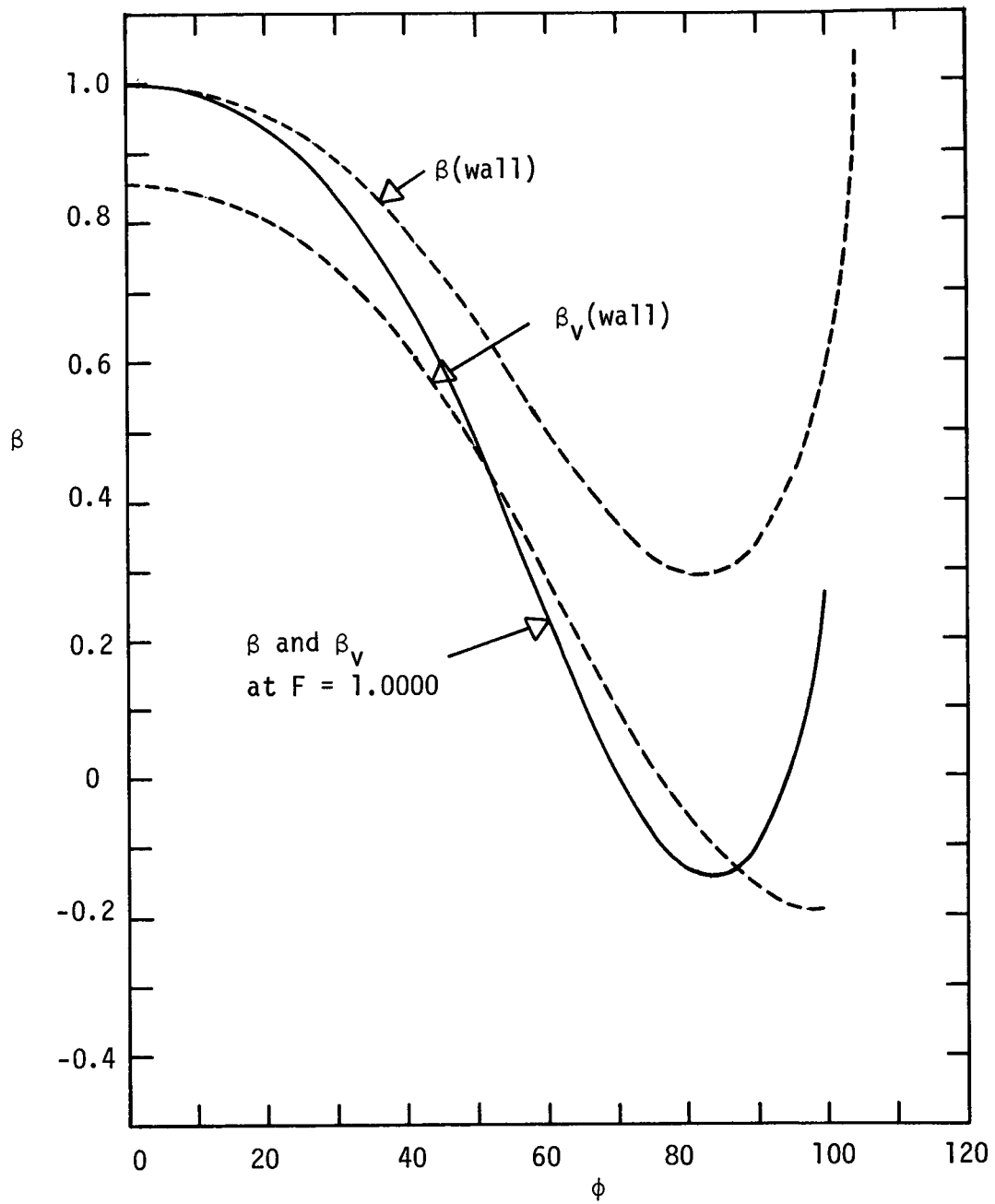


Figure 2.7 Viscous Pressure Gradient Parameter Distribution at $Re_d = 175$.

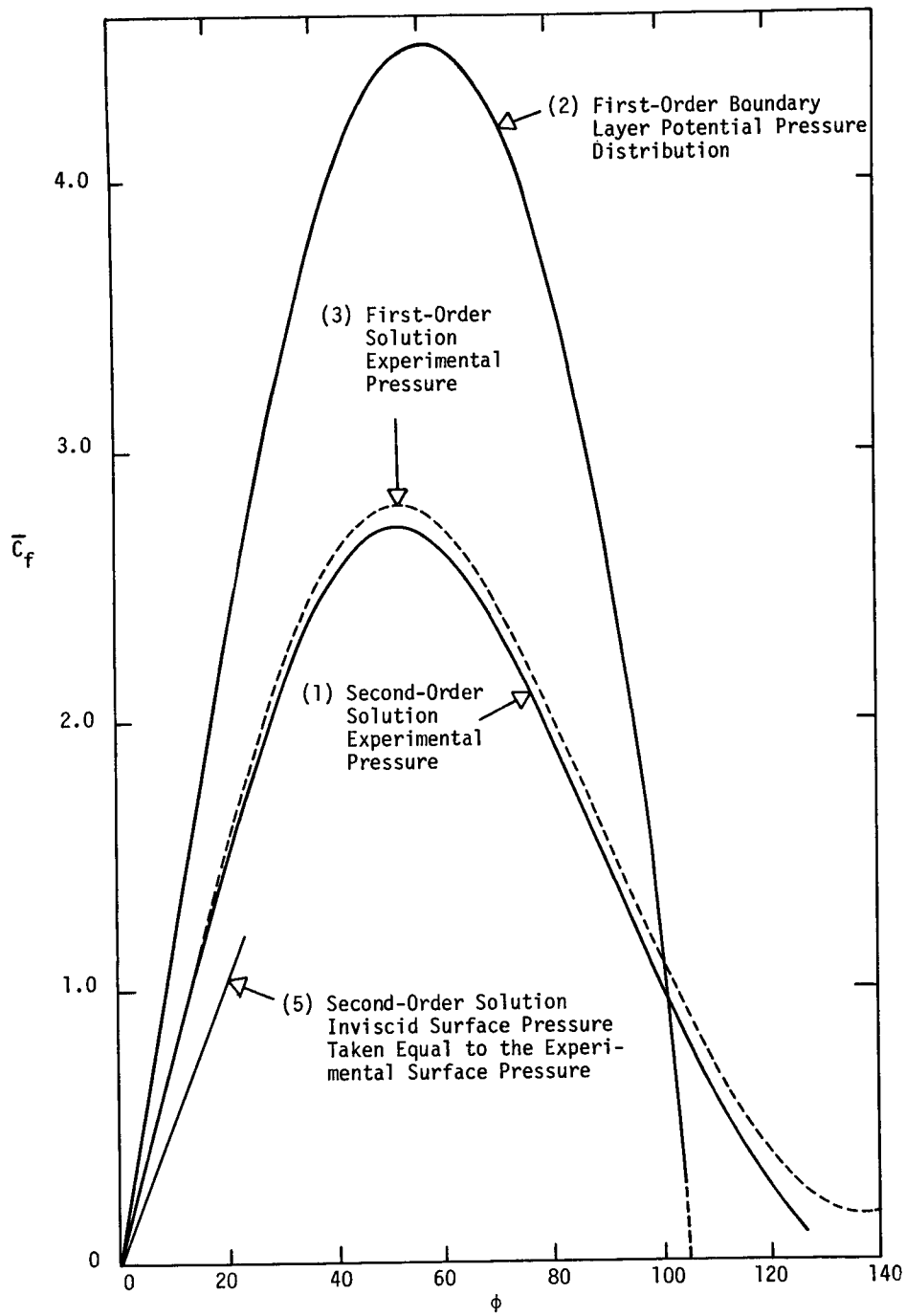


Figure 2.8 Surface Shear Stress Distributions (a) $Re_d = 40$.

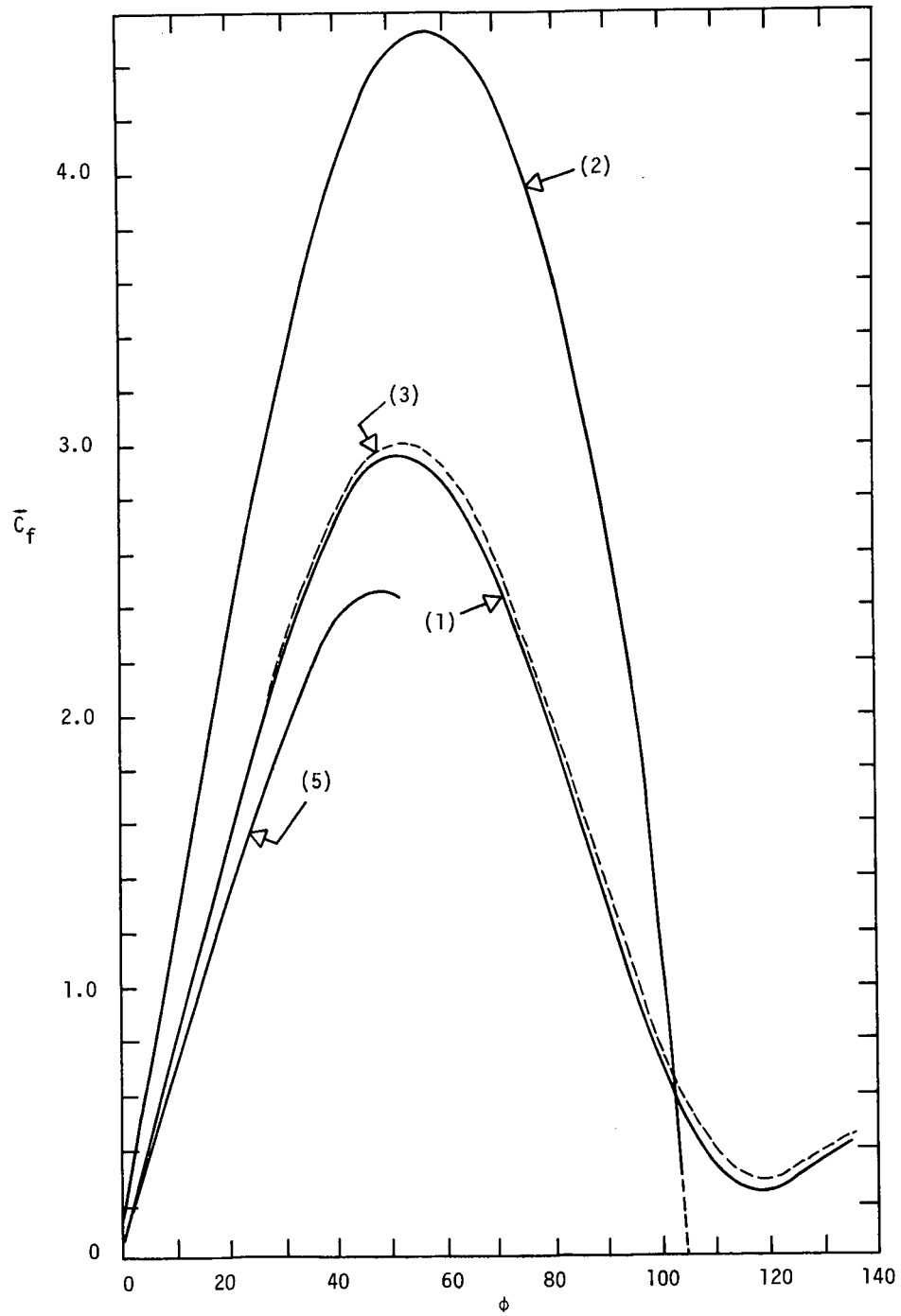


Figure 2.8 Continued (b) $Re_d = 174$

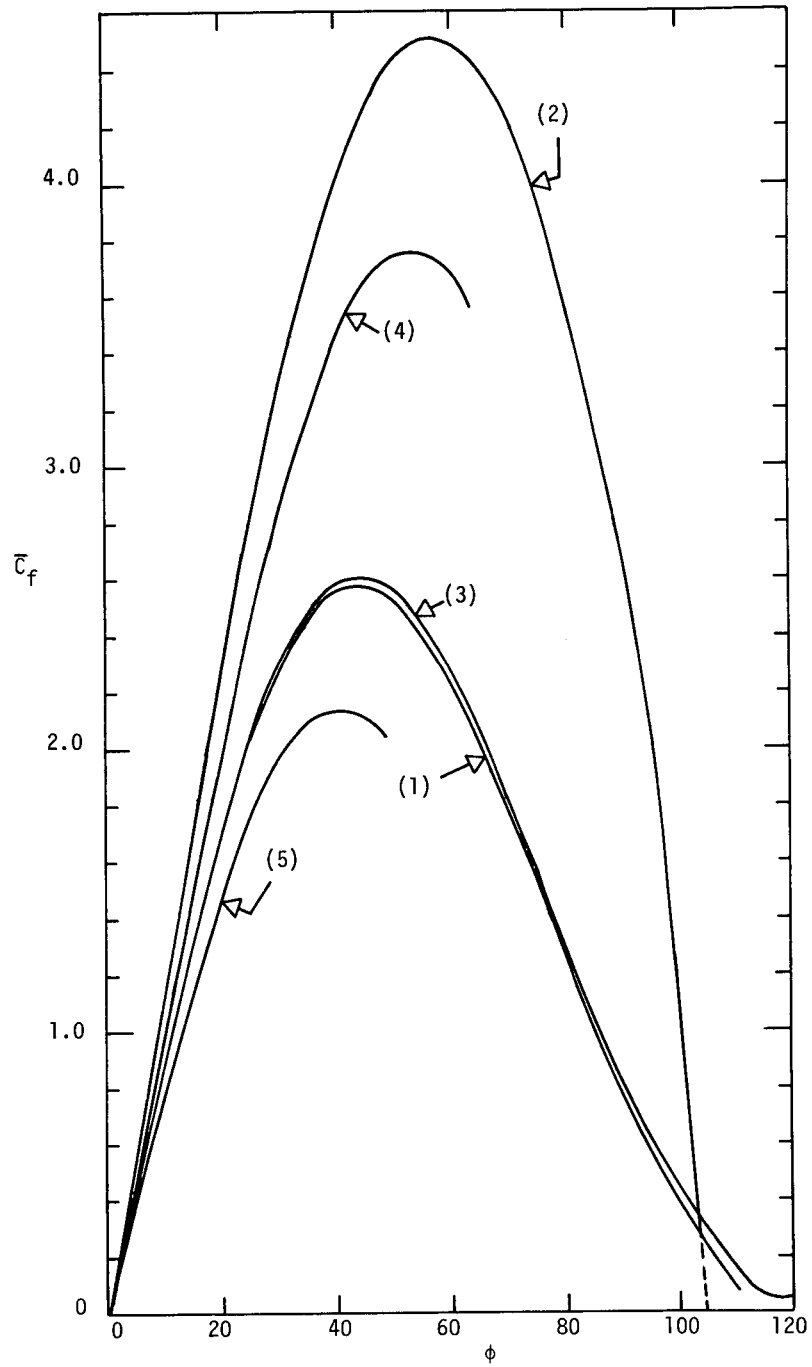


Figure 2.8 Continued (c) $Re_d = 175$.

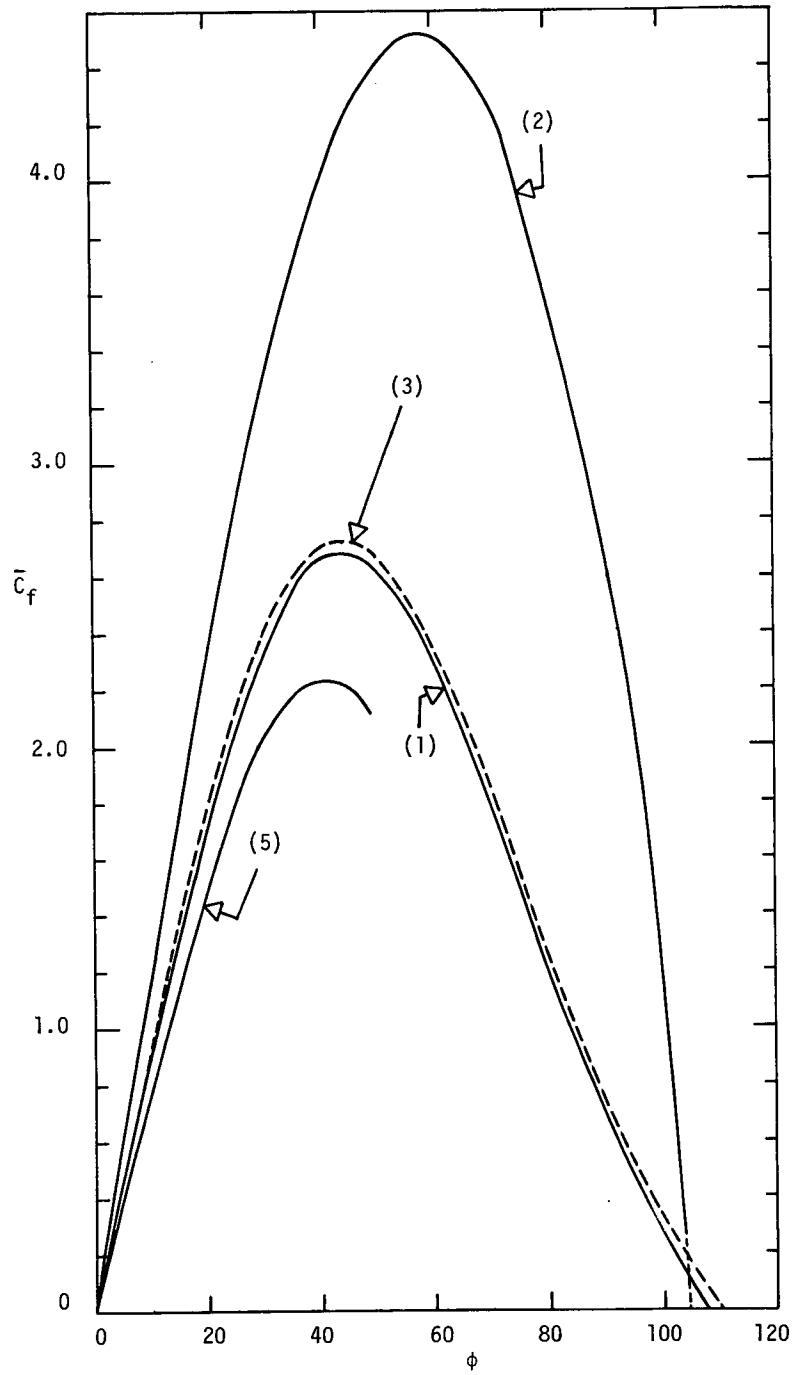


Figure 2.8 Continued (d) $Re_d = 177$.

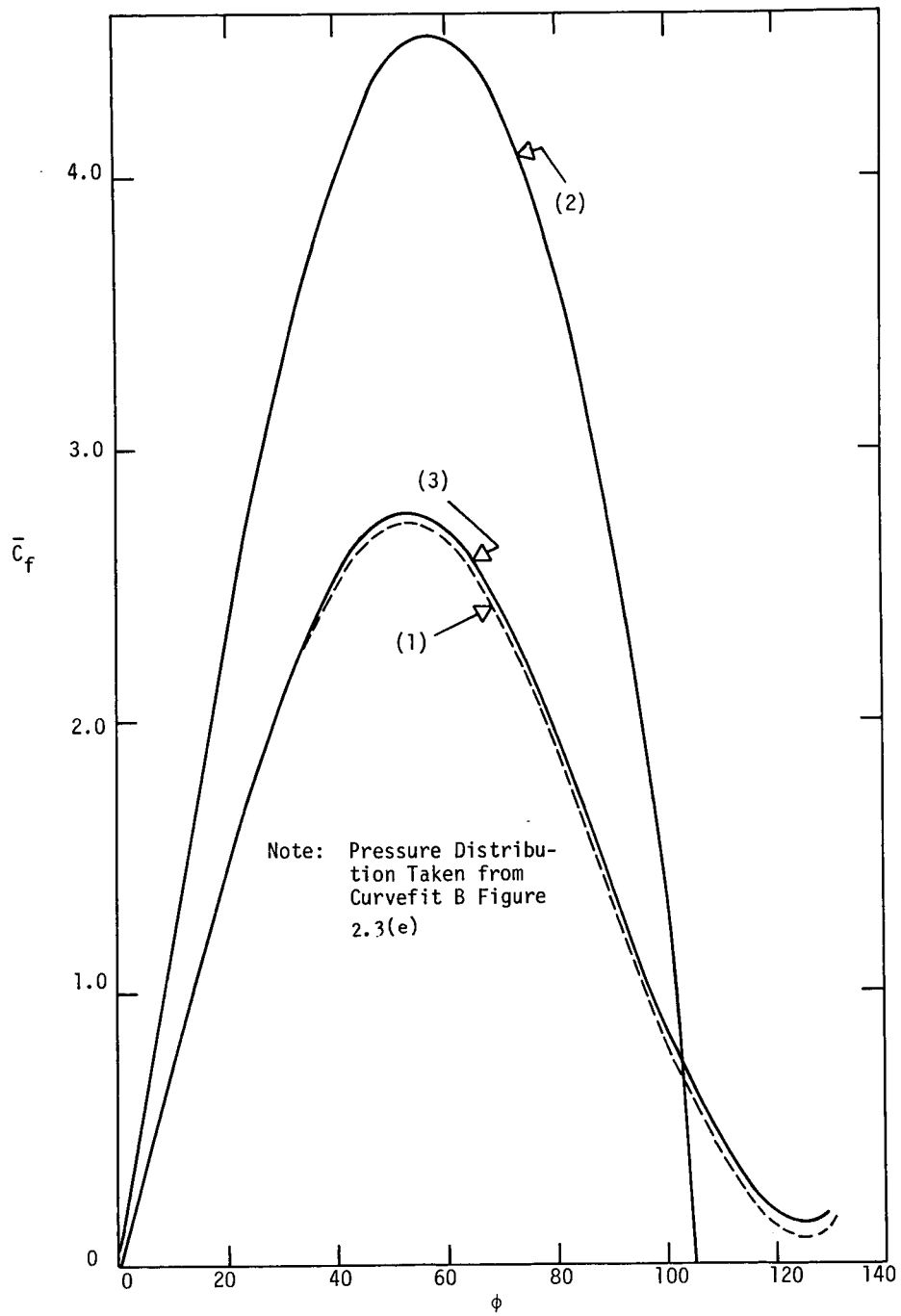


Figure 2.8 Concluded (e) $Re_d = 200$.

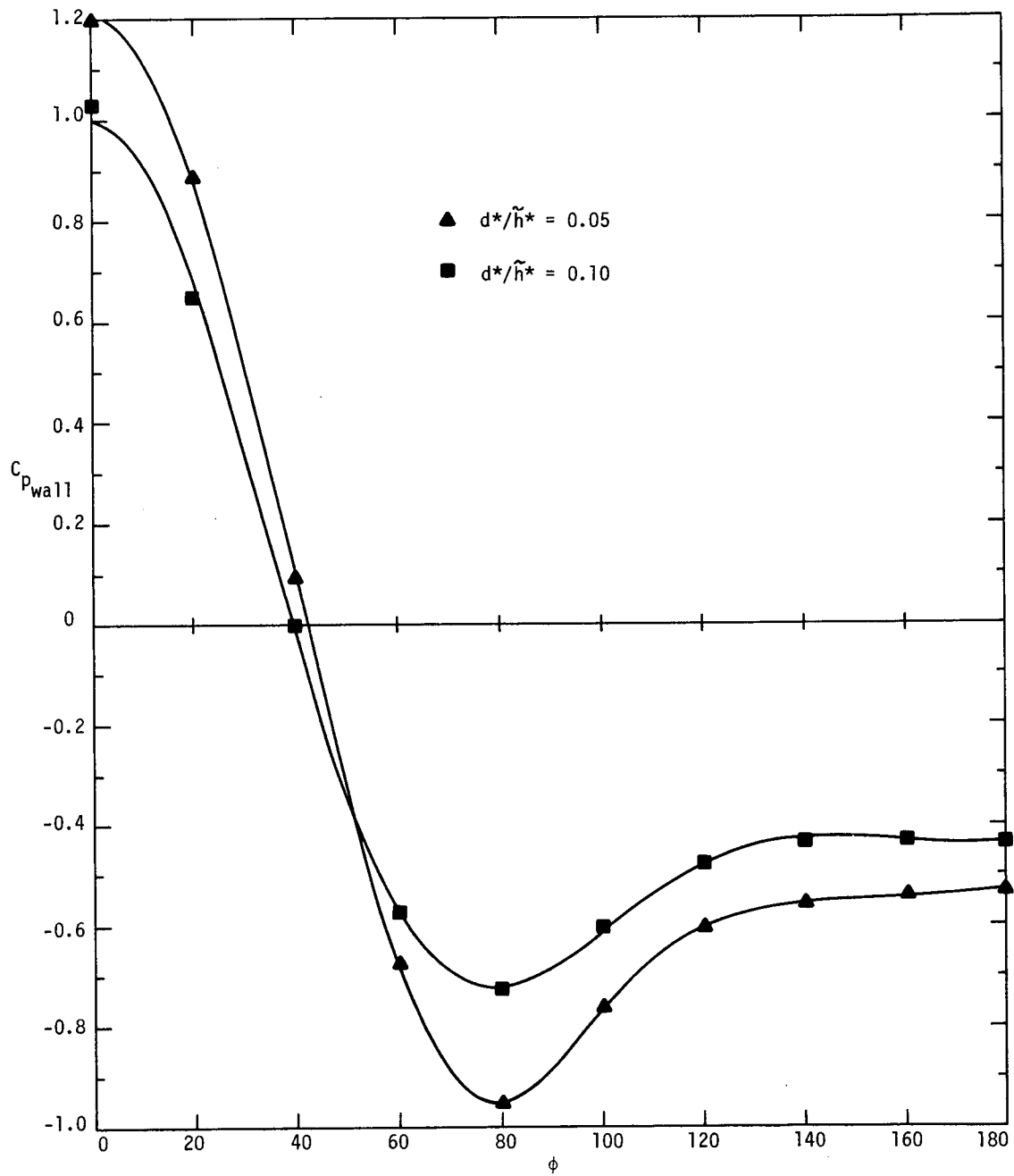


Figure 2.9 Test Tunnel Wall Effects on Experimental Pressure Data.

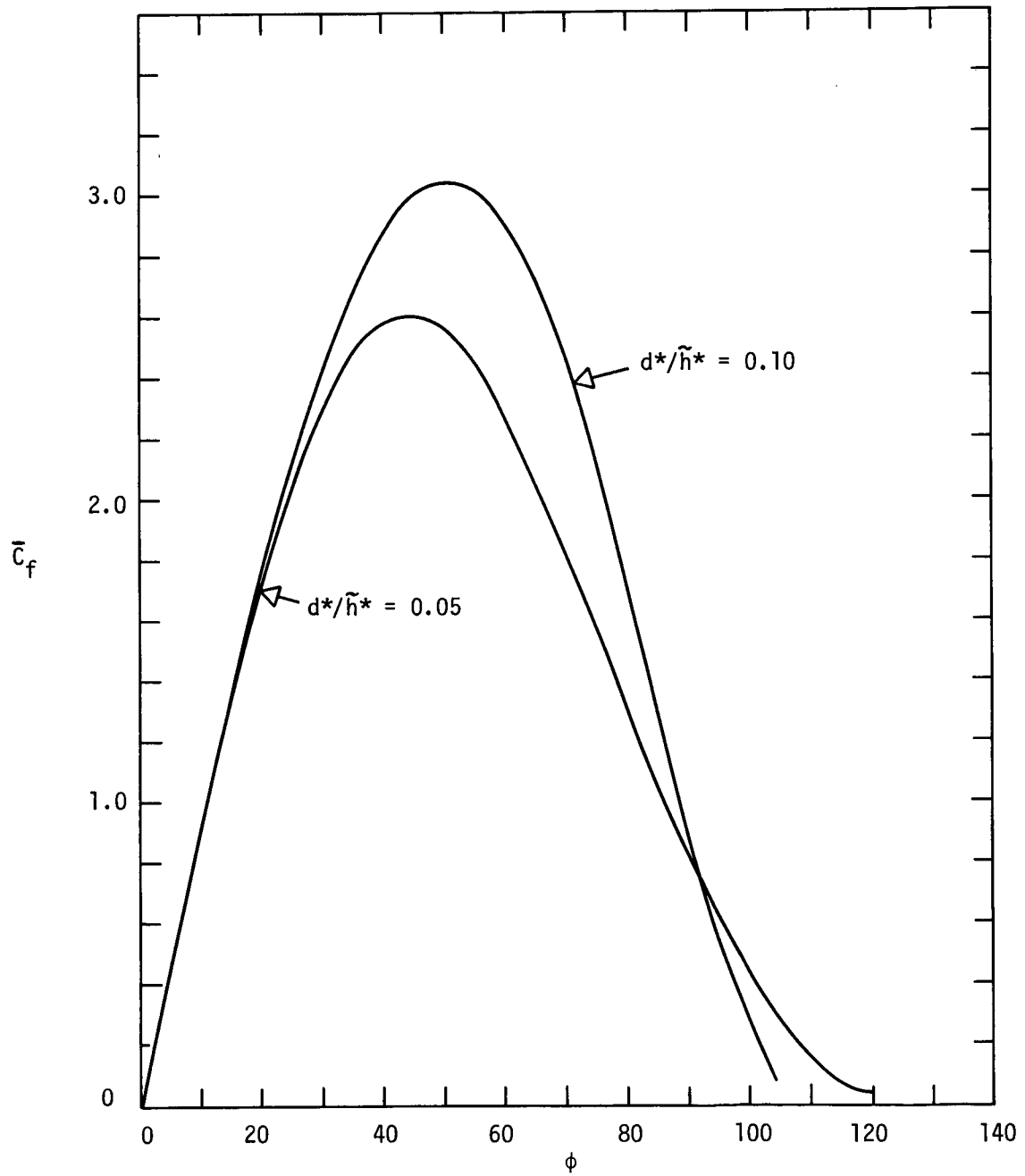


Figure 2.10 Test Tunnel Wall Effects on Computed Shear Stress Results.

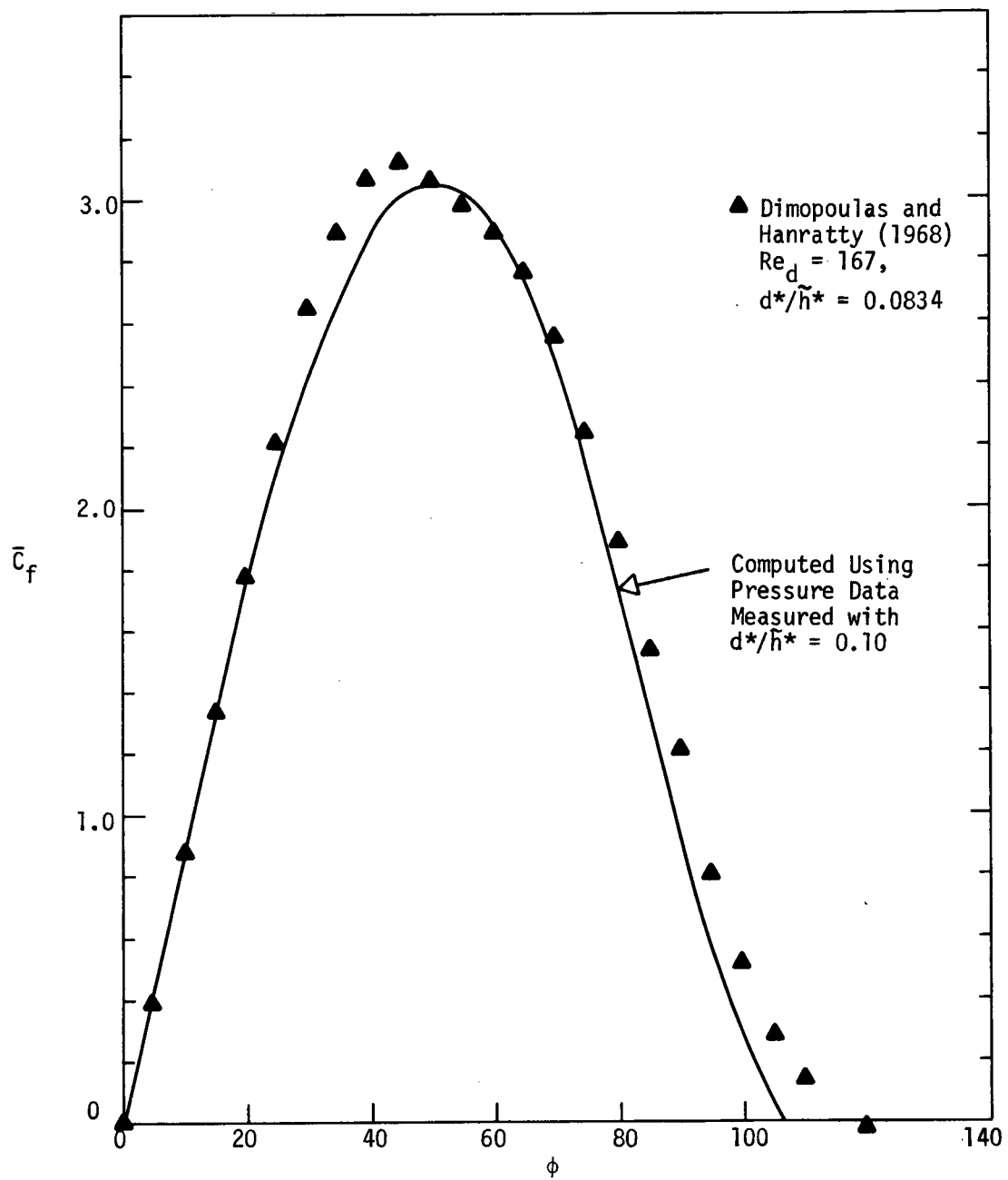


Figure 2.11 Comparison of Experimental and Numerical Shear Stress Distributions.

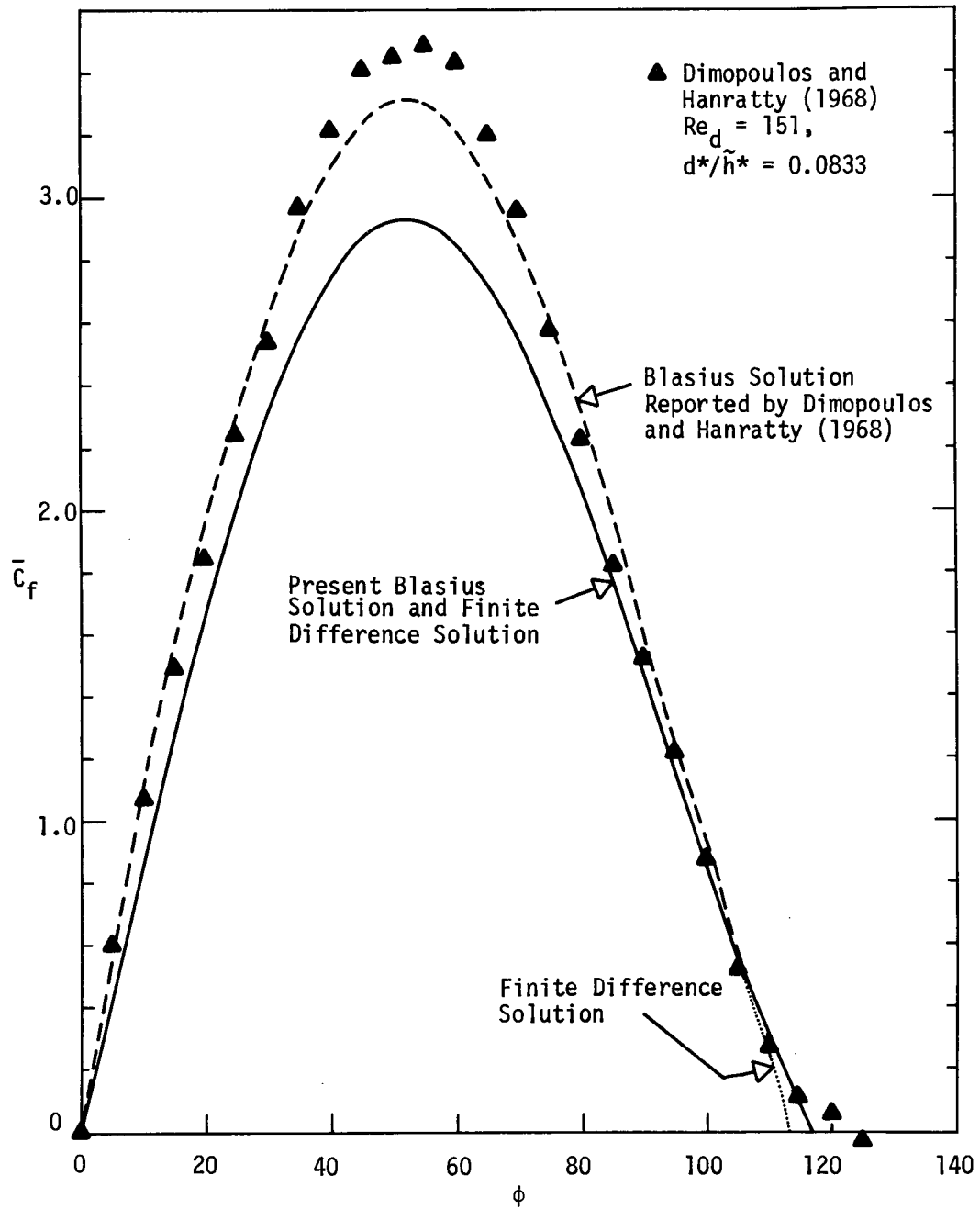


Figure 2.12 Comparison of Experimental and Analytical Shear Stress Distributions.

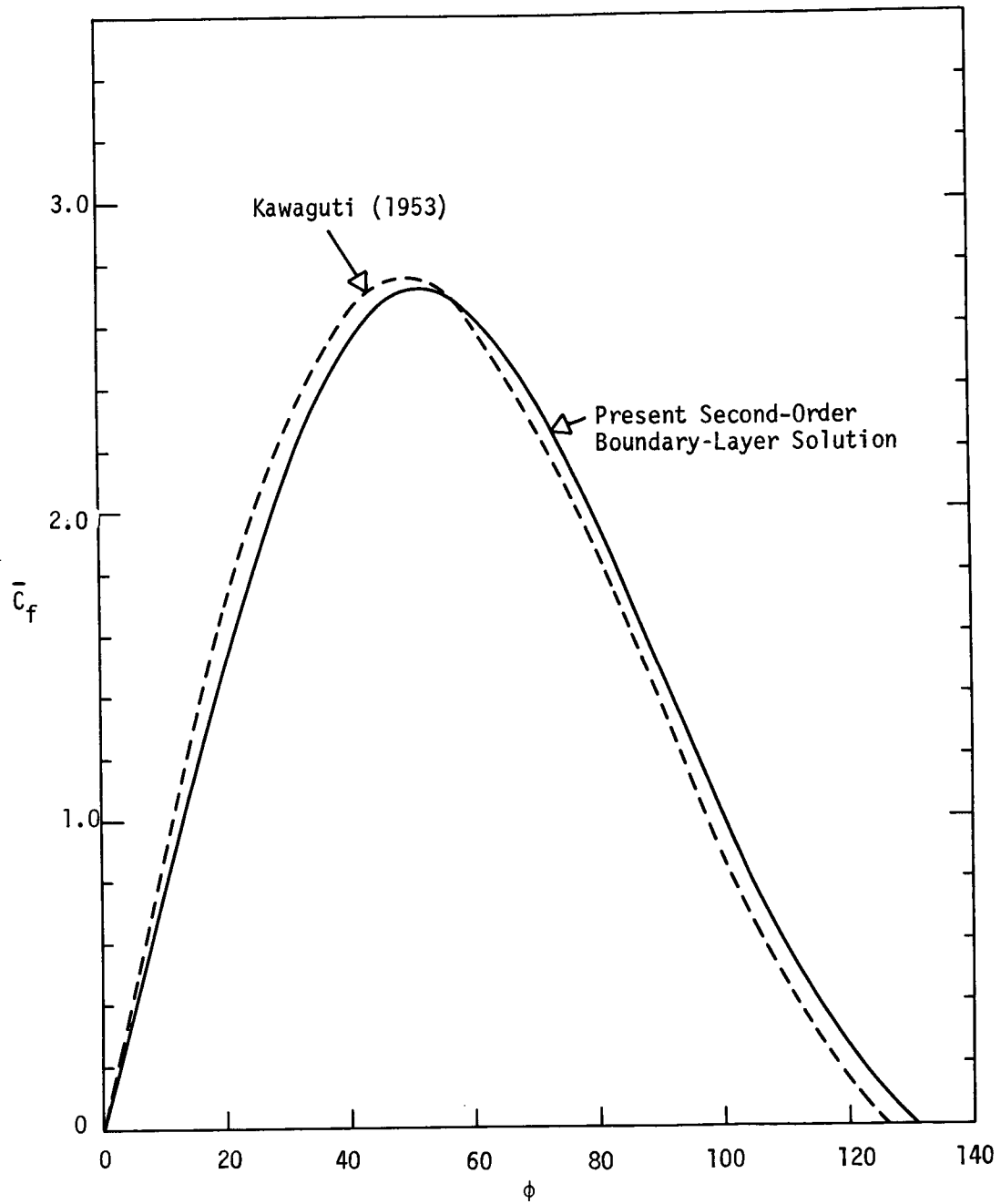


Figure 2.13 Comparison of Higher-Order Boundary Layer Solutions with Navier Stokes Solutions at $Re_d = 40$.

(K)

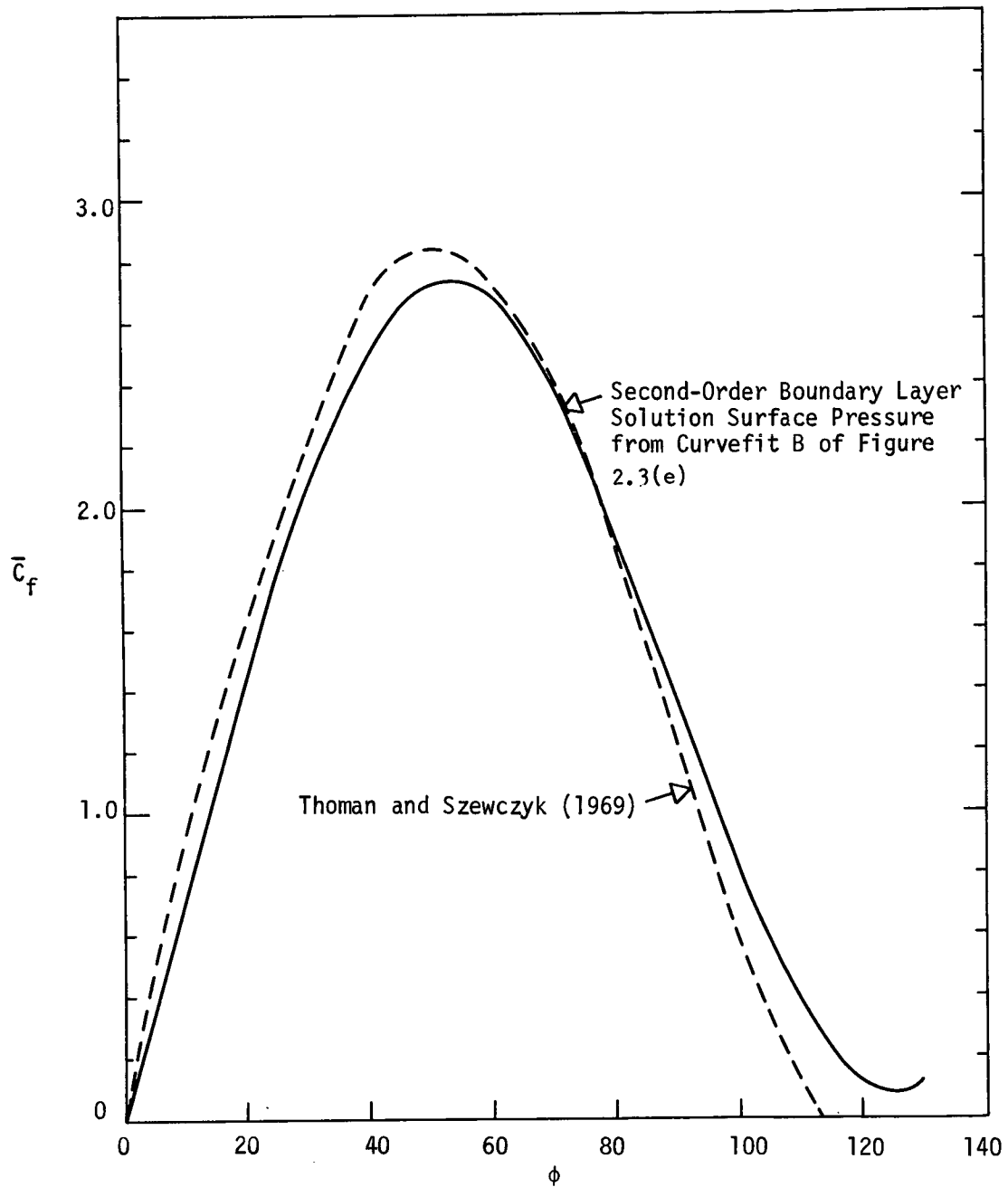


Figure 2.14 Comparison of Higher-Order Boundary-Layer Solutions with Navier Stokes Solutions at $Re_d = 200$.

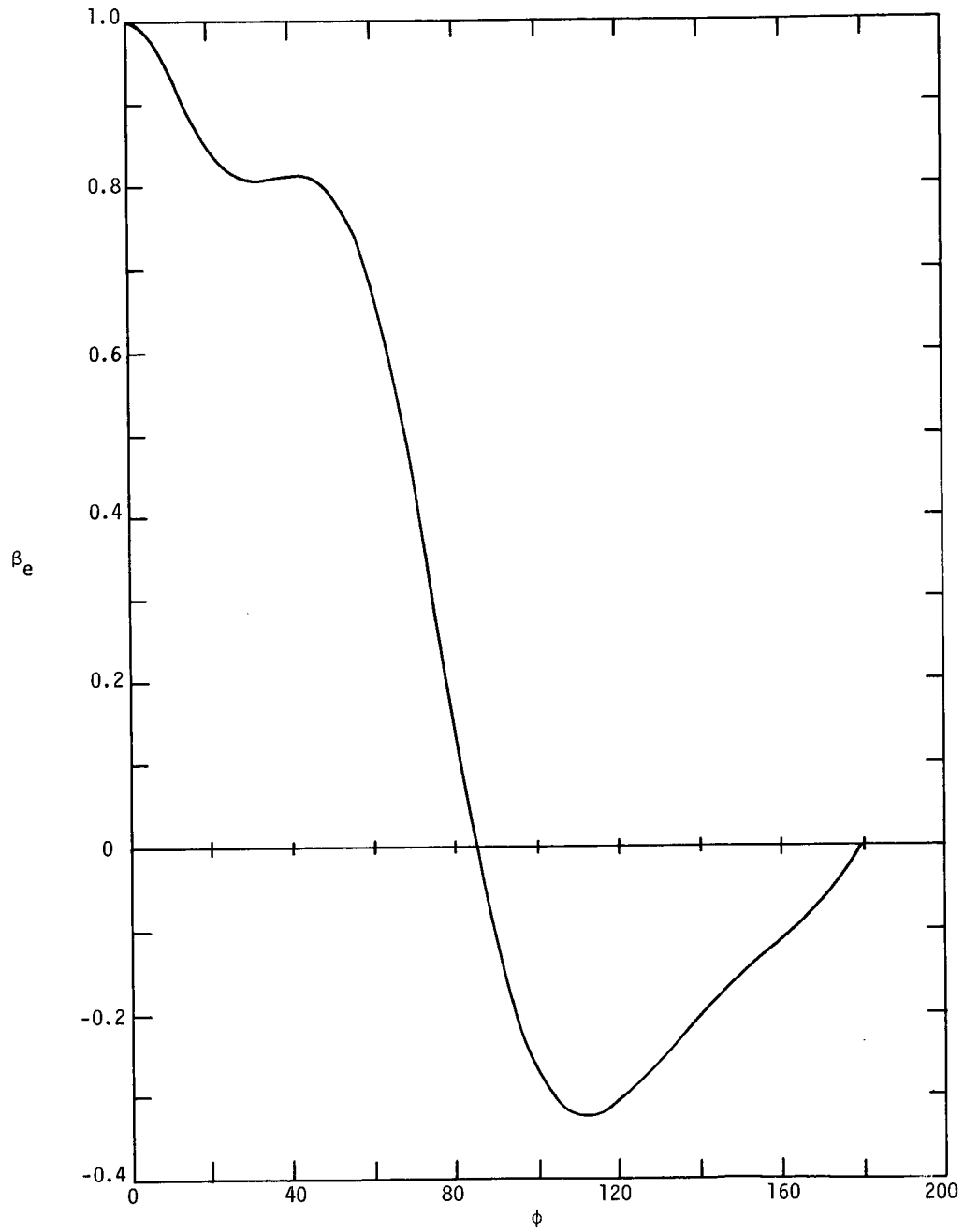


Figure 2.15 Inviscid Pressure Gradient Parameter Distribution Using Curvefit A at $Re_d = 200$.

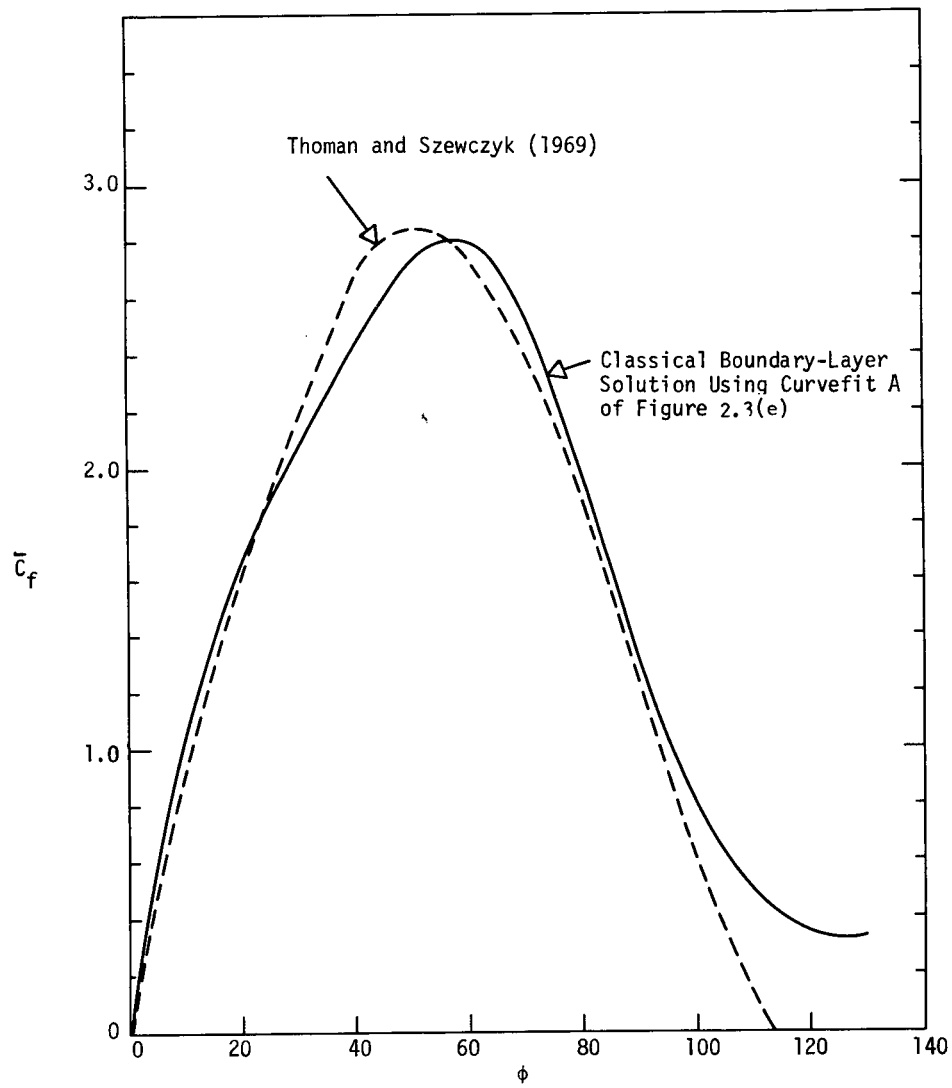


Figure 2.16 Shear Stress Distributions for Curvefit A at $Re_d = 200$.

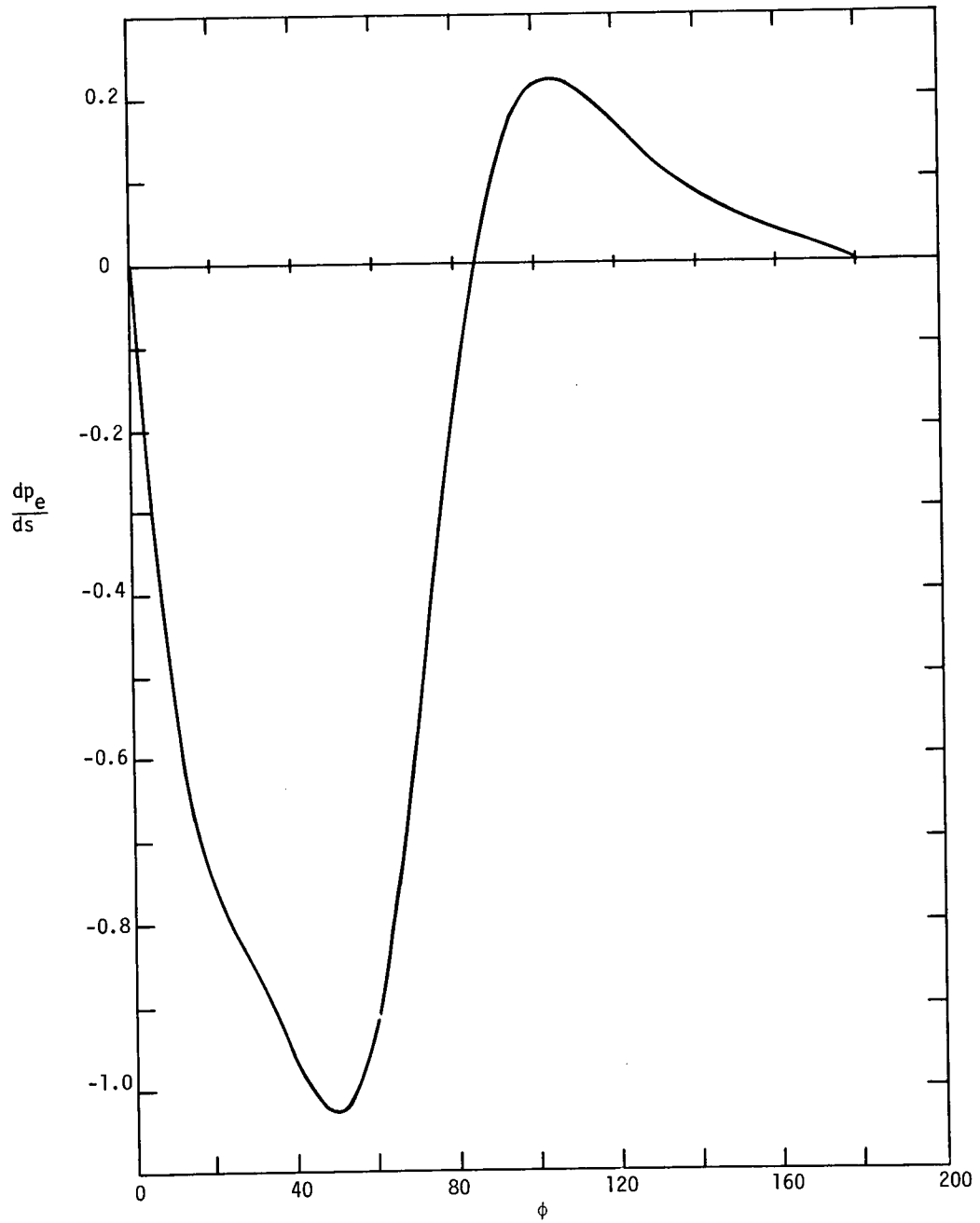


Figure 2.17 Inviscid Surface Pressure Gradient Distribution for Curvefit A at $Re_d = 200$.

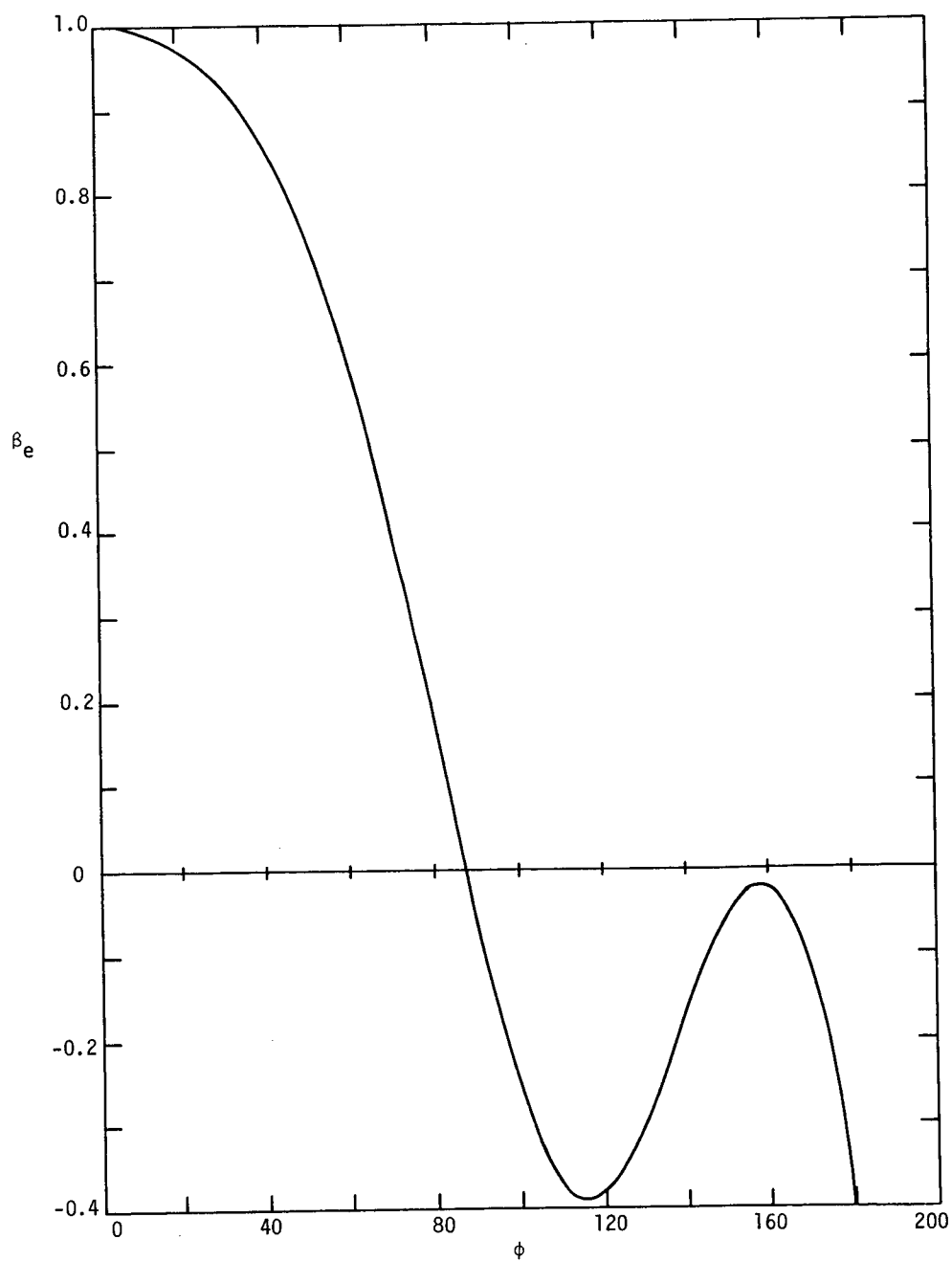


Figure 2.18 Inviscid Pressure Gradient Parameter Distribution Using Curvefit B at $Re_d = 200$.

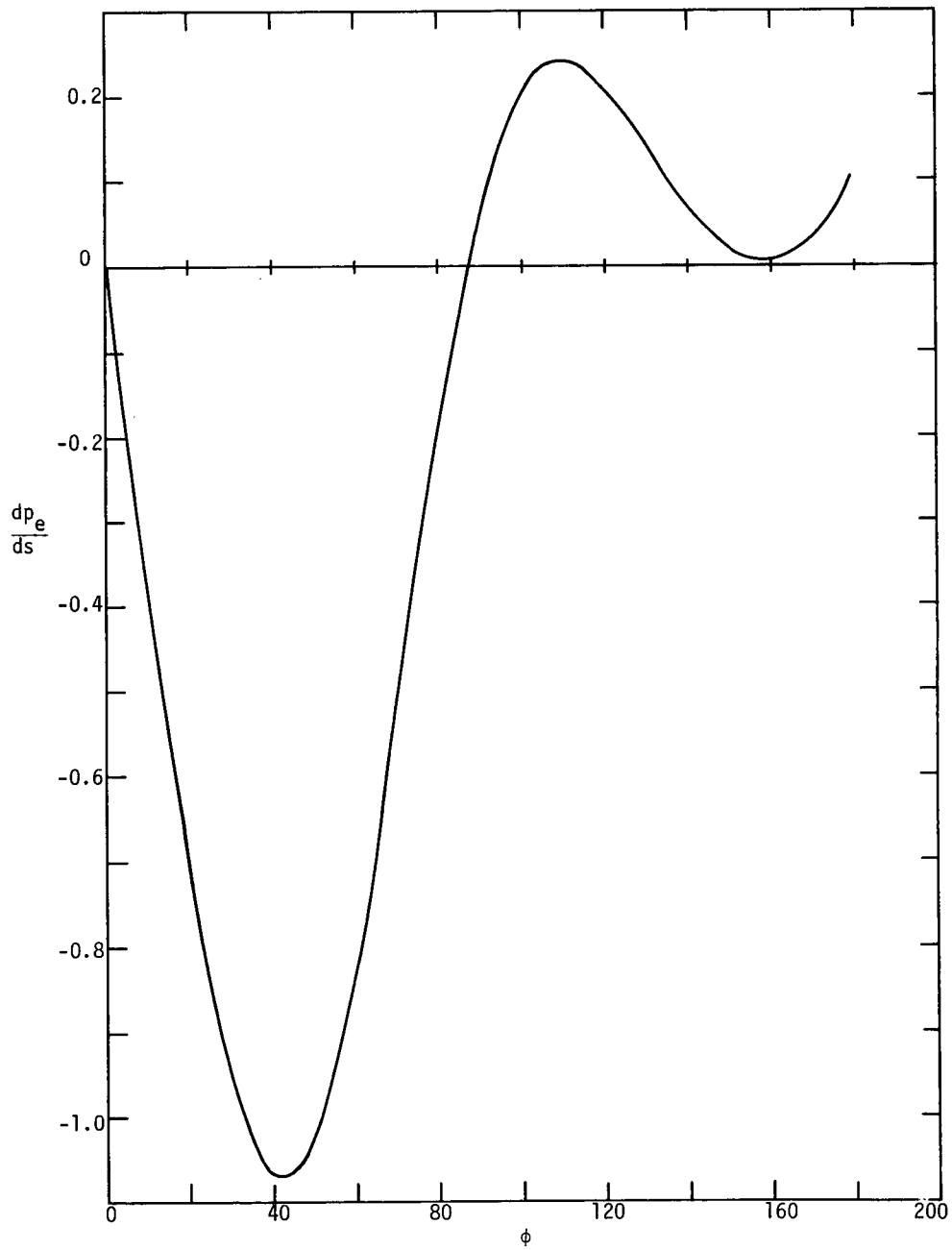


Figure 2.19 Inviscid Surface Pressure Gradient Distribution for Curvefit B at $Re_d = 200$.

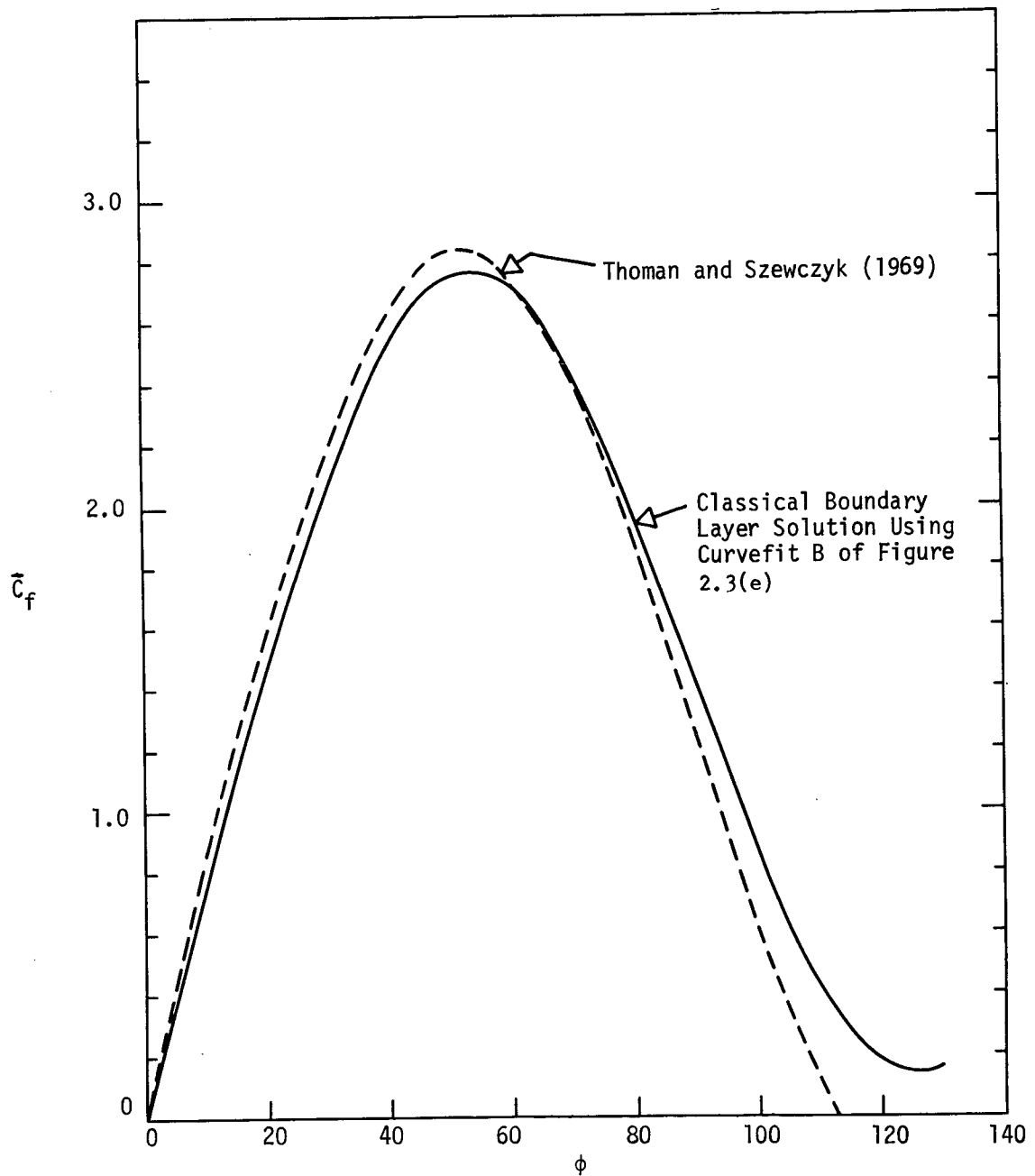


Figure 2.20 Shear Stress Distribution for Curvefit B at $Re_d = 200$.

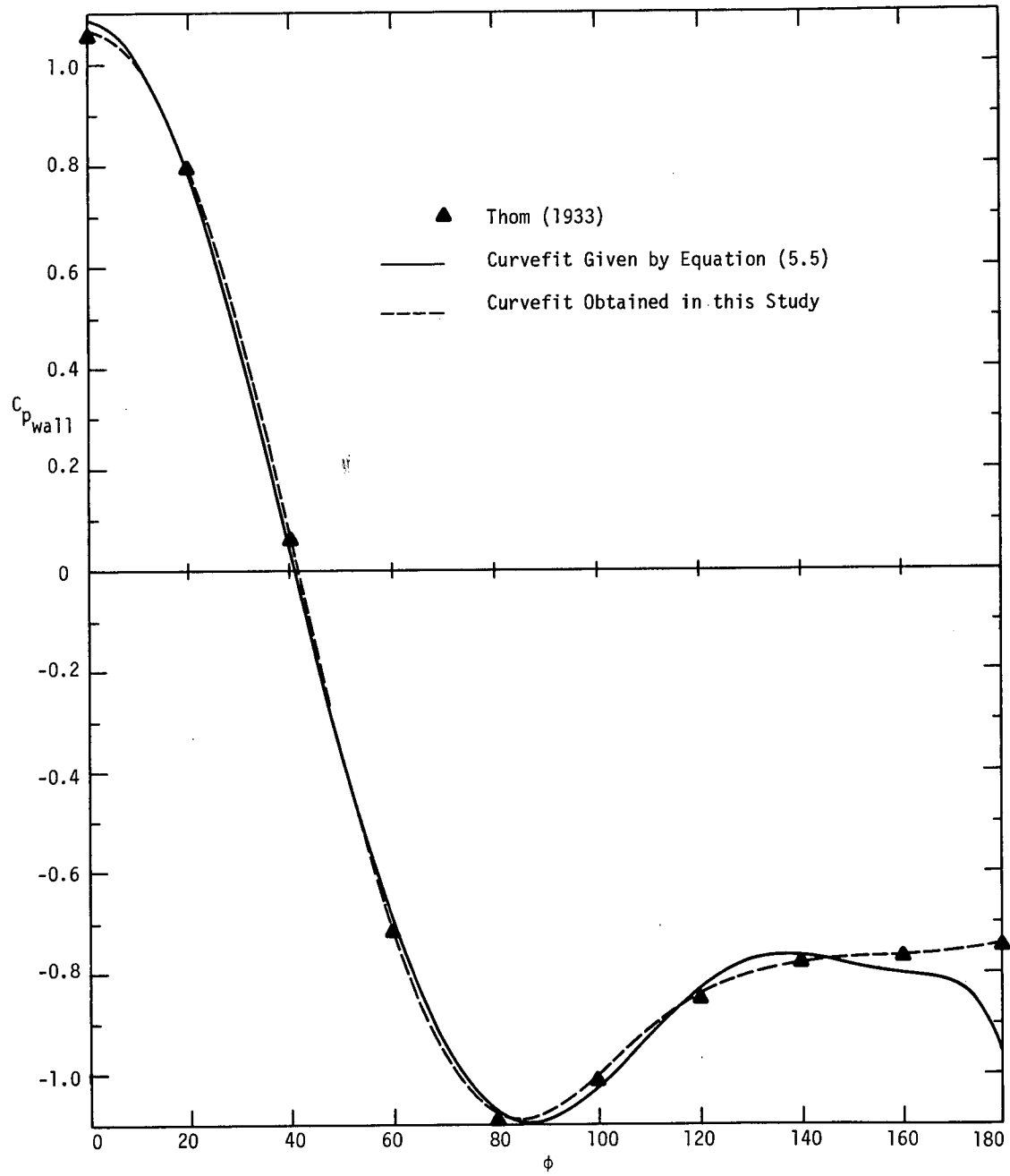


Figure 2.21 Comparison of Wall Pressure Curvefits to Experimental Data at $Re_d = 174$.

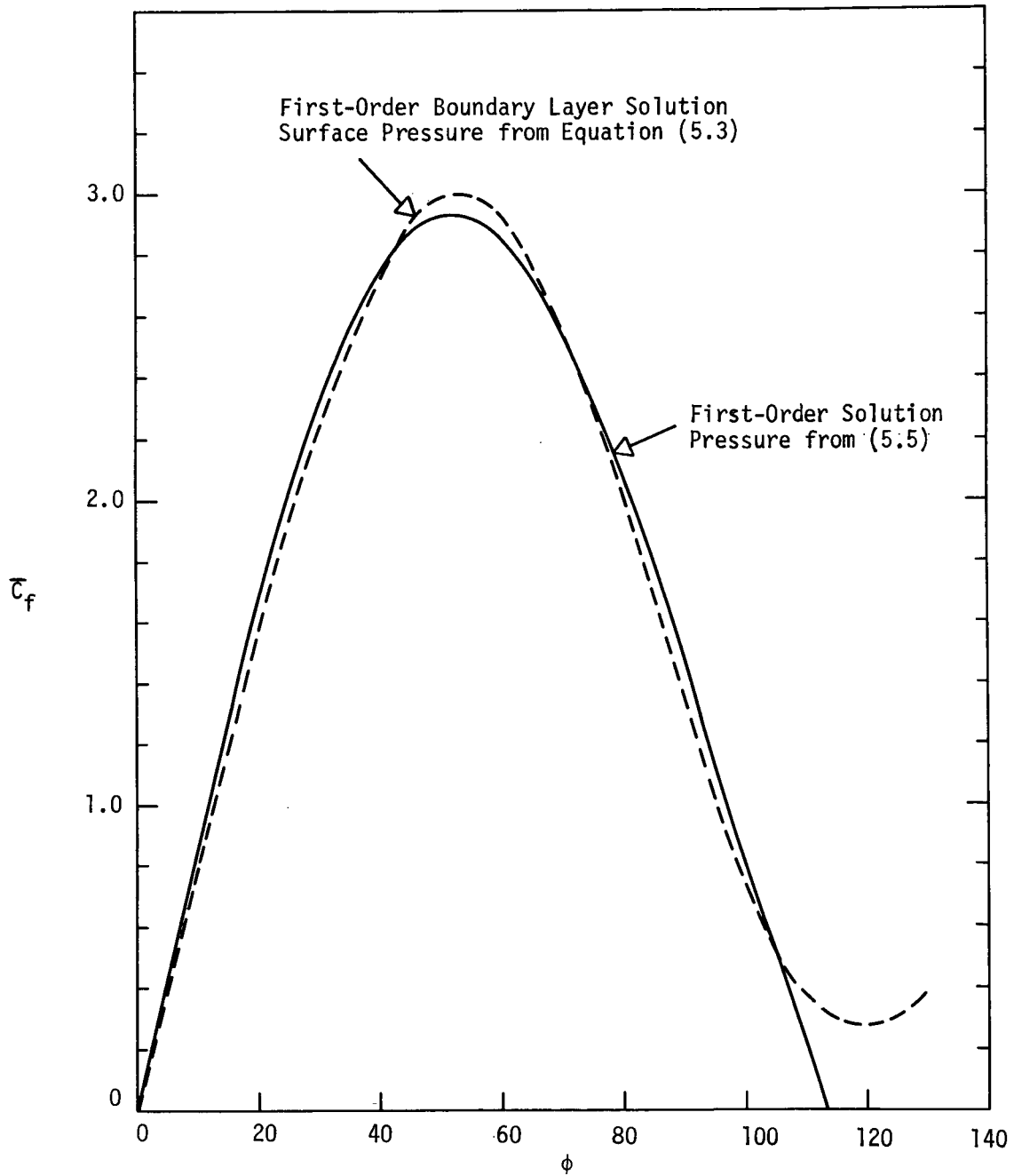


Figure 2.22 Effect of Wall Pressure Curvefits on Surface Shear Stress at $Re_d = 174$.

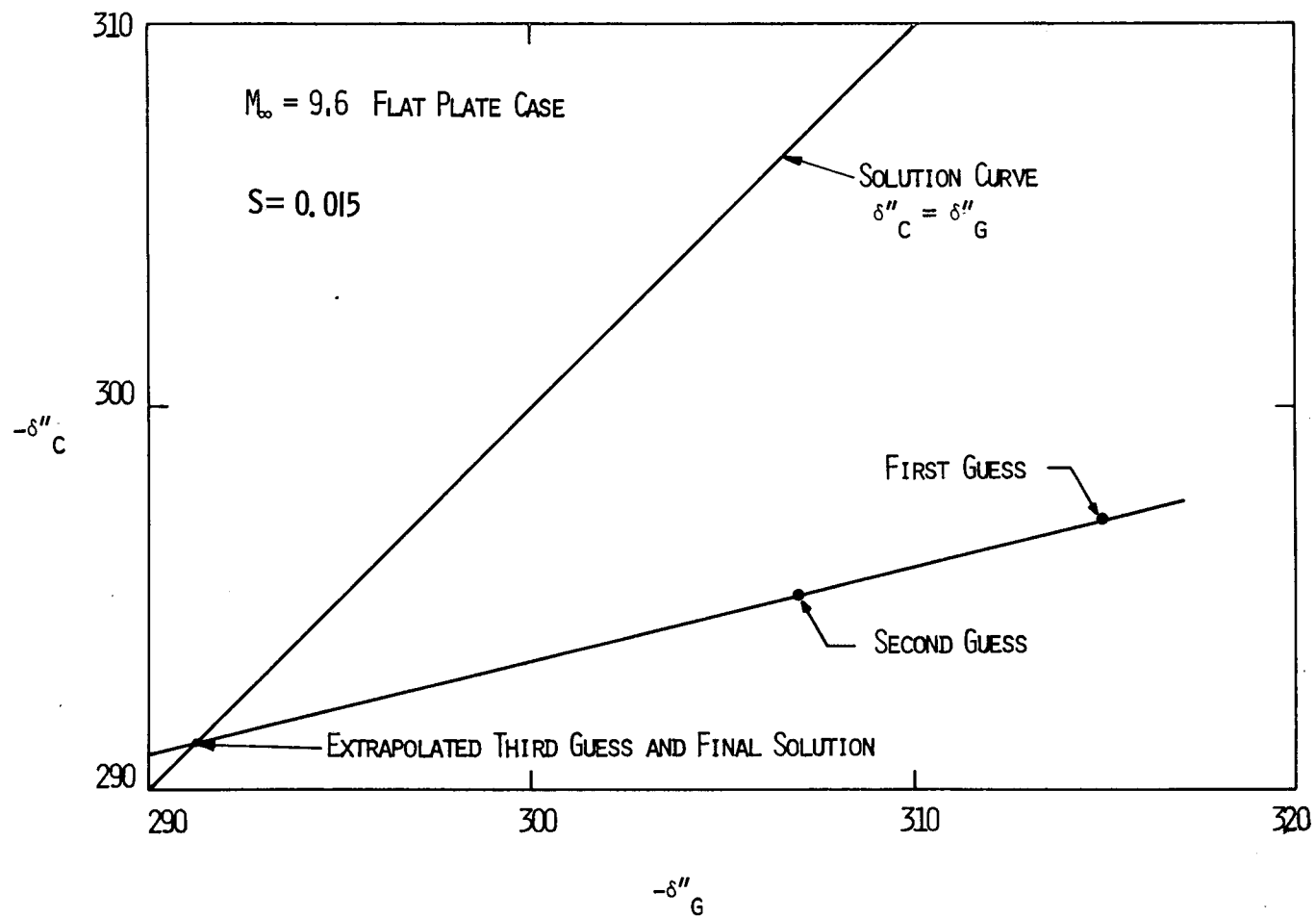


FIGURE 3.1 VARIATION OF ASSUMED AND CALCULATED VALUES OF δ''

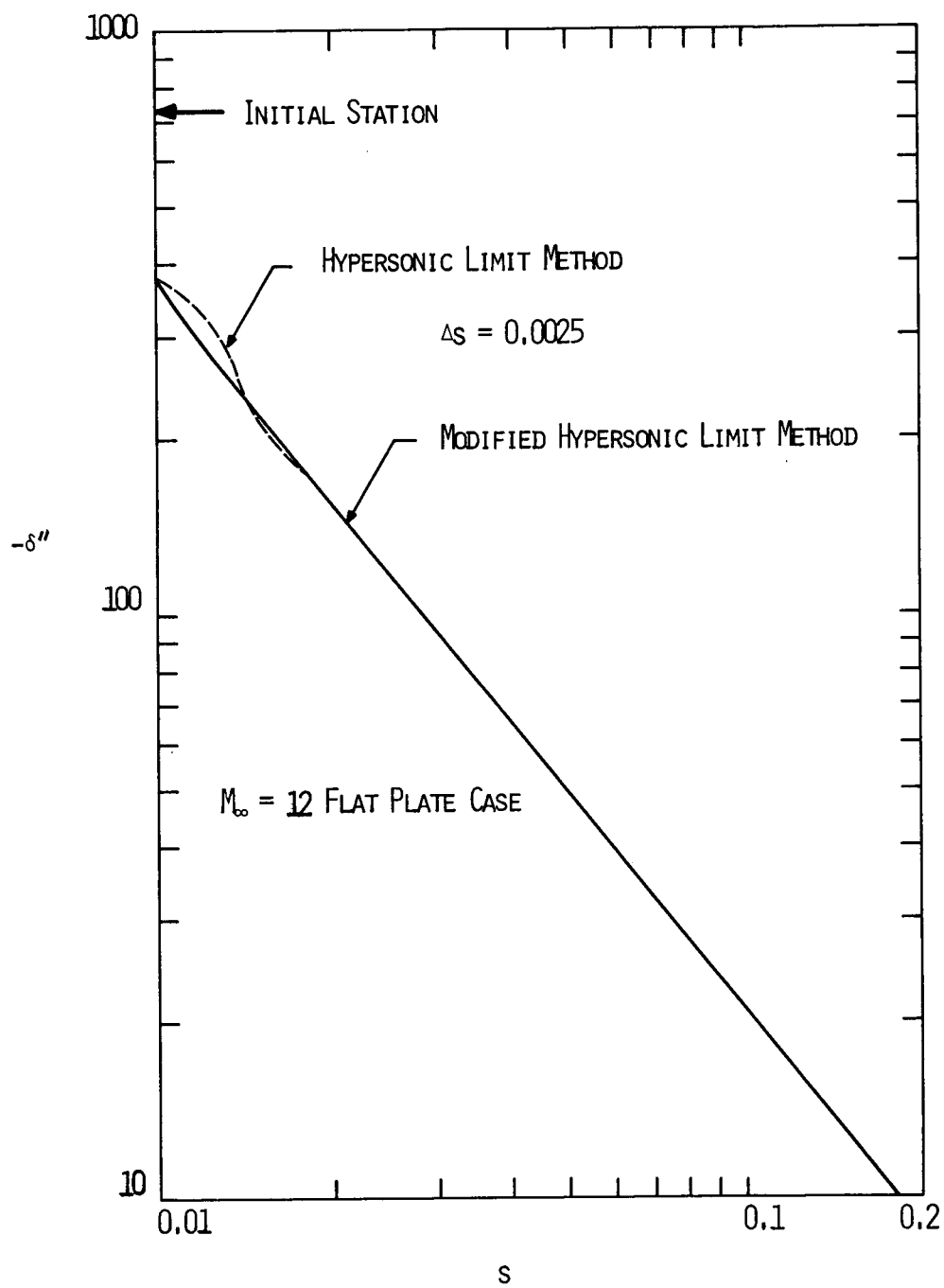


FIGURE 3.2 INFLUENCE OF INITIAL PROFILES ON δ''

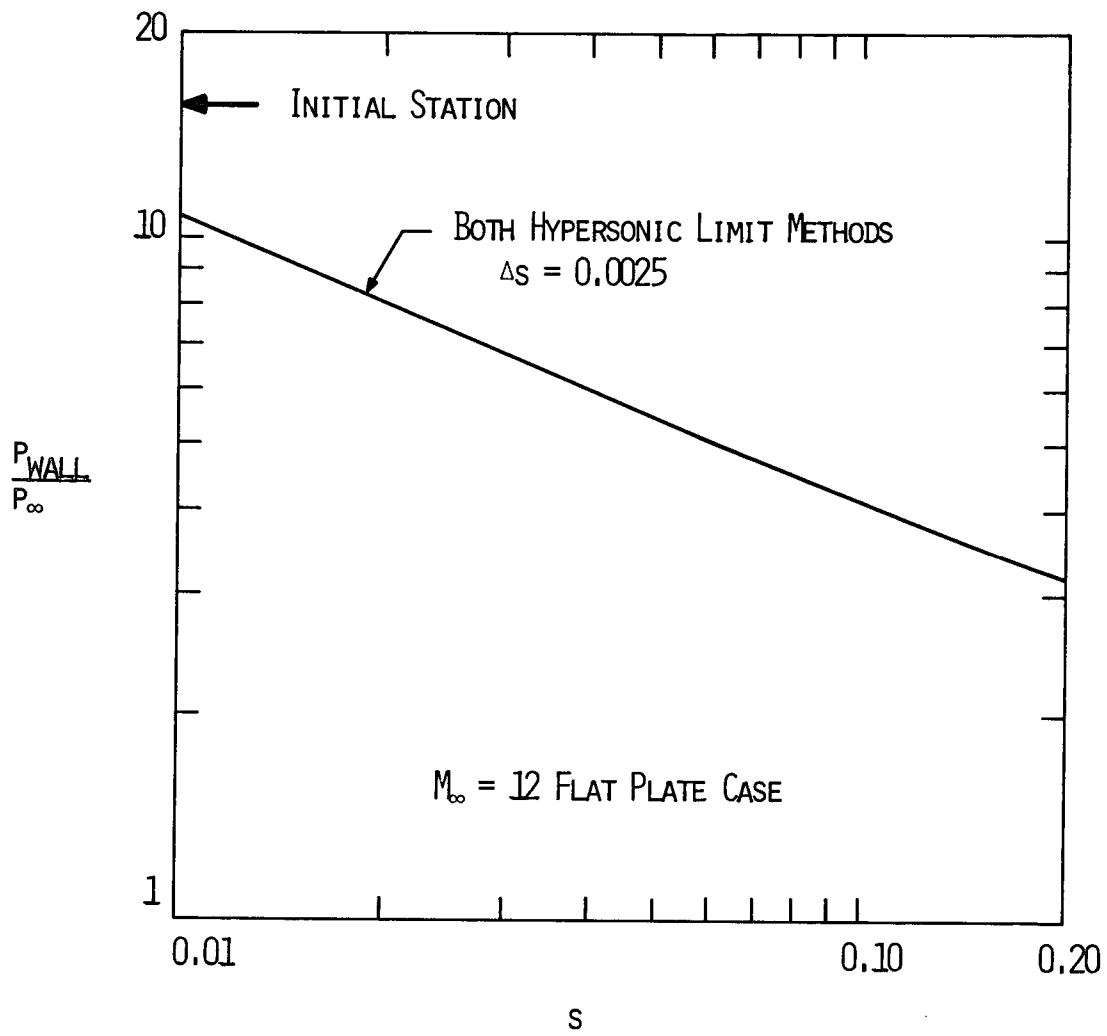


FIGURE 3.3 INFLUENCE OF INITIAL PROFILES ON WALL PRESSURE

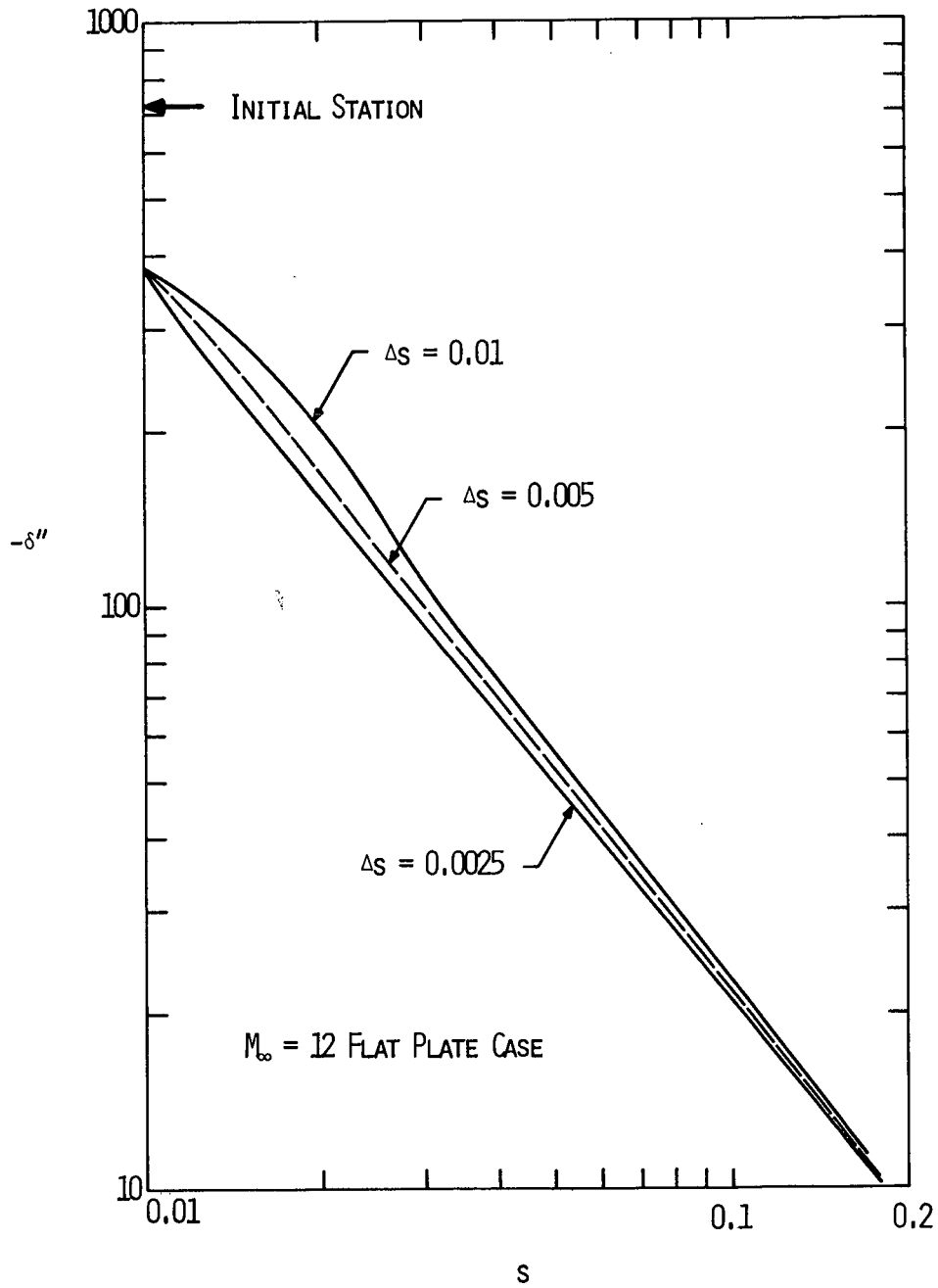


FIGURE 3.4 EFFECT OF STEP SIZE ON FLAT PLATE
LEADING EDGE SOLUTION

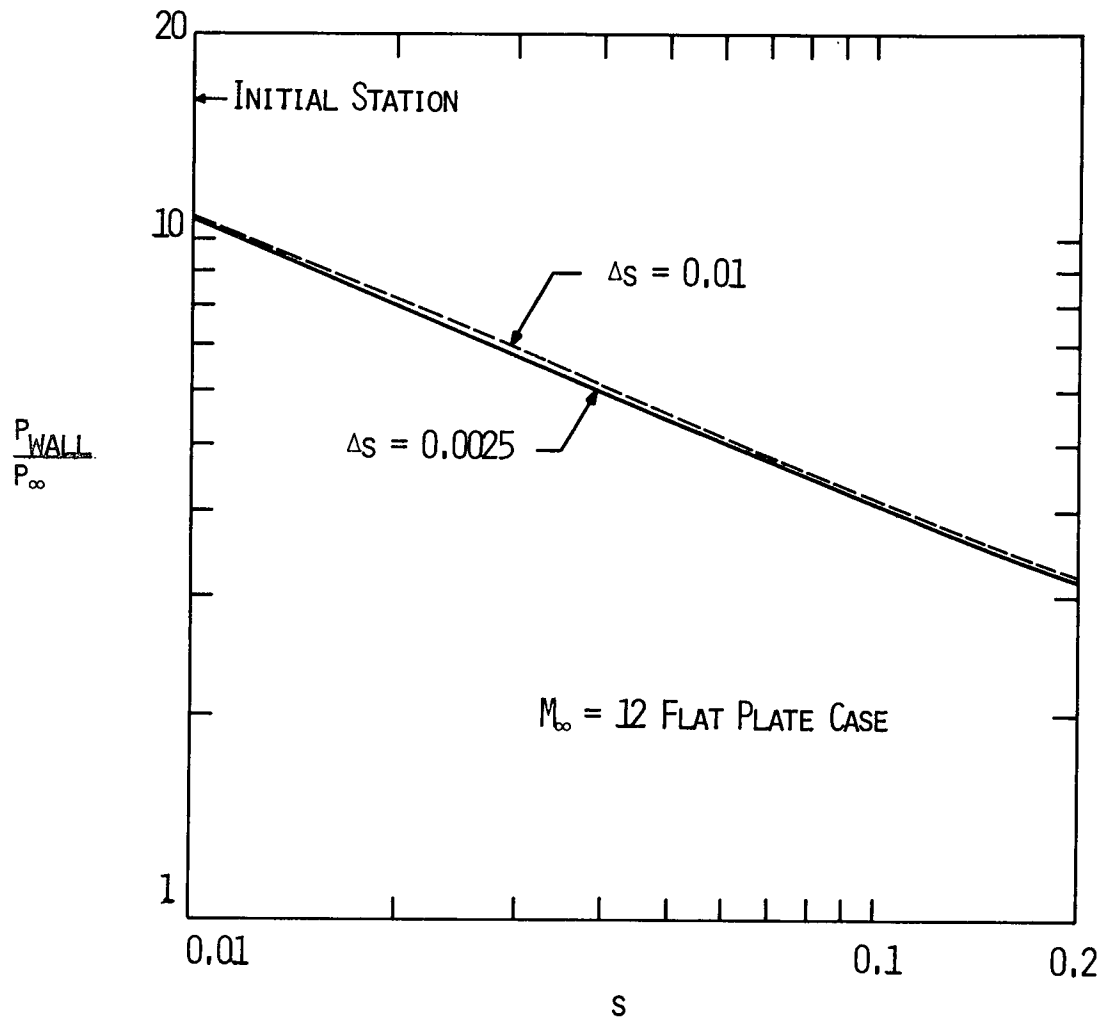


FIGURE 3.5 EFFECT OF STEP SIZE ON WALL PRESSURE

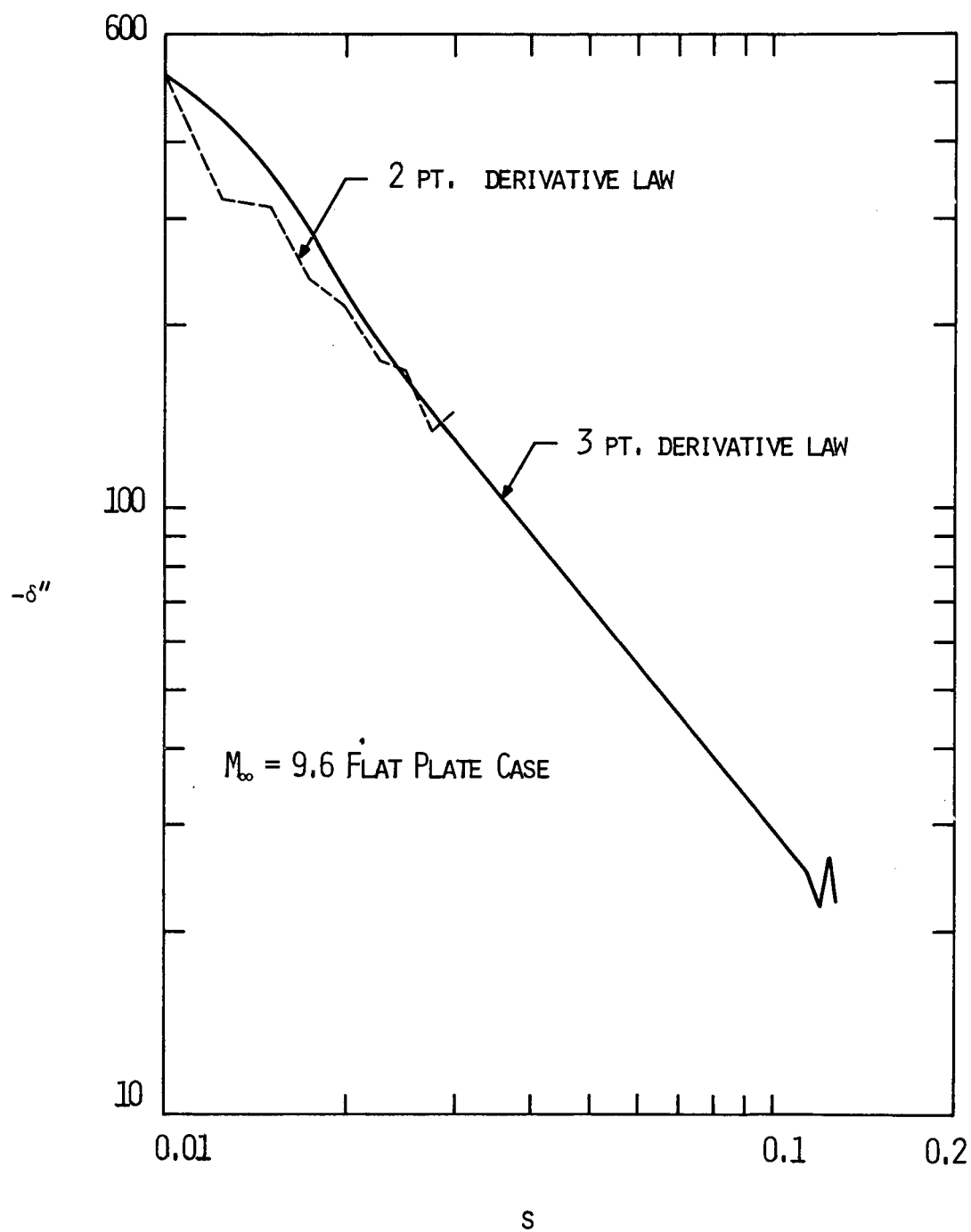


FIGURE 3.6 THE EFFECT OF DERIVATIVE LAWS ON OSCILLATORY BEHAVIOR

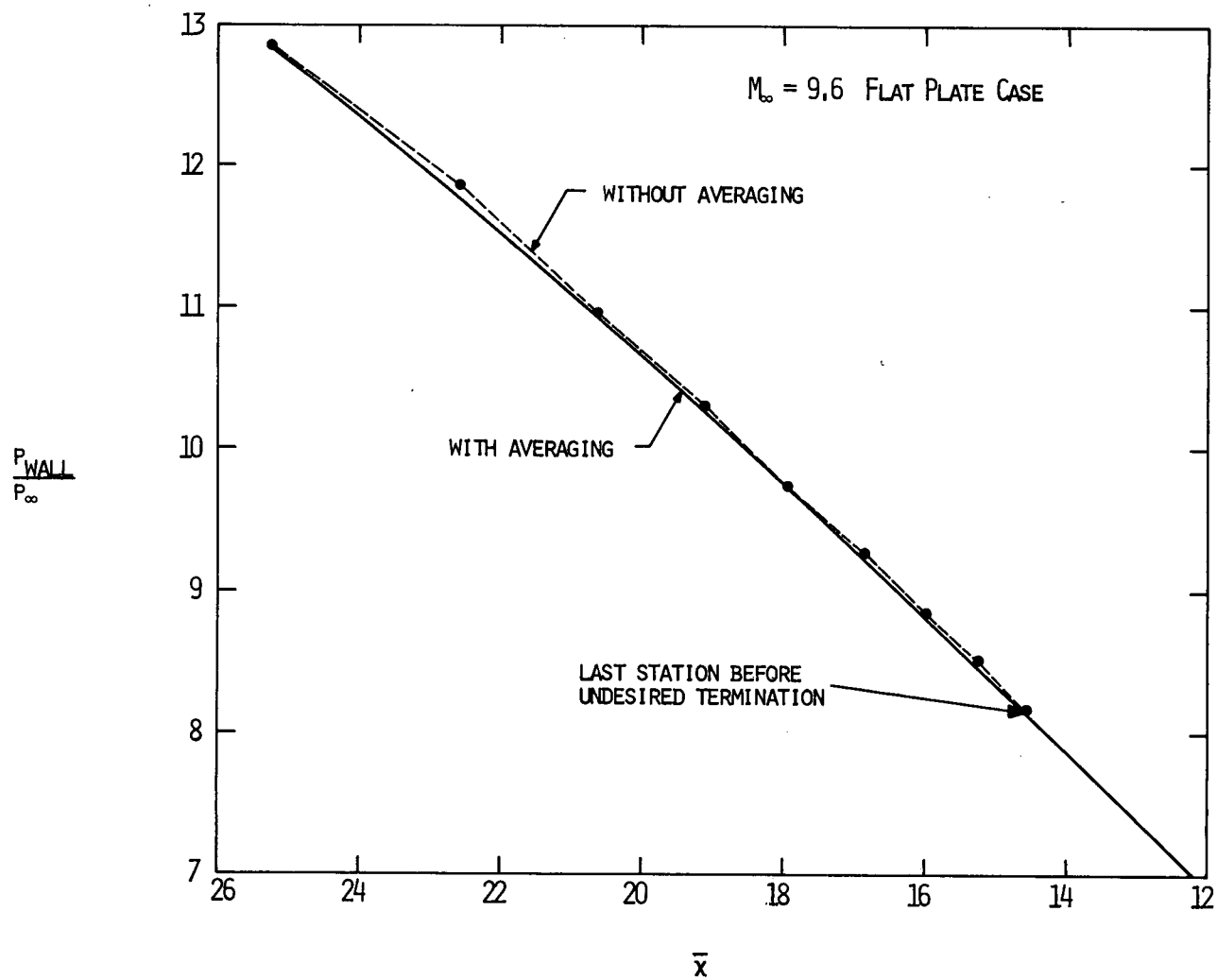


FIGURE 3.7 EFFECT OF AVERAGING V PROFILES ON WALL PRESSURE

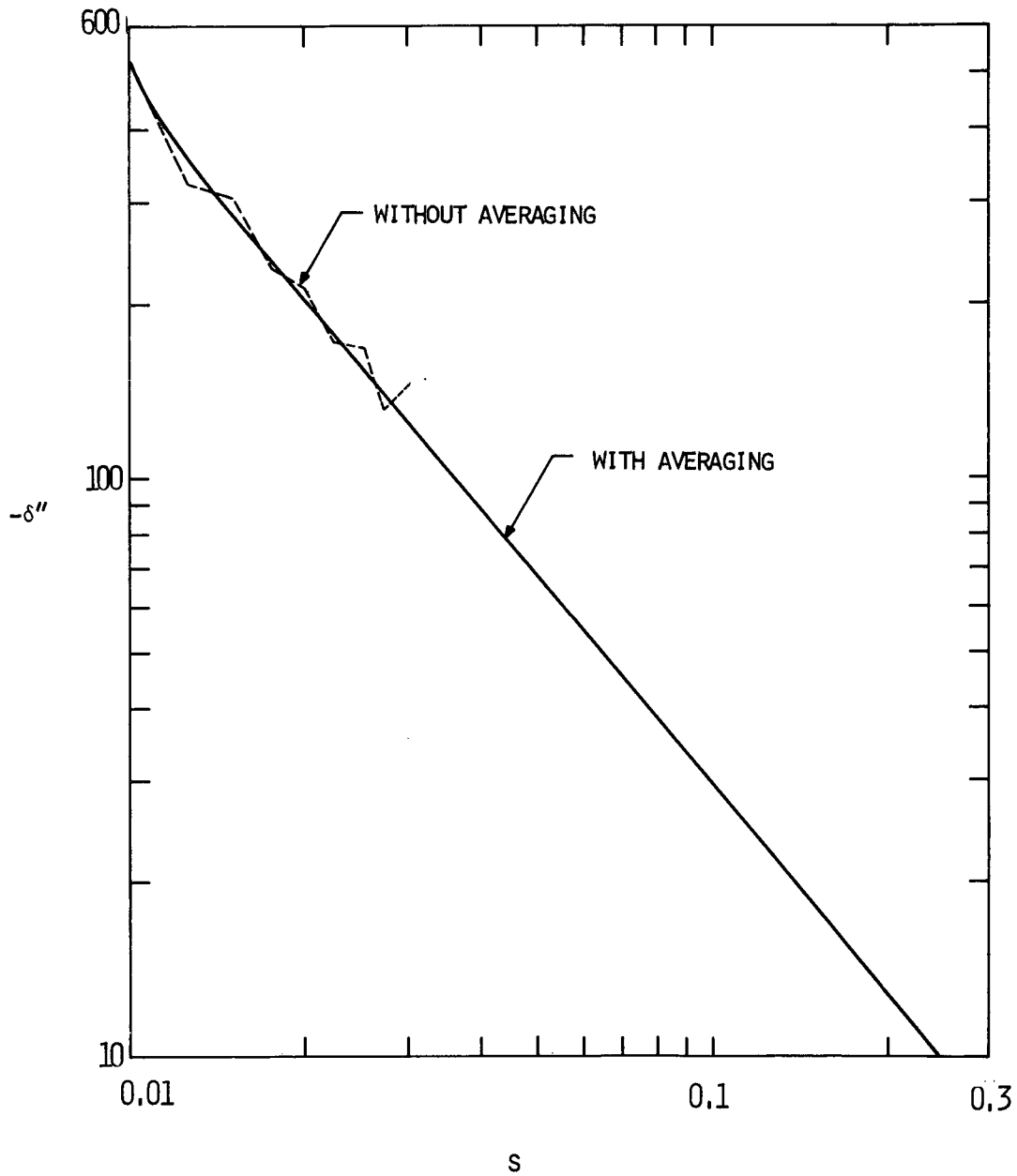


FIGURE 3.8 INFLUENCE OF AVERAGING THE NORMAL VELOCITY FOR THE $M_\infty = 9.6$ FLAT PLATE CASE

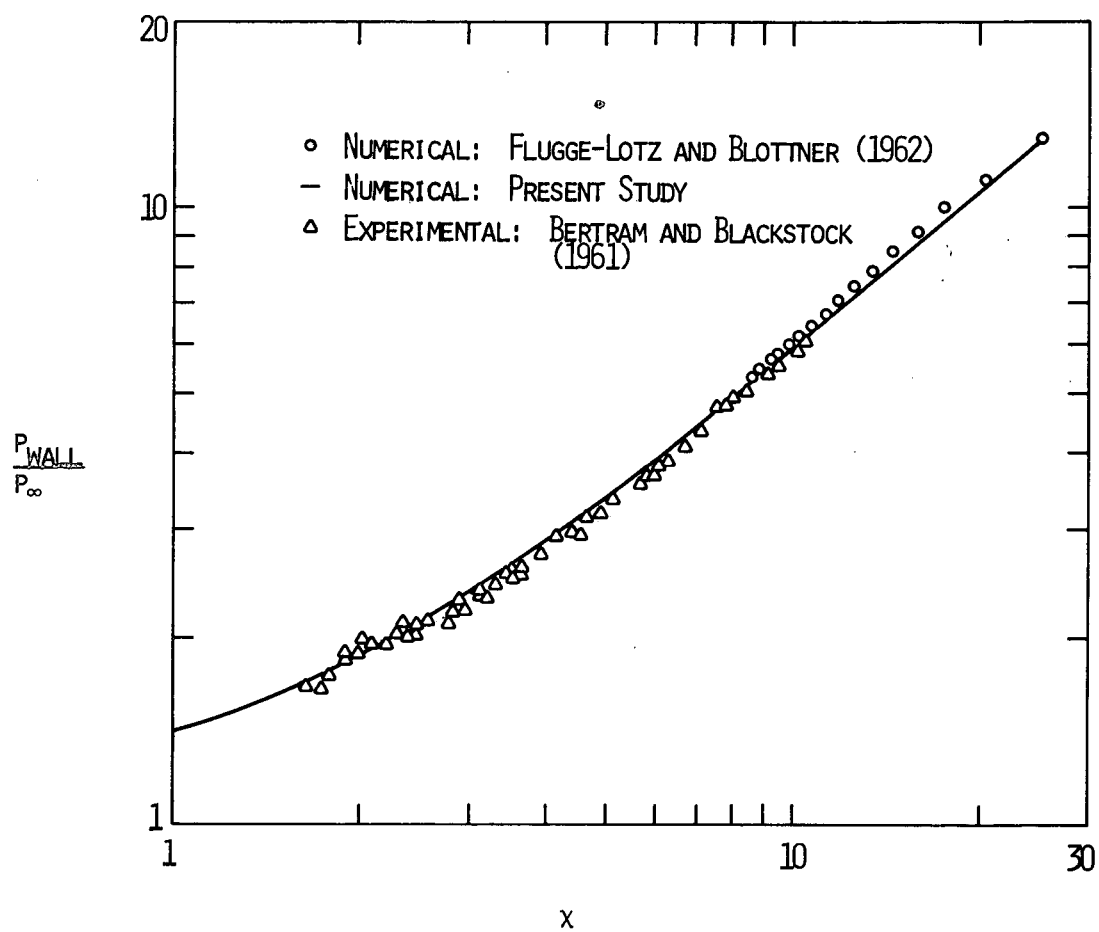


FIGURE 3.9 INDUCED PRESSURE ON NEARLY INSULATED FLAT PLATE AT $M_{\infty} = 9.6$

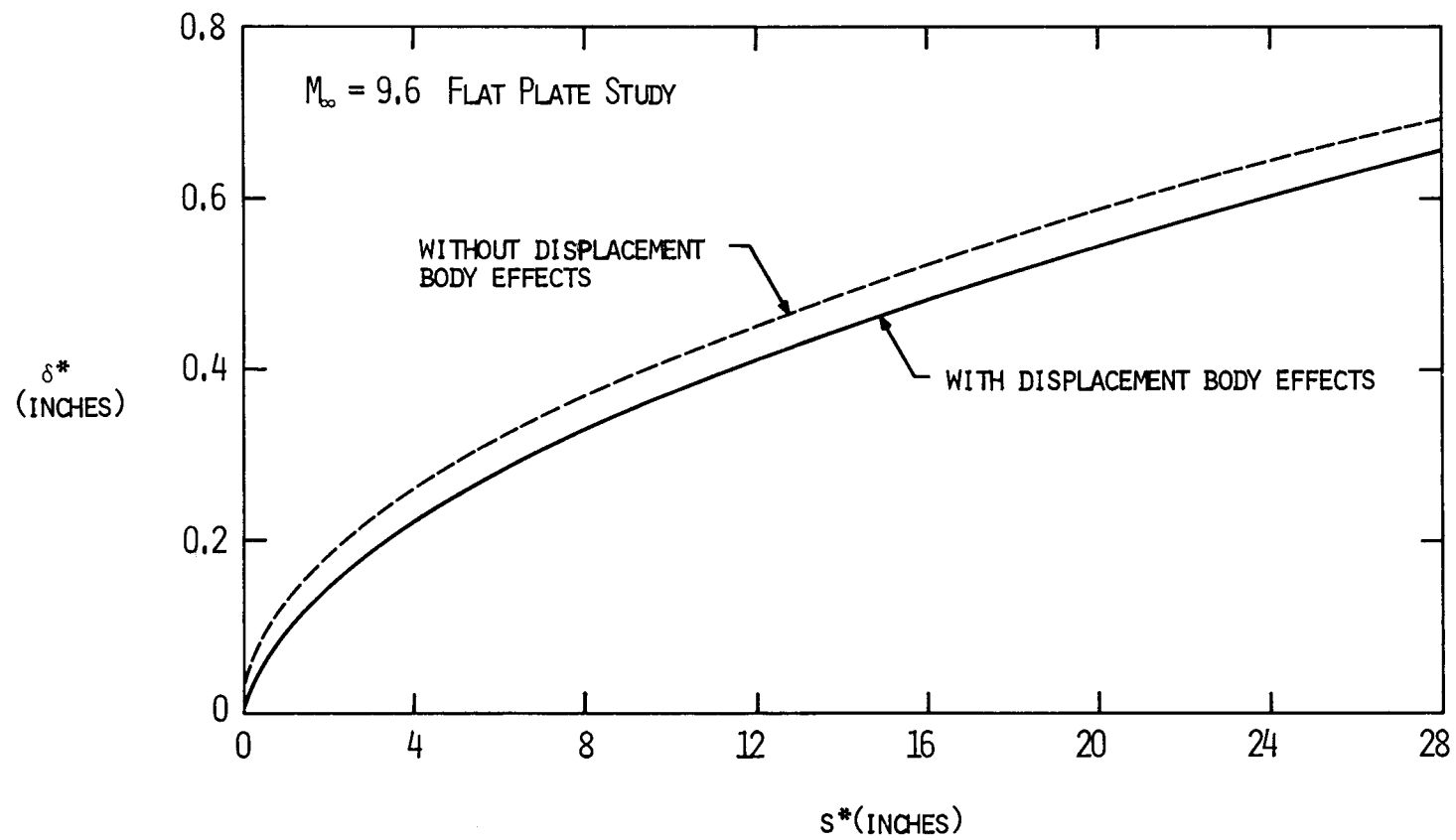


FIGURE 3.10 DISPLACEMENT BODY EFFECTS ON FLAT PLATE DISPLACEMENT THICKNESS

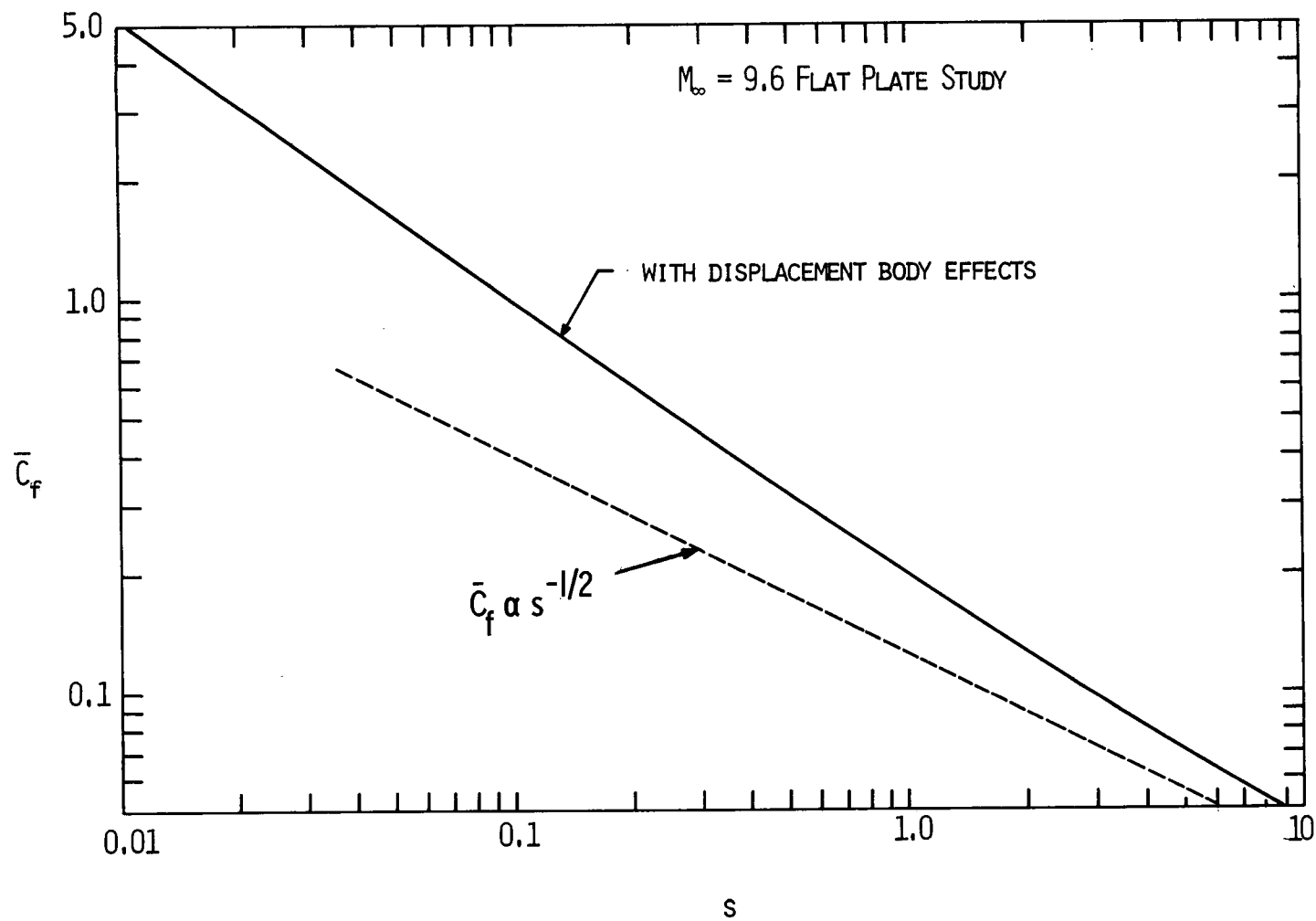


FIGURE 3.11 DISPLACEMENT BODY EFFECT ON FLAT PLATE SKIN FRICTION

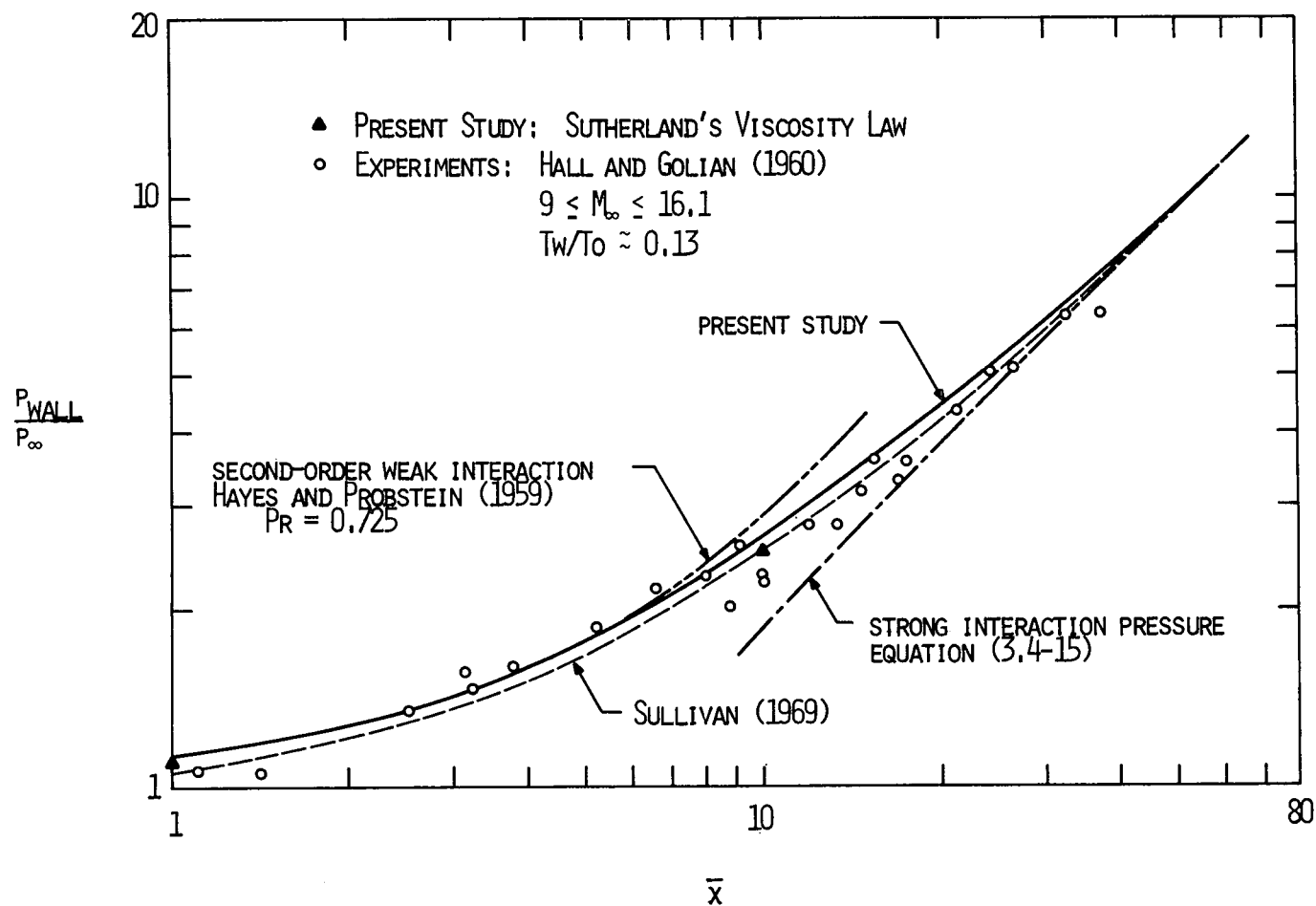


FIGURE 3.12 INDUCED PRESSURE ON A FLAT PLATE AT $M_{\infty} = 12$

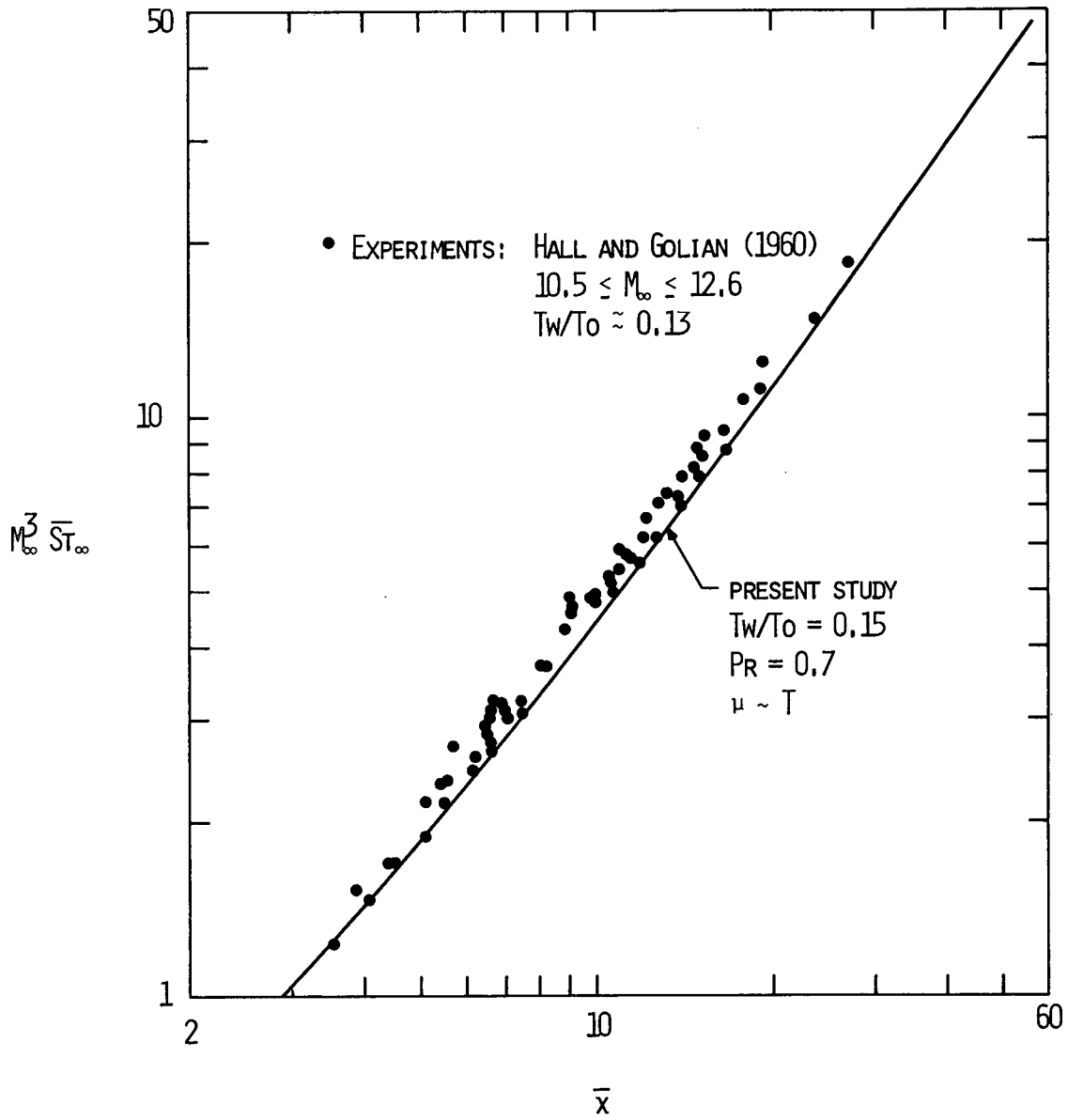


FIGURE 3.13 COMPARISON OF THEORY WITH EXPERIMENT -
 HYPERSONIC FLAT PLATE HEAT TRANSFER DISTRIBUTION

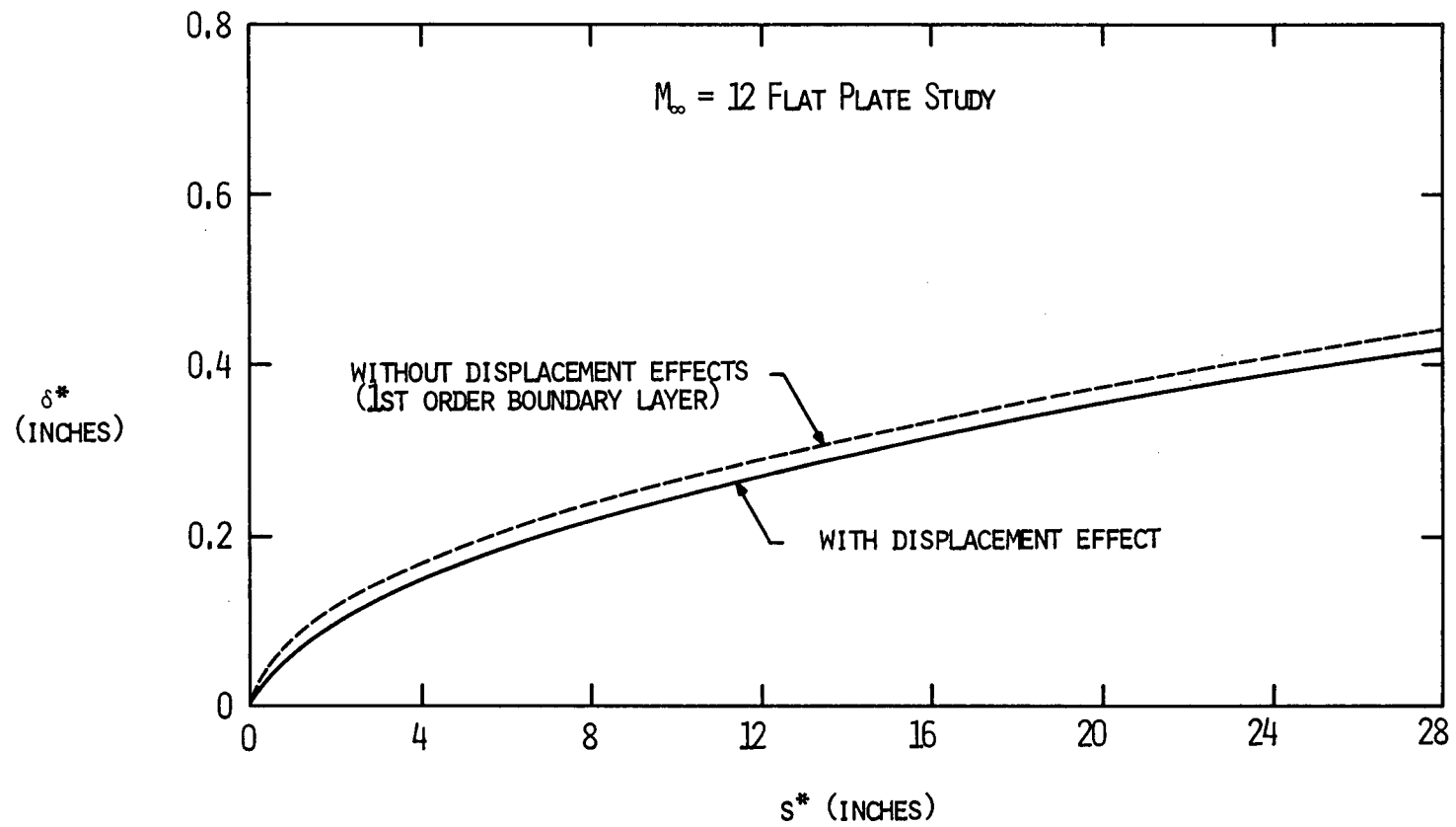


FIGURE 3.14 DISPLACEMENT BODY EFFECTS ON FLAT PLATE DISPLACEMENT THICKNESS

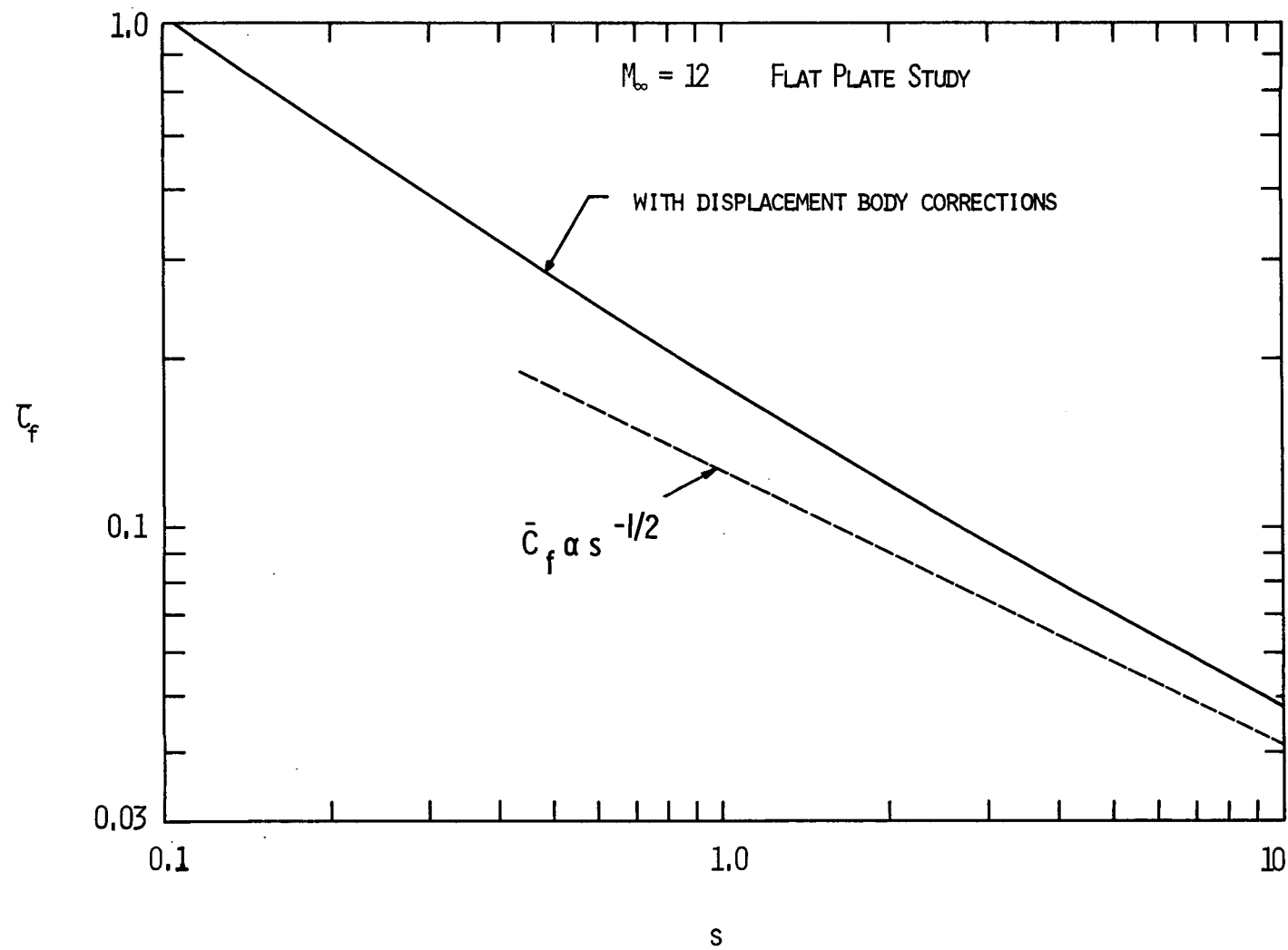


FIGURE 3.15 DISPLACEMENT BODY INFLUENCE ON FLAT PLATE SKIN FRICTION

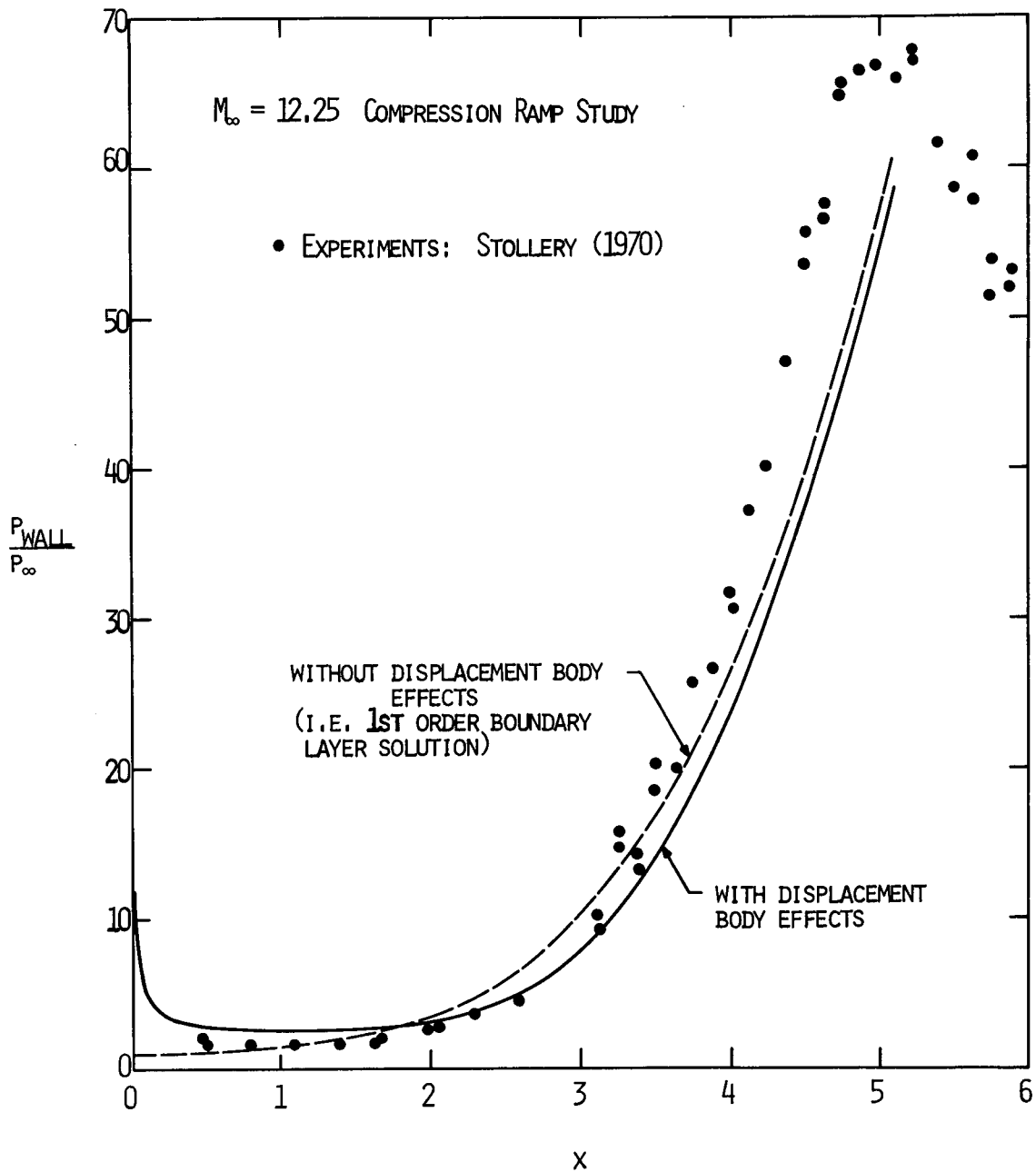


FIGURE 3.16 DISPLACEMENT BODY EFFECTS ON WALL PRESSURE -
NO CURVATURE CORRECTIONS

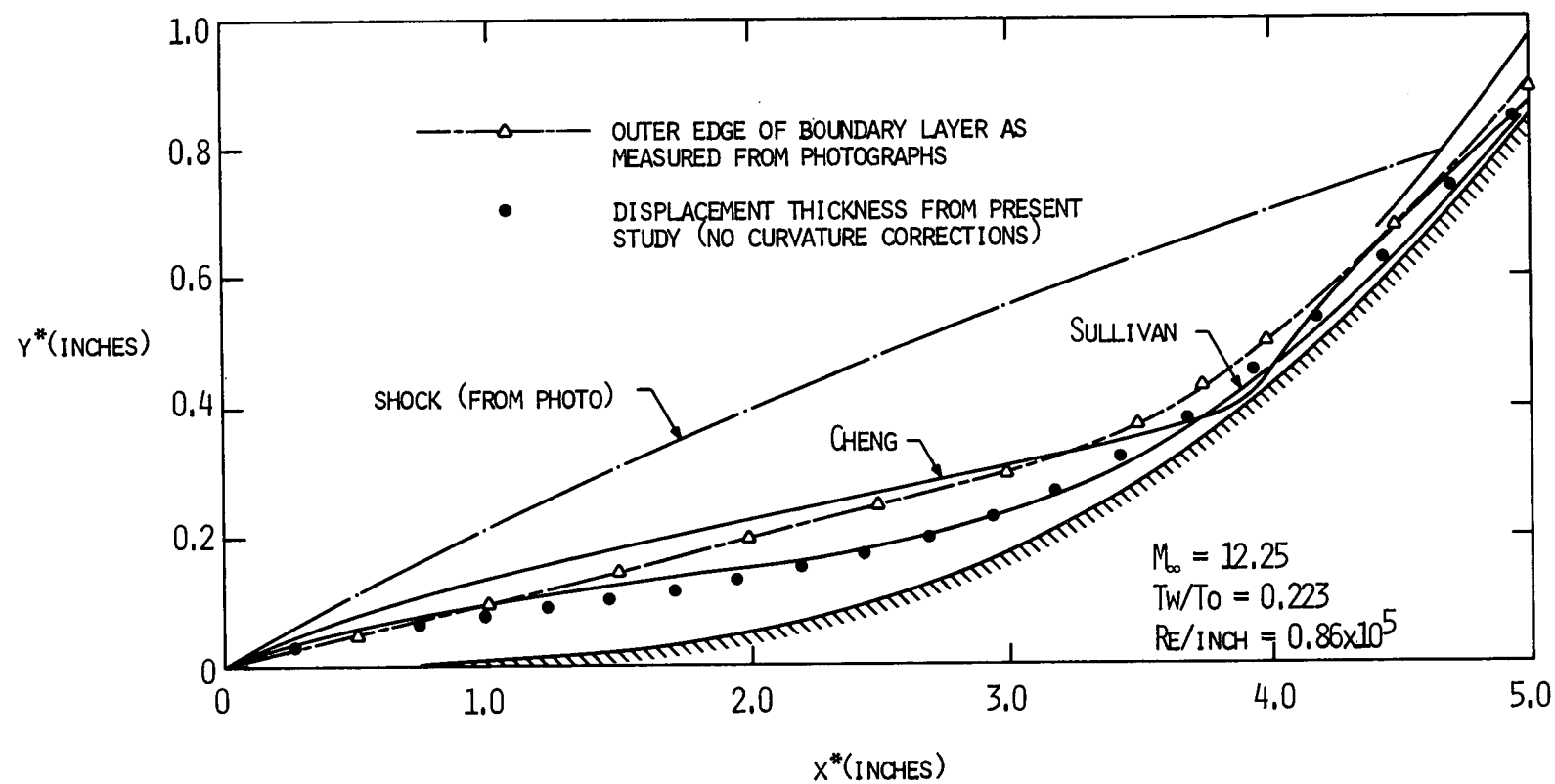


FIGURE 3.17 BOUNDARY LAYER GROWTH OVER A CUBIC BODY

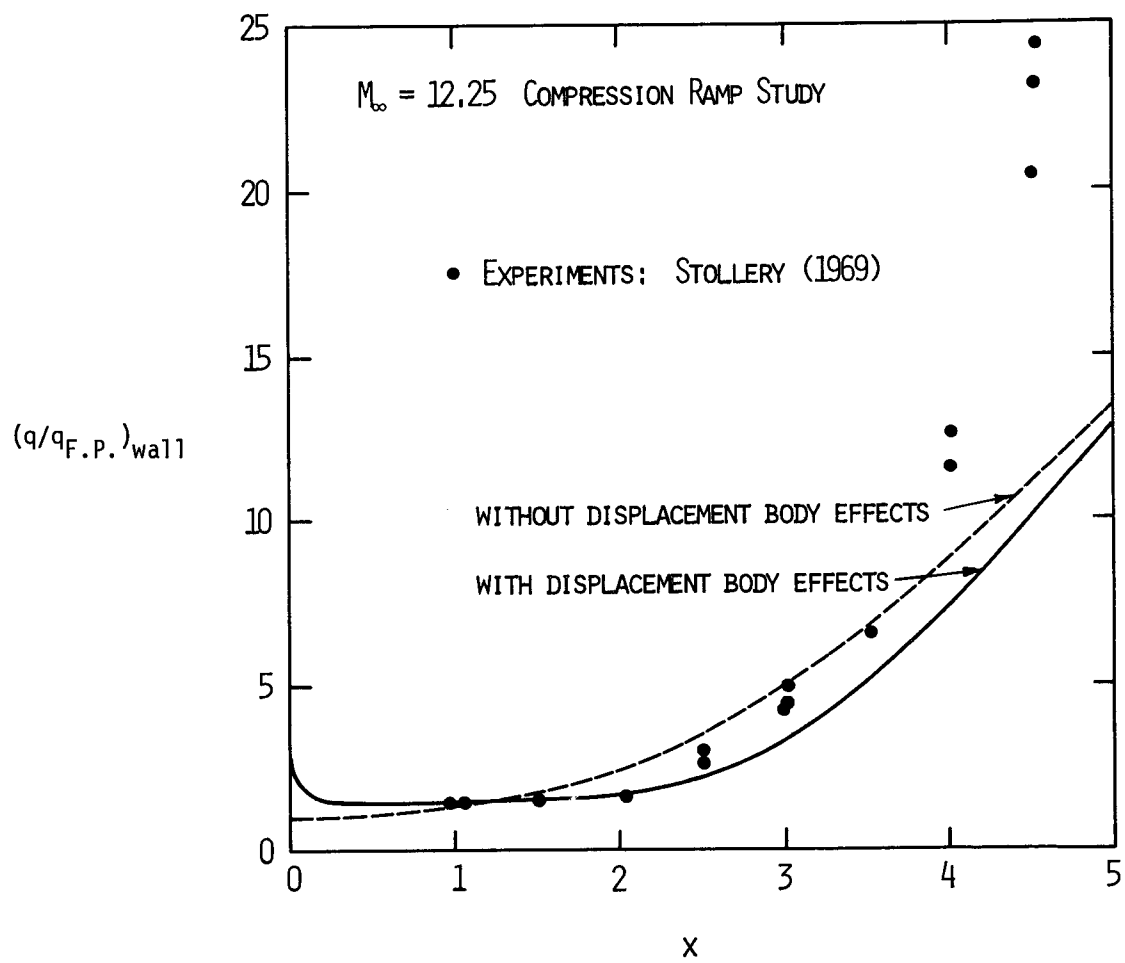


FIGURE 3.18 DISPLACEMENT BODY EFFECTS ON WALL HEAT TRANSFER

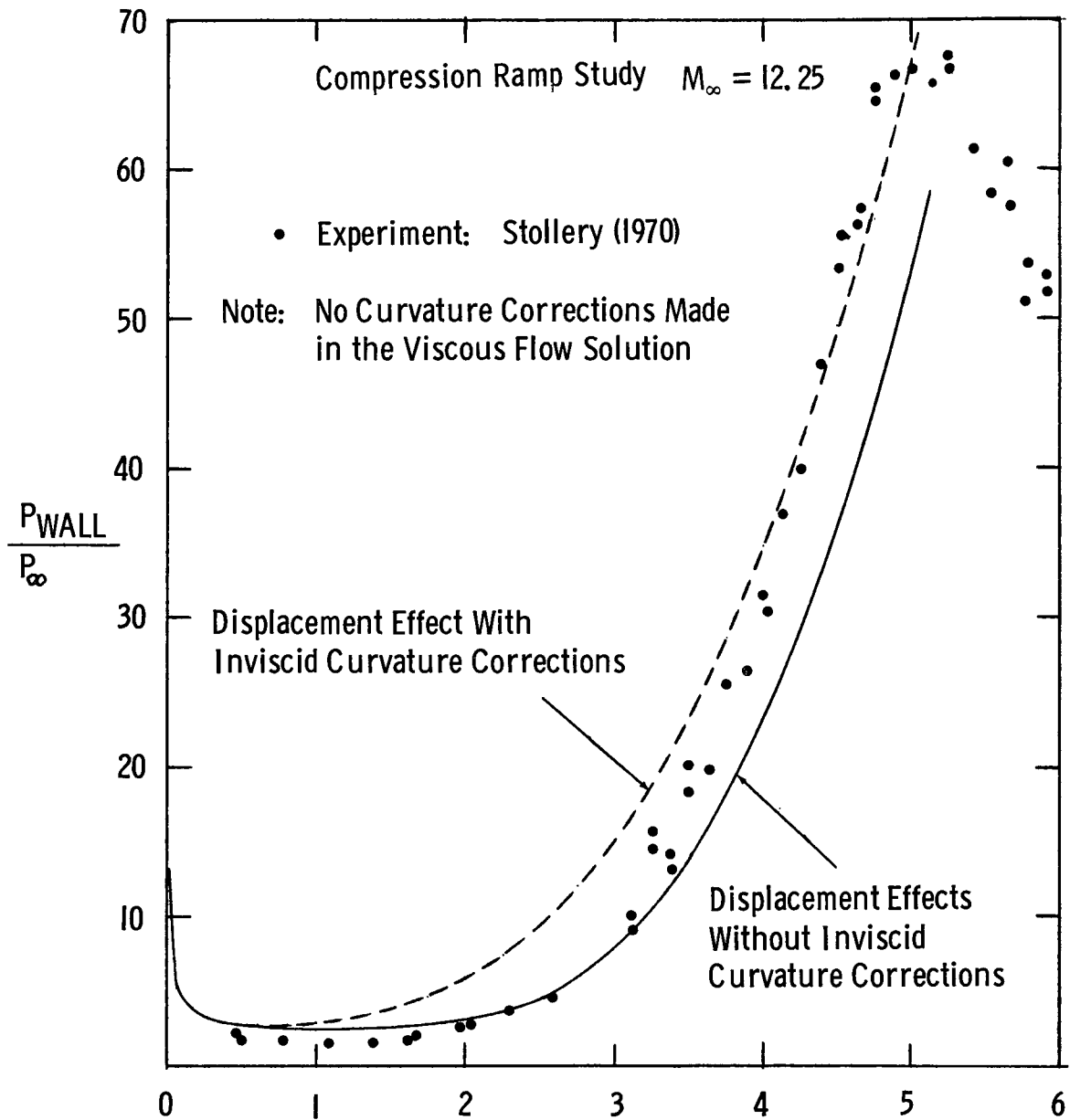


FIGURE 3.19 EFFECTS OF INVISCID CURVATURE CORRECTIONS ON WALL PRESSURE

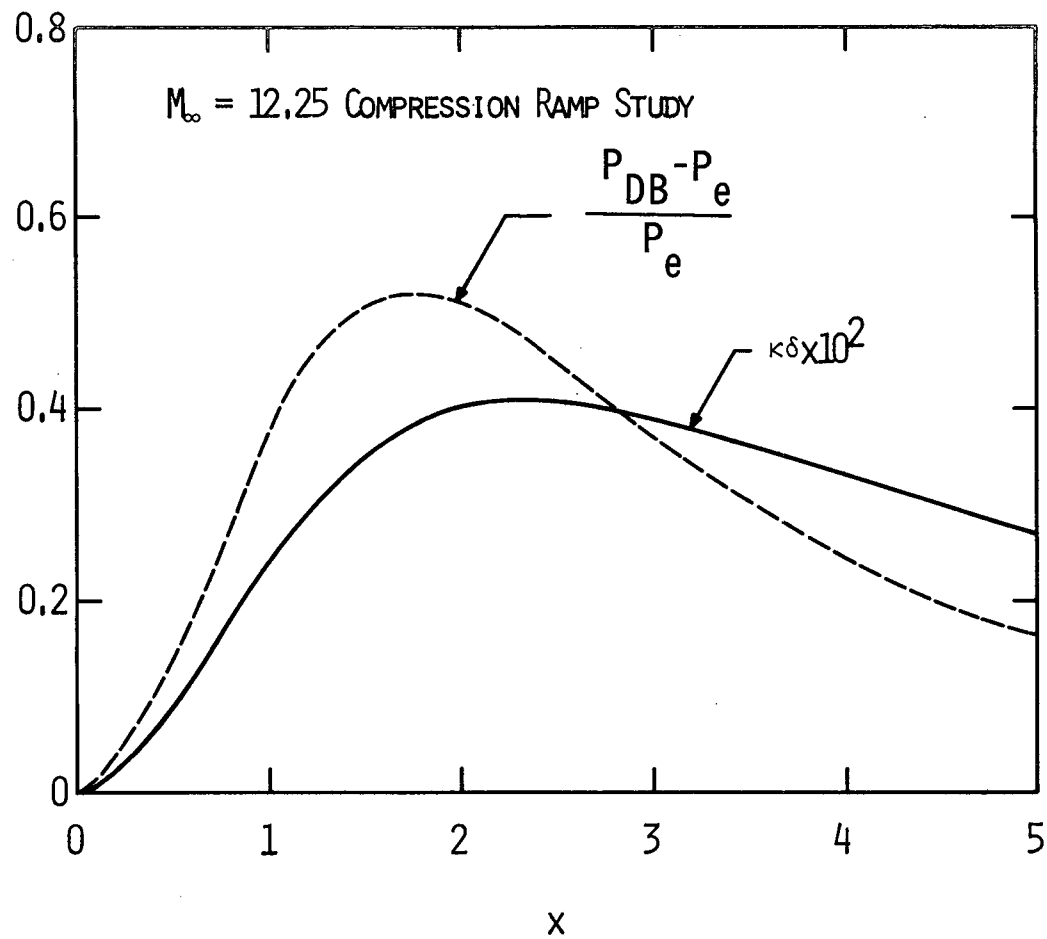


FIGURE 3.20 INFLUENCE OF INVISCID CURVATURE CORRECTIONS

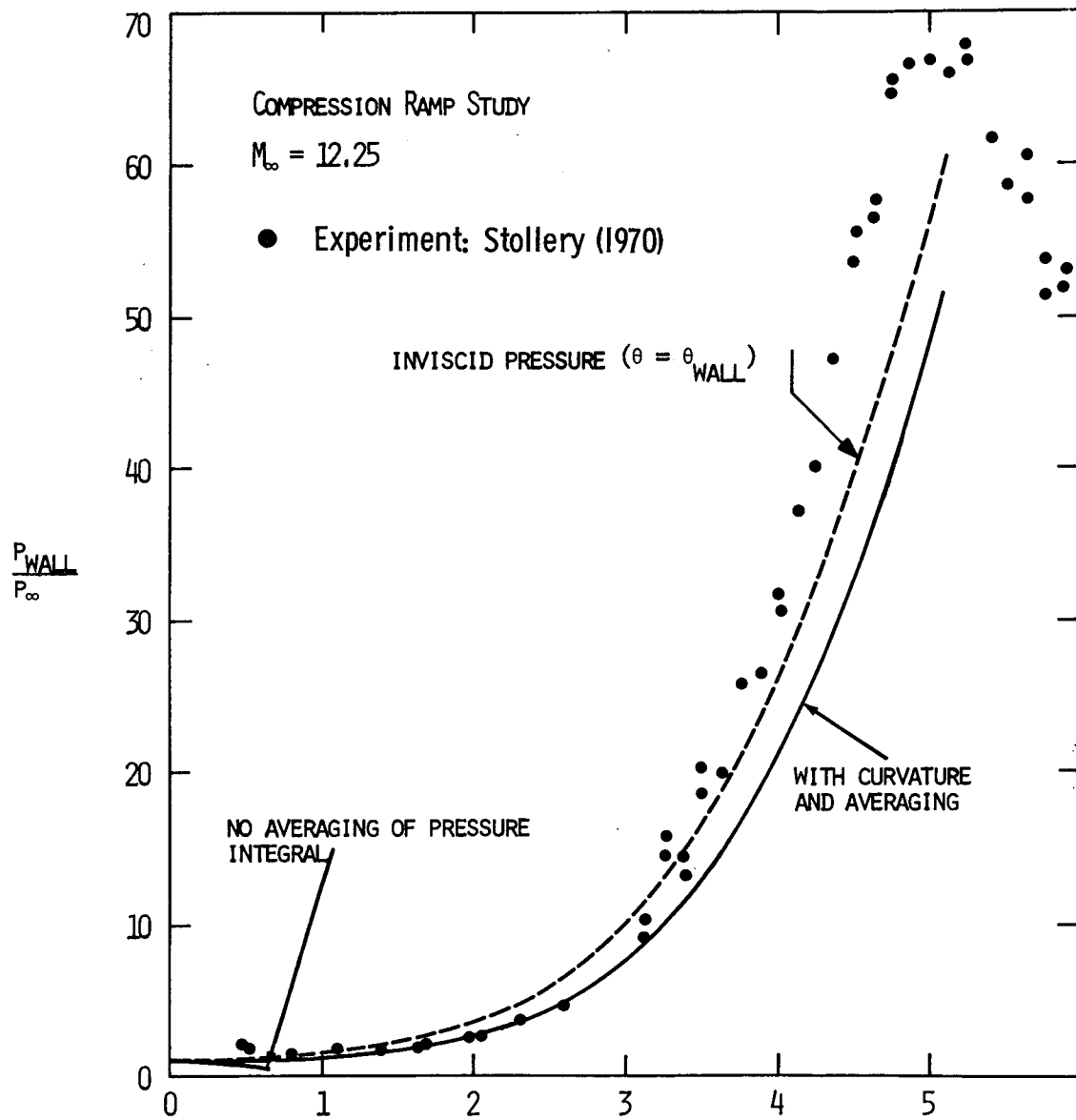


FIGURE 3.21 EFFECT OF CURVATURE ON NON-INTERACTING SOLUTION

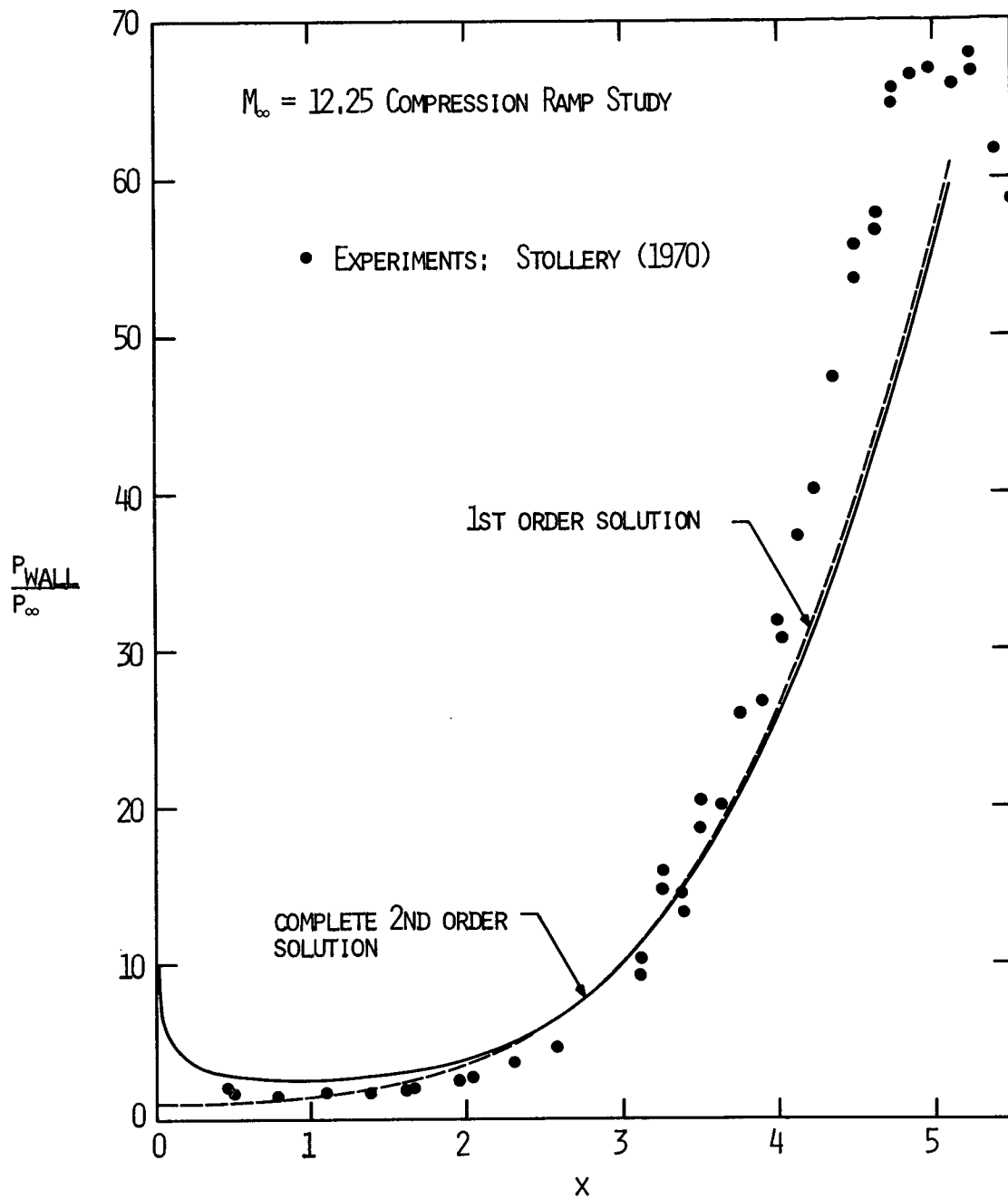


FIGURE 3.22 THE INFLUENCE OF DISPLACEMENT BODY AND CURVATURE EFFECTS ON WALL PRESSURE

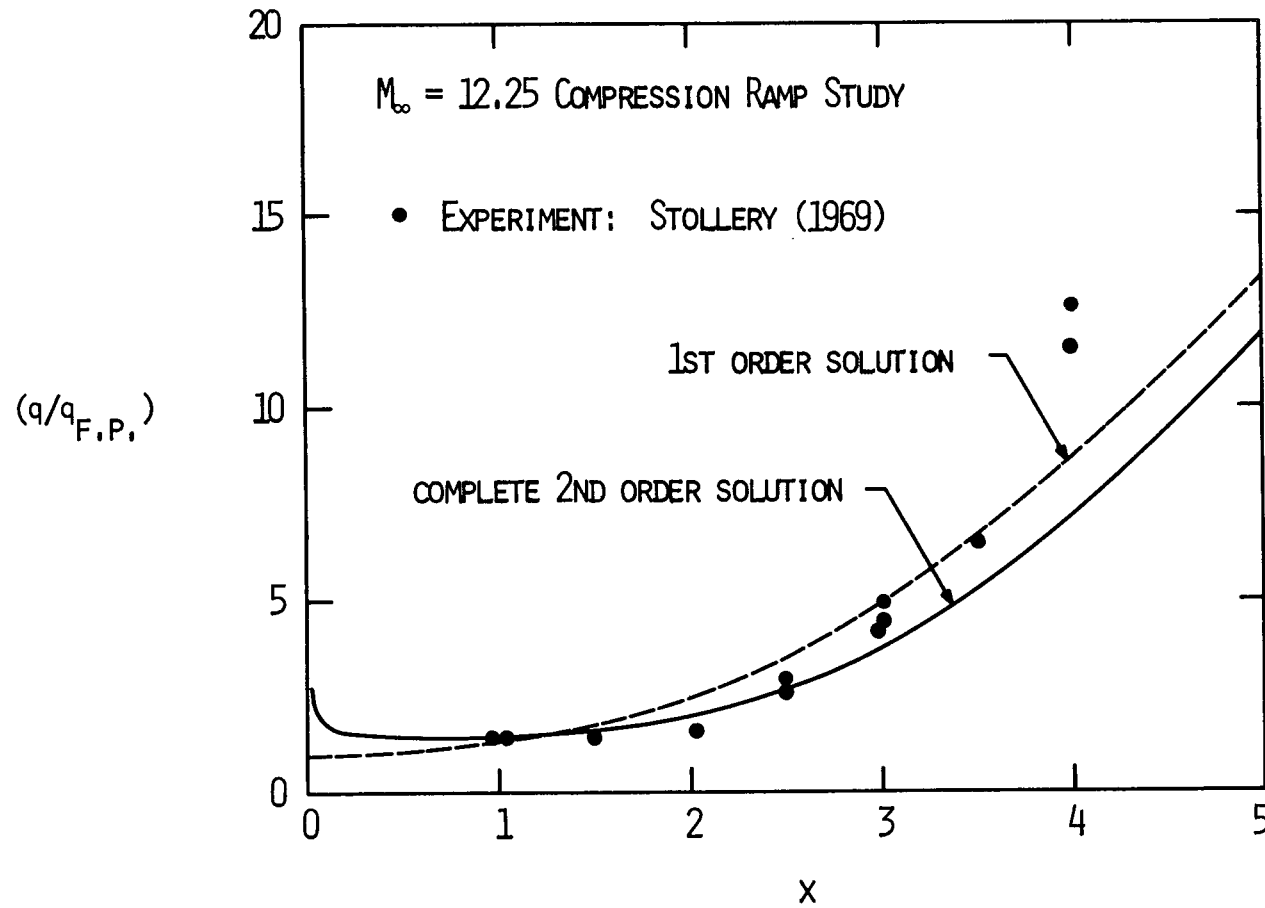


FIGURE 3.23 THE INFLUENCE OF DISPLACEMENT AND CURVATURE EFFECTS ON WALL HEAT TRANSFER

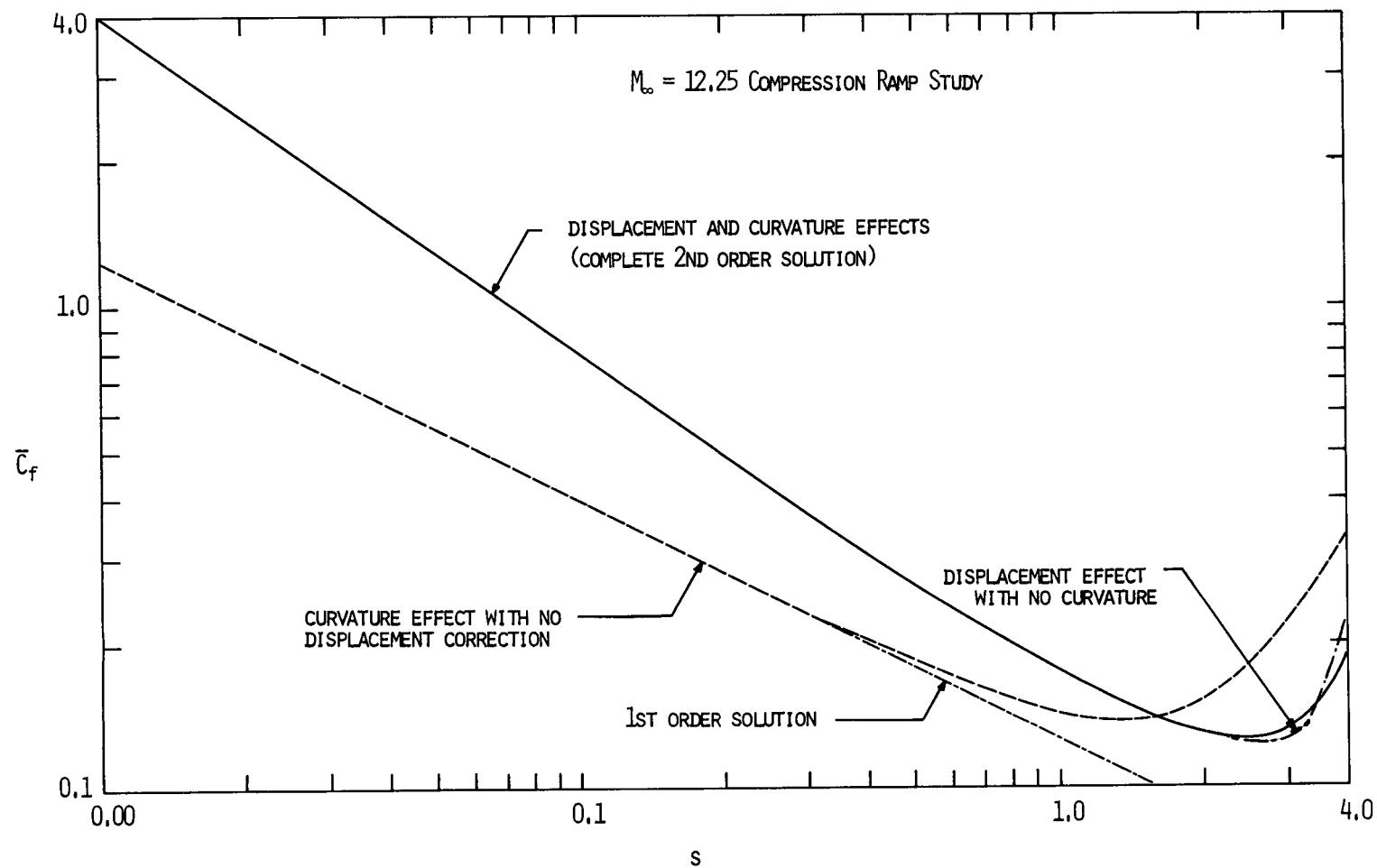


FIGURE 3.24 THE INFLUENCE OF DISPLACEMENT BODY AND CURVATURE EFFECTS ON SKIN FRICTION

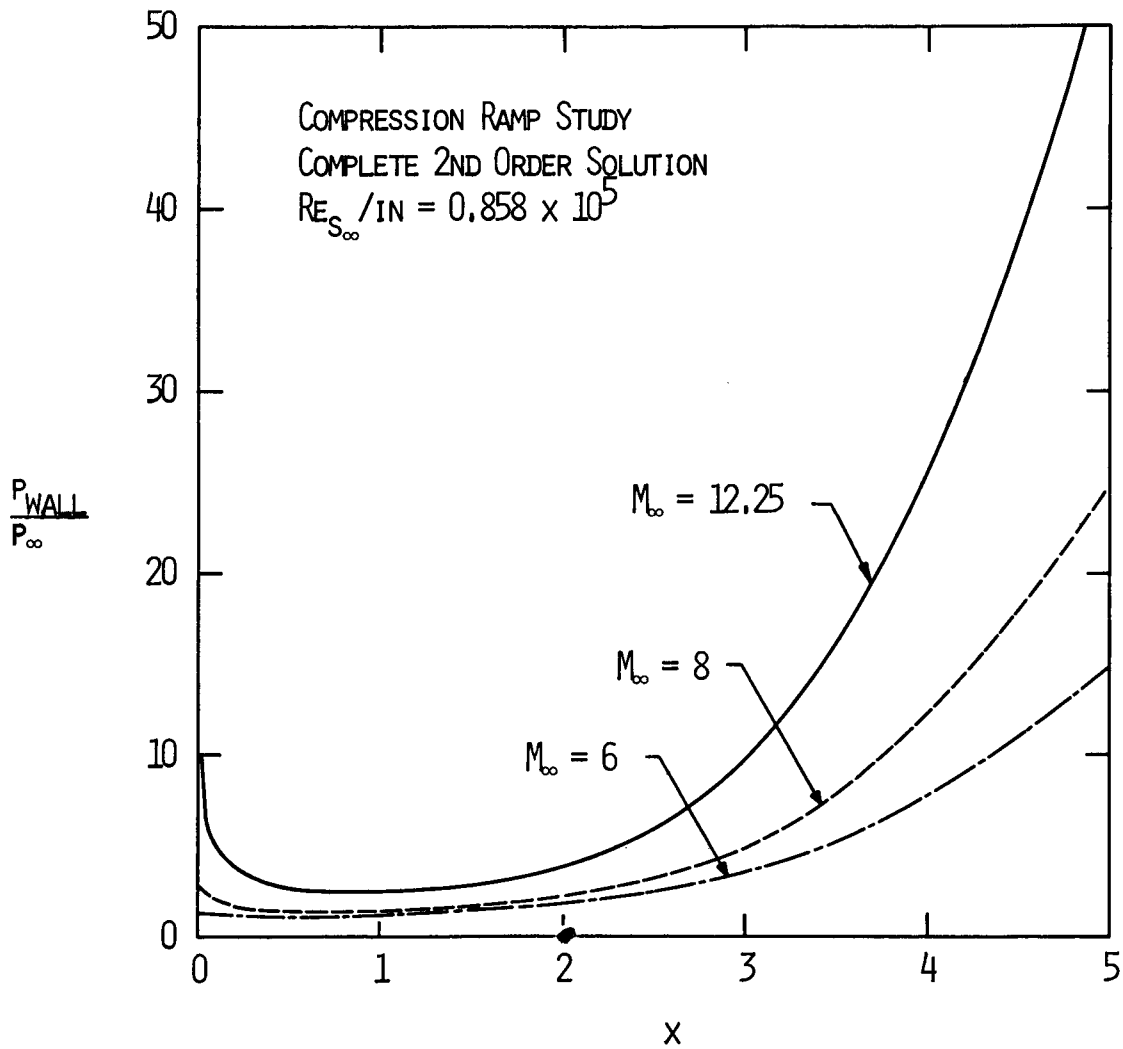


FIGURE 3,25 EFFECT OF FREE-STREAM MACH NUMBER ON WALL PRESSURE

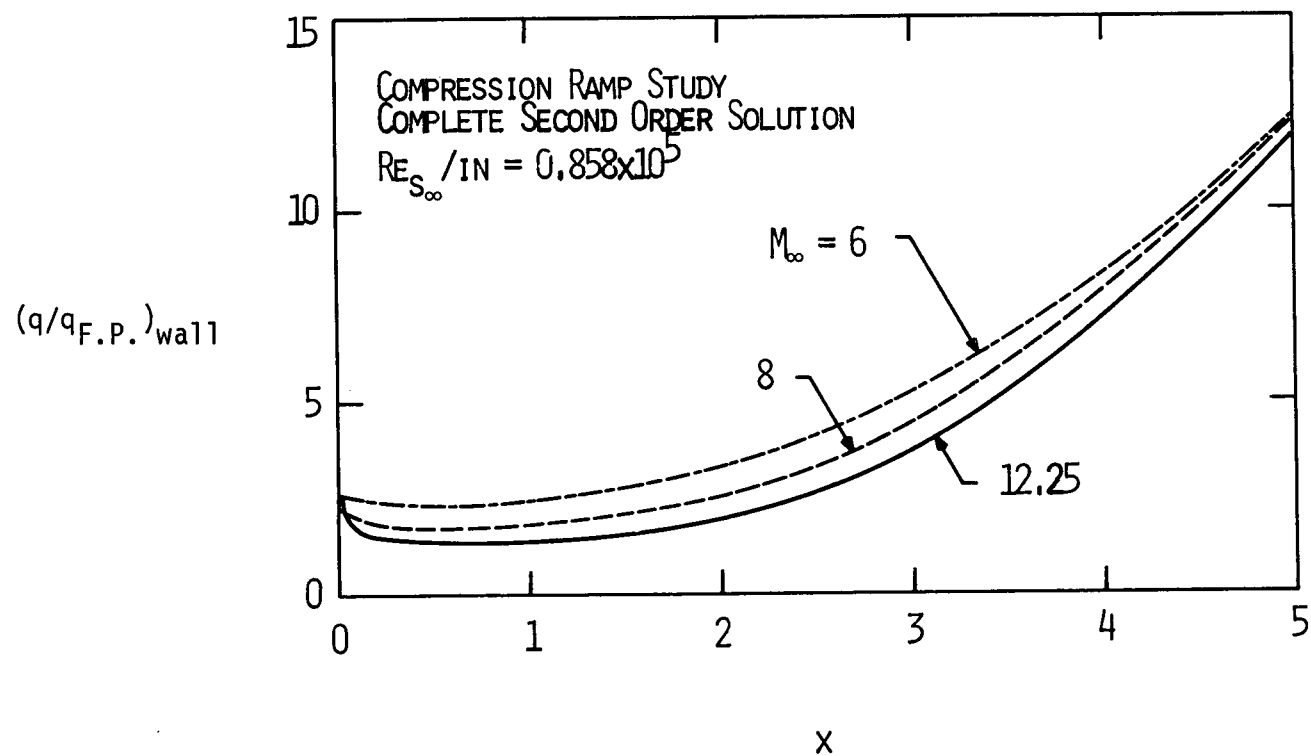


FIGURE 3.26 FREE STREAM MACH NUMBER INFLUENCE ON WALL HEAT TRANSFER

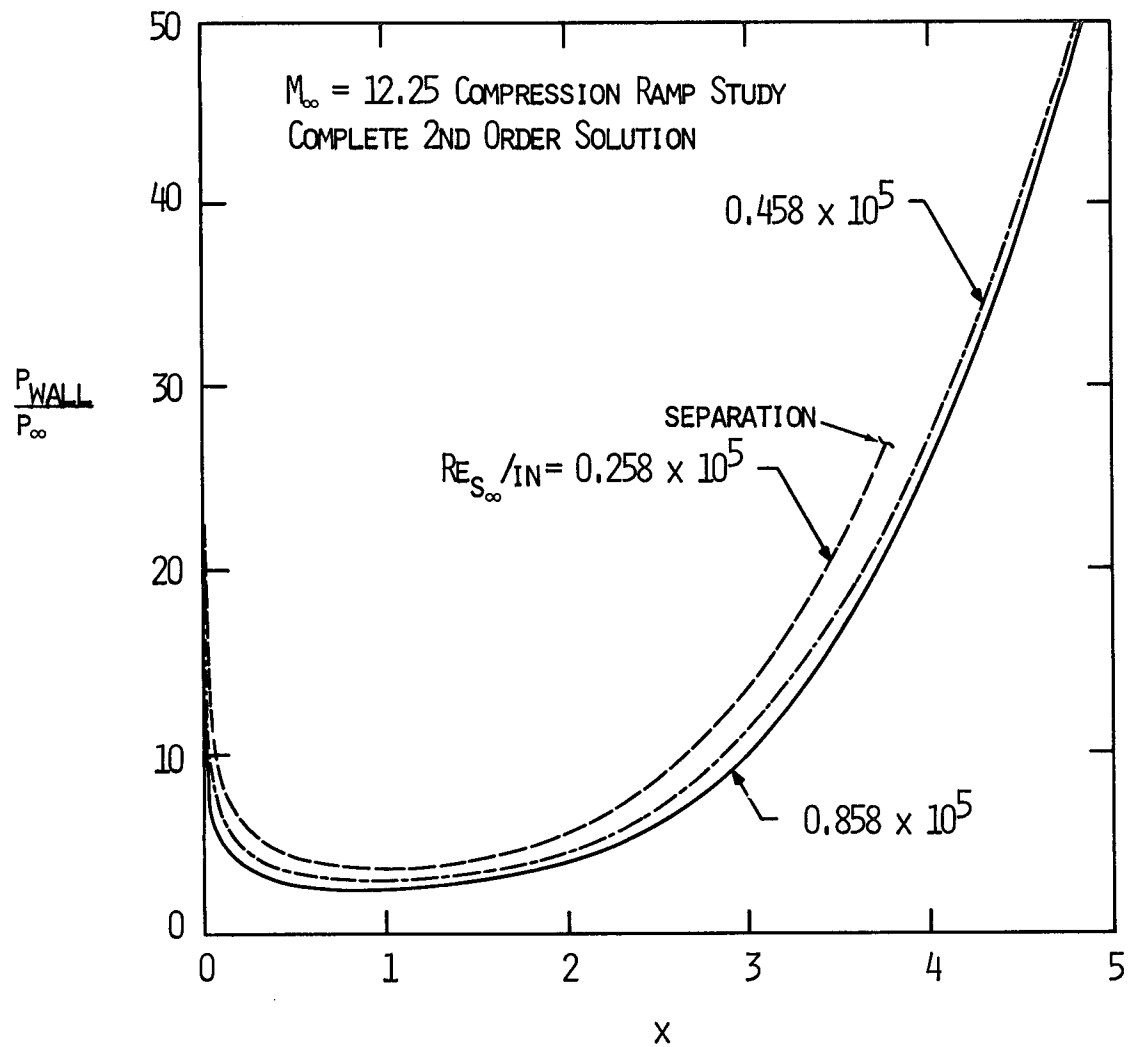


FIGURE 3.27 EFFECT OF FREE STREAM UNIT REYNOLDS NUMBER ON WALL PRESSURES

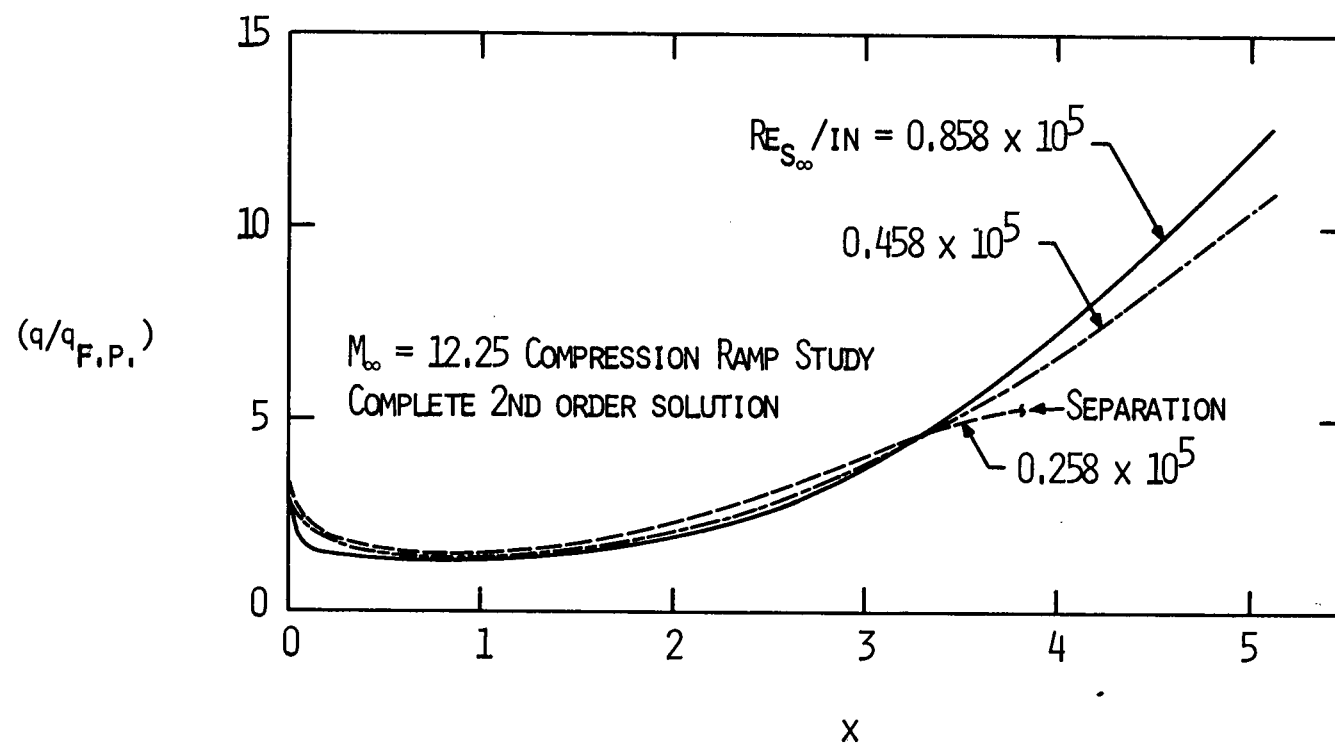


FIGURE 3.28 EFFECT OF FREE-STREAM REYNOLDS NUMBER ON HEAT TRANSFER TO WALL

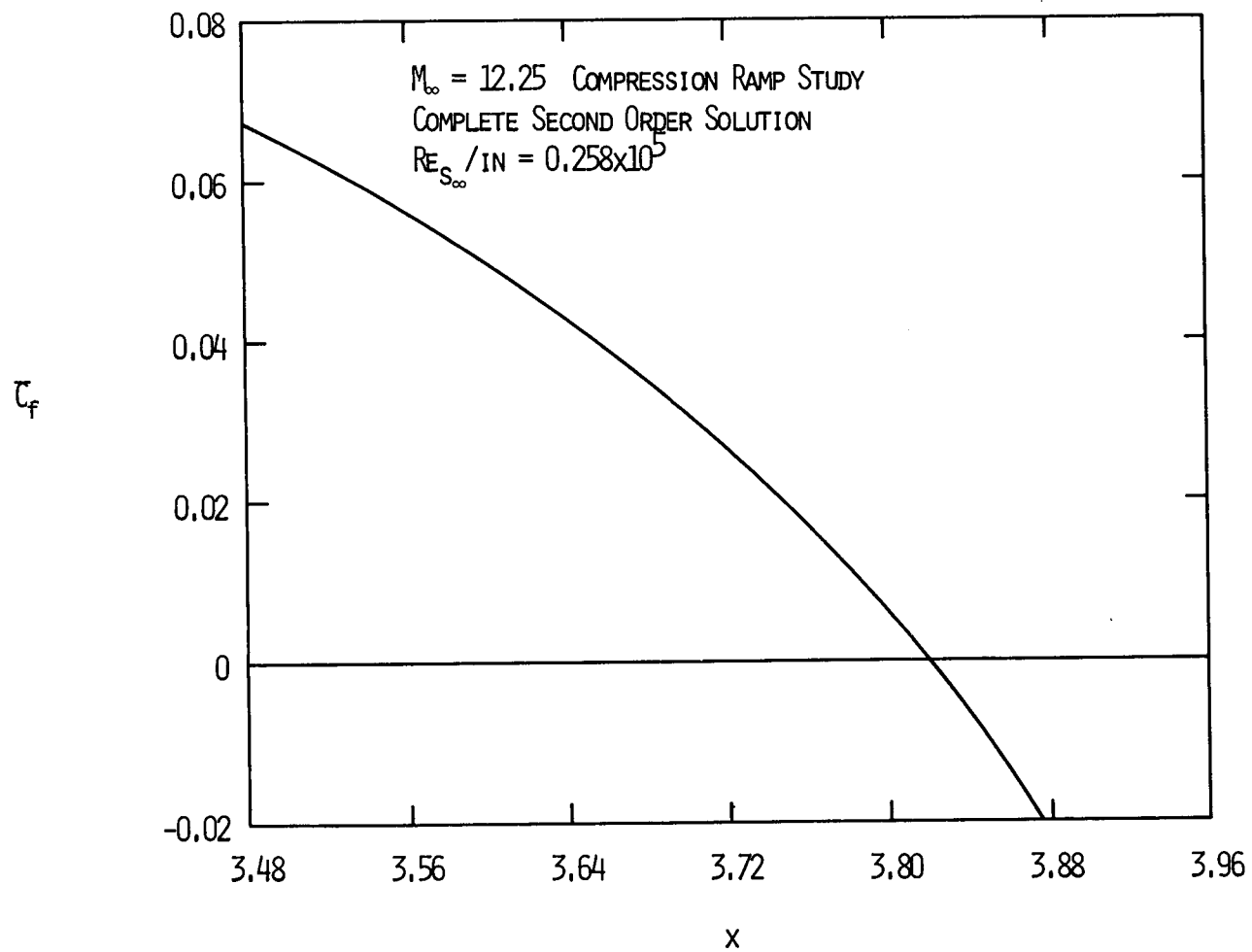


FIGURE 3.29 SKIN FRICTION DISTRIBUTION NEAR SEPARATION

VIII. ACKNOWLEDGEMENTS

The author would like to extend his appreciation to the following individuals or organizations:

To the Office of Naval Research who supported much of this study under contract number N0014-70-C-0024 Task 061-180.

To Dr. R. T. Davis under whom the author took most of his formal viscous flow and numerical analysis courses and whose support and contributions have been invaluable.

To Dr. M. J. Werle, the chairman of my committee, the author would like to extend special thanks for his patience, suggestions, and criticisms which the author considered to be invaluable. Appreciation is also extended to my entire committee.

Finally, the author would like to thank the National Aeronautics and Space Administration, Langley Research Center for allowing him to complete this study - especially the personnel of the 8-Foot Tunnels Branch.

IX. VITA

The author was born in the city of [REDACTED]. He attended public schools in the town of Poquoson, Virginia, where he graduated in 1958 from Poquoson High School. After attending the University of Richmond for one semester, he accepted a four-year apprenticeship with the Newport News Shipbuilding and Dry Dock Company, which he completed in 1963. Upon graduation from the Apprentice School, he entered Virginia Polytechnic Institute where he received his Bachelor of Science degree in engineering mechanics in 1967.

Since October of 1970, the author has been employed at the National Aeronautics and Space Administration, Langley Research Center, Hampton, Virginia.

[REDACTED]